TOR VERGATA
UNIVERSITÀ DEGLI STUDI DI ROMA

UNIVERSITÀ DEGLI STUDI DI ROMA "TOR VERGATA"
Facoltà di Scienze Matematiche Fisiche e Naturali

Scuola di Dottorato in Fisica

Ciclo XXXVII

Tesi di Dottorato

Ground-State and Many-Body Properties of Low-Dimensional Materials

Supervisors:

Prof. Olivia Pulci
Prof. Maurizia Palummo

External Supervisors:

Prof. Letizia Chiodo
Dr. Margherita Marsili

PhD Coordinator:

Prof. Massimo Bianchi

PhD Candidate:

Simone Grillo

ANNO ACCADEMICO 2024-2025

So scared of getting older
I'm only good at being young.

Contents

Abstract

This Thesis explores the ground-state and many-body properties of low-dimensional materials, focusing on their unique electronic, optical, and mechanical characteristics. Low-dimensional materials, including two-dimensional systems like graphene, one-dimensional materials such as nanowires, and zero-dimensional materials such as quantum dots, exhibit quantum confinement effects that significantly alter their properties compared to bulk materials. The Thesis not only explores the intrinsic properties of low-dimensional materials but also demonstrates how these properties can be tailored and controlled for specific applications. For example, the strong light absorption and excitonic effects observed in tellurene and 1D semiconducting wires suggest their potential use in high-efficiency solar cells and photodetectors. Moreover, the modulation of second-harmonic generation in materials like MoS_2 and WSe_2 by electric fields or charge doping offers new avenues for developing non-linear optical devices. The comprehensive analysis of zero-dimensional polyyne rings under electric fields sheds light on their potential for future terahertz technologies.
By employing state-of-the-art computational methods such as the GW approximation and the Bethe-Salpeter Equation, this work provides a more accurate depiction of quasi-particle and excitonic behaviors, advancing the understanding of many-body interactions in low-dimensional systems.
The Thesis is divided as follows:

- **Chapter 1** introduces the significance of low-dimensional materials, highlighting their classification into 2D, 1D, and 0D systems. The chapter underscores the importance of understanding their excited-state properties, which play a crucial role in their interaction with light, response to external stimuli, and optoelectronic applications.

- **Chapter 2** provides the theoretical background for ground-state properties, discussing the many-body problem and the Born-Oppenheimer approximation. It introduces density functional theory, explaining the Hohenberg-Kohn theorems and the Kohn-Sham equations, which simplify the complex many-body problem into a set of single-particle equations. The chapter also delves into the challenges of DFT, such as the band gap problem and the approximation of the exchange-correlation functional, as well as its computational implementations.

- **Chapter 3** covers the theoretical background for electronic properties, focusing on methods to study excited states. It introduces photoemission spectroscopy and the Green's functions formalism, including the Lehmann representation and Hedin's equations. The chapter emphasizes the GW approximation, which corrects the limitations of DFT in predicting quasi-particle energies and provides more accurate descriptions of electronic properties in low-dimensional materials.

- **Chapter 4** examines optical properties, detailing how light interacts with matter in low-dimensional systems. It discusses the calculation of optical properties using DFT and the GW approximation, introducing the concept of exciton and the Bethe-Salpeter Equation to describe the formation and behavior of electron-hole pairs in these systems.
- **Chapter 5** presents the results and discussions, exploring the properties of different low-dimensional materials. For 2D materials, it investigates tellurene polymorphs, highlighting their potential for solar energy harvesting due to the strong exciton anisotropy and high optical absorbance. Furthermore, it discusses how second-harmonic generation in MoS_2 and WSe_2 can be induced and modulated by the application of an electric field or by charge doping, exploring the physics behind non-linear optics phenomena. In 1D materials, this thesis focuses on excitonic effects in semiconducting atomic wires identified through high-throughput screening of exfoliable bulk systems. For 0D materials, it explores the tunable electric-field-driven terahertz splitting in the polyyne C_{18} carbon ring, offering valuable insights into the excited-state properties of these carbon systems.
- **Chapter 6** concludes the thesis, summarizing the contributions to the understanding of ground-state and excited-state properties in low-dimensional materials.

Keywords: DFT, MBPT, BSE, 2D, 1D, 0D, tellurene, TMD, wire, cyclocarbons, exciton, non-linear optics

Abbreviations and symbols

AFM	atomic force microscopy
BSE	Bethe-Salpeter equation
BZ	Brillouin zone
CBM	conduction band minimum
CC	cyclo[n]carbon
CNT	carbon nanotube
DFT	density functional theory
GGA	generalized gradient approximation
GTO	gaussian-type orbital
HF	Hartree-Fock
HOMO	highest occupied molecular orbital
HK	Hohenberg-Kohn
HT	high-throughput
IPA	independent-particle approximation
IQP	independent quasi-particle
IR	infra-red
KS	Kohn-Sham
LDA	local density approximation
LFE	local-field effects
LUMO	lowest unoccupied molecular orbital
MBE	molecular beam epitaxy
MBPT	many-body perturbation theory
ML	monolayer
MO	molecular orbital
PBE	Perdew-Burke-Ernzerhof
PCE	power conversion efficiency
PPA	plasmon-pole approximation
PW	plane wave
QE	Quantum ESPRESSO
QP	quasi-particle
RPA	random-phase approximation
SCC	short-circuit current
SHG	second-harmonic generation
SOC	spin-orbit coupling
SOJTE	second-order Jahn-Teller effect
UV	ultra-violet

VBM	valence band maximum
vdW	van der Waals
TDA	Tamm-Dancoff approximation
TDDFT	time-dependent density functional theory
THz	Terahertz
XC	exchange-correlation
0D	zero-dimensional
1D	one-dimensional
1L	monolayer
2D	two-dimensional
2L	bilayer
3D	three-dimensional

Chapter 1

Introduction

In recent years, low-dimensional materials have attracted substantial attention due to their unique electronic, optical, and mechanical properties, drastically different from their bulk counterparts. These materials exhibit quantum confinement effects that fundamentally alter their behavior, making them ideal candidates for applications in emerging technologies such as nanoelectronics, photonics, energy conversion, and quantum computing.
Low-dimensional materials can be classified on the basis of the number of spatial dimensions in which electrons are free to move:

- Two-dimensional (2D) materials, such as graphene and other Xenes, hexagonal boron nitride (h-BN), and transition metal dichalcogenides (TMDs), consist of single or few layers of atoms and exhibit remarkable properties such as high mobility, tunable band gaps, and large exciton binding energies.
- One-dimensional (1D) materials, including nanowires and nanotubes, confine electrons along one axis, resulting in highly anisotropic charge transport and exciton dynamics.
- Zero-dimensional (0D) materials, like quantum dots and carbon nanorings, confine electrons in all directions, leading to discrete energy levels and strong quantum effects.

One of the most intriguing aspects of low-dimensional materials is their excited-state properties, which describe how these materials behave when they absorb energy and transition to higher-energy states. Understanding these properties is crucial because they directly influence how these materials interact with light, respond to external stimuli, and conduct electricity under non-equilibrium conditions. Excited states in low-dimensional systems are highly sensitive to environmental factors such as temperature, strain, and dielectric environment. As a result, they provide a wealth of information about the intrinsic properties of the material. Although ground-state properties are often sufficient for understanding equilibrium behaviors, many of the most promising applications of low-dimensional materials depend on excited states, which provide deeper insights into phenomena such as electron-hole pair formation, optical absorption, luminescence, and photocatalysis.
The study of excited states is essential for several reasons:

- **Fundamental understanding of quantum phenomena**: low-dimensional materials exhibit quantum confinement, where the motion of electrons and holes is restricted in one or

more dimensions. This confinement significantly alters the density of states and leads to pronounced excitonic effects — where bound electron-hole pairs (excitons) play a dominant role in the material's optical properties. In 2D materials like TMDs, excitons can have binding energies an order of magnitude larger than those in bulk semiconductors. Similarly, in 1D systems like nanowires and 0D systems like quantum dots, excitonic effects are magnified, making them crucial for both fundamental quantum mechanics and potential applications.

- **Optoelectronic applications**: many of the potential applications of low-dimensional materials arise from their excited-state behavior. For example, 2D materials exhibit exceptional optical absorption and can be engineered for use in photodetectors, light-emitting diodes (LEDs), and solar cells. The ability to tune optical properties via exciton manipulation, band gap engineering, and light-matter interaction allows for the development of high-efficiency devices with customizable characteristics. This makes the understanding of excited states vital for the design of next-generation optoelectronic devices. Similarly, low-dimensional materials are considered highly promising candidates for photovoltaics and photocatalysis, owing to their ability to absorb and convert sunlight into electricity or chemical energy efficiently. Tunable band gaps, using different means, allow for optimized absorption across different regions of the solar spectrum, while their strong exciton binding enhances charge separation and transport. This makes them particularly suitable for solar harvesting and water-splitting applications.

- **Emerging technologies**: beyond traditional electronics and photonics, the excited-state properties of low-dimensional materials are key to realizing advanced technologies such as quantum computing and spintronics. For example, materials with strong spin-orbit coupling (SOC), such as topological insulators or monolayers of TMDs, can be used to manipulate electron spins for information processing at the quantum level. Similarly, single-photon emitters based on excitonic recombination in 0D materials are essential for the development of quantum light sources for quantum communication.

The focus of this thesis is on leveraging advanced computational techniques, including Density Functional Theory (DFT) and Many-Body Perturbation Theory (MBPT), to explore the excited-state properties of these systems. These computational methods, especially post-DFT techniques like the GW approximation and the Bethe-Salpeter Equation (BSE), are essential for accurately predicting these features and represent the state-of-the-art in the field of theoretical and computational condensed matter physics.
In conclusion, the study of excited-state properties in low-dimensional materials is not only a fundamental scientific endeavor but also a gateway to numerous applications that will shape the future of technology. By exploring the intricate behaviors of electrons in these confined systems, this work aims to contribute to a broader understanding of their potential and provide a foundation for future innovations and technologies.

Chapter 2

Theoretical Background: Ground-State Properties

In this chapter, we review the theoretical background of density functional theory (DFT), its limitations, and its practical implementations. While the main results presented in this thesis were obtained using post-DFT methods, DFT remains the foundation of almost every ab initio calculation, providing an essential tool for the prediction of the crystal structure and the electronic and optical properties of materials.

2.1 The Many-Body Problem

The study of systems composed of many interacting particles probably represents the main issue in the field of condensed matter physics and, in general, in quantum mechanics. Such systems, consisting, e.g., of electrons and ions, can be described by the following Hamiltonian:

$$H = T_{ion} + T_e + V_{ee} + V_{e-ion} + V_{ion-ion} \tag{2.1}$$

where the terms in (2.1) correspond to:

- $T_{ion} = -\frac{\hbar^2}{2} \sum_I \frac{\nabla^2_{R_I}}{M_I}$, the kinetic energy of the ions;
- $T_e = -\frac{\hbar^2}{2m} \sum_i \nabla^2_{r_i}$, the kinetic energy of the electrons;
- $V_{ee} = \frac{1}{2} \sum_{i \neq j} \frac{e^2}{|\mathbf{r}_i - \mathbf{r}_j|}$, the Coulomb potential due to the electron-electron interactions (repulsive term);
- $V_{e-ion} = -\sum_{i,I} \frac{Z_I e^2}{|\mathbf{R}_I - \mathbf{r}_i|}$, the Coulomb potential due to the electron-ion interactions (attractive term);

- $V_{ion-ion} = \frac{1}{2} \sum_{I \neq J} \frac{Z_I Z_J e^2}{|\mathbf{R}_I - \mathbf{R}_J|}$, the Coulomb potential due to the ion-ion interactions (repulsive term).

Here we have considered the most general case in which ions can all possess different masses. Coordinates $\mathbf{r}_i$ and $\mathbf{R}_I$ are the sets of spatial coordinates of electrons and nuclei, respectively. For the sake of simplicity, the spin contributions have been neglected.
Solving the Schrödinger equation associated with Hamiltonian (2.1) would, in principle, allow us to calculate the wavefunction of the many-body system, thus providing access to all its physical properties. In theory, this argument holds regardless of the number of interacting particles. However, in practice, even for a few particles and using robust numerical methods, finding the exact solution to the many-body Schrödinger equation is a highly complex task. Moreover, when dealing with systems like molecules or solids, where the number of interacting particles can be on the order of 10^{23}, solving this problem exactly becomes essentially impossible.
Therefore, we need appropriate approximations that enable us to manipulate and simplify the problem.

2.2 The Born-Oppenheimer Approximation

The first approximation is motivated by the significant difference in the masses of nuclei and electrons: this disparity, typically ranging from 3 to 5 orders of magnitude, results in the orbital period of electrons being around 10^{-17} s, while the characteristic periods of nuclear motion are about 10^{-13} s. Due to this large difference, it is reasonable to decouple the dynamics of the nuclei from those of the electrons. This decoupling is conceptually achieved through the so-called *adiabatic principle*. In this context, the principle can be summarized as follows: initially, the nuclei are considered as *fixed* at selected spatial configurations, and the focus is placed on the behavior of the electrons as a function of the chosen nuclear coordinates. This approach allows us to determine the so-called *adiabatic potential energy surfaces*, as depicted in Fig. 2.1, which represent the potential energy landscape of the nuclear Hamiltonian. Once these adiabatic surfaces $E_i(R)$ are known as functions of the nuclear coordinates (collectively denoted by R), the nuclear dynamics can then be studied.
Born and Oppenheimer demonstrated how to exploit this principle to describe the interdependence between electronic properties and nuclear dynamics [1]. Consequently, this approach is generally referred to as the *Born-Oppenheimer approximation*. As mentioned earlier, this approximation results in an electronic Hamiltonian with fixed nuclear positions (or, more generally, fixed ion positions):

$$\begin{aligned} H_e \phi_m(\mathbf{r}_i, \{R_I\}) &= (T_e + V_{ee} + V_{e-ion} + V_{ion-ion}) \phi_m(\mathbf{r}_i, \{R_I\}) \\ &= E_m(\{R_I\}) \phi_m(\mathbf{r}_i, \{R_I\}) \end{aligned} \tag{2.2}$$

where the dependence from R_I is only parametric, and a nuclear Hamiltonian:

$$H_{ion} \chi_s(R_I) = [T_{ion} + E_s(R_I)] \chi_s(R_I) = E \chi_s(R_I) \tag{2.3}$$

in which the nuclei (or ions) move in the potential $E_s(R)$ due to the electrons.

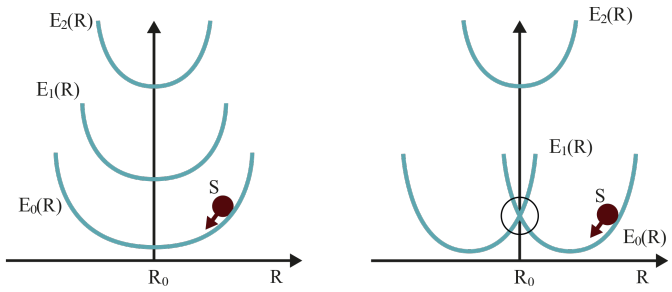

Figure 2.1: *Schematic representation of adiabatic potential energy surfaces $E_i(R)$, where the multi-dimensional nuclear variable R is represented as a one-dimensional parameter. (Left) The adiabatic surface of interest is supposed non-degenerate, and the nuclear dynamics of the system S is mostly determined by the single non-degenerate potential surface under consideration. (Right) Two (or more) adiabatic surfaces are degenerate at R_0, and the nuclear dynamics of the system S is determined by the whole set of degenerate adiabatic surfaces.*

Solving Eqs. (2.2) and (2.3) provides the wavefunctions and energies of both the electrons and the nuclei. The problem we aim to address is now represented by a system of interacting electrons in the external field created by the nuclei.
However, even with this significant simplification, solving the electronic Eq. (2.2) remains a problem involving $4N$ variables, N being the total number of electrons. To avoid dealing with the full $4N$-variable equation, one may consider an integrated variable to describe the system, such as the electronic density:

$$n(\mathbf{r}) \equiv N \int |\Psi(\mathbf{r}, \mathbf{r}_2, ..., \mathbf{r}_N)|^2 d\mathbf{r}_2 ... d\mathbf{r}_N$$

where Ψ is the N-electron wavefunction. We will explore this idea in the next section.

2.3 Density Functional Theory (DFT)

The idea of shifting the focus from the complex many-body ground-state wavefunction to the more manageable ground-state one-body electron density $n(\mathbf{r})$ originated from early efforts to develop variational methods. These methods aimed to express the energy and other physical observables of a system as functionals of the electron density. Notable examples of such efforts include the density-dependent exchange functional introduced by the works of Thomas and Fermi and Slater [2–4]. However, it was the groundbreaking work of Hohenberg and Kohn [5] (1964) and Kohn and Sham [6] (1965) — work that eventually earned W. Kohn the Nobel Prize in Chemistry in 1998 — that provided a solid theoretical foundation for the use of electron density. This revolutionary development

is known as *Density Functional Theory* (DFT).
DFT is based on the principle that any ground-state property of a many-body system, particularly the ground-state energy, can be expressed as a functional of the ground-state electron density $n_0(\mathbf{r})$. This allows the reformulation of the many-body problem into one that depends on the density of independent particles within an effective mean-field potential, which approximates the interacting system. The resulting independent-particle equations are known as the Kohn-Sham equations (see Sec. 2.3.2).

2.3.1 The Hohenberg-Kohn Theorems

DFT is based on the theorems first proved by Hohenberg and Kohn [5]. This approach applies to any system of interacting particles in an external potential $V_{\text{ext}}(\mathbf{r})$, including the many-body problem of interacting electrons and fixed nuclei, where the Hamiltonian can be written as:

$$\begin{aligned} H &= -\sum_i \frac{\hbar^2 \nabla_i^2}{2m} + \frac{1}{2}\sum_{i\neq j} \frac{e^2}{|\mathbf{r}_i - \mathbf{r}_j|} - \sum_{i,I} \frac{Z_I e^2}{|\mathbf{r}_i - \mathbf{R}_I|} \\ &= -\sum_i \frac{\hbar^2 \nabla_i^2}{2m} + \frac{1}{2}\sum_{i\neq j} \frac{e^2}{|\mathbf{r}_i - \mathbf{r}_j|} + \sum_i V_{ext}(\mathbf{r}_i) \end{aligned} \tag{2.4}$$

The first Hohenberg and Kohn theorem reads:

Theorem 1 . *For any system of interacting particles in an external potential $V_{ext}(\boldsymbol{r})$, and with a non-degenerate ground state, the potential $V_{ext}(\boldsymbol{r})$ is determined uniquely, except for a constant, by the ground-state particle density $n_0(\boldsymbol{r})$.*

This theorem can be proved via a *reductio ad absurdum*. The procedure is reported schematically in Fig. 2.2
We introduce the set of external potentials $\{V_{\text{ext}}(\mathbf{r})\}$, the set of ground-state wavefunctions $\{\Psi_0\}$ and the set of electron ground-state densities $\{n_0(\mathbf{r})\}$. Since the wavefunctions are solutions of the equation:

$$H|\Psi_0\rangle = E|\Psi_0\rangle$$

with H containing $V_{\text{ext}}(\mathbf{r})$, we can define a mapping C from the set of the external potentials $\{V_{\text{ext}}(\mathbf{r})\}$ to the set of wavefunctions $\{\Psi_0\}$. Then, we can define a mapping D from the wavefunctions set to the densities set $\{n_0(\mathbf{r})\}$, since the density is defined as:

$$n_0(\mathbf{r}) = N \int \Psi_0(\mathbf{r}, \mathbf{r}_2, ...\mathbf{r}_N)\Psi_0^*(\mathbf{r}, \mathbf{r}_2, ...\mathbf{r}_N) d\mathbf{r}_2 ... d\mathbf{r}_N$$

Here, we suppose that the ground state of the system Ψ_0 is non-degenerate (anyway, the restriction of non-degeneracy, as well as other assumptions, can be relaxed when required).

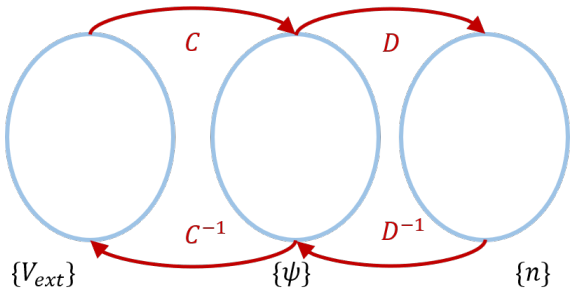

Figure 2.2: *Mappings between the sets of external potentials* $\{V_{\text{ext}}\}$*, wavefunctions* $\{\psi\}$ *and densities* $\{n\}$*, and their inverse*

To prove the theorem, we suppose that the inverse maps of C and D do not exist. Let us first assume that C^{-1} does not exist. If so, two external potentials $V_{\text{ext}}^{(1)}(\mathbf{r})$ and $V_{\text{ext}}^{(2)}(\mathbf{r})$, which differ by more than a constant, can be associated to a single wavefunction Ψ_0. We can then write the eigenvalue equations for the corresponding Hamiltonians (differing only for the potential) and subtract them:

$$(H_1 - H_2)|\Psi_0\rangle = (E_1 - E_2)|\Psi_0\rangle$$
$$(V_{\text{ext}}^{(1)} - V_{\text{ext}}^{(2)})|\Psi_0\rangle = (E_1 - E_2)|\Psi_0\rangle$$

Since $V_{\text{ext}}^{(1)}(\mathbf{r})$ and $V_{\text{ext}}^{(2)}(\mathbf{r})$ differ by more than a constant, $V_{\text{ext}}^{(1)}(\mathbf{r}) - V_{\text{ext}}^{(2)}(\mathbf{r})$ is not zero. However, Ψ_0 is the same for both equations, implying that $V_{\text{ext}}^{(1)}(\mathbf{r}) - V_{\text{ext}}^{(2)}(\mathbf{r}) = const$, contradicting the initial assumption. This implies that C^{-1} must exist, meaning that the external potential $V_{\text{ext}}(\mathbf{r})$ is uniquely determined by the ground-state wavefunction Ψ_0.
Similarly, if the inverse mapping D^{-1}, from densities to wavefunctions, does not exist, then it is possible to associate two different wavefunctions ψ_1 and ψ_2 with a single ground-state density $n(\mathbf{r})$. However, the external potentials $V_{\text{ext}}^{(1)}$ and $V_{\text{ext}}^{(2)}$ associated with these wavefunctions are different. We can calculate the ground-state energies E_1 and E_2 using the respective Hamiltonians for these states. Since the ground state is non-degenerate, these energies are always smaller than the expectation values obtained by using the same Hamiltonians with any other states. Therefore, in practice:

$$E_1 = \langle\psi_1|H_1|\psi_1\rangle < \langle\psi_2|H_1|\psi_2\rangle = \langle\psi_2|H_2 - V_{\text{ext}}^{(2)} + V_{\text{ext}}^{(1)}|\psi_2\rangle$$
$$E_1 < E_2 + \int n(\mathbf{r})\left(V_{\text{ext}}^{(1)}(\mathbf{r}) - V_{\text{ext}}^{(2)}(\mathbf{r})\right)d^3\mathbf{r}$$

In a similar way

$$E_2 = \langle\psi_2|H_2|\psi_2\rangle < \langle\psi_1|H_2|\psi_1\rangle = \langle\psi_1|H_1 - V_{\text{ext}}^{(1)} + V_{\text{ext}}^{(2)}|\psi_1\rangle$$
$$E_2 < E_1 + \int n(\mathbf{r})\left(V_{\text{ext}}^{(2)}(\mathbf{r}) - V_{\text{ext}}^{(1)}(\mathbf{r})\right)d^3\mathbf{r}$$

Summing the two results, one obtains

$$E_1 + E_2 < E_1 + E_2$$

which is impossible, so an inverse mapping D^{-1} must exist. □
The validity of this theorem implies the following important consequence corollary:

Corollary 1 . *All the properties of the system are completely determined given only the ground-state density* $n_0(\boldsymbol{r})$.

Since we proved that the two mappings exist, we can consider any observable and write it as a functional of the ground-state density:

$$\langle \Psi_0 | \hat{O} | \Psi_0 \rangle = \hat{O}[\Psi_0] = \hat{O}[\Psi_0[n_0]] = \hat{O}[n_0]$$

The second Hohenberg-Kohn theorem states the following.

Theorem 2 . *A universal functional* $F_{\mathrm{HK}}[n]$ *of the density* $n_0(\boldsymbol{r})$ *can be defined, independently of the external potential* $V_{\mathrm{ext}}(\boldsymbol{r})$. *For any particular* $V_{\mathrm{ext}}(\boldsymbol{r})$, *the exact ground-state energy of the system is the global minimum of the energy functional and the density that minimizes the functional is the exact ground-state density* $n_0(\boldsymbol{r})$.

The first part is easily proven once one has carefully defined the meaning of a functional of the space density[1].
According to the Corollary (1), all properties are uniquely determined if the ground-state density $n_0(\mathbf{r})$ is specified. Consequently, all these properties can be viewed as functionals of $n_0(\mathbf{r})$, including the total energy functional:

$$E[n_0] = T[n_0] + W[n_0] + V_{\mathrm{ext}}[n_0] \equiv F_{\mathrm{HK}}[n_0] + V_{\mathrm{ext}}[n_0], \tag{2.5}$$

The Hohenberg-Kohn functional

$$F_{\mathrm{HK}}[n_0] = \langle \psi[n_0] | T + W | \psi[n_0] \rangle, \tag{2.6}$$

with T being the electron kinetic energy and W the electron-electron interaction, is a universal functional, because it remains the same for all systems. The only term that varies from one system to another is V_{ext}.
Moving to the second part of Theorem 2, the energy given by Eq. (2.5) in terms of the Hohenberg-Kohn functional, evaluated for the correct ground-state density $n_0(\mathbf{r})$, is indeed lower than the value of this expression for any other density. It follows that, if the functional $F_{\mathrm{HK}}[n]$ is known, then by minimizing the total energy of the system with respect to variations in the density $n_0(\mathbf{r})$, one would find the exact ground-state properties. However, it is not known explicitly, and must be thus appropriately approximated.

[1]The original proof of Hohenberg and Kohn is restricted to densities $n(\mathbf{r})$ that are ground-state densities of the electron Hamiltonian with some external potential V_{ext}. Such densities are called "V-representable". An alternate functional definition due to Levy and Lieb loosens this restriction to densities that can be generated from an N-electron wavefunction or "V-representable" [7].

2.3.2 The Kohn-Sham Equations

The work by Kohn and Sham [6] represents a cornerstone of modern computational quantum chemistry and condensed matter physics, providing a practical framework for solving the complex many-body problem of interacting electrons in a system. Derived from DFT, this approach simplifies the many-body problem into a set of self-consistent single-electron Schrödinger equations (which are exactly solvable in theory), thereby making the problem more tractable without sacrificing significant accuracy. By introducing a fictitious system of non-interacting electrons that possess the same ground-state density as the real, interacting system, this procedure allows for an efficient calculation of electronic properties of atoms, molecules, and solids. The electrons are assumed to be uncorrelated, except for what is required to satisfy the exclusion principle. An effective potential, that is purely a function of the particle density, is then included to approximate the effects of many-body correlation. Indeed, it can be shown that the ground-state density of the interacting many-body system can be generated from a simpler system of non-interacting particles. All the many-body interactions are abstracted away into an effective potential in which the electrons move. Let us consider two systems with the same density, one composed of interacting electrons, while the other has non-interacting electrons. Let us suppose that the interacting and non-interacting systems have the same density, namely

$$n(\mathbf{r}) \equiv n_{\mathrm{I}}(\mathbf{r}) = n_{\mathrm{NI}}(\mathbf{r}) = \sum_i |\phi_i(\mathbf{r})|^2$$

where the $\{\phi_i\}$ are the independent-particle orbitals and the subscripts I and NI stand for *interacting* and *non-interacting*, respectively. We can then write the equations of the non-interacting and interacting systems as

$$\mathrm{NI}: \qquad \left(-\frac{\hbar^2}{2m}\nabla^2 + V_{\mathrm{eff}}(\mathbf{r})\right)\phi_i(\mathbf{r}) = \epsilon_i\phi_i(\mathbf{r}) \tag{2.7}$$

$$\mathrm{I}: \qquad \left(-\sum_i \frac{\hbar^2\nabla_i^2}{2m} + \frac{1}{2}\sum_{i\neq j}\frac{e^2}{|\mathbf{r}_i-\mathbf{r}_j|} - \sum_{i,I}\frac{Z_I e^2}{|\mathbf{r}_i-\mathbf{R}_I|}\right)\Psi(\mathbf{r}) = E\Psi(\mathbf{r}) \tag{2.8}$$

The energy functionals of these systems are:

$$E_{\mathrm{NI}}[n] = T_{\mathrm{NI}}[n] + \int V_{\mathrm{eff}}(\mathbf{r})n(\mathbf{r})d^3\mathbf{r} \tag{2.9}$$

$$E_{\mathrm{I}}[n] = T_{\mathrm{I}}[n] + W[n] + \int V_{\mathrm{ext}}(\mathbf{r})n(\mathbf{r})d^3\mathbf{r} \tag{2.10}$$

with $V_{\mathrm{eff}}(\mathbf{r})$ being the effective potential in the non-interacting system and $V_{\mathrm{ext}}(\mathbf{r})$ the external potential introduced before. We can rewrite the latter by summing and subtracting $T_{\mathrm{NI}}[n]$, $E_{\mathrm{H}}[n]$, i.e. the Hartree energy defined as:

$$E_{\mathrm{H}}[n] \equiv \int \frac{n(\mathbf{r})n(\mathbf{r}')}{|\mathbf{r}-\mathbf{r}'|}d^3\mathbf{r}d^3\mathbf{r}'$$

and by introducing the exchange and correlation energy functional $E_{\rm xc}[n]$, which stands for a correction term due to exchange (x) and correlation (c) effects:

$$E_{\rm xc}[n] = T_{\rm I}[n] - T_{\rm NI}[n] - E_{\rm H}[n] + W[n] \tag{2.11}$$

In this way, we obtain the total energy functional of the interacting system, the so-called *Kohn-Sham functional*:

$$E_{\rm I}[n] = T_{\rm NI}[n] + E_{\rm H}[n] + E_{\rm xc}[n] + \int V_{\rm ext}(\mathbf{r}) n(\mathbf{r}) d^3\mathbf{r} \tag{2.12}$$

We aim to find the $V_{\rm eff}(\mathbf{r})$ that ensures the same ground-state density and, consequently, the same ground-state energy, in accordance with the Hohenberg-Kohn theorems. To achieve this, we minimize the functional derivatives of the two energy functionals[2]:

$$\begin{aligned}
\left.\frac{\delta E_{\rm NI}}{\delta n}\right|_{n=n_0} &= 0 = \left[\frac{\delta T_{\rm NI}}{\delta n} + V_{\rm eff}(\mathbf{r})\right]\Bigg|_{n=n_0} \\
\left.\frac{\delta E_{\rm NI}}{\delta n}\right|_{n=n_0} &= 0 = \left[\frac{\delta T_{\rm NI}}{\delta n} + V_{\rm H}(\mathbf{r}) + V_{\rm xc}(\mathbf{r}) + V_{\rm ext}(\mathbf{r})\right]\Bigg|_{n=n_0}
\end{aligned}$$

where we named $V_{\rm H}(\mathbf{r}) = \int \frac{n(\mathbf{r}')}{|\mathbf{r}-\mathbf{r}'|} d^3\mathbf{r}'$ the Hartree potential and $V_{\rm xc}(\mathbf{r})$ the functional derivative of the exchange and correlation energy (2.11). By comparing these results, we get an expression for the effective potential (also known as *Kohn-Sham potential*):

$$V_{\rm eff}(\mathbf{r}) = V_{\rm H}(\mathbf{r}) + V_{\rm xc}(\mathbf{r}) + V_{\rm ext}(\mathbf{r}) \tag{2.13}$$

By substituting $V_{\rm eff}(\mathbf{r})$ in Eq. (2.7), we obtain the *Kohn-Sham equations*:

$$\left(-\frac{\hbar^2}{2m}\nabla^2 + \int \frac{n(\mathbf{r}')}{|\mathbf{r}-\mathbf{r}'|} d^3\mathbf{r}' + V_{\rm xc}(\mathbf{r}) + V_{\rm ext}(\mathbf{r})\right)\phi_i(\mathbf{r}) = \epsilon_i \phi_i(\mathbf{r}) \tag{2.14}$$

These single-particle differential equations depend on the electron density, which is not known *a priori*. By solving the equations self-consistently, using trial functions to provide an initial guess for the electron density of the system, one can iterate the process until the desired precision threshold is reached. We will revisit this point in Sec. 2.4.1.
Now, by multiplying on the left by $\phi^*(\mathbf{r})$, integrating over $d^3\mathbf{r}$ and summing over i, we obtain:

[2]Here, we apply the standard variational procedure, minimizing the functional with respect to $n(\mathbf{r})$, under the constraint of the normalization of the wavefunctions $\{\phi_i(\mathbf{r})\}$ (the Lagrange multipliers method).
The functional derivative of $G[f(\mathbf{r})]$ is defined as

$$\delta G[f(\mathbf{r})] = \int \frac{\delta G[f(\mathbf{r})]}{\delta f(\mathbf{r})} \delta f(\mathbf{r}) d(\mathbf{r})$$

$$\sum_i \epsilon_i = E_{\mathrm{NI}}[n] = T_{\mathrm{NI}}[n] + \int \frac{n(\mathbf{r})n(\mathbf{r}')}{|\mathbf{r}-\mathbf{r}'|} d^3\mathbf{r} d^3\mathbf{r}' + \int V_{\mathrm{xc}}(\mathbf{r})n(\mathbf{r})d^3\mathbf{r} + \int V_{\mathrm{ext}}(\mathbf{r})n(\mathbf{r})d^3\mathbf{r}$$
$$= T_{\mathrm{NI}}[n] + 2E_{\mathrm{H}} + \int V_{\mathrm{xc}}(\mathbf{r})n(\mathbf{r})d^3\mathbf{r} + \int V_{\mathrm{ext}}(\mathbf{r})n(\mathbf{r})d^3\mathbf{r}$$

By comparing $E_{\mathrm{I}}[n]$ (2.12) and $E_{\mathrm{NI}}[n]$ (2.9), we find that the ground-state energy of the interacting system can be expressed in terms of the non-interacting one, plus a correction that depends solely on the density, that is

$$E_{\mathrm{I}}[n] = \sum_i \epsilon_i - E_{\mathrm{H}} - \int V_{\mathrm{xc}}(\mathbf{r})n(\mathbf{r})d^3\mathbf{r} + E_{\mathrm{xc}}[n]$$

We first notice that the Kohn-Sham equations are standard differential equations with a rigorously local effective potential; any difficulty in the procedure is confined to making a reasonable guess of the exchange-correlation functional $E_{xc}[n]$, which is generally not known a priori. Conceptually, the Kohn-Sham equations exactly determine the electron density and the electronic energy of the ground state. However, the orbital energies ε_i appearing in the Eq. (2.14) are purely formal Lagrange multipliers and do not have a direct physical interpretation, as is the case in Koopmans' theorem [8]. Any identification of the ε_i with one-particle energies, whether occupied or unoccupied, must be justified on a case-by-case basis. The exact Kohn-Sham theory only guarantees that the eigenvalue of the highest occupied state has a physical meaning [9]. This can be understood by considering that the true many-body fully interacting system must have the same ionization energy as the Kohn and Sham system since they are both assumed to have the same density. Nonetheless, Kohn-Sham eigenvalues are usually used to describe band structures, also taking into account empty states. This leads to a fundamental problem which is discussed in the next section.

2.3.3 The Band Gap Problem in DFT

As mentioned in the previous section, DFT is a ground-state theory. In spite of this, it has been regularly used throughout the years to compute, for example, band structures and optical properties of materials, which actually involve excited states[3]. In this framework, the excited states are treated as functionals of the ground-state density. As a result, the band structures obtained from these calculations typically have band gaps that are systematically underestimated, often up to 50% of the experimental values for semiconductors and insulators [10]. This discrepancy arises in the first place because the Kohn-Sham equations are single-particle differential equations, which neglect all possible many-body contributions; however, it is mainly due to an intrinsic limitation of DFT.
In non-metallic systems, the nature of the states changes discontinuously at the band gap [11]. The band gap is defined as the difference between the valence band maximum (VBM) and the conduction band minimum (CBM)[4]. For an insulating N-particle system, the difference between

[3] This is due to the fact that DFT is computationally enormously more affordable than any excited-state theory and the results are generally in good qualitative — but not quantitative — agreement with experiments.

[4] In molecular systems, these gap edges are referred to as the *highest occupied molecular orbital* (HOMO) and the *lowest unoccupied molecular orbital* (LUMO), respectively.

the vacuum level and the VBM is the energy required to remove an electron from the system, known as *ionization energy* $I = [E(N-1) - E(N)]$; whereas, using the CBM, one gets the energy required to add an electron to the system, known as *electron affinity* $A = [E(N) - E(N+1)]$. Thus, the band gap energy can be defined as

$$E_{\text{gap}} = I - A \tag{2.15}$$

It is important to note that the definition in Eq. (2.15) involves total energies, as the entire system is affected by the removal or addition of an electron. Since the chemical potential μ can be written as the functional derivative of the ground-state energy with respect to the density, i.e.

$$\mu = \frac{\delta E[n]}{\delta n}$$

the ionization energy (I) and the electron affinity (A) can be expressed in terms of the functional derivatives of the energy, and so the band gap[5]

$$\begin{aligned} I = E(N-1) - E(N) &= -\frac{\delta E[n]}{\delta n^-} = \mu^- \\ A = E(N) - E(N+1) &= -\frac{\delta E[n]}{\delta n^+} = \mu^+ \\ E_{\text{gap}} = I - A = \frac{\delta E[n]}{\delta n^+} - \frac{\delta E[n]}{\delta n^-} &= \Delta \frac{\delta E[n]}{\delta n} \end{aligned}$$

Here, $\Delta \frac{\delta E[n]}{\delta n}$ indicates the discontinuity of the functional derivative. The $\pm$ signs in the derivative denote right and left derivatives, where $\mu^+ = \mu(N+\delta)$ and $\mu^- = \mu(N-\delta)$. The band gap is therefore given by the discontinuity in the functional derivative of the ground-state energy. Now, considering both the energy gap of the interacting (2.12) and non-interacting systems (2.9), we can write:

$$\begin{aligned} E^{\text{I}}_{\text{gap}} &= \Delta \frac{\delta T_{\text{NI}}[n]}{\delta n} + \Delta \frac{\delta E_{\text{xc}}[n]}{\delta n} = \Delta \frac{\delta T_{\text{NI}}[n]}{\delta n} + \Delta V_{\text{xc}} \\ E^{\text{NI}}_{\text{gap}} &= \Delta \frac{\delta T_{\text{NI}}[n]}{\delta n} \end{aligned}$$

In the non-interacting system, the only discontinuity arises from the kinetic energy functional $T_{NI}[n]$, since the external potential and the Hartree potential are both continuous functionals of the density. In the interacting system, however, $E_{xc}[n]$ may be discontinuous. Comparing the two expressions above, we obtain the important relation:

$$E^{\text{I}}_{\text{gap}} = E^{\text{NI}}_{\text{gap}} + \Delta V_{xc}$$

[5]It can be shown that by definition $\frac{\partial E(N)}{\partial N} \equiv \frac{\delta E[n]}{\delta n}$.

This shows (recalling the discussion in Sec. 2.3.2) that the band gap obtained from the Kohn-Sham eigenvalues differs from that of the real interacting system by a quantity equal to the discontinuity of the exchange-correlation potential.

2.3.4 The Exchange-Correlation Functional

To solve the Kohn-Sham equations (2.14), the central task is to find an approximation for the exchange-correlation (XC) functional that accurately reproduces the complex effects of electron exchange and correlation. A significant advantage of this approach is that, because these effects are typically short-ranged, they can be well approximated using a local or semi-local functional of the electron density. This allows for practical and computationally feasible implementations that still capture the essential physics of many-electron systems.
To approximate the exact XC functional, we introduce the quantity $n_{\mathrm{xc}}(\mathbf{r}, \mathbf{r}')$, known as the *XC hole*[6]. This quantity represents a region around each electron in an interacting system where the probability of finding another electron is reduced, a consequence of both the Pauli exclusion principle and electron-electron repulsion. We also modulate the strength of electronic interactions using a coupling constant λ: with a fixed electron density, $\lambda = 1$ corresponds to the fully interacting, physical system, while $\lambda = 0$ corresponds to the non-interacting, fictitious system. The XC functional can thus be viewed as the energy resulting from the interaction between an electron and its XC hole across all values of λ:

$$E_{\mathrm{xc}}[n(\mathbf{r})] = \frac{1}{2} \int n(\mathbf{r}) d^3\mathbf{r} \int \frac{n_{\mathrm{xc}}(\mathbf{r}, \mathbf{r}')}{|\mathbf{r} - \mathbf{r}'|} d^3\mathbf{r}' \tag{2.16}$$

where the XC hole $n_{\mathrm{xc}}(\mathbf{r}, \mathbf{r}')$ is the averaged $n^{\lambda}_{\mathrm{xc}}(\mathbf{r}, \mathbf{r}')$ over the coupling constant λ:

$$n_{\mathrm{xc}}(\mathbf{r}, \mathbf{r}') = \int_0^1 n^{\lambda}_{\mathrm{xc}}(\mathbf{r}, \mathbf{r}') d\lambda$$

The XC hole satisfies the sum rule

$$\int n_{\mathrm{xc}}(\mathbf{r}, \mathbf{r}') d^3\mathbf{r}' = -1$$

[6]The *exchange hole* refers to the region around a given electron where the probability of finding another electron of the same spin is reduced due to the Pauli exclusion principle. As a result, each electron creates a "hole" around itself, lowering the electron density in its immediate vicinity for electrons with parallel spins. This reduction in probability density is purely a quantum mechanical effect and does not involve any explicit interaction between electrons; rather, it arises from the antisymmetry requirement of the many-electron wavefunction.
The *correlation hole*, on the other hand, accounts for the electron-electron repulsion effects beyond the Pauli exclusion principle. This includes the dynamic correlation where electrons avoid each other due to their mutual Coulomb repulsion. Unlike the exchange hole, the correlation hole affects the spatial distribution of all electrons, regardless of their spins. This results in a further depletion of electron density around a given electron, reflecting the likelihood that other electrons, due to their repulsive interaction, will be found less frequently in its proximity.
Together, the XC hole describes the total reduction in electron density around a given electron due to both quantum mechanical exchange effects and electron-electron repulsion. These concepts are crucial for constructing accurate XC in DFT.

which implies that the XC hole has a deficit of exactly one electron, therefore an electron and its hole have no net charge. Now we can define another useful quantity, the XC energy per particle:

$$\epsilon_{\mathrm{xc}}[n(\mathbf{r})] = \frac{1}{2}\int \frac{n_{\mathrm{xc}}(\mathbf{r},\mathbf{r}')}{|\mathbf{r}-\mathbf{r}'|}d^3\mathbf{r}'$$

We can now rewrite the XC energy functional (2.16) as:

$$E_{\mathrm{xc}}[n(\mathbf{r})] = \int n(\mathbf{r})\epsilon_{\mathrm{xc}}[n(\mathbf{r})]d^3\mathbf{r}$$

This is the quantity we aim to approximate. Different types of approximations vary in how they construct the XC energy per particle by sampling the density around each electron in distinct ways. In the following sections, we will present some general forms that are particularly relevant to solid-state systems.

2.3.5 Local Density Approximation (LDA)

The most common approximation arises from assuming that the system approaches the limit of a homogeneous electron gas, leading to what is known as the *local density approximation* (LDA), first introduced by Kohn and Sham in 1965 [6]. In principle, this is justified in systems with reasonably a slowly-varying spatial density $n(\mathbf{r})$, at most locally constant. Here, we decompose E_{xc} into separate contributions accounting for both exchange (x) and correlation (c). In the case of a homogeneous electron gas, the exchange term possesses a straightforward analytic form.

$$E_{\mathrm{x}}^{\mathrm{LDA}}[n] = -\frac{3}{4}\left(\frac{3}{\pi}\right)^{\frac{1}{3}}\int n(\mathbf{r})^{\frac{4}{3}}d^3\mathbf{r}$$

The correlation term is more complex and is not known exactly, except in the low and high density limits. For intermediate densities, among the various forms, the more commonly used are the Rayleigh-Schrödinger perturbation [12], computational methods like Quantum Monte Carlo — due to Ceperley and Alder [13] — or analytical expressions like the one given by Perdew and Zunger [14]. As an approximation for a homogeneous electron gas, one would expect better results for systems that closely resemble this ideal state, such as simple metals, and poorer results for highly inhomogeneous systems like molecules. Surprisingly, the LDA approach has proven successful across a broad range of systems, despite significant density fluctuations. Part of the reason lies in the fact that, in many materials, the effects of exchange and correlation are typically short-ranged, allowing them to be effectively captured by a local functional [7]. Combined with a spinorial description of the DFT, it is called *local spin density approximation* (LSDA).

2.3.6 General Gradient Approximation (GGA)

The next level of approximation involves considering not only the electron density but also its gradient $\nabla n(\mathbf{r})$. This extension leads to the *generalized gradient approximation* (GGA) [15] for the XC functional, where the functional takes the form

$$E_{\rm xc}^{\rm GGA}[n] = \int n(\mathbf{r})\epsilon_{\rm xc}(n(\mathbf{r}), \nabla n(\mathbf{r}))d^3\mathbf{r}$$

XC functionals in GGA are semi-local. GGA typically improves predictions of total energies and energy differences over LDA. However, despite these advances, GGA still struggles to reliably determine band gaps. This limitation arises because GGA, like LDA, does not adequately capture the non-locality of XC effects, which is crucial for accurately describing band gaps in semiconductors and insulators. Thus, while GGA represents a significant improvement over LDA in many respects, challenges in band gap predictions persist, motivating ongoing research into more advanced XC functionals.

2.3.7 Hybrid Functionals

Another rung of the ladder is given by hybrid functionals, a large family of XC functionals, mostly developed and used in the computational chemistry community, that incorporate a portion of exact exchange $E_x^{\rm HF}$ as obtained from the HF theory, with the rest of the XC energy obtained from other sources (*ab initio* or empirical). The exchange term energy is

$$E_x^{\rm HF} = -\frac{1}{2}\sum_{ij}\int\int \psi_i^*(\mathbf{r}_1)\psi_j^*(\mathbf{r}_2)\frac{1}{r_{12}}\psi_j(\mathbf{r}_1)\psi_i(\mathbf{r}_2) \tag{2.17}$$

and it is expressed in terms of the Kohn–Sham orbitals rather than the density. This scheme allows to improve many molecular properties, such as atomization energies, bond lengths and vibration frequencies, which tend to be poorly described with simple ab initio functionals [16]. Each specific hybrid functional is built as a linear combination of LDAs, GGAs, and HF contributions, with the coefficients chosen, empirically or not, to optimize selected set of observables (bond lengths, band gaps, etc.). For example, the popular B3LYP (Becke, three-parameter, Lee-Yang-Parr) [17–19] is written as

$$E_{xc}^{\rm B3LYP} = E_{xc}^{\rm LDA} + a_0(E_x^{\rm HF} - E_x^{\rm LDA}) + a_x(E_x^{\rm GGA} - E_x^{\rm LDA}) + a_c(E_c^{\rm GGA} - E_c^{\rm LDA})$$

where $a_=$0.2, $a_x = 0.72$, $a_c = 0.81$ are three empirical parameters, $E_x^{\rm GGA}$ and $E_c^{\rm GGA}$ are the GGA energy functionals, formulated with the Becke88 [15] exchange functional and the correlation functional of Lee, Yang and Parr and $E_c^{\rm LDA}$ is the Vosko-Wilk-Nusair [20] LSDA correlation functional. Another example of hybrid potential is PBE0 [21]:

$$E_{xc}^{\rm PBE0} = aE_x^{\rm HF} + (1-a)E_x^{\rm PBE} + E_c^{\rm HF}$$

This potential is based on the Perdew-Burke-Ernzerhof (PBE) XC functional by Perdew et al. [16] The mixing coefficient $a = 1/4$ is obtained by perturbation theory and thus not empirical.
A more refined (and computationally expensive) class of hybrid functionals is that of the *range-separated hybrids*. Unlike conventional hybrid functionals, in these functionals, the exchange energy is separated into short-range and long-range components. Typically, a portion of the exact

exchange is applied at long ranges, while a different functional is used for short-range interactions. This approach helps to better capture both local correlation effects and long-range Coulomb interactions, leading to more accurate descriptions of electronic properties, especially in systems with significant long-range interactions, such as in molecular systems, van der Waals complexes, and materials with strong correlation effects. An example of this type of hybrid functionals is the Heyd–Scuseria–Ernzerhof (HSE) XC functional [21]:

$$E_{xc}^{\mathrm{HSE}} = aE_x^{\mathrm{HF,SR}}(\omega) + (1-a)E_x^{\mathrm{PBE,SR}}(\omega) + E_x^{\mathrm{PBE,LR}} + E_c^{\mathrm{PBE}} \tag{2.18}$$

where the superscripts SR and LR stand for short-range and long-range, respectively. a is the mixing parameter and ω is an adjustable parameter controlling the short-rangeness of the interaction. Standard values of $a = 1/4$ and $\omega = 0.2$ (usually referred to as HSE06) have been shown to give good results for most systems.
In this Thesis, hybrid functionals were used to tackle the shortcomings of DFT in zero-dimensional systems, as shown in Sec. 6.1.

2.4 Methods and Implementations in DFT

Having established the foundational principles of DFT through the Hohenberg-Kohn theorem, which demonstrates that the ground-state properties of a system are uniquely determined by its electron density, and the Kohn-Sham equations, which provide a practical framework for solving the many-electron problem, we now embark on a deeper exploration of DFT. In particular, the following sections address practical issues concerning the actual resolution of Kohn-Sham equations, the methods and implementations needed to tackle DFT at a computational level.

2.4.1 The Self-Consistent Approach

The self-consistent approach lies at the heart of solving the Kohn-Sham equations in DFT. It involves iterative adjustment of the electron density and the effective potential V_{eff} (2.13) until a consistent solution is achieved, ensuring that the total energy functional reaches a minimum. This is schematically depicted in the diagram of Fig. 2.3.

1. **Initial Guess:** Begin with an initial guess for the electron density $n^{(0)}(\mathbf{r})$.

2. **Effective Potential Calculation:** Compute the effective potential $V_{\mathrm{eff}}^{(0)}(\mathbf{r})$ by varying the total energy functional with respect to the electron density. This potential is used in Eq. (2.14) to solve for the Kohn-Sham states.

3. **Solve Kohn-Sham Equations:** Solve the Kohn-Sham equations (2.14) with the initial guess of the electron density and the effective potential $V_{\mathrm{eff}}^{(0)}(\mathbf{r})$. This involves solving an eigenvalue problem for each orbital, constituting the main computational effort.

4. **Update Electron Density:** From the Kohn-Sham orbitals, calculate the new electron density $n^{(1)}(\mathbf{r})$.

5. **Convergence Check:** Compare $n^{(1)}(\mathbf{r})$ with $n^{(0)}(\mathbf{r})$ to check for convergence. If the change is below a predefined threshold, the self-consistency is achieved, and the calculation concludes. If convergence criteria are not met, update V_{eff} using the new density $n^{(1)}(\mathbf{r})$ and repeat the process from step 3.

This iterative process continues until self-consistency between the calculated electron density and the effective potential is achieved. This methodology ensures that the Kohn-Sham equations accurately describe the electronic structure of the system under consideration.

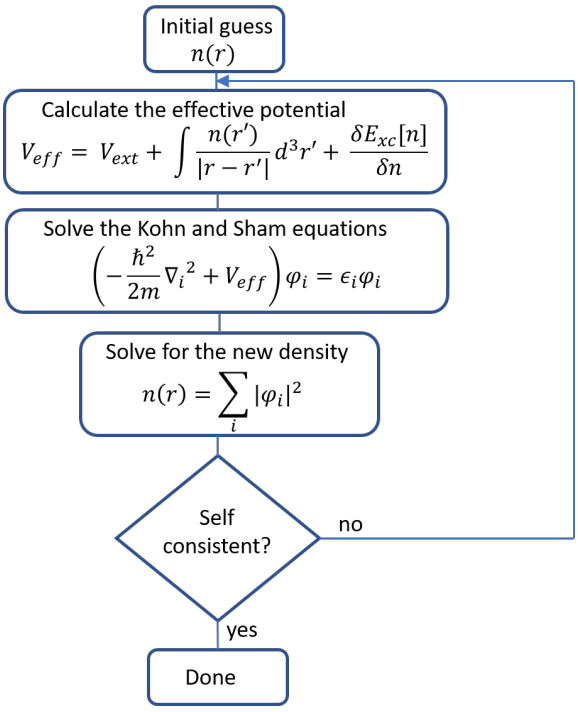

Figure 2.3: *Flow chart of the self consistent calculations performed when using Density Functional Theory.*

2.4.2 The Plane Waves Expansion

The choice of plane waves (PWs) as a basis set to expand the Kohn-Sham eigenfunctions is one of the most common approaches used in computational methods for DFT calculations, particularly for studying infinite periodic systems like crystals. This formulation is implemented in the software we used for all DFT calculations in this work, *Quantum* ESPRESSO (QE) [22, 23]. The advantage of using PWs is that the kinetic energy operator is diagonal in the plane wave representation, simplifying the calculations. Additionally, the matrix elements of the effective potential V_{eff} (2.13) can be efficiently computed using Fourier transforms, enhancing computational efficiency.
Let us start off by stating that the wavefunction of an electron in a periodic crystalline potential

has the same periodicity as the potential. This is a consequence of Bloch's theorem [24]. Given a wavevector $\mathbf{k}$ in the first Brillouin Zone of the reciprocal lattice, the *j-th* Kohn-Sham eigenfunction $\phi_{j,\mathbf{k}}(\mathbf{r})$ reads:

$$\phi_{j,\mathbf{k}}(\mathbf{r}) = u_j(\mathbf{r})e^{i\mathbf{k}\cdot\mathbf{r}} \tag{2.19}$$

The functions $u_j(\mathbf{r})$ have the same periodicity of the lattice and can be expressed in PWs, with the wavevectors $\mathbf{G}$ being the reciprocal lattice vectors

$$u_j(\mathbf{r}) = \sum_{\mathbf{G}} c_{j,\mathbf{G}} e^{i\mathbf{G}\cdot\mathbf{r}}$$

where $c_{j,\mathbf{G}}$ are the PWs coefficients. Consequently, we can write the wavefunction (2.19) of the electron in the band j as

$$\phi_{j,\mathbf{k}}(\mathbf{r}) = \sum_{\mathbf{G}} c_{j,\mathbf{k}+\mathbf{G}} e^{i(\mathbf{k}+\mathbf{G})\cdot\mathbf{r}} \tag{2.20}$$

Now, by introducing the Fourier transform in the reciprocal space of the effective potential $V_{\text{eff}}(\mathbf{r}) \equiv V_{\text{ext}}(\mathbf{r}) + V_{\text{H}}(\mathbf{r}) + V_{\text{xc}}(\mathbf{r})$,

$$V_{\text{eff}}(\mathbf{r}) = \sum_{\mathbf{G}} \bar{V}_{\text{eff}}(\mathbf{G}) e^{i\mathbf{G}\cdot\mathbf{r}}$$

we obtain a simpler expression of the Kohn-Sham equations in reciprocal space

$$\sum_{\mathbf{G}'} \left[\frac{1}{2}|\mathbf{k}+\mathbf{G}|^2 \delta_{\mathbf{G},\mathbf{G}'} + \bar{V}_{\text{eff}}(\mathbf{G}-\mathbf{G}') \right] c_{j,\mathbf{k}+\mathbf{G}'} = \epsilon(\mathbf{k}) c_{j,\mathbf{k}+\mathbf{G}'} \tag{2.21}$$

where the first term is the kinetic contribution and is diagonal. The calculation is exact with an infinite sum over $\mathbf{G}$ vectors.
Following an intuitive consideration due to Herring [25], it is easily seen that a pure expansion of crystal states into PWs is seriously flawed by the so-called *variational collapse* problem. Indeed, since core states are strongly localized in real space, their accurate description would require a large number of PWs, and then a prohibitive number of equations like (2.21) to solve. For instance, to reproduce the 1s state of bulk Silicon ($Z = 14$), the number of equations to be solved should be of the order of $(10^6 \times 10^6)$. It is clear that reproducing core states using PWs is basically impossible. DFT codes make use of a parameter known as the kinetic cutoff E_{cut} to limit the number of PWs used to expand Kohn-Sham eigenfunctions, since the first terms have the highest contribution. We truncate the sum on $\mathbf{G}$ such that

$$\frac{1}{2}|\mathbf{k}+\mathbf{G}|^2 \leq E_{\text{cut}}$$

One needs to check for the convergence of the results with respect to E_{cut}. The advantage is that the precision of the results can be improved by increasing E_{cut}. Indeed, it is important to keep in mind that the number of PWs, N_{PW}, grows as

$$N_{\mathrm{PW}} \sim \frac{\Omega}{6\pi^2}(E_{\mathrm{cut}})^{\frac{3}{2}}$$

where Ω is the volume of the primitive unit cell. However, the number of PWs required to describe highly curved wavefunctions lengthens the calculations. This is especially true in the case of the core electrons in atoms. In the next section, we present a way to work around this issue.

2.4.3 Pseudopotentials

To address the variational collapse and the high computational cost associated with the PW formulation, especially in the region around atoms, we employ the so-called *pseudopotential method* [7]. In the core region of atoms, the electronic wavefunction exhibits significant oscillations, necessitating a large number of PWs for an accurate description. Moreover, the core electronic structure is generally unaffected by the chemical bonds formed by outer electrons. Valence electrons do not experience the full Coulomb potential of the nucleus directly; instead, they encounter a potential that is screened by the core electrons. To simplify calculations, the pseudopotential approximation replaces the strong and singular ionic potential in the core region with a weaker pseudopotential. This transformation leads to the concept of *pseudo*-atoms and *pseudo*-wavefunctions. These *pseudo*-wavefunctions are required to represent the genuine crystalline wavefunctions only outside the core region and should be compared, to ensure accuracy and reliability, to the *all-electron* wavefunctions, which are derived using the actual atomic potential.
Given r_{core}, a parametric radius that defines the core region, any valid pseudopotential must fulfill the following conditions (see Fig. 2.4):

- for $r > r_{\mathrm{core}}$, i.e. outside the core region, the pseudopotential and the original potential must be identical,
- for $r > r_{\mathrm{core}}$, the valence pseudo-wavefunctions are the same as those obtained for a reference configuration of the chosen atom,
- for $r < r_{\mathrm{core}}$, i.e. inside the core region, the pseudo-wavefunction must not have any node,
- the valence states of the pseudo-atom must be equal to those obtained from the resolution of the Schrödinger equation for the real atom.

When the pseudopotential is constructed to reproduce the exact electron density of the system, it is referred to as *norm-conserving*. Using pseudopotentials in conjunction with PWs to expand the Kohn-Sham eigenfunctions becomes, in this context, a convenient choice.

[7] The introduction of this method is based on the experimental evidence showing that the physical properties of materials are primarily determined by valence electrons. Core electrons, which are localized closer to the nucleus and possess less energy, can be considered frozen in their atomic configuration. Therefore, they have minimal impact on the properties of the material, allowing the focus to be placed on the behavior of valence electrons for more accurate and efficient modeling and analysis.

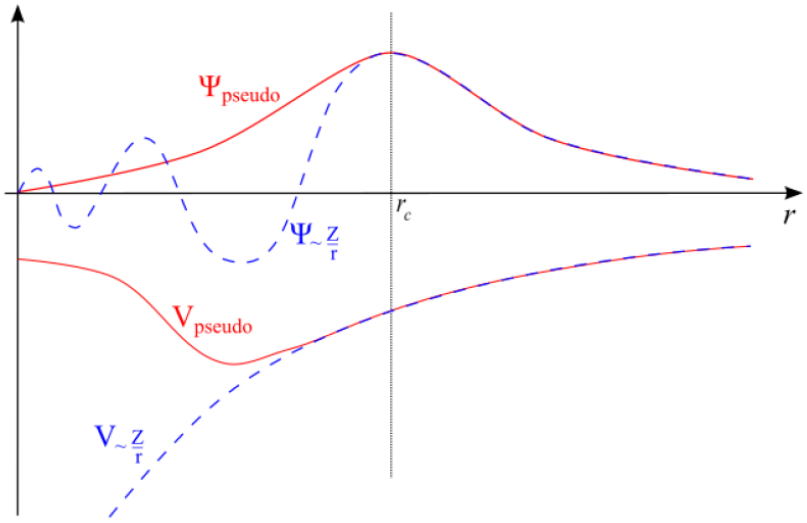

Figure 2.4: *Comparison of a wave function in the Coulomb potential of the nucleus (blue) to the one in the pseudopotential (red). The real and the pseudo-wavefunction and potentials match above a certain radius* r_{core}*, called core radius.*

2.4.4 The Semi-Core Problem

When generating a pseudopotential, several parameters need to be optimized, including the choice of core and valence states. A simplistic approach might consider valence states as those that contribute to chemical bonding and core states as those that do not. However, the situation can be more complex, and what works for DFT may not be sufficient for post-DFT methods.
For example, in the case of chalcogens, whose typical outer electronic configuration is $nd^i(n+1)s^j(n+1)p^k$, it is not always evident that the lower ns and np states can be safely included in the core. The problem arises because nd states are localized in the same spatial region as ns and np states, which are deeper than $(n+1)s$ and $(n+1)p$. This can lead to an underestimation of the exchange energy when performing more refined calculations [26].
A pseudopotential that uses a more naive choice of valence states may yield good results in solids with weak or metallic bonding but may fail in compounds with stronger bonding. This is often the case for many transition and noble metals. Including semi-core states in the valence can improve pseudopotential transferability but will make it "heavier" (requiring a higher kinetic energy cutoff).

2.4.5 Brillouin Zone Sampling

Due to Bloch's theorem, which ensures the periodicity of wavefunctions in a crystal lattice, it suffices to consider wavevectors $\mathbf{k}$ that belong to the first Brillouin Zone (BZ). Indeed, any wavevector $\mathbf{k}'$ outside the BZ can be mapped to an equivalent vector $\mathbf{k}$ inside the zone. Thus, for periodic systems, rather than computing integrals of observables in real space, it is more convenient to

work in reciprocal space and perform integrations over vectors $\mathbf{k}$ (or equivalently, $\mathbf{k}$-points) within the first BZ. In practice, because electron wavefunctions exhibit only gradual variations over small distances in reciprocal space, we can approximate the integral of any function $F(\mathbf{k})$ by a weighted discrete sum

$$\int_{\mathrm{BZ}} F(\mathbf{k})d\mathbf{k} = \frac{1}{\Omega}\sum_j w_j F(\mathbf{k}_j)$$

where Ω is the volume of the reciprocal cell of the crystal, and w_j is the weight associated with the k-point $\mathbf{k}_j$. The number of $\mathbf{k}$-points significantly affects the precision of the results, so it must be adjusted by verifying the convergence of the total energy with increasing $\mathbf{k}$-points. One common method for selecting k-point positions is the Monkhorst-Pack method [27], which distributes $\mathbf{k}$-points uniformly in reciprocal space on a grid within the BZ.

$$\mathbf{k}_j = x_{1,j}\mathbf{b}_1 + x_{2,j}\mathbf{b}_2 + x_{3,j}\mathbf{b}_3$$

where $\mathbf{b}_1$, $\mathbf{b}_2$, $\mathbf{b}_3$ are reciprocal lattice vectors and

$$x_{ij} = \frac{l_i}{n_j}, \quad j = 1, ..., n_j$$

l_i represents the lengths of the reciprocal lattice vectors, and n_j denotes the number of special $\mathbf{k}$-points in the set. Typically, crystal symmetries are employed to further reduce the required number of $\mathbf{k}$-points by adjusting the corresponding weights w_j.

2.4.6 Including Spin in DFT

An approximate Hamiltonian for a system of interacting electrons in an electromagnetic field, including spin, can be written as

$$H = \sum_i \left[\frac{\mathbf{\Pi}_i^2}{2m} - \mu_B \sigma_i \cdot \mathbf{B}(\mathbf{r}_i) + q\phi(\mathbf{r}_i)\right] + \frac{1}{2}\sum_{ij}\frac{q^2}{|\mathbf{r}_i - \mathbf{r}_j|}$$

where $\mathbf{\Pi} = \mathbf{p} - q\mathbf{A}(\mathbf{r})$, $\mathbf{A}(\mathbf{r})$ is the electromagnetic vector potential, q is the charge, $\mu_B = \hbar q/2m$ the Bohr magneton, σ_i are the Pauli matrices, $\mathbf{B}$ is the magnetic field and $\phi(\mathbf{r})$ the scalar potential. Before reformulating DFT starting from this Hamiltonian, we make a further simplification. We set $\pi_i = \mathbf{p}_i$, neglecting the coupling of the electron orbital momentum with the magnetic field. We then rewrite this Hamiltonian by introducing the 2×2 matrix of the external one-body potential

$$V_{\mathrm{ext}}^{\sigma,\sigma'} = \begin{pmatrix} q\phi(\mathbf{r}) - \mu_B B_z(\mathbf{r}) & -\mu_B(B_x(\mathbf{r}) - iB_y(\mathbf{r})) \\ -\mu_B(B_x(\mathbf{r}) + iB_y(\mathbf{r})) & q\phi(\mathbf{r}) + \mu_B B_z(\mathbf{r}) \end{pmatrix}$$

with σ, σ' being the spin indices [8]. As in the standard Kohn-Sham formulation, one can introduce an auxiliary system that, in this case, consists of a gas of non-interacting electrons with spin, having the same spin-density as the many-body system. The wavefunctions of this auxiliary system are Slater determinants of two-component, one-electron spinors $\psi_i(\mathbf{r},\sigma)$. The system is now described by the spin-density, which is expressed as

$$\begin{aligned} n_{\sigma\sigma'}(\mathbf{r}) &= \sum_i \psi_i^*(\mathbf{r},\sigma)\psi_i(\mathbf{r},\sigma') \\ &= \sum_i \begin{pmatrix} \psi_i(\mathbf{r},\uparrow)^*\psi_i(\mathbf{r},\uparrow) & \psi_i(\mathbf{r},\uparrow)^*\psi_i(\mathbf{r},\downarrow) \\ \psi_i(\mathbf{r},\downarrow)^*\psi_i(\mathbf{r},\uparrow) & \psi_i(\mathbf{r},\downarrow)^*\psi_i(\mathbf{r},\downarrow) \end{pmatrix} \end{aligned}$$

By means of the Pauli matrices $\boldsymbol{\sigma} = (\sigma_x, \sigma_y, \sigma_z)$, it is possible to write the spin-density matrix of the system as

$$\begin{aligned} n_{\sigma\sigma'}(\mathbf{r}) &= \frac{1}{2}\left(n(\mathbf{r})\mathbb{1} + \boldsymbol{\sigma}\cdot\mathbf{m}\right) \\ &= \frac{1}{2}\begin{pmatrix} n(\mathbf{r}) + m_z((\mathbf{r})) & m_x(\mathbf{r}) + im_y(\mathbf{r}) \\ m_x(\mathbf{r}) - im_y(\mathbf{r}) & n(\mathbf{r}) - m_z(\mathbf{r}) \end{pmatrix} \end{aligned}$$

where $n(\mathbf{r})$ is the usual charge density

$$n(\mathbf{r}) = \mathrm{Tr}(n_{\sigma\sigma'}(\mathbf{r})) = \sum_{i,\sigma} \psi_i^*(\mathbf{r},\sigma)\psi_i(\mathbf{r},\sigma)$$

and the three-dimensional vector $\mathbf{m}(\mathbf{r})$ is the *magnetization density*, defined as

$$\mathbf{m}(\mathbf{r}) = \sum_{\sigma\sigma'}\sum_i \psi_i^*(\mathbf{r},\sigma)\boldsymbol{\sigma}_{\sigma\sigma'}\psi_i(\mathbf{r},\sigma')$$

When introducing spin in DFT, the fundamental quantities are thus four real densities that can be chosen to be either the four components of $n_{\sigma\sigma'}$ or the charge density $n(\mathbf{r})$ plus the three components of $\mathbf{m}(\mathbf{r})$. This general formulation is often referred to as the *non-collinear* case.
The kinetic energy functional (using from now on atomic units) is diagonal in the spin indices and is given by

$$T_{\mathrm{NI}}[n_{\sigma\sigma'}(\mathbf{r})] = \sum_{i,\sigma} \langle\psi_{i,\sigma}| -\frac{1}{2}\boldsymbol{\nabla}^2 |\psi_{i,\sigma}\rangle$$

The energy due to the interaction between the electrons and the external potential reads

$$E_{\mathrm{ext}}[n_{\sigma\sigma'}] = \sum_{\sigma,\sigma'} \int d^3\mathbf{r}\, V_{\mathrm{ext}}^{\sigma,\sigma'}(\mathbf{r}) n_{\sigma\sigma'}(\mathbf{r})$$

[8] One can show that the ground-state energy of the many-body Hamiltonian is a functional of $n_{\sigma\sigma'}(\mathbf{r})$ [28], though $V_{\mathrm{ext}}^{\sigma,\sigma'}(\mathbf{r})$ is not uniquely determined by the spin-density.

while the Hartree energy can be written in terms of the charge density only, $E_{\rm H}[n(\mathbf{r})]$. The unknown XC part of the total energy functional will also incorporate spinors through the density, becoming $E_{\rm xc}[n_{\sigma\sigma'}(\mathbf{r})]$ [9].
By minimizing the total energy functional with respect to the orbitals $\psi_i(\sigma)$, while keeping into account the orthogonality constraint of the one-electron wavefunctions

$$\sum_{\sigma} \langle \psi_{i,\sigma} | \psi_{j,\sigma} \rangle = \delta_{ij}$$

we obtain the single-particle Kohn-Sham equations in the non-collinear case

$$\begin{aligned} -\frac{1}{2}\boldsymbol{\nabla}^2\psi_i(\mathbf{r},\sigma) + V_{\rm H}(\mathbf{r})\psi_i(\mathbf{r},\sigma) + \frac{\delta E_{\rm xc}}{\delta n}\psi_i(\mathbf{r},\sigma) \\ + \sum_{\sigma'}\left(V_{\rm ext}^{\sigma,\sigma'}(\mathbf{r})\psi_i(\mathbf{r},\sigma') + \mu_B \frac{\delta E_{\rm xc}}{\delta \mathbf{m}} \cdot \boldsymbol{\sigma}^{\sigma,\sigma'}\psi_i(\mathbf{r},\sigma')\right) = \epsilon_i\psi_i(\mathbf{r},\sigma) \end{aligned} \tag{2.22}$$

We can define the exchange and correlation potential $V_{\rm xc}$ and magnetic field $\mathbf{B}_{\rm xc}$ as

$$V_{\rm xc}(\mathbf{r}) = \frac{\delta E_{\rm xc}}{\delta n} \qquad \text{and} \qquad \mathbf{B}_{{\rm xc},\alpha}(\mathbf{r}) = -\frac{\delta E_{\rm xc}}{\delta \mathbf{m}}$$

and a spin-dependent self-consistent local potential as

$$V_{\rm loc}^{\sigma,\sigma'}(\mathbf{r}) = V_{\rm ext}^{\sigma,\sigma'}(\mathbf{r}) + [V_{\rm H}(\mathbf{r}) + V_{\rm xc}(\mathbf{r})]\delta^{\sigma,\sigma'} - \mu_B \mathbf{B}_{\rm xc}(\mathbf{r}) \cdot \boldsymbol{\sigma}^{\sigma,\sigma'}$$

to obtain Eq. (2.22) in the compact form

$$\sum_{\sigma'}\left[-\frac{1}{2}\boldsymbol{\nabla}^2\delta^{\sigma,\sigma'} + V_{\rm loc}^{\sigma,\sigma'}(\mathbf{r})\right]\psi_i(\mathbf{r},\sigma') = \epsilon_i\psi_i(\mathbf{r},\sigma) \tag{2.23}$$

2.4.7 Spin-Orbit Coupling (SOC)

Spin-orbit coupling (SOC) can be included in the solution of the Kohn-Sham equations, where the resulting eigenvalues are subsequently used as input for calculations beyond DFT. The inclusion of spin-orbit coupling necessitates a non-collinear treatment of spin.
SOC is fundamentally a relativistic effect that emerges from the relativistic formulation of quantum mechanics. Starting from Dirac's Hamiltonian for an electron in a central potential, an approximate SOC term can be derived by considering the non-relativistic limit. This SOC contribution can then be added to the non-relativistic Hamiltonian as a perturbation [7]

$$H_{SO} \propto \frac{1}{2c^2 r}\frac{dV}{dr}\mathbf{L}\cdot\mathbf{S}$$

[9] If we consider the version of LDA taking into account relativistic effects, namely LSDA, the XC energy depends on the density and on the modulus of the magnetization density $\mathbf{m}(\mathbf{r})$, so we have $E_{xc}[n,|m|]$.

where V denotes the system potential, r represents the radial coordinate with respect to the atomic nucleus, and $\mathbf{L}$ and $\mathbf{S}$ are, respectively the orbital angular momentum and the electron spin operators. The term $\frac{1}{r}\frac{dV}{dr}$ becomes significant primarily near the nucleus of a heavy atom, where r is small and $\frac{dV}{dr}$ is large.
SOC has a very profound effect on the energy band structure of solids. For example, in semiconductors such as GaAs, SO gives rise to a splitting of the VBM (Fig. 2.5). In a tight-binding picture without spin, the electron states at the valence band edges are p-like (orbital angular momentum $l = 1$). With SOC taken into account, we obtain electronic states with total angular momentum $j = 3/2$ (4-fold degenerate) and $j = 1/2$. These states are split in energy by a quantity Δ_0, which is referred to as the SO splitting energy. The value of this splitting is small for light atoms like Si ($\Delta_0 \simeq 0.044\,eV$), but it is significant for semiconductors composed of heavy atoms such as GaAs ($\Delta_0 \simeq 0.34\,eV$) or InSb ($\Delta_0 \simeq 0.82\,eV$). The effect is even more evident in elemental Te and it is somehow dependent on dimensionality. These examples illustrate how the motion of crystal electrons is affected by SOC.

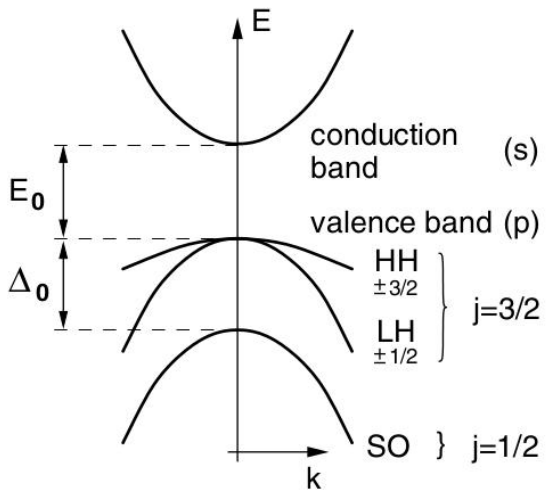

Figure 2.5: *Qualitative sketch of the band structure of GaAs close to the fundamental gap. Note that the state with $j = 3/2$ is 4-fold degenerate near the band-edge: these four bands are called heavy-holes (HH) and light-holes (LH) because of the different effective mass. The split-off (SO) band is separated by Δ_0 from the heavy and light hole bands at Γ ($k = 0$) point.*

In this work, SOC corrections were included, when necessary, as implemented in the QE suite [29,30], in which SOC is introduced in the non-local part of the pseudopotential, which becomes a 2×2 matrix operating on the spinor wavefunctions and separate pseudopotential projectors are used for each $j = l \pm \frac{1}{2}$.
The SO interaction in the KS Hamiltonian is therefore introduced through the pseudopotentials that are solutions of the four-component all-electron Dirac equations [31] for the atoms. Further details on fully-relativistic pseudopotentials are given in the next section.

2.4.8 Fully-Relativistic Pseudopotentials

In order to apply the above formalism to a real material, we use a relativistic pseudopotential as the external potential. Typically, no external magnetic field is applied, and $V_{ext}^{\sigma,\sigma'}$ is diagonal with respect to spin indices. A pseudopotential is applied to both spin components, consisting of a local part $V_{loc}(\mathbf{r})$ and a non-local part. The non-local part can be expressed by introducing projectors onto orbital angular momentum channels around each atom i

$$V_{NL} = \sum_i \sum_{l,m_l} E_l^i \left|\beta_l^i Y_{l,m_l}^i\right\rangle \left\langle\beta_l^i Y_{l,m_l}^i\right|$$

Since the radial components of solutions from a fully-relativistic atomic Dirac-like equation depend on both the total angular momentum j and the orbital angular momentum l, while the radial components of solutions from non-relativistic or scalar-relativistic equations depend only on l, this pseudopotential can be constructed to include scalar-relativistic effects but not SOC.
If the pseudopotential is derived from components of the solutions of the Dirac equation, projectors ($\beta_{l,j}$) and pseudopotential coefficients $E_{l,j}$ are obtained for each combination of l and j. To project them into states with well-defined total angular momentum, the spin-angle functions

$$Y_{l,1/2}^{j,m_j} = \begin{pmatrix} \left(\frac{l+m+1}{2l+1}\right)^{1/2} Y_{l,m} \\ \left(\frac{l-m}{2l+1}\right)^{1/2} Y_{l,m+1} \end{pmatrix}, \qquad Y_{l,1/2}^{j,m_j} = \begin{pmatrix} \left(\frac{l-m+1}{2l+1}\right)^{1/2} Y_{l,m-1} \\ -\left(\frac{l+m}{2l+1}\right)^{1/2} Y_{l,m} \end{pmatrix} \tag{2.24}$$

are defined for $j = l+1/2$ and $j = l-1/2$, respectively. In the first case $m = m_j - 1/2$, while in the second $m = m_j + 1/2$. Introducing (2.24) in the non-local part of the pseudopotential, we obtain

$$V_{NL} = \sum_i \sum_{l,j,m_j} E_{l,j}^i \left|\beta_{l,j}^i Y_{l,1/2}^{i,j,m_j}\right\rangle \left\langle\beta_{l,j}^i Y_{l,1/2}^{i,j,m_j}\right|$$

Therefore V_{NL} is a 2×2 matrix in the spin indexes. This pseudopotential includes both scalar relativistic and SOC effects.
If we then introduce the Clebsch-Gordan coefficients $\alpha_{m_j}^{\sigma,l,j}$, a unitary matrix $U_{m_j,m'}^{\sigma,l,j}$ which selects the appropriate spherical harmonics

$$Y_{l,1/2}^{j,m_j,\sigma} = \alpha_{m_j}^{\sigma,l,j} \sum_{m'=-l}^{l} U_{m_j,m'}^{\sigma,l,j} Y_{l,m'}$$

we can summarize all in the *non-local pseudopotential* as

$$V_{NL}^{\sigma,\sigma'} = \sum_i \sum_{l,j,m,m'} E_{l,j,m,m'}^{i,\sigma,\sigma'} \left|\beta_{l,j}^i Y_{l,m}^i\right\rangle \left\langle\beta_{l,j}^i Y_{l,m'}^i\right|$$

with the new coefficients

$$E^{i,\sigma,\sigma'}_{l,j,m,m'} = E^{i}_{l,j} \sum_{m_j=-j}^{j} \alpha^{\sigma,l,j}_{m_j} U^{\sigma,l,j}_{m_j,m} \alpha^{\sigma',l,j}_{m_j} U^{*,\sigma',l,j}_{m_j,m'}$$

where $-l < m < l$ and $-l < m' < l$.
The coefficients of the non-local pseudopotential become then spin-dependent, but the projectors are still written in terms of spherical harmonics as in a scalar-relativistic pseudopotential.

Chapter 3

Theoretical Background: Excited-State Properties

Electronic Properties

In the first part of this chapter, we introduce the many-body perturbation theory (MBPT) framework, which overcomes the limitations of DFT in accurately describing the excited states properties of materials. In the many-body approach, the key quantity is the Green's function. The Green's function contains much more information than the electronic density, but it is also a more complex object, making MBPT methods generally more computationally expensive than DFT. In the following sections, we introduce some physical concepts fundamental to MBPT and discuss common approximations used to calculate electronic and optical properties.

3.1 Photoemission Spectroscopy

In a direct photoemission spectroscopy experiment, an electron is emitted from a sample due to the absorption of a photon (see Fig. 3.1). The absorbed photon excites the electron, which can escape only from a depth on the order of nanometers, so that it is the surface layer which is analyzed. By measuring the kinetic energy of the photoemitted electron, we obtain information on the electronic properties of the system. In an independent-particle (IP) picture (like DFT Kohn-Sham equations), the kinetic energy of the emitted electron gives the energy ϵ_i^{IP} of the state the electron was occupying before the interaction with the photon. In the photoemission spectrum, if the weakly interacting picture is almost valid, this should give rise to a delta peak at this energy. In real experiments, however, the actual spectra are much more complex than a series of delta peaks at energies ϵ_i[1]. Indeed, experimental photoemission spectra reveal peaks that are shifted, renormalized, and broadened (thus having a finite width) compared to the IP ones. This is due to the many-body interactions within the system, not captured by the almost IP approach, which results in what are known as

[1] Real photoemission spectra exhibit additional features, called *satellites*, which are due to the many-body nature of the problem and are attributed to other excitations in the system induced by the absorbed photon. However, this part will not be discuss in the present thesis.

quasi-particle (QP) peaks. To put it simple, the emitted electron leaves a hole behind in its previous state, causing the remaining electrons to relax and screen the newly-created positive charge. This *excited* state[2] has a finite lifetime, which is inversely related to the width of the QP peak: a delta peak (zero width) corresponds to an infinite lifetime (as in the ideal IP picture), whereas a broader peak indicates stronger many-body effects and a shorter lifetime. Therefore, the width of the QP peak provides a measure of the interactions due to the presence of a hole: electrons of higher energy tend to fill the hole, reflecting the system's instability.
The N-electron system, originally in its ground state $\left|\Psi_0^N\right\rangle$ with total energy E_0^N, is now excited to a state with $N-1$ electrons, $\left|\Psi_i^{N-1}\right\rangle$ with energy E_i^{N-1}, where i stands for the single-particle state where the hole was created.

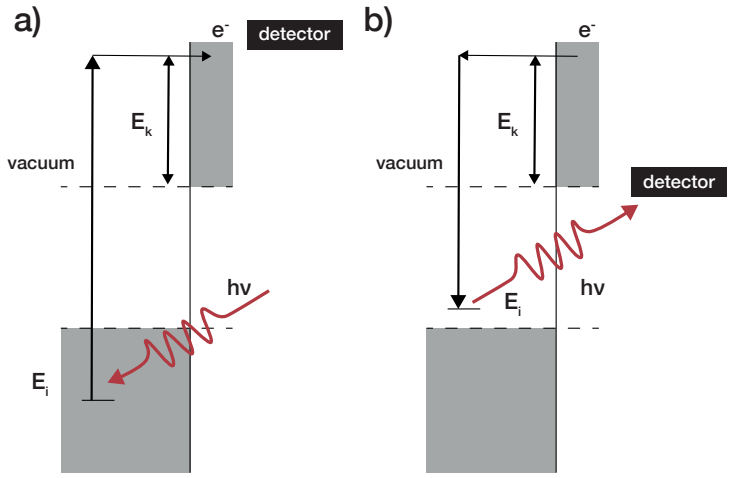

Figure 3.1: *Photoemission* (**a**) *and inverse photoemission* (**b**) *experiments. The electron kinetic energy out of the material and its energy level in the material are marked as* E_k *and* E_i *respectively. The energy of the absorbed* (**a**)*, emitted* (**b**) *photon is* $h\nu$*.*

Conversely, in an inverse photoemission, the reverse process occurs: an electron is absorbed by the system, resulting in the emission of a photon. The system is then excited to a state of $N+1$ electrons, represented by the ket $\left|\Psi_i^{N+1}\right\rangle$ with energy E_i^{N+1}. Therefore, direct and inverse photoemission experiments provide information about electron removal and addition energies, or, in other words, the energies of the occupied and unoccupied states, $\epsilon_{i,\mathrm{occ}} = E_0^N - E_i^{N-1}$ and $\epsilon_{i,\mathrm{unocc}} = E_i^{N+1} - E_0^N$, re-

[2] An excited state is any quantum state of a system that has a higher energy than a chosen starting point, usually the ground state. The lifetime of the excited state is usually short: spontaneous or induced emission of a quantum of energy (such as a photon or a phonon) usually occurs shortly after the system is promoted to the excited state, returning the system to a state with lower energy (a less excited state or the ground state). This return to a lower energy level is often loosely described as decay and is the inverse of excitation. Long-lived excited states are often called metastable.

spectively. In the following section, we will illustrate how removal and addition energies of electrons in a many-body interacting system are encoded in the so-called single-particle Green's function. Next, we introduce the concept of *self-energy* from a qualitative point of view. The self-energy, denoted by Σ, theoretically includes all many-body interactions and depends on the energy of the QP states, making its evaluation significantly more complex than the quantities used in the previous chapter to model interactions. In general, Σ is a complex function; its real part provides the QP energies, while its imaginary part gives the width of the QP peak. If the system is not allowed to relax — meaning the hole is frozen and electrons cannot fall into it — the lifetime of the excited state is assumed to be infinite. This is known as the *static approximation* to Σ, i.e. $\mathrm{Im}(\Sigma) = 0$. On the contrary, a *dynamic* Σ yields complex quasi-particle energies, whose imaginary parts are related to the lifetimes of the associated excited states. A quantitative treatment of the self-energy is presented in section 3.4.

3.2 The Green's Functions Formalism

To introduce Green's functions, we switch to a second quantization[3] description of the many-particles system. We limit the discussion to fermions and to zero-temperature formalism, considering the system at equilibrium. We introduce the fermionic creation and annihilation operators $\hat{a}_i^\dagger$ and $\hat{a}_i$, which satisfy the anticommutation[4] rules $\{\hat{a}_i, \hat{a}_j\} = \{\hat{a}_i^\dagger, \hat{a}_j^\dagger\} = 0$ and $\{\hat{a}_i, \hat{a}_j^\dagger\} = \delta_{ij}$. As the names suggest, these operators act on a fermionic state by adding or removing a particle, respectively [32]. By expanding these operators into the position basis $|\mathbf{r}\rangle$, we obtain the field operators [5]:

$$\hat{\psi}(\mathbf{r}) = \sum_i \varphi_i(\mathbf{r})\hat{a}_i$$
$$\hat{\psi}^\dagger(\mathbf{r}) = \sum_i \varphi_i^*(\mathbf{r})\hat{a}_i^\dagger$$

where $\varphi_i(\mathbf{r}) = \langle \mathbf{r}|i\rangle$ are single-particle wavefunctions. All many-particle operators in second quantization, like total energy, density, etc., can be written in terms of the field operators $\hat{\psi}$ and $\hat{\psi}^\dagger$, and the calculation of their quantum averages can be easily performed with the help of the anticommutation relations[6]. Next, it is convenient to introduce the so-called *Heisenberg representation*, in which both operators and wavefunctions have a time dependence [33]. Given the Hamiltonian $\hat{H}$ of the system, the field operator in this representation reads $\hat{\psi}(\mathbf{r}, t) = e^{i\hat{H}t}\hat{\psi}(\mathbf{r})e^{-i\hat{H}t}$, which removes a fermion at position r at time t. Similarly, $\hat{\psi}^\dagger(\mathbf{r}', t') = e^{i\hat{H}t'}\hat{\psi}^\dagger(\mathbf{r}')e^{-i\hat{H}t'}$ creates a fermion at r' at time t'. With these definitions, we can now introduce the *single-particle Green's function*:

[3] Second quantization, also referred to as occupation number representation, is a formalism used to describe and analyze quantum many-body systems. In this approach, the quantum many-body states are represented in the Fock state basis, which are constructed by filling up each single-particle state with a certain number of identical particles. The second quantization formalism introduces the creation and annihilation operators to construct and handle the Fock states, providing useful tools to the study of the quantum many-body theory.

[4] We define the anticommutator $\{.,.\}$ of the fermionic operators A and B as $\{A, B\} = AB + BA$.

[5] Contrary to the previous chapter, here we will consistently denote operators using the symbol $\hat{}$ to avoid confusion.

[6] Now it holds $\{\hat{\psi}(\mathbf{r}), \hat{\psi}(\mathbf{r}')\} = \{\hat{\psi}^\dagger(\mathbf{r}), \hat{\psi}^\dagger(\mathbf{r}')\} = 0$ and $\{\hat{\psi}(\mathbf{r}), \hat{\psi}^\dagger(\mathbf{r}')\} = \delta(\mathbf{r} - \mathbf{r}')$.

$$G(\mathbf{r},t;\mathbf{r}',t') = -i\left\langle \Psi_0^N \right| \hat{T}\left[\hat{\psi}(\mathbf{r},t)\hat{\psi}^\dagger(\mathbf{r}',t')\right]\left|\Psi_0^N\right\rangle \tag{3.1}$$

where $\left|\Psi_0^N\right\rangle$ is the many-body ground state for a system of N interacting electrons, and $\hat{T}$ is the time-ordering operator. Here and in the following, we take $\hbar = 1$, neglect spin to simplify the notation and we impose the normalization condition $\left\langle \Psi_0^N \middle| \Psi_0^N \right\rangle = 1$ is fullfilled. To clarify the meaning of $\hat{T}$, we can rewrite Eq. (3.1) as:

$$G(\mathbf{r},t;\mathbf{r}',t') = \begin{cases} -i\left\langle \Psi_0^N \right| \hat{\psi}(\mathbf{r},t)\hat{\psi}^\dagger(\mathbf{r}',t')\left|\Psi_0^N\right\rangle & t > t' \\ \;\; i\left\langle \Psi_0^N \right| \hat{\psi}^\dagger(\mathbf{r}',t')\hat{\psi}(\mathbf{r},t)\left|\Psi_0^N\right\rangle & t < t' \end{cases} \tag{3.2}$$

This form of the Green's function is non-local both in space and time, and has the physical interpretation of a single-particle propagator. Indeed, for $t > t'$, $G(\mathbf{r},t;\mathbf{r}',t')$ represents the probability amplitude that a particle created at $(\mathbf{r}',t')$ will be annihilated at $(\mathbf{r},t)$, describing the propagation of a conduction electron. For $t < t'$, the Green's function instead describes the propagation of a hole, which can be seen as a fermion moving backward in time.
It is straightforward to show [32] that the ground-state expectation value of any single-particle operator $\hat{O}$ can be written as:

$$\langle \hat{O}(\mathbf{r}) \rangle = \int d\mathbf{r}\hat{\psi}^\dagger(\mathbf{r})\hat{O}(\mathbf{r})\hat{\psi}(\mathbf{r}) = -i \lim_{t'\to t^+} \lim_{\mathbf{r}'\to\mathbf{r}} \mathrm{Tr}[O(\mathbf{r})G(\mathbf{r},t;\mathbf{r}',t')]$$

where Tr[...] is the trace of the matrix product and t^+ is an infinitesimal time later than t, in order to ensure the correct time ordering. In particular, we can express the ground-state expectation value of the density operator $\hat{n}(\mathbf{r})$ as:

$$\langle \hat{n}(\mathbf{r}) \rangle = \int d\mathbf{r}'\hat{\psi}^\dagger(\mathbf{r}')\delta(\mathbf{r}-\mathbf{r})'\hat{\psi}(\mathbf{r}') = -iG(\mathbf{r},t;\mathbf{r},t^+) \tag{3.3}$$

To summarize, $G(\mathbf{r},t;\mathbf{r}',t')$ is the single-particle Green's function, describing the propagation of a single fermion added to or subtracted from a system of N interacting particles. Although Eq. (3.1) implies the loss of much detailed information about the ground state, the single-particle Green's function still contains the observable properties of greatest interest:

1. the expectation value of any single-particle operator in the ground state of the system, as seen above,

2. the ground-state energy of the system[7],

3. The excitation energies of the system.

The third point is discussed in details in the next section.

[7] For details, see [32]

3.2.1 The Lehmann Representation

In this section, we delve deeper into the physical meaning of the single-particle time-ordered Green's function and establish the following points: (i) the poles of the Green's function in the frequency domain correspond to the electron addition and removal energies; (ii) the imaginary part of the Green's function, known as the spectral function A, is directly related to the measured photoemission spectra.
If we consider the case where there are no time-dependent external potentials, the system is stationary and G depends only on the time difference $\tau = t - t'$. By inserting in Eq. (3.2) the complete set of many-body excited states $\left|\Psi_n^{N\pm1}\right\rangle$, solutions of the fully-interacting Hamiltonian, and taking a Fourier transform in time, we obtain the so-called *Lehmann representation* of the Green's function:

$$G(\mathbf{r},\mathbf{r}',\omega) = \sum_n \frac{f_n(\mathbf{r}) f_n^*(\mathbf{r}')}{\omega - \epsilon_n + i\eta\, sgn(\epsilon_n - \mu)} \tag{3.4}$$

where μ is the chemical potential and η an infinitesimal positive number, i.e. $\eta \to 0^+$. Furthermore,

$$f_n(\mathbf{r}) = \begin{cases} \left\langle \Psi_0^N \right| \hat{\psi}(\mathbf{r}) \left| \Psi_n^{N+1} \right\rangle & \epsilon_n > \mu \\ \left\langle \Psi_n^{N-1} \right| \hat{\psi}(\mathbf{r}) \left| \Psi_0^N \right\rangle & \epsilon_n < \mu \end{cases} \tag{3.5}$$

are the Lehmann amplitudes and

$$\epsilon_n = \begin{cases} E_n^{N+1} - E_0^N & \epsilon_n - \mu > 0 \\ E_0^N - E_n^{N-1} & \epsilon_n - \mu < 0 \end{cases} \tag{3.6}$$

are the excitation energies for adding ($\epsilon_n - \mu > 0$) or removing ($\epsilon_n - \mu < 0$) a fermion from the system.
This representation of G is extremely useful in clarifying one of the most important pieces of information provided by the single-particle Green's function. By examining the denominator of Eq. (3.4), it is immediately apparent that the time-Fourier transform of G has its poles at the single-particle excitation energies of the system (Fig. 3.2). Consider the case of adding an electron to a material: as this electron propagates through the system, it will be surrounded by a positively polarized region due to the electron-electron repulsion. The combination of the electron and this induced polarization cloud can be thought of as a QP, specifically a quasi-electron in this context. A similar reasoning applies to the case of electron removal, where the created QP is referred to as a quasi-hole. The energies ϵ_n (3.6) and the corresponding Lehmann amplitudes f_n (3.5) can be approximately interpreted as the excitation energies and wavefunctions of these QPs. Such interpretation is consistent to the simpler case of a system of independent particles, as the Kohn-Sham auxiliary system. Indeed, by Fourier-transforming Eq. (3.4) in space, we obtain the form:

$$\begin{aligned} G(\mathbf{k},\omega) &= \sum_n \frac{f_{n\mathbf{k}}\, f_{n\mathbf{k}}^*}{\omega - \epsilon_{n\mathbf{k}} + i\eta\, sgn(\epsilon_{n\mathbf{k}} - \mu)} \\ &= \sum_{n\mathbf{k}} G_{n\mathbf{k}}(\omega) \end{aligned} \tag{3.7}$$

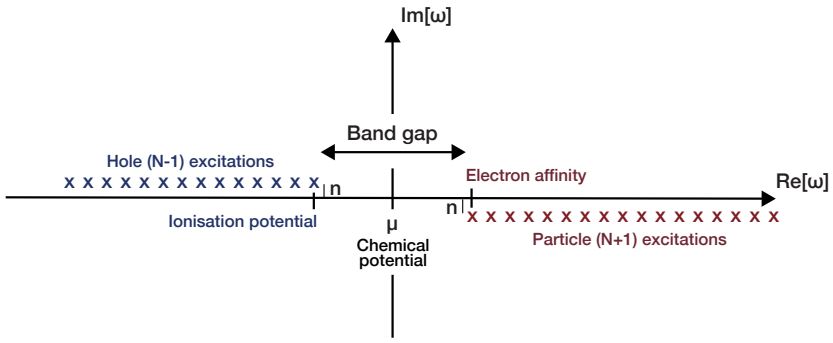

Figure 3.2: *Schematic representation of the location of the poles of the time-ordered Green's function. The ionization potential is the energy required to remove an electron ($I = E_N^0 - E_{N-1}^0$) from the system, the electron affinity the energy required to add an electron ($A = E_N^0 - E_{N+1}^0$). μ is the chemical potential and the superscript 0 indicates the N-particle ground state*

In the non-interacting system, the field operators connect only one state to the ground state, so that the *non-interacting Green's function* $G_{\mathbf{k}}^0(\omega)$ has only a single pole, namely:

$$G_{\mathbf{k}}^0(\omega) = \frac{f_{n\mathbf{k}}}{\omega - \epsilon_{n\mathbf{k}} - i\eta} + \frac{1 - f_{n\mathbf{k}}}{\omega - \epsilon_{n\mathbf{k}} + i\eta}$$

It is straightforward to demonstrate that in this case the $\epsilon_{n\mathbf{k}}$ correspond to the energies of the single particle levels $\phi_{n\mathbf{k}}$ of Eq. (2.14), while the amplitudes $f_{n\mathbf{k}}$ coincide with the occupation number of the same states.
We now focus on the imaginary part of the single-particle Green's function to obtain an important quantity for the interpretation of spectroscopy experiments. Indeed, from the Lehmann representation of the Green's function (3.4), we can define the *spectral function* as[8]

$$A(\mathbf{r}, \mathbf{r}', \omega) = \frac{1}{\pi} \mathrm{Im}\, G(\mathbf{r}, \mathbf{r}', \omega)$$

The spectral functions are then real functions of ω, always positive, and related to the Lehmann amplitudes of one-particle excitations. It should be noticed that the spectral function contains the same information as G. Using the Cauchy integral representation, the Green's function can be recovered from the spectral function. When taking the contour as represented in Fig. 3.3, the Green's function G can be written in a compact form as

$$G(\mathbf{r}, \mathbf{r}'; \omega) = \int_C d\omega' \, \frac{A(\mathbf{r}, \mathbf{r}', \omega')}{\omega - \omega'}$$

[8] For a general discussion on spectral functions, we refer the reader to Ref. [33].

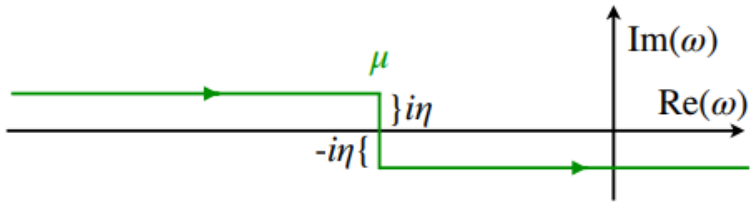

Figure 3.3: *Integration contour C adopted in Eq. (3.8).*

Similarly to what we have shown for the G (3.3), it can be shown that the ground-state electronic density can be derived from A

$$\int_{-\infty}^{\mu} A(\mathbf{r},\mathbf{r}',\omega)\,d\omega = \left\langle \Psi_0^N \middle| \hat{\psi}^\dagger(\mathbf{r})\hat{\psi}(\mathbf{r}) \middle| \Psi_0^N \right\rangle = \langle \hat{n}(\mathbf{r}) \rangle$$

The spectral function plays a crucial role in the analysis and interpretation of spectroscopic experiments. It encapsulates the essential information about the single-particle excitations in a system, linking theoretical models with experimental measurements. This is made clear if we rewrite A for a general diagonal element in reciprocal space:

$$A_{\mathbf{k}}(\omega) = \frac{1}{\pi} \frac{|\mathrm{Im}\,\Sigma_{n\mathbf{k}}(\omega)|}{[\omega - \epsilon^0_{\mathbf{k}} - \mathrm{Re}\,\Sigma_{n\mathbf{k}}(\omega)]^2 + [\mathrm{Im}\,\Sigma_{n\mathbf{k}}(\omega)]^2}$$

If we start by considering the non-interacting picture, where the self-energy Σ vanishes, the spectral function consists of a series of δ-peaks centered at the non-interacting single-particle energies $\epsilon^0_{\mathbf{k}}$. When we introduce interactions, the self-energy shifts the peaks by $\mathrm{Re}\,\Sigma_{n\mathbf{k}}(\omega)$ and broadens them by $\Gamma_{n\mathbf{k}} = \mathrm{Im}\,\Sigma_{n\mathbf{k}}(\omega)$. Due to the one-to-one correspondence with the non-interacting peaks, this structure is called QP peak [33]. The quantity $\Gamma_{n\mathbf{k}}$ is also known as QP lifetime. A schematic representation is provided in Fig. 3.4.
In the interacting case, we also observe the appearance of other peaks, called satellites, which arise from the imaginary part of the self-energy. These are due to additional excitations that occur when a particle is added to or removed from the system, such as plasmons and atomic-like excitations. If these satellite peaks have too much weight in the spectrum, the single-particle picture is no longer valid, and we describe the system as *strongly correlated*. The experimental analogous that allows to measure such spectral functions (and hence the QP levels of the system) are direct and inverse photoemission, shown in Fig. 3.1. Experimental measures of the full band structure of a system can be carried out within Angle-Resolved Photoemission Spectroscopy (ARPES) [34,35].

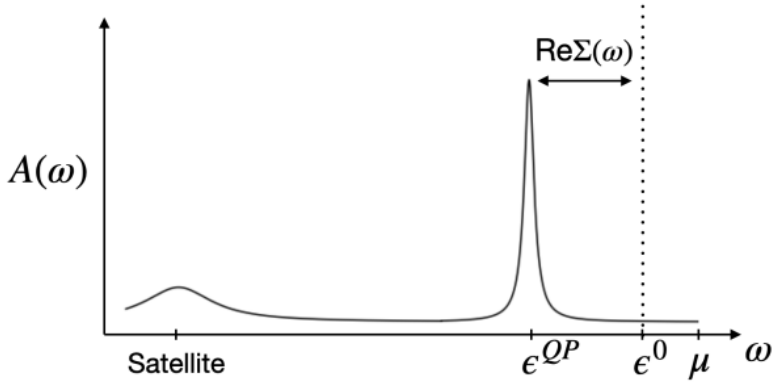

Figure 3.4: *Effects of the many-body self-energy: the delta-like independent-particle peak* (ϵ^0) *is shifted* ($\epsilon^0 \to \epsilon^0 + \mathrm{Re}\,\Sigma_{n\mathbf{k}}(\omega)$) *and its weight is redistributed between the QP peak* (ϵ^{QP}) *and satellites.*

3.2.2 The Dyson Equation for G

From the equations of motion (EOM) of $\hat{\psi}(\mathbf{r}, t)$ and $\hat{\psi}^\dagger(\mathbf{r}', t')$ [36], an EOM for G can be derived[9] [37]

$$\left[i\frac{\partial}{\partial t_1} - h(1) \right] G(1;2) = \delta(1;2) - i \int v(1;3) G_2(1,3;2,3^+)\, d3 \tag{3.8}$$

where we introduce the compact notation $(\mathbf{r}_j, t_j) \to j$. In this expression, we find

$$\hat{h} = -\frac{\boldsymbol{\nabla}^2}{2} + \hat{V}_{\mathrm{ext}}$$

the one-particle term of the Hamiltonian and

$$v(1;2) = \delta(t_1 - t_2) \frac{1}{|\mathbf{r}_1 - \mathbf{r}_2|}$$

$v(1,2)$ the Coulomb interaction. G_2 is the *two-particle Green's function*, defined as

$$G_2(1,2;3,4) = -\left\langle \Psi_0^N \middle| \hat{T}\left[\hat{\psi}(1)\hat{\psi}(2)\hat{\psi}^\dagger(4)\hat{\psi}^\dagger(3) \right] \middle| \Psi_0^N \right\rangle \tag{3.9}$$

The equation for the one-particle Green's function G, Eq. (3.8), involves the two-particle Green's function G_2, which describes the creation and annihilation of pairs of particles. Similarly, the EOM for G_2 can also be derived, and one finds that G_2 depends on G_3, and so on. This procedure leads to new equations for the Green's functions that depend on the Green's functions themselves in a non-linear way. The solutions are therefore non-perturbative in the interaction strength v. This can be understood as follows: the propagation of the first electron (described by G) can create

[9] To be precise, we obtain two coupled EOMs for G, with the second one being equivalent but involving the time derivative acting on the left-hand side. Additionally, these differential equations are meaningful only if they are accompanied by an initial condition, which in this case is $G_0(1,2) = 1$.

an electron-hole pair, which can in turn induce a cascade of other electron-hole pairs. Solving the equations for all these processes is as complex as solving the full many-body problem, thus necessitating perturbation theory. If the goal is to calculate one-particle properties, the strategy is to find a good approximation for G_2 in terms of G. For calculating two-particle properties, such as optical properties, one should find approximations for G_3 in terms of G_2. The explicit calculation of the exact Green's function is not possible for the system of interest (real solids). The solution to this problem relies in Wick's theorem [38] and Feynman diagrams [32,39], allowing us to compute an approximate expression of G. This forms the basis of MBPT. In the case of a system of interacting electrons, using this theory allows for the Green's function to be obtained with high accuracy.
To obtain an expression for G_2 in terms of G, one can employ Schwinger's functional-derivative method [32]. This method involves the introduction of a perturbing, time-dependent external potential U_{ext}. This perturbation acts as a tool for differentiation, and at the conclusion of the differentiation process, U_{ext} is typically reduced to a static external potential V_{ext}.
Let χ denote the response of the density to changes in the external potential, or in other words, the *polarizability* of the system

$$\chi(1;2) = \frac{\delta n(1)}{\delta U_{\text{ext}}(2)}$$

We define an effective potential V_{eff} that includes the external potential U_{ext} and the Coulomb potential created by the induced charge, V_{H}, as

$$V_{\text{eff}}(1) = U_{\text{ext}}(1) + V_{\text{H}}(1)$$

with

$$V_{\text{H}}(1) = \int v(1;3)\chi(3;2)U_{\text{ext}}(2)\, d2d3$$

In contrast to the previous chapter, this effective potential does not include an XC contribution.
The polarizability χ is typically referred to as the *reducible polarizability*, where "reducible" indicates that the differentiation is performed with respect to U_{ext} and not V_{eff}. Therefore, we define the *irreducible polarizability*[10] as

$$P = \frac{\delta n(1)}{\delta V_{\text{eff}}(2)} = -i\frac{\delta G(1;1^+)}{\delta V_{\text{eff}}(2)} \tag{3.10}$$

where we have used the relation between the density and the Green's function, Eq. (3.3). The *dielectric function* ε can also be expressed in terms of the effective potential as

$$\varepsilon^{-1}(1;2) = \frac{\delta V_{\text{eff}}(1)}{\delta U_{\text{ext}}(2)} = \delta(1;2) + \int v(1;3)\chi(3;2)\, d3 \tag{3.11}$$

Combining Eqs. (3.10) and (3.11) and using the chain rule we obtain the geometric series, we obtain the inverse

[10] Sometimes defined as $\tilde{\chi}$.

$$\varepsilon(1;2) = \delta(1;2) - \int v(1;3)P(3;2)\,d3$$

The functional derivative of the Green's function with respect to the external potential can be written as [32]

$$\frac{\delta G(1;2)}{\delta U_{\text{ext}}(3)} = G(1;2)G(3;3^+) - G_2(1,3;2,3^+) \tag{3.12}$$

This last relation allows to eliminate the two-particle Green's function dependence in Eq. (3.8). Indeed, by inserting Eq. (3.12) in Eq. (3.8), we find a new expression for the EOM of G

$$\left[i\frac{\partial}{\partial t_1} - h(1)\right] G(1;2) = \delta(1;2) - i\int v(1;3)G(3;3^+)G(1;2)\,d3 + i\int v(1^+;3)\frac{\delta G(1;2)}{\delta U_{\text{ext}}(3)}\,d3 \tag{3.13}$$

It must be noticed that $-iG(3,3^+)$ is the electronic density $n(3)$ and therefore the term $-i\int v(1,3)G(3,3^+)\,d3$ is simply the Hartree potential. If we now define the self-energy Σ as

$$i\int v(1^+;3)\frac{\delta G(1;2)}{\delta U_{\text{ext}}(3)}\,d3 = \int \Sigma(1;3)G(1;2)\,d3 \tag{3.14}$$

then the EOM (3.13), can be rewritten as follows

$$\left[i\frac{\partial}{\partial t_1} - h(1) - V_H(1)\right] G(1;2) = \delta(1;2) - \int \Sigma(1;3)G(1;2)\,d3 \tag{3.15}$$

Since the Hartree term is local, it can be included in the single-particle Hamiltonian, that is $\hat{h}_0 = -\boldsymbol{\nabla}^2/2 + \hat{V}_{\text{ext}} + \hat{V}_H = \hat{h} + \hat{V}_H$. Let us now define the non-interacting Green's function G_0 as the Green's function obtained using as Lehmann amplitudes the wave functions ϕ_i and energies ϵ_i^0. The EOM of G_0 is:

$$\left[i\frac{\partial}{\partial t_1} - h_0(1)\right] G_0(1;2) = \delta(1;2) \tag{3.16}$$

Combining Eqs. (3.15) and (3.16) it can be seen that the link between G_0 and G is

$$G(1;2) = G_0(1;2) + \int G_0(1;3)\Sigma(3;4)G(4;2)\,d3d4 \tag{3.17}$$

which is the so-called *Dyson equation* [40] for G, often expressed symbolically as

$$G = G_0 + G_0\Sigma G$$

The *irreducible* self-energy Σ implicitly contains all the many-body interaction terms of the problem. Eq. (3.17), also depicted in Fig. 3.5 using Feynman diagrams [32], is fundamentally important

because it allows for the description of G in terms of perturbative expansions, where the lowest order is represented by the non-interacting Green's function G_0. The benefit of using perturbative expansions is that we can truncate the series at a desired order, thus including only the necessary physics without needing to solve the full problem to obtain the properties of interest. Eq. (3.17) is an integral equation with the self-energy Σ as the kernel, which encapsulates the effective coupling (the Coulomb interaction v). The self-energy Σ can also be treated within the perturbative expansion framework [32]. We will discuss the self-energy in more detail in the following sections.

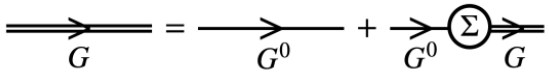

Figure 3.5: *Dyson equation for G in terms of Feynman diagrams. We can interpret this expansion in terms of a bare propagation G_0 and an effective interaction Σ.*

3.3 The Quasi-Particle Concept

By taking the time Fourier transform of Eq. (3.15), using the Lehmann representation (3.4) for G, and considering the limit $\omega \to \epsilon_n$ (while replacing $f_i(\mathbf{r})$ with $\phi_i(\mathbf{r})$), we obtain a reformulation of the Dyson equation

$$\hat{h}_0(\mathbf{r})\phi_i(\mathbf{r}) + \int \Sigma(\mathbf{r}, \mathbf{r}', \epsilon_i)\phi_i(\mathbf{r}')d\mathbf{r}' = \epsilon_i\phi_i(\mathbf{r}) \tag{3.18}$$

This is a Schrödinger-like equation, known as the *quasi-particle equation* [33]. When we compare Eq. (3.18) to the Kohn-Sham equation (2.14), we see that they have the same form except for the self-energy replacing the XC potential of DFT[11]. This comparison makes the interpretation of the Lehmann amplitudes clear: they are the *quasi-particle wavefunctions*.
In condensed matter physics, the concept of QP is a powerful tool for understanding the complex interactions within many-body systems. Introducing QPs allows us to partially retain the one-particle picture, as each QP associated with an electron. However, electrons in a solid are not independent particles; the Coulomb interaction between them is screened by the presence of all other electrons. This screening reduces the Coulomb interaction due to the dielectric constant of the medium, ε. When an electron is injected into a sample, the repulsive Coulomb interaction creates a polarization cloud around the additional electron (see Fig. 3.6). This occurs because the Coulomb potential of the electron repels surrounding electrons, resulting in an effective positive charge density appearing around the electron. Thus, in this case, a QP consists of an electron and its screening cloud. The electron and the cloud interact via a screened Coulomb potential, often called W, which is smaller than the bare one v (see Appendix A)

$$W(1;2) = \int d3\, \varepsilon^{-1}(1;3)v(2;3) \tag{3.19}$$

[11]Note that we can recover the KS equations (2.14) by taking $\Sigma(\mathbf{r}, \mathbf{r}', \omega) = V_{xc}[n(\mathbf{r})]\delta(\mathbf{r} - \mathbf{r}')$, which express the locality of V_{xc}

W is a dynamic quantity, in contrast to v, since it is frequency-dependent. Fig. 3.6 represents W as the effective potential at $\mathbf{r}'$ induced by the QP at $\mathbf{r}$. W is then the combination of the potential of the bare electron and its screening cloud. The same picture can be used for holes but, in this case, an effective negative charge screens the bare interaction between holes.

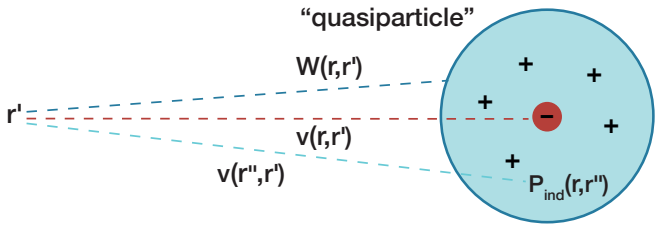

Figure 3.6: *Simplified representation of the quasiparticle and screening potential W.*

3.4 The Self-Energy

Eq. (3.18) can be separated into two parts: one part is given by the non-interacting Hamiltonian $\hat{h}_0$, where electrons interact only via the Hartree term, and the other part contains Σ, which accounts for all the many-body XC interactions representing all electron-electron interactions beyond those included by the Hartree potential. In summary, the self-energy is the effective potential that an additional particle experiences due to the polarization induced by its propagation.
It should be noticed that Eq. (3.18) is not linear in ϵ_i, and Σ is a function of ϵ_i itself. In addition, the self-energy is non-local and non-Hermitian. Consequently, the wavefunctions ϕ_i are not orthogonal, and the energies ϵ_i are in general not real. Indeed, the imaginary part of ϵ_i accounts for the finite lifetimes of the QP. The real part of ϵ_i defines the electron addition or removal energy, thus representing the energies used to describe the band structure. Starting from Eq. (3.14), it can be shown that Σ has the following expression:

$$\Sigma(1;2) = -i \int v(1^+;3) G(1;4) \frac{\delta G^{-1}(4;2)}{\delta U_{\text{ext}}(3)} \, d3d4 \tag{3.20}$$

Thus, to calculate the excitation energies ϵ_i, approximations to Σ are needed. In this section, we discuss two common approximations for Σ, while in Sec. 3.5.1, we will introduce the GW approximation, which is widely used in the context of MBPT and is central to this thesis.
The simplest approximation for the self-energy is to neglect it entirely by setting $\Sigma = 0$. In the context of Eqs. (3.15) and (3.18), this approximation corresponds to a classical system where particles interact only through the Hartree potential. This is thus referred to as the *Hartree approximation*.
A first approach to introduce quantum effects through the self-energy is to approximate Σ to first order in the Coulomb potential:

$$\Sigma_{\text{x}}(1;2) = iG(1;2)v(1^+;2) \tag{3.21}$$

Here, Σ_{x} is known as the *Fock self-energy* and it accounts for the exchange between indistinguishable electrons. The standard expression for the Fock exchange can be derived from definition Eq. (3.21) using the real-space representation of the Green's function

$$\Sigma_{\mathrm{x}}(\mathbf{r}_1, \mathbf{r}_2) = -\sum_{i}^{\mathrm{occ}} \phi_i(\mathbf{r}_1)\phi_i^*(\mathbf{r}_2)v(\mathbf{r}_1, \mathbf{r}_2) \tag{3.22}$$

It is important to note that:

- In Eq. (3.22), Σ_{x} is obtained by summing over occupied states, which can be represented as $\sum_i \Theta(\mu - \epsilon_i)$, where Θ is the step function. In frequency space, static self-energies depend only on occupied states because terms with negative times (removal excitations) are retained in G.

- The Fock self-energy is static, resulting in purely real energies for the system. Therefore, there is no distinction between Lehmann amplitudes and one-particle wavefunctions, and an extra particle in the system represents an excited state with an infinite lifetime.

- The interaction v is assumed to be instantaneous.

When the electron interactions are described using the Fock self-energy in addition to the Hartree potential, the approximation is known as *Hartree-Fock* (HF). Such self-energy is static and unscreened, i.e. does not consider dynamical effects like charge oscillations and retarded responses to the potential. It is well-known [41] that the Hartree-Fock eigenvalues are not accurate approximations for electron energies in a solid. Specifically, Hartree-Fock tends to overestimate band gaps significantly compared to DFT. This discrepancy highlights the need to include additional terms in the self-energy. While in HF exchange effects are fully considered, correlation effects are completely neglected. The importance of correlation becomes evident when considering the concept of QP and the screening potential W discussed in the previous section.

3.5 Hedin's Equations

So far, we have demonstrated the connection between the Green's function of a system, the associated QP energy levels, and their experimental counterpart. However, we have not yet proposed a practical scheme to obtain these quantities. This task is indeed very challenging because it requires the knowledge of the exact self-energy to be inserted in Eq. (3.18). Additionally, the complexity is increased by the fact that the self-energy is dynamical, meaning that it has a frequency dependence. More than 50 years ago, Lars Hedin proposed an iterative procedure to address this problem. This procedure starts from a closed (self-consistent) set of Dyson's equations, known as *Hedin's equations* [42]:

$$\Sigma(1;2) = i \int G(1;4)W(1^+;3)\tilde{\Gamma}(4,2;3)\, d3d4 \tag{3.23}$$

$$G(1;2) = G_0(1;2) + \int G_0(1;3)\Sigma(3;4)G(4;2)\, d3d4 \tag{3.24}$$

$$\tilde{\Gamma}(1,2;3) = \delta(1;2)\delta(1;3) + \int \frac{\delta\Sigma(1;2)}{\delta G(4;5)} G(4;6)G(7;5)\tilde{\Gamma}(6,7;3)\, d4d5d6d7 \tag{3.25}$$

$$P(1;2) = -i \int G(1;3)G(4;1)\tilde{\Gamma}(3,4;2)\, d3d4 \tag{3.26}$$

$$W(1;2) = v(1;2) + \int v(1;3)P(3;4)W(4;2)\, d3d4 \tag{3.27}$$

We have introduced here the irreducible *vertex function*

$$\tilde{\Gamma}(1,2;3) = -\frac{\delta G^{-1}(1;2)}{\delta V_{\text{eff}}(3)}$$

responsible for the introduction of two-particle effects in the irreducible polarizability P[12]. Here, "irreducible" still highlights that the differentiation is performed with respect to V_{eff}.
A formal proof of these equations is beyond the scope of this introduction, and we refer to the relevant literature for their derivation [33, 41, 42]. Hedin's equations are exact, meaning they exactly describe the many-body problem. Unfortunately, the complexity of these equations, and particularly Eq. (3.25), prevents us from solving them exactly, necessitating analytical approximations. Specifically, we start from the functional form of the self-energy Σ in terms of the Green's function G. By beginning with an approximate form of Σ, it is possible to iterate along the so-called Hedin's pentagon, as shown in Fig. 3.7, and solve the equations self-consistently. The final step of this cyclic iterative procedure is determined by the physics we aim to describe.

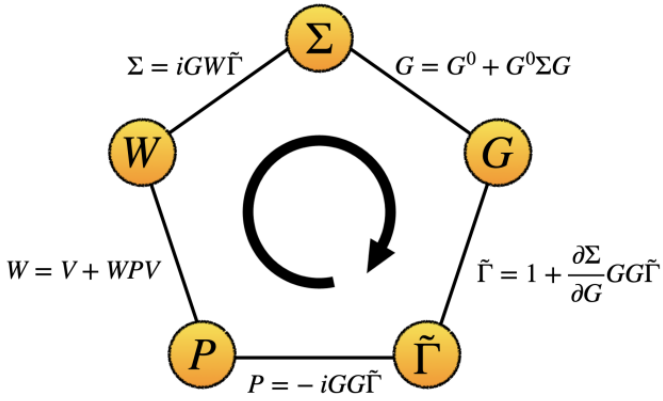

Figure 3.7: *The Hedin pentagon is a suggestive representation of Hedin's equations, Eqs. (3.23)-(3.27). In the corners, we have the fundamental quantities and along the sides the equation linking them in a closed scheme.*

[12] Also denoted as $\tilde{\chi}$.

3.5.1 The *GW* Approximation

According to Hedin's equations, the self-energy is symbolically written $\Sigma = iGW\tilde{\Gamma}$. Assuming that W is small, one can expect that retaining only the first-order perturbation in W should be accurate. This straightforward approach to solve the problem was suggested by Hedin in his seminal work [42]. It involves a single iteration over Hedin's pentagon (Fig. 3.7), starting from $\Sigma = 0$ and neglecting vertex corrections, i.e. $\tilde{\Gamma}(1,2;3) = \delta(1;2)\delta(1;3)$. Practically, this is done by skipping the vertex part in the pentagon and going directly from G to P. Following the loop in Fig. 3.7, we obtain the first order expression of Eqs. (3.23) - (3.27)

$$\Sigma(1;2) = 0 \tag{3.28}$$
$$G(1;2) = G_0(1;2) \tag{3.29}$$
$$\tilde{\Gamma}(1,2;3) = \delta(1;2)\delta(1;3) \tag{3.30}$$
$$P(1;2) = -iG(1;2^+)G(2;1^+) = P_0(1;2) \tag{3.31}$$
$$W(1;2) = v(1;2) + \int v(1;3)P_0(3;4)W(4;2)\, d3d4 = W_0(1;2) \tag{3.32}$$

Starting from $\Sigma = 0$ results in the Green's function being the independent-particle one. This, in turn, leads to the so-called *random-phase approximation* (RPA) for the polarizability P_0 (3.31) and the screening W_0 (3.32). We refer the reader to Appendix A for more details. Finally, we complete the first iteration of the loop to obtain a new approximation for the self-energy Σ

$$\Sigma_{\mathrm{GW}}(1;2) = iG(1;2)W(1^+;2) = iG_0(1;2)W_0(1^+;2) \tag{3.33}$$

Thus, the self-energy is then expressed as the product of G_0 and W_0. Due to this concise form, this approximation is called the *GW approximation*, whose diagrammatic expression is depicted in Fig. 3.8. Specifically, a single iteration on the Hedin's pentagon is properly called (single-shot) G_0W_0. More advanced self-consistent *GW* calculations can be performed [43, 44], but usually the G_0W_0 method is good enough to describe the QP band structure of a material within the accuracy of tens of meV.

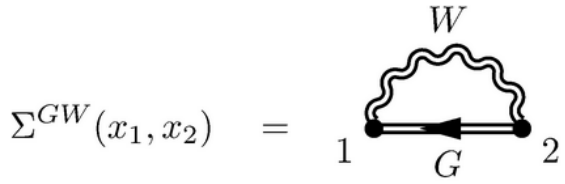

Figure 3.8: *Diagrammatic representation of the self-energy (3.33) in the GW approximation.*

The most important difference from the HF approximation is that, in the *GW* approximation, polarization effects are taken into account, which screen the propagation of the extra particle (electron or hole). *GW* also considers the relaxation of the system, unlike HF. As a result, the self-energy is dynamic, and the QP lifetime, given by the imaginary part of the QP energies, is

finite. When compared to the Fock self-energy in Eq. (3.21), we can see that, in addition to the static exchange term Σ_{x}, the GW self-energy Σ_{GW} has a dynamic part originating from W. We can separate Σ_{GW} into two terms corresponding to the exchange part, Σ_{x} (as in Eq. (3.21)), and the correlation, Σ_{c}, defined as

$$\Sigma_{\mathrm{c}}(1;2) = iG_0(1;2)W_{\mathrm{p}}(1^+;2)$$

where W_{p}, the polarizable part of W_0, is simply

$$W_{\mathrm{p}} = W_0 - v$$

and accounts for correlation effects. W_{p} carries all the dynamic effects of Σ.
To summarize, the GW approximation is based on the assumption that the terms proportional W^n, with $n > 1$, which appears in the vertex function (3.25), are negligible compared to the linear contribution in W, as a result of the electronic screening of the bare Coulomb interaction. The GW approximation generally yields electronic properties in very good agreement with experiments for a wide range of materials [45]. Commonly, G_0W_0 calculations are based on an LDA or GGA result as a starting point. In other words, they use the KS energies and wavefunctions as the non-interacting ones. We will talk more about this topic in the next sections.

3.6 Methods and Implementations in MBPT

3.6.1 The Plasmon-Pole Approximation (PPA)

One of the major computational challenges in calculating self-energy is computing the frequency-dependent screened interaction. Due to its erratic behavior along the real axis, a very large number of real frequencies are typically needed to achieve a converged result. However, it is reasonable to expect that approximate models, which can capture the main physical features of the screened interaction, could provide sufficiently accurate results while significantly reducing computational effort. This is precisely what we will show in this section.
We start from the definition of the GW self-energy (3.33) in the frequency space, that is

$$\Sigma_{\mathrm{GW}}(\omega) = -\int \frac{d\omega'}{2\pi i} e^{i\omega' 0^+} G(\omega + \omega')W(\omega')$$

The non-interacting Green's function G_0 used in the approximation is not the Hartree one, but the one built on the non-interacting KS single-particle orbitals $\phi^{\mathrm{KS}}_{n\mathbf{k}}$, G_0^{KS}. This is a convenient choice as in the $\phi^{\mathrm{KS}}_{n\mathbf{k}}$ there is already an attempt to include XC effects, encoded in V_xc potential. As discussed in the previous section, the self-energy can be split into the (Fock) exchange part, Σ_x, and in the frequency-dependent correlation part, Σ_c. The diagonal elements read[13]

$$\Sigma_{n\mathbf{k}} = \langle n\mathbf{k}| \Sigma_x |n\mathbf{k}\rangle + \langle n\mathbf{k}| \Sigma_c |n\mathbf{k}\rangle$$

[13]Here, we denote the KS orbitals $\phi^{\mathrm{KS}}_{n\mathbf{k}}$ as $|n\mathbf{k}\rangle$

and can be expanded in PWs as

$$\Sigma^x_{n\mathbf{k}} = -\sum_m^{occ} \int \frac{d\mathbf{q}}{(2\pi)^3} \sum_{\mathbf{G}} v(\mathbf{q}+\mathbf{G}) |\rho_{nm}(\mathbf{k},\mathbf{q},\mathbf{G})|^2 f_{m,\mathbf{k}-\mathbf{q}}$$

for the first term[14] and

$$\begin{aligned}\Sigma^c_{n\mathbf{k}}(\omega) = i\sum_m^{N_b} \int \frac{d\mathbf{q}}{(2\pi)^3} \sum_{\mathbf{G}\mathbf{G}'} v(\mathbf{q}+\mathbf{G}) \rho_{nm}(\mathbf{k},\mathbf{q},\mathbf{G}) \rho^*_{nm}(\mathbf{k},\mathbf{q},\mathbf{G}') \\ \times \int d\omega'\, G^0_{m,\mathbf{k}-\mathbf{q}}(\omega-\omega') \varepsilon^{-1}_{\mathbf{G}\mathbf{G}'}(\mathbf{q},\omega')\end{aligned} \tag{3.34}$$

for the second term[15]. The quantities

$$\rho_{nm}(\mathbf{k},\mathbf{q},\mathbf{G}) = \langle n\mathbf{k}|\, e^{i(\mathbf{q}+\mathbf{G})\cdot\mathbf{r}}\, |m\mathbf{k}-\mathbf{q}\rangle$$

are the dipole matrix elements of orbital pairs, also known as screening matrix elements. We also note that, by definition, $W_{\mathbf{G}\mathbf{G}'}(\mathbf{q},\omega) = \varepsilon^{-1}_{\mathbf{G}\mathbf{G}'}(\mathbf{q},\omega) v(\mathbf{q}+\mathbf{G}')$ is the screened Coulomb interaction (see Appendix A). It is clear that the screened potential, and thus Σ_c, can be computed once the dynamical screening matrix $\varepsilon^{-1}_{\mathbf{G}\mathbf{G}'}(\mathbf{q},\omega)$ is known. This matrix can be computed using the Dyson equation for the reducible polarizability χ, using the RPA (see Appendix A for more details). Usually, the integral in Eq. (3.34) is computationally demanding due to the large number of frequencies required for numerical integration. This integral can be evaluated analytically using well-known model, the *plasmon-pole approximation* (PPA) [46]. This approximation models the inverse screening matrix $\varepsilon^{-1}_{\mathbf{G}\mathbf{G}'}(\mathbf{q},\omega)$ with a single-pole function, given by:

$$\varepsilon^{-1}_{\mathbf{G}\mathbf{G}'}(\mathbf{q},\omega) = \delta_{\mathbf{G}\mathbf{G}'} + \frac{\Omega^2_{\mathbf{G}\mathbf{G}'}(\mathbf{q})}{\omega^2 - \bar{\omega}^2_{\mathbf{G}\mathbf{G}'}(\mathbf{q})} \tag{3.35}$$

This corresponds to assigning all the spectral weight of the dielectric function at a plasmon excitation pole. $\Omega_{\mathbf{G}\mathbf{G}'}(\mathbf{q})$ and $\bar{\omega}_{\mathbf{G}\mathbf{G}'}(\mathbf{q})$ are parameters[16] that can be obtained by imposing different constraints [47], which distinguish different "flavors" of the PPA. This approximation is implemented in the YAMBO code [48, 49], used in this thesis to compute MBPT.
It is important to note that while the PPA reduces the computational effort required to compute $\varepsilon^{-1}_{\mathbf{G},\mathbf{G}'}(\mathbf{q},\omega)$, it remains a formidable task when simulating large systems with many atoms and/or large cell sizes. The dielectric matrix can be very large, and inverting it twice for each $\mathbf{q}$ point is computationally demanding. However, the PPA has the significant advantage of avoiding the need to compute the inverse of the dielectric matrix at multiple frequency points, thus making the frequency integrals amenable to analytic expression. The PPA typically performs very well for semiconductors. This success can be attributed to the fact that the self-energy calculation involves an integral over frequencies. If the model accurately captures the average characteristics of the true

[14] In the case of Σ_x, the sum runs over occupied states only.
[15] In the case of Σ_c, the sum runs over all bands, including the unoccupied ones.
[16] For instance, they are matrices.

dielectric function, the results remain highly accurate. However, a significant limitation of the PPA is that it cannot be used to calculate QP lifetimes, as the self-energy is real within this approximation. Additionally, some systems may exhibit a shape for $\varepsilon^{-1}_{\mathbf{G},\mathbf{G}'}(\mathbf{q},\omega)$ that deviates from the form assumed in the PPA. For example, in metals, the dielectric function often has a broader peak, and in more complex materials or interfaces, multiple peaks may be present, causing the PPA to fail.

3.6.2 The Perturbative Approach

In the G_0W_0 approximation (often referred to as "one-shot GW"), mentioned in Sec. 3.5.1, the self-energy operator is usually constructed using the DFT eigenvalues and eigenfunctions. The QP energies are then computed using first-order perturbative correction to the DFT energies.
The quasiparticle equation (3.18), computed at the QP energy $\epsilon^{QP}_{n\mathbf{k}}$, which we can explicitly rewrite as

$$\left[-\frac{\hbar^2\nabla^2}{2m} + V_H(\mathbf{r}) + V_{\text{ext}}(\mathbf{r})\right]\Psi^{\text{QP}}_{n\mathbf{k}}(\mathbf{r}) + \int \Sigma(\mathbf{r},\mathbf{r}',\epsilon^{\text{QP}}_{n\mathbf{k}})\Psi^{\text{QP}}_{n\mathbf{k}}(\mathbf{r}')d\mathbf{r}' = \epsilon^{\text{QP}}_{n\mathbf{k}}\Psi^{\text{QP}}_{n\mathbf{k}}(\mathbf{r}),$$

and the Kohn-Sham equation

$$\left[-\frac{\hbar^2\nabla^2}{2m} + V_{\text{H}}(\mathbf{r}) + V_{\text{ext}}(\mathbf{r})\right]\phi^{\text{KS}}_{n\mathbf{k}}(\mathbf{r}) + V_{\text{xc}}(\mathbf{r})\phi^{\text{KS}}_{n\mathbf{k}}(\mathbf{r}) = \epsilon^{\text{KS}}_{n\mathbf{k}}\phi^{\text{KS}}_{n\mathbf{k}}(\mathbf{r})$$

look very similar, as both are single-particle equations with an XC term. Following Hybertsen and Louie [50], if we consider the KS wavefunctions as a good approximation of the QP wavefunctions, $\Psi^{\text{QP}}_{n\mathbf{k}}(\mathbf{r}) \simeq \phi^{\text{KS}}_{n\mathbf{k}}(\mathbf{r})$[17], we can interpret the non-local and energy-dependent operator $\hat{\Sigma} - \hat{V_{\text{xc}}}$ as a perturbation of the KS Hamiltonian. As a result, we can express the QP energies $\epsilon^{\text{QP}}_{n\mathbf{k}}$ using first-order perturbation theory. This gives us the following expression[18]:

$$\epsilon^{\text{QP}}_{n\mathbf{k}} \simeq \epsilon^{\text{KS}}_{n\mathbf{k}} + \langle n\mathbf{k}|\,\Sigma(\epsilon^{\text{QP}}_{n\mathbf{k}}) - V_{\text{xc}}\,|n\mathbf{k}\rangle \tag{3.36}$$

Given that this approach involves only the diagonal elements of the self-energy, solving this equation is less computationally demanding compared to finding the poles of the fully-interacting Green's function. This approximation is valid if the self-energy's diagonal elements are dominant in the basis of the DFT orbitals, which is generally the case except in some special situations [44, 51], where other approaches are needed. This is particularly true for isolated atoms or molecules, where the KS orbitals do not decay sufficiently at large distances.
Since the electron self-energy in Eq. (3.36) depends on the QP energies, this would, in principle, require a self-consistent solution. In practical calculations, this energy dependence is simplified by considering the linearized self-energy in the vicinity of the KS eigenvalue. This approximation is given by:

$$\Sigma(\epsilon^{\text{QP}}_{n\mathbf{k}}) \sim \Sigma(\epsilon^{\text{KS}}_{n\mathbf{k}}) + \left.\frac{\partial\Sigma(\epsilon)}{\partial\epsilon}\right|_{\epsilon=\epsilon^{\text{KS}}_{n\mathbf{k}}}(\epsilon^{\text{KS}}_{n\mathbf{k}} - \epsilon^{\text{QP}}_{n\mathbf{k}}) \tag{3.37}$$

[17] For the sake of simplicity, we will use the notation $|n\mathbf{k}\rangle$ for the wavefunctions $\phi^{\text{KS}}_{n\mathbf{k}}(\mathbf{r})$.
[18] Implicitly, we rewrite $V_{\text{xc}}(\mathbf{r})\phi^{\text{KS}}_{n\mathbf{k}}(\mathbf{r}) = \int d\mathbf{r}\, V_{\text{xc}}(\mathbf{r}')\phi^{\text{KS}}_{n\mathbf{k}}(\mathbf{r}')\delta(\mathbf{r}-\mathbf{r}')$

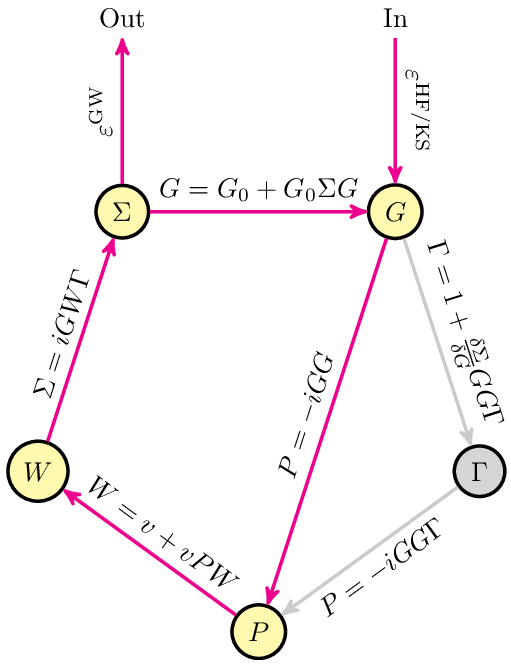

Figure 3.9: *Schematic depiction of the G_0W_0 perturbative approach on the Hedin's pentagon.*

In this way, the self-energy and its first derivative need to be computed only once, in correspondence of the KS energy. If we also define the renormalization factor $Z_{n\mathbf{k}}$ as

$$Z_{n\mathbf{k}} = \left[1 - \langle n\mathbf{k}| \frac{\partial\Sigma(\epsilon)}{\partial\epsilon}\Big|_{\epsilon-\epsilon^{\mathrm{KS}}_{n\mathbf{k}}} |n\mathbf{k}\rangle\right]^{-1} \tag{3.38}$$

by inserting Eq. (3.37) in Eq. (3.36) and using (3.38), we finally obtain an expression for the self-energy corrections to the DFT band structure at the G_0W_0 level of approximation

$$\epsilon^{\mathrm{QP}}_{n\mathbf{k}} = \epsilon^{\mathrm{KS}}_{n\mathbf{k}} + Z_{n\mathbf{k}} \langle n\mathbf{k}| \Sigma(\epsilon^{\mathrm{KS}}_{n\mathbf{k}}) - V_{\mathrm{xc}} |n\mathbf{k}\rangle \tag{3.39}$$

Eq. (3.39) is the expression used in this thesis to evaluate QP corrected electronic bands starting from DFT eigenenergies. We emphasize that this approach is reasonable if the KS states obtained within DFT can be considered good approximations of the QP wavefunctions. This heavily depends on the choice of the XC functional used, as discussed in Sec. 2.3.4. However, if this is the case, many-body effects encoded in the self-energy operator can be properly included by simply adding to the DFT energies $\epsilon^{\mathrm{KS}}_{n\mathbf{k}}$ the expectation value of the operator $\hat{\Sigma} - \hat{V}_{\mathrm{xc}}$ in the corresponding KS states.
To summarize, the G_0W_0 calculations present in this Thesis follow this scheme:

- an initial DFT ground-state calculation is performed to obtain the input wavefunctions and energies, to construct the non-interacting single-particle Green's function G_0^{KS},

- G_0^{KS} is used to compute the independent-particle irreducible polarizability[19] $P_0(1;2) = -iG_0^{KS}(1;2^+)G_0^{KS}(2;1^+$
- the microscopic dielectric matrix is computed and inverted (see Appendix A),
- the inverse macroscopic dielectric matrix is obtained for the full frequency range using the PPA, and the screened interaction W_0 is evaluated as in Eq. (3.19), within RPA,
- the expectation value of the self-energy calculated at the KS energies and its first derivative are computed as $\Sigma_{G_0W_0}(1;2) = iG_0^{KS}(1;2)W_0(1^+;2)$,
- the self-energy is used in Eq. (3.39) to compute the QP corrections to the KS eigenvalues.

The whole procedure is depicted schematically in Fig. 3.9. All integrals over the scattering vectors **q** in the BZ are numerically discretized using a uniform Monkhorst-Pack mesh to sample the BZ. QP corrections are highly sensitive to the **q**-sampling (closely related to the **k**-sampling) of the BZ, and achieving properly converged results typically requires much denser grids compared to those used in self-consistent DFT calculations.

3.6.3 Self-Consistent *GW*

Sometimes, the one-shot G_0W_0 approximation can yield poor results, particularly for compounds with electrons in d orbitals or strongly localized systems (as molecules). The main reason behind this failure is that the DFT starting point with local or semi-local XC functionals may give a band gap too small compared with the experimental one, and a G_0W_0 calculation is not able to correct this error. In order to overcome this issue, a possible solution is to use as starting point a hybrid functional, or alternatively to solve the *GW* equations in a self-consistent manner[20]. In this approach, the QP eigenvalues and wavefunctions obtained from the previous cycle are used in each iteration. For the first iteration, the LDA/GGA eigenvalues and eigenfunctions are employed.
Fully self-consistent *GW* calculations are generally challenging to implement, may sometimes yield incorrect results, and are practically computationally prohibitive for most realistic materials. However, for many systems, DFT wavefunctions are already quite good, and self-consistency on eigenvalues only can be sufficient (see Ref. [53]). This self-consistency is usually performed either for G only or for both G and W. Generally, this procedure results in larger band gaps and can significantly reduce the dependency of the *GW* results on the choice of the DFT functional.

3.6.4 *GW* Calculations in Low-Dimensional Systems

We now address fundamental aspects of QP calculations in low-dimensional systems, which constitute the focus this work.
In DFT calculations for low-dimensional materials, low-dimensional **k**-grids are typically used, such as $N \times N \times 1$ for a 2D sheet oriented perpendicular to the z direction. This choice can lead to numerical issues in the convergence of many-body results due to the divergence of the Coulomb potential at small **q**, which appears in all key equations. To address this issue, the YAMBO code employs the so-called Random Integration Method (RIM), which utilizes Monte Carlo integration

[19] Notice that, in this approximation for Eq. (3.31), we are substituting the interacting Green's function G with the non-interacting one, G_0

[20] It has been demonstrated that, to correct this issue, vertex corrections should in principle be considered [52].

with randomly selected **q**-points. For example, as shown in Eq. (3.21), the exchange self-energy diagonal matrix element is given by:

$$\langle n\mathbf{k}|\,\Sigma_x\,|n\mathbf{k}\rangle = -\int \frac{d\mathbf{q}}{(2\pi)^3}\sum_{\mathbf{G}}\frac{4\pi}{|\mathbf{q}+\mathbf{G}|^2}|\rho_{nm}(\mathbf{k},\mathbf{q},\mathbf{G})|^2 f_{m,\mathbf{k}-\mathbf{q}}$$

Assuming that the integrand is a smooth function of momentum, the integral can be approximated as

$$\langle n\mathbf{k}|\,\Sigma_x\,|n\mathbf{k}\rangle \simeq \sum_{\mathbf{q}_i}\sum_{\mathbf{G}} F(\mathbf{q}_i,\mathbf{G})\int_{sBZ(\mathbf{q}_i)}\frac{d\mathbf{q}}{(2\pi)^3}\,\frac{4\pi}{|\mathbf{q}+\mathbf{G}|^2}$$

where the small BZ (sBZ) relative to a given $\mathbf{q}_i$-point are the BZs of the momenta lattice vectors. They are chosen in such a way to cover the whole BZ. In the RIM run-level, the code calculates the integrals of the symmetrized Coulomb potential

$$\int_{sBZ(\mathbf{q}_i)}\frac{d\mathbf{q}}{(2\pi)^3}\,\frac{4\pi}{|\mathbf{q}+\mathbf{G}||\mathbf{q}+\mathbf{G}'|}$$

In a PWs basis set framework, low-dimensional materials are represented using a supercell technique, which involves a 3D crystal characterized by a unit cell with a size L along the non-periodic direction(s). This size must be sufficiently large to avoid unphysical interactions between periodic images of the system. In DFT calculations, these spurious interactions can be mitigated by choosing relatively small values of L; generally, a vacuum region of $12-20$ Å between periodic copies is sufficient to decouple periodic images of the material due to the short-range nature of the XC functional V_{xc}. However, because the bare Coulomb interaction is long-ranged, *GW* calculations often require impractically large supercells along the non-periodic direction(s) to ensure that periodic repetitions are not coupled by Coulomb interactions. To address this issue, a real-space cutoff for the Coulomb potential can be used. As discussed in detail in Refs. [54,55], this involves defining the electron-electron potential as:

$$\bar{v}(\mathbf{r}) = \begin{cases} v(\mathbf{r}) & \text{if } \mathbf{r}\in S \\ 0 & \text{otherwise} \end{cases}$$

i.e. the Coulomb interaction is manually set to zero outside of a region space S of choice. Usually, this region is chosen based on the symmetry of the system (spherical for 0D systems, cylindrical for 1D, etc.) In this way, properly converged QP corrections can be obtained using supercells with length L along the non-periodic direction(s) which are comparable to those used in DFT calculations.

Optical Properties

In absorption experiments, unlike in photoemission experiments, the incident photons are absorbed by the material, transferring their energy to excite electrons from occupied to unoccupied states. To accurately predict the measured optical spectra, it is essential to account for the Coulomb interaction between the excited electrons and the holes they leave behind. In other words, the many-body neutral electronic excitations, denoted as $\left|\Psi_0^N\right\rangle \rightarrow \left|\Psi_i^N\right\rangle$*, can be conveniently described using electron-hole pairs, which are new QP states known as excitons. When the Coulomb interaction between electrons and holes is strong, bound excitons can form, leading to optical transitions at energies below the electronic gap. These excitonic effects not only create new states below the gap but also alter the intensity of optical peaks compared to what is predicted by the independent quasi-particle approach. To accurately describe the optical spectra, it is necessary to solve a two-particle effective Hamiltonian, which, in the framework of MBPT, is known as the Bethe-Salpeter Equation. The formal derivation of this equation will be introduced in the following sections.*

3.7 Light-Matter Interaction

When light interacts with a solid, photons excite electrons, causing transitions to excited states. In this section, we will review the semi-classical theory of a solid's response to an electromagnetic field. For simplicity, we start by considering a single-particle Hamiltonian.
An electromagnetic field is generally described by a scalar potential ϕ and a vector potential $\mathbf{A}$. Electrodynamics allows a certain degree of freedom in specifying the potentials $(\phi, \mathbf{A})$, called *gauge* freedom. For our discussion, we can choose the *Coulomb gauge*, which imposes $\nabla \cdot \mathbf{A} = 0$ and $\phi = 0$. In the presence of an electromagnetic field, the kinetic energy operator of an electron $(\mathbf{p}^2/2)$ is replaced by

$$\frac{1}{2}\left[\mathbf{p} - \frac{1}{c}\mathbf{A}(\mathbf{r}, t)\right]^2$$

The vector potential $\mathbf{A}$ can generally be treated as a small perturbation to the electrons in the solid. Consequently, the quadratic term $\mathbf{A}(\mathbf{r}, t)^2$, allowing $\mathbf{A}$ to be treated as a linear perturbation. Within this approximation, the one-electron Hamiltonian h can be separated into a term h_0, which describes the system without an electromagnetic field, and a perturbation term h', which includes the interaction between the electron and the field.
The vector potential of a field of frequency ω has the form

$$\mathbf{A}(\mathbf{r}, t) = \mathbf{A}_1(\mathbf{r}, t) + \mathbf{A}_1^*(\mathbf{r}, t)$$

with

$$\mathbf{A}_1(\mathbf{r}, t) = A\mathbf{e}_0 e^{i\mathbf{q}\cdot\mathbf{r} - \omega t}$$

where A is the amplitude and $\mathbf{e}_0$ is the polarization vector, perpendicular to the propagation vector $\mathbf{q}$. The electric field is related to the vector potential by

$$\mathbf{E}(\mathbf{r},t) = -\frac{1}{c}\frac{d}{dt}\mathbf{A}(\mathbf{r},t)$$

Therefore, if we write the electric field in the form $\mathbf{E} = \mathbf{E}_1 + \mathbf{E}_1^*$, we have the following definition for $\mathbf{E}_1$

$$\mathbf{E}_1(\mathbf{r},t) = \frac{i\omega}{c} A\mathbf{e}_0 e^{i\mathbf{q}\cdot\mathbf{r}-\omega t} \tag{3.40}$$

In addition, we can define the *electric displacement* vector $\mathbf{D}(\mathbf{r},t)$ as

$$\mathbf{D}(\mathbf{r},t) = \varepsilon_{\mathrm{M}}(\omega)\mathbf{E}_1(\mathbf{r},t) + \varepsilon_{\mathrm{M}}^*(\omega)\mathbf{E}_1^*(\mathbf{r},t) \tag{3.41}$$

where $\varepsilon_{\mathrm{M}}(\mathbf{q},\omega)$ is the macroscopic dielectric function of the material and it is generally a complex function, i.e. $\varepsilon_{\mathrm{M}} = \varepsilon_1 + i\varepsilon_2$.
To relate the dielectric function with the quantum states of the electron in the solid, we use the average rate of energy density loss (energy per unit volume, per unit time) from an electromagnetic field in a medium with dielectric function $\varepsilon_{\mathrm{M}}(\mathbf{q},\omega)$. This rate of energy loss is defined as:

$$\frac{1}{4\pi}\left\langle \mathbf{E}\cdot\frac{d\mathbf{D}}{dt}\right\rangle = \frac{\omega}{2\pi}\int_0^{2\pi/\omega}\left(\mathbf{E}\cdot\frac{d\mathbf{D}}{dt}\right) = \frac{1}{2\pi c^2}|A|^2\omega^3\varepsilon_2(\mathbf{q},\omega) \tag{3.42}$$

where we have used Eq. (3.40) and (3.41) and the definition of time average over an oscillation period $2\pi/\omega$.
According to time-dependent perturbation theory, the probability of a transition between an initial state $|i\rangle$ and a final state $|f\rangle$ due to the perturbation h' is given by[21]:

$$\frac{dW_{if}(\omega)}{dt} = \frac{2\pi}{c^2}|\langle f|\,\mathbf{A}(\mathbf{r}_f,t)\cdot\mathbf{p}_i\,|i\rangle\,|^2\delta(\epsilon_f-\epsilon_i-\omega)\delta_{\sigma_i,\sigma_f} \tag{3.43}$$

The states $|i\rangle$ and $|f\rangle$ and the energies ϵ_i and ϵ_f are eigenfunctions and eigenstates of the many-body Hamiltonian $H_0 = \sum_j h_{0,j}\cdot\sigma_i$, where the σ_f are the spin states and the delta function ensures the energy conservation in the transition. Since the absorbed photon has a frequency ω, this corresponds to a loss rate of $(dW/dt)\omega$. Summing Eq. (3.43) over all possible initial and final states, introducing the occupation of every state through the Fermi distribution $f(\epsilon)$, we have the expression of the rate of energy loss per unit volume

$$\begin{aligned}\frac{\omega}{\Omega}\frac{dW}{dt} &= \frac{\omega}{\Omega}\sum_{if}\sum_{\sigma_i,\sigma_f}\frac{dW_{if}}{dt}f(\epsilon_i)(1-f(\epsilon_f)) \\ &= \frac{4\pi\omega}{\Omega c^2}|A|^2\sum_{if}|\langle f|\,e^{i\mathbf{q}\cdot\mathbf{r}}\mathbf{e}_0\cdot\mathbf{p}_i\,|i\rangle\,|^2\delta(\epsilon_f-\epsilon_i-\omega)f(\epsilon_i)[1-f(\epsilon_f)]\end{aligned} \tag{3.44}$$

[21] Here and in the following, every equation is in units of $\hbar$.

where Ω is the volume of the unit cell. It should be noted that in the case of semiconductors and insulators, the Fermi distribution function takes on values of 0 or 1. Therefore, in these cases, the term $f(\epsilon_i)(1-f(\epsilon_f))$ can be simplified or removed from the equation. By comparing Eq. (3.42) and Eq. (3.44), we can relate the imaginary part of the macroscopic dielectric function to the quantum states of the electrons in the solid:

$$\varepsilon_2(\mathbf{q}) = \frac{8\pi^2}{\Omega\omega^2} \sum_{if} \left| \langle f | \, e^{i\mathbf{q}\cdot\mathbf{r}} \mathbf{e}_0 \cdot \mathbf{p}_i \, | i \rangle \right|^2 \delta(\epsilon_f - \epsilon_i - \omega) f(\epsilon_i)(1 - f(\epsilon_f)) \tag{3.45}$$

which corresponds to *Fermi's golden rule* (sum over independent transitions) for the dielectric function. For photons with energy below ~ 100 eV, the following approximation is valid: the momentum $\mathbf{q}$ of the photon is negligible compared to that of the electron $\mathbf{k}$. As a consequence, the limit $\mathbf{q} \to 0$ is usually taken in expression (3.45). Due to momentum conservation, the initial and final states of the electron will have the same $\mathbf{k}$, and Eq. (3.45) can be rewritten in the following simplified form:

$$\varepsilon_2(\omega) \equiv \varepsilon_2(0,\omega) = \frac{8\pi^2}{\Omega\omega^2} \sum_{\mathbf{k}nn'} | \, \langle n\mathbf{k} | \, \mathbf{e}_0 \cdot \mathbf{p} \, | n'\mathbf{k} \rangle \, |^2 \delta(\epsilon_{n\mathbf{k}} - \epsilon_{n'\mathbf{k}} - \omega) f_{n\mathbf{k}}(1 - f_{n'\mathbf{k}}) \tag{3.46}$$

where $|n\mathbf{k}\rangle$, $\epsilon_{n\mathbf{k}}$ and $f_{n\mathbf{k}}$ are respectively the wavefunction, the eigenvalue and the occupation number of state n. For further details, we refer the reader to Ref. [56]. The quantity $| \, \langle n\mathbf{k} | \, \mathbf{e}_0 \cdot \mathbf{p} \, | n'\mathbf{k} \rangle \, |^2$ represents the probability associated to a direct transition from the valence-band state $|n'\mathbf{k}\rangle$, which is assumed to be occupied, to the conduction-band state $\langle n\mathbf{k}|$, which is assumed to be empty, at the $\mathbf{k}$-th point in the BZ. The direct transition contributes to ε_2 only if the argument of the δ function in Eq. (3.46) is zero, meaning that the incident photon energy $\hbar\omega$ is equal to the energy difference between the valence and the conduction bands at $\mathbf{k}$. In Eq. (3.46), we have a sum over $\mathbf{k}$-points as well as sums over the conduction and valence bands n, n'. Therefore, from a computational perspective, we need both a very dense $\mathbf{k}$-mesh to accurately sample the BZ and a sufficiently large number of bands to include all the transitions we want to observe.
From the imaginary part of the dielectric function $\varepsilon_2(\omega)$ (3.46), the real part $\varepsilon_1(\omega)$ can be obtained through the Kramers-Kronig relations [57],

$$\varepsilon_1(\omega) = 1 + \frac{2}{\pi} \mathcal{P} \int_0^\infty \frac{\omega' \varepsilon_2(\omega') - \omega \varepsilon_2(\omega)}{\omega'^2 - \omega^2} d\omega' \tag{3.47}$$

where $\mathcal{P}$ denotes the principal value. Once the dielectric function $\varepsilon_M = \varepsilon_1 + i\varepsilon_2$ is known, other macroscopic optical properties can be obtained from it.
In this context, the *joint density of states* (JDOS) can be easily obtained from the delta function in Eq. (3.45),

$$\text{JDOS} = \frac{1}{\Omega} \sum_{\mathbf{k}} \delta(\epsilon_{n\mathbf{k}} - \epsilon_{n'\mathbf{k}} - \omega) \tag{3.48}$$

The JDOS quantifies the number of pairs of valence- and conduction-band states with an energy difference in the range between ω and $\omega + d\omega$. It is useful for identifying transitions that contribute

to features in the absorption spectra.

3.8 Calculation of the Optical Properties

3.8.1 Optical Properties from DFT

The Kohn-Sham eigenvalues and wavefunctions, Eq. (2.14), can be used as a first step to calculate the optical properties of materials. By inserting $\phi^{\mathrm{KS}}_{n\mathbf{k}}$ and $\epsilon^{\mathrm{KS}}_{n\mathbf{k}}$ in Eq. (3.46), we obtain the so-called *independent-particle approximation* (IPA) for the optical absorption of the material. Within the DFT framework, it is possible to go beyond the IPA by including *local-field effects* (LFE), which account for the inhomogeneity of the density distribution in real systems. To achieve this, we rely on linear response theory, as discussed in Appendix A. Here, we show that it is possible to relate the inverse of the microscopic dielectric function $\varepsilon^{-1}(\mathbf{q},\omega)$ to the reducible polarization χ via Eq. (10):

$$\varepsilon^{-1}(\mathbf{q},\omega) = \delta_{\mathbf{GG'}} + v(\mathbf{q}+\mathbf{G})\chi_{\mathbf{GG'}}(\mathbf{q},\omega) \tag{3.49}$$

where $\chi_{\mathbf{GG'}}(\mathbf{q},\omega)$ is defined by Eq. (3.49) as

$$\chi_{\mathbf{GG'}}(\mathbf{q},\omega) = \chi^0_{\mathbf{GG'}}(\mathbf{q},\omega) + \sum_{\mathbf{G_2},\mathbf{G''}} \chi^0_{\mathbf{GG_2}}(\mathbf{q},\omega)[v(\mathbf{q}+\mathbf{G_2})\delta_{\mathbf{G_2},\mathbf{G''}} + f^{\mathrm{xc}}_{\mathbf{G_2},\mathbf{G''}}]\chi_{\mathbf{G''G'}}(\mathbf{q},\omega) \tag{3.50}$$

within the TDDFT formalism. In principle, Eq. (3.50) is exact if one knows the expression of f^{xc}. However, this is not the case for real systems. In standard DFT, f^{xc} is neglected: this is known as the RPA (see Sec. 3.5.1), which consists of considering only the Hartree term (coming from v) in the kernel. If we also neglect the Hartree term, we revert at the IPA, as there is no kernel and $\chi = \chi_0$. Thus, if we take χ_0 from Eq. (8) of Appendix A, the dielectric function can be calculated from χ_0, according to Eq. (10), as

$$\varepsilon^{-1} = 1 + v\chi_0$$

Taking now the macroscopic average, as in Eq. (17), we obtain again the Fermi's golden rule of Eq. (3.45), which neglects LFE.
It is important to emphasize that DFT is a ground-state theory and, in principle, cannot directly account for optical properties. Many-body contributions, such as excitonic effects, which can be significant in some systems, are neglected in DFT. Nonetheless, DFT results are often quite reliable for gaining a qualitative understanding of absorption spectra. Since DFT often underestimates the band gap of semiconductors, a common approach to address this when calculating optical properties is to apply a rigid shift to the conduction band eigenvalues. The next step consists in considering QP corrections to the band structure in order to improve the description of the system.

3.8.2 Optical Properties within the GW Approximation

The GW approximation can be used in optical property calculations by replacing the Kohn-Sham eigenvalues and wavefunctions with QP energies and wavefunctions to determine the independent-particle polarizability χ_0. This is sometimes referred to as independent QP (IQP) approximation. The main advantage of using QP energies and wavefunctions for calculating optical properties is that it provides access to the *true* electronic gap. However, as discussed in the introduction, this alone is not sufficient. We must also account for the interaction between the excited electron and the hole left behind, which affects the absorption energy thresholds, making them lower than the electronic gap. Consequently, we are still missing a critical component of the absorption spectrum: *excitons*. We will address this issue in the following sections.

3.8.3 Excitons

In the 1930s, Yakov Frenkel studied the optical properties of insulators and proposed that energy transfer occurs through "electron excitation waves" rather than the commonly known heat carriers, i.e. phonons [58]. This type of excitation involves an excited electron moving outside the closed electronic shell and a hole left behind by the missing electron. Due to their opposite charges, the electron and hole form a neutral bound state that is not confined to a specific atom. Consequently, this electron-hole (e-h) pair can migrate to neighboring atoms and transport energy, leading to measurable dissipation. These "excitation waves" are known as *Frenkel excitons*. They are typically highly localized in space, with an exciton radius on the order of a few angstroms, and possess very strong binding energies relative to the fundamental electronic gap. Frenkel excitons are typically found in organic materials and confined systems, such as clusters and molecules.
This concept was later extended to semiconductors, where the dielectric constant is generally higher than in wide band-gap materials. In these cases, the electron and hole can form a bound state with a radius spanning several unit cells without dissociating into free particles. Additionally, the e-h pairs can move almost freely within the crystal, and their behavior can be described by a hydrogen-like problem where the potential is screened by the material's static dielectric constant. This leads to a discrete spectrum, indexed by the principal quantum number n. This type of exciton is known as a *Wannier-Mott exciton*, and its energy states are well represented by a hydrogen-like Hamiltonian [59]. This kind of excitons are common in inorganic semiconductors, especially in the low-dimensional cases.
As illustrated in Fig. 3.10, excitonic states are found inside the band gap; thus, the formation of excitons requires less energy than the energy needed for a valence electron to transition directly to the conduction band. This results in a lower threshold for photon absorption and creates a difference between the so-called "optical gap" and the actual electronic gap[22], which corresponds exactly to the exciton binding energy. Generally, the binding energy of Frenkel excitons is greater than that of Wannier-Mott excitons.
The hydrogen-like equation of motion proposed by Wannier imposes symmetries on excitons, requiring optical transitions to adhere to parity conditions. Excitonic states that obey the correct parity can be formed or recombine through photon absorption or emission and are referred to as optically active or *bright* excitons. In contrast, those that do not conform to these conditions,

[22] In this Thesis, we only take into account direct excitons, meaning excitons arising from transitions involving states with the same momentum (direct).

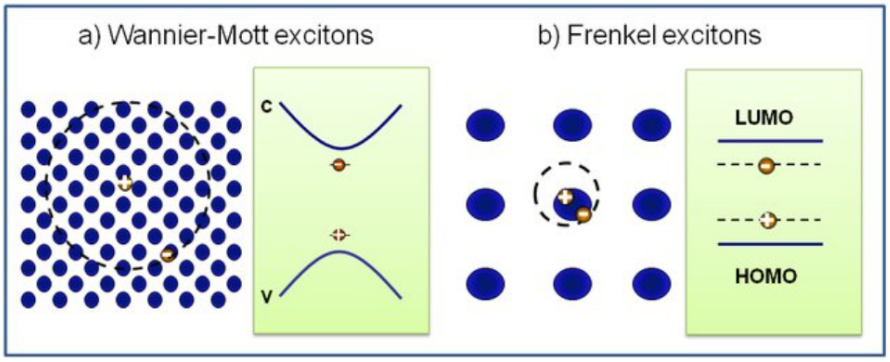

Figure 3.10: *Simplified representation of Wannier-Mott and Frenkel excitons.*

within the dipole selection rules, are termed optically forbidden or *dark* excitons. *Bright* excitons have a non-zero (excitonic) oscillator strength and result in resonant peaks in the linear optical spectra (such as absorption), while *dark* excitons do not contribute to these spectra. In addition to dipole selection rules, spin-selection rules are also significant.
Thus, describing optical properties requires considering excited states that differ significantly from those involved in photoemission spectroscopy. In photoemission, the final state of the system can be considered formally charged, as an electron is either removed or added. In contrast, in absorption processes, the system is left in a *neutral* excited state after exchanging energy with the probe, making the interaction between electrons and holes crucial. These two QPs (i.e. the created quasi-electron and the quasi-hole) interact among each other and therefore constitute a correlated pair, generally referred to as an exciton. As the e-h interaction is mainly attractive, the energy of this composite QP can be lower than the one of the free pair, so that exciton is considered as bound. This interaction is not captured by the *GW* approximation, therefore an ab initio investigation of this type of excitations requires a different treatment. Such treatment enables an accurate description of many experimental observables, like optical absorption and electron energy loss spectroscopy (EELS). To account for this interaction, it is essential to consider the presence of both the hole and the electron simultaneously. Within the Green's function formalism, this requires dealing with a two-particle (e-h) Green's function propagator and solving the Bethe-Salpeter Equation (BSE). We will develop the BSE formalism in the next section.

3.8.4 The Bethe-Salpeter Equation (BSE)

Solving the Bethe-Salpeter equation (BSE) [33, 41, 60] yields much more precise results because it is designed to compute e-h excited states, including the interaction between the electron, promoted from a valence band to a conduction band, and the hole left behind. The BSE is based on MBPT and is much more computationally demanding than alternatives such as TDDFT, which is not covered in this thesis. This is due to the BSE's explicit dependence on the two-particle Green's function. The motion of the electron and the hole cannot be described by a single-particle Green's function because they do not move independently. Instead, the two-particle Green's function is necessary to account for excitonic effects, which are the interactions between the electron and the

hole in their correlated motion.
We have already encountered the two-particle Green's function in Sec. 3.2.2, as it enters in the EOM of the one-particle Green's function. Its definition in Eq. (3.9) allows us to define the two-particle correlation function L, by subtracting from G_2 the uncorrelated contribution:

$$L(1,2;3,4) = iG_2(1,2;3,4) - iG(1;3)G(2;4) \tag{3.51}$$

L is called *four-point reducible polarizability*. By choosing appropriate time orderings, we can describe different processes: for example, the choice of $t_3 = t_1^+$ and $t_4 = t_2^+$ corresponds to the propagation of an e-h pair. Moreover, L is deeply connected to the reducible polarizability χ. In fact, the two quantities differ by just a prefactor that can be deduced from the Feynman rules for the polarizability and those for the G_2. It holds:

$$\chi(1;2) = -iL(1,2;1^+,2^+) \tag{3.52}$$

Similarly to χ, we can then define the independent e-h polarizability L_0 as

$$L_0(1,2;3,4) = -iG(1;3)G(2;4) \tag{3.53}$$

It can be shown [60, 61] that L satisfies a Dyson-like equation, the *Bethe-Salpeter equation*

$$L(1,2;3,4) = L_0(1,2;3,4) + \int L_0(1,2;5,6)\,\Xi(5,6;7,8)\,L(7,8;3,4)\,d5d6d7d8 \tag{3.54}$$

Ξ is the BSE kernel, accounting for the interaction among these two particles, and it is composed of two terms:

$$\Xi(5,6;7,8) = \delta(5;6)\delta(7;8)v(5;7) + i\frac{\delta\Sigma(5;7)}{\delta G(6;8)}. \tag{3.55}$$

The first contribution corresponds to the 4-point Coulomb interaction, also called *electron-hole exchange*, while the second term, called *direct term*, features the variation of the self-energy with respect to the variation of the Green's function. It is possible to obtain this expression as a second iteration of Hedin's equations Eq. (3.23)-(3.27), where we recalculate the vertex correction Γ. The kernel Ξ is the link between the non-interacting L_0 and the true L, analogous to the self-energy Σ that links G_0 and G in Eq. (3.17). The GW approximation can be used for the Σ in this kernel, giving

$$i\frac{\delta\Sigma(5;7)}{\delta G(6;8)} \approx -\frac{\delta[G(5;7)W(5;7)]}{\delta G(6;8)}. \tag{3.56}$$

so that Eq. (3.55) becomes

$$\Xi(5,6;7,8) = \delta(5;6)\delta(7;8)v(5;7) - \delta(5;6)\delta(7;8)W(5;7) - G(5;7)\frac{\delta W(5;7)}{\delta G(6;8)} \tag{3.57}$$

The last term, $G\delta W/\delta G$, is the variation of the screening due to the excitation and is usually neglected, being a second-order effect. With this approximation to the kernel Ξ, the BSE can be finally written at the GW level as

$$L(1,2;3,4) = L_0(1,2;3,4) + \int L_0(1,2;5,6)\left[\delta(5;6)\delta(7;8)v(5;7) - \delta(5;6)\delta(7;8)W(5;7)\right] L(7,8;3,4)\, d5d6d7d8 \quad (3.58)$$

To obtain optical spectra, one could derive L from Eq. (3.58), then contract it to obtain the reducible polarizability $\chi(1;2) = -iL(1,2;1^+,2^+)$. This can then be used to determine ϵ_{M} (see Appendix A). However, solving Eq. (3.58) involves inverting the BSE kernel, which can be prohibitively expensive for systems with many electrons, especially when numerous unoccupied states are needed for convergence and when a dense sampling of the BZ is required. Alternatively, the problem can be reformulated as a two-particle Hamiltonian in the e-h space.

3.8.5 Effective Two-Particle Hamiltonian

It is interesting to take the time Fourier transform[23] of L. In frequency space, this means that the energy of the e-h pairs can be obtained as the poles of

$$L(\omega) = \int d\omega' \int d\omega''\, L(\omega,\omega',\omega'') \quad (3.59)$$

where

$$L(\omega,\omega',\omega'') = L_0(\omega,\omega',\omega'') + \frac{1}{(2\pi)^4}\int d\omega_3 \int d\omega_4\, L_0(\omega,\omega',\omega_3)\,\Xi(\omega,\omega_3,\omega_4)\,L(\omega,\omega_4,\omega'') \quad (3.60)$$

is obtained by time Fourier transform of Eq. (3.54) (for simplicity, we do not make explicit the dependence on spatial coordinates to simplify the notation). The GW approximated first-order BSE kernel Ξ transforms as

$$\Xi(\omega,\omega_3,\omega_4) \approx -iv + iW(\omega_3 - \omega_4) \quad (3.61)$$

Looking at Eq. (3.61), we can notice the frequency dependence of the electron- electron screened interaction. In the following we will use the static-screening approximation, by which we approximate $W(\omega_3 - \omega_4)$ with its static component, denoted in the following as W_s. This approximation is generally valid if the excitation energies of e-h pairs are smaller than the plasmon frequency characterizing the system. Substituting Eq. (3.61) (with its static approximation) in Eq. (3.60) and computing the integrals over ω and ω' in Eq. (3.59), we obtain

$$L(\omega) = L_0(\omega) + L_0(\omega)[-iv + W_s]L(\omega) \quad (3.62)$$

[23] In the following we will restrict our attention to the simultaneous propagation of a single e-h pair.

where

$$L_0(\omega) = -i \int d\omega' \, G\left(\omega' + \frac{\omega}{2}\right) G\left(\omega' - \frac{\omega}{2}\right) \tag{3.63}$$

To proceed further, we now write L and L_0 in the basis of independent particle states. In practice, we assume that the single-particle Green's functions appearing in L_0 are given by

$$G(\mathbf{r}_1, \mathbf{r}_2, \omega) = \sum_{n_i} \frac{\phi^{\mathrm{KS}}_{n_i}(\mathbf{r}_1)\phi^{*\mathrm{KS}}_{n_i}(\mathbf{r}_2)}{\omega - \epsilon^{\mathrm{QP}}_{n_i} + i\eta sgn(\epsilon^{\mathrm{QP}}_{n_i} - \mu)} \tag{3.64}$$

where we have made explicit the dependence on spatial coordinates and used the compact notation $n_i \equiv (n\mathbf{k})$. The Green's function in Eq. (3.64) describes the propagation of QPs (electron and holes) having as wavefunctions the KS states and energies equal to QP-corrected KS eigenvalues. By defining the basis transformation of 4-variables functions $F(\mathbf{r}_1, \mathbf{r}_2, \mathbf{r}_3, \mathbf{r}_4, \omega)$ as

$$F_{n_1 n_2 n_3 n_4}(\omega) = \int d\mathbf{r}_1 d\mathbf{r}_2 d\mathbf{r}_3 d\mathbf{r}_4 \, \phi^{*\mathrm{KS}}_{n_1}(\mathbf{r}_1)\phi^{*\mathrm{KS}}_{n_2}(\mathbf{r}_2)F(\mathbf{r}_1, \mathbf{r}_2, \mathbf{r}_3, \mathbf{r}_4, \omega)\phi^{\mathrm{KS}}_{n_3}(\mathbf{r}_3)\phi^{\mathrm{KS}}_{n_4}(\mathbf{r}_4) \tag{3.65}$$

We can project Eq. (3.62) on the basis of the single-particle KS states: via algebraic manipulation we obtain

$$L_{n_1 n_2 n_3 n_4}(\omega) = 2i \left[H^{\mathrm{exc}} - \omega\right]_{n_1 n_2 n_3 n_4} (f_{n_2} - f_{n_4}) \tag{3.66}$$

n_i being the indexes running over KS states while f_{n_i} is the occupation factor for n_i-state and where we have introduced the excitonic Hamiltonian

$$H^{\mathrm{exc}}(n_1, n_2, n_3, n_4) = (\epsilon^{\mathrm{QP}}_{n_2} - \epsilon^{\mathrm{QP}}_{n_1})\delta_{n_1 n_4}\delta_{n_2 n_3} + (f_{n_1} - f_{n_3})\Xi(n_1, n_2, n_3, n_4) \tag{3.67}$$

The presence of the factor $(f_{n_4} - f_{n_3})$ implies that only the matrix elements of the excitonic Hamiltonian H^{exc}, in which the states labeled by n_3 and n_4 have different occupations, contribute. To make the expression of H^{exc} more clear, we make explicit the indices n_i by associating to each of them a conduction (c) or a valence (v) band index at a given $\mathbf{k}$-point[24], according to the occupation factors f, assuming $T = 0$ K. In this way, we can express the excitonic Hamiltonian as a block-matrix

$$H^{\mathrm{exc}} = \begin{bmatrix} H^{\mathrm{res}}_{(vc,v'c')} & K^{\mathrm{coupl}}_{(vc,v'c')} \\ [K^{\mathrm{coupl}}_{(vc,v'c')}]^* & [H^{\mathrm{res}}_{(vc,v'c')}]^* \end{bmatrix} \tag{3.68}$$

$H^{\mathrm{res}}_{(vc,v'c')}$ is the *resonant* term, which consists of positive frequency transitions only. The off-diagonal terms $K^{\mathrm{coupl}}_{(vc,v'c')}$ are the *coupling* terms, as they mix positive and negative frequency transitions (excitations and de-excitations). The last term is the anti-resonant one, concerning only negative

[24]Here, we will limit our description to vertical transitions only.

energy transitions (important for photoluminescence). In most of the cases, we can safely neglect the off-diagonal terms, as often these matrix elements are small with respect to the energy range of transitions. This approximation is called the Tamm-Dancoff approximation (TDA) [62, 63] and allows us to consider $H^{\text{exc}} \approx H^{\text{res}}$, which is an Hermitian matrix, whose eigenvalues corresponds to the energies of the correlated e-h pairs accessible in the system.
Using the extended notation (n$\mathbf{k}$) for the KS states, we can write (the two blocks of labels refer to the electron and to the hole)

$$H^{\text{res}}_{(vc\mathbf{k},v'c'\mathbf{k}')} = (\epsilon^{\text{QP}}_{c\mathbf{k}} - \epsilon^{\text{QP}}_{v\mathbf{k}})\delta_{cc'}\delta_{vv'}\delta_{\mathbf{k}\mathbf{k}'} + K^{d}_{(vc\mathbf{k},v'c'\mathbf{k}')} + K^{x}_{(vc\mathbf{k},v'c'\mathbf{k}')} \tag{3.69}$$

where

$$K^{d}_{(vc\mathbf{k},v'c'\mathbf{k}')} = -\int d\mathbf{r} \int d\mathbf{r}'\, \phi^{*\text{KS}}_{c\mathbf{k}}(\mathbf{r})\phi^{\text{KS}}_{c'\mathbf{k}'}(\mathbf{r})\, W_s(\mathbf{r},\mathbf{r}')\, \phi^{\text{KS}}_{v\mathbf{k}}(\mathbf{r}')\phi^{*\text{KS}}_{v'\mathbf{k}'}(\mathbf{r}') \tag{3.70}$$

is called the direct BSE kernel, while

$$K^{x}_{(vc\mathbf{k},v'c'\mathbf{k}')} = 2\int d\mathbf{r} \int d\mathbf{r}'\, \phi^{*\text{KS}}_{c\mathbf{k}}(\mathbf{r})\phi^{\text{KS}}_{v\mathbf{k}}(\mathbf{r})\, v(|\mathbf{r}-\mathbf{r}'|)\, \phi^{\text{KS}}_{c'\mathbf{k}'}(\mathbf{r}')\phi^{*\text{KS}}_{v'\mathbf{k}'}(\mathbf{r}') \tag{3.71}$$

is the exchange kernel. Looking at Eqs. (3.69)-(3.71), the physical meaning of H^{res} is transparent. The first term in Eq. (3.69) corresponds to the energies of the independent QP transitions from a valence state ($v\mathbf{k}$) to a conduction state ($c\mathbf{k}$). The direct kernel K^d accounts for the attractive coupling between the electron and the hole, governed by the *static screened interaction*[25] W_s, while the exchange kernel K^x represents a repulsive term, which stems from the Hartree potential.
Notice that the excitonic Hamiltonian given by Eq. (3.69) is valid for system with negligible SOC. In these cases, excitons can have a singlet (triplet) spin structure, where the electron and the hole have equal (opposite) spin projections. As optically active excitons must be of singlet type, in the following we will only focus on this particular spin-configuration, for which the exchange term is different from zero. We point out that triplet-exciton energies can be obtained from Eq. (3.69) by neglecting the exchange kernel contribution [41,64]. We will generalize the BSE for SOC calculations in Sec. 3.8.7.
The diagonalization of Eq. (3.69) results in

$$H^{\text{res}}_{(vc\mathbf{k},v'c'\mathbf{k}')}A^{\lambda}_{v'c'\mathbf{k}'} = E_{\lambda}A^{\lambda}_{vc\mathbf{k}} \tag{3.72}$$

where λ indexes the different excitonic states. Eq. (3.72) yields the exciton energies E_λ, together with the eigenvectors $|\lambda\rangle = \sum_{vc\mathbf{k}} A^{\lambda}_{vc\mathbf{k}}\,|vc\mathbf{k}\rangle$, where the $A^{\lambda}_{vc\mathbf{k}}$ are called *envelope functions*. The square modulus of A^λ defines the weight of the single-particle transitions $(v\mathbf{k}) \to (c\mathbf{k})$ to the corresponding excitonic state λ. A general formulation of the BSE, though beyond the scope of this thesis, includes excitons with a transferred momentum $\mathbf{q}$ between the valence v and conduction c states, considering both direct and indirect excitons. The resulting eigenvalues $E_\lambda(\mathbf{q})$ represent the exciton dispersion, also known as the *excitonic band structure*. The long-wavelength limit can be

[25] The term "static" means that, instead of calculating the screened interaction W as in the *GW* case (see Eq. (11) of Appendix A), here we consider the *static* dielectric function, which is defined, starting from Eq. (10), as $\varepsilon_s^{-1}(\mathbf{q},\omega = 0) = \delta_{\mathbf{G}\mathbf{G}'} + v(\mathbf{q}+\mathbf{G})\chi_{\mathbf{G}\mathbf{G}'}(\mathbf{q},\omega=0)$

obtained by simply letting $\mathbf{q} \to 0$.
As already mentioned, the excitonic Hamiltonian is not necessarily Hermitian. However, its resonant part is. Starting from the spectrum of H^{res} (3.72), it is possible to derive the macroscopic dielectric function $\epsilon_{\text{M}}(\omega)$, whose imaginary part is proportional to the absorption spectrum obtained in optical spectroscopy (see Appendix A). We notice that, when the macroscopic dielectric function is evaluated, the bare Coulomb interaction appearing in the exchange kernel (3.71) is substituted by a potential not including the long range contribution [61], i.e. $v(\mathbf{q}+\mathbf{G})$ is set to zero for each $\mathbf{q}$, if $\mathbf{G} = 0$. This accounts for the fact that optical spectroscopy describes the macroscopic response of the system to an external perturbation. In practice, this quantity is evaluated as

$$\varepsilon_{\text{M}}(\omega) = 1 - \frac{8\pi}{\Omega} \sum_{\lambda} \frac{|D^j_\lambda|^2}{\omega - E_\lambda + i\eta} \tag{3.73}$$

where Ω is the unit cell volume, λ runs over the excitonic eigenstates with energy E_λ and

$$D^j_\lambda = \sum_{vc\mathbf{k}} A^\lambda_{vc\mathbf{k}} (\hat{\mathbf{j}} \cdot \mathbf{d}_{vc\mathbf{k}}) \tag{3.74}$$

is the dipole strength for exciton λ, assuming light polarized along direction $\hat{\mathbf{j}}$. This quantity determines if a given exciton can be optically excited by electromagnetic radiation with a certain polarization. We notice that Eq. (3.74) is an average of the single-particle interband transition dipole $\mathbf{d}_{vc\mathbf{k}}$, weighted by the contribution of each transition $(v\mathbf{k}) \to (c\mathbf{k})$ to the corresponding exciton. Thus, in order to obtain the macroscopic dielectric function, it is necessary to diagonalize the excitonic Hamiltonian and determine the QP wavefunctions, which are used to compute the dipole matrix elements in the numerator of Eq. (3.73). Commonly, Kohn-Sham wavefunctions are assumed to be a good approximation of the QP wavefunctions. Hence, the interband dipoles $\mathbf{d}_{vc\mathbf{k}}$ are often computed as [65]

$$\mathbf{d}_{vc\mathbf{k}} = \frac{1}{\epsilon^{\text{KS}}_{c\mathbf{k}} - \epsilon^{\text{KS}}_{v\mathbf{k}}} \left(\langle \phi^{\text{KS}}_{v\mathbf{k}} | \, \mathbf{p} \, | \phi^{\text{KS}}_{c\mathbf{k}} \rangle + \langle \phi^{\text{KS}}_{v\mathbf{k}} | \, [\mathbf{r}, \hat{V}_{\text{NL}}] \, | \phi^{\text{KS}}_{c\mathbf{k}} \rangle \right)$$

where $\hat{V}_{\text{NL}}$ is the non-local part of the KS potential, due to the non-locality of pseudopotentials and $\mathbf{p}$ is the linear momentum. The dielectric function obtained by solving the BSE exhibits poles at the eigenvalues of the excitonic Hamiltonian, which are no longer simply the differences between the energies of occupied and unoccupied QP states. This causes the spectral features to shift, typically to lower energies compared to the IPA. Each eigenstate of the excitonic Hamiltonian (3.72) is a superposition of independent QP transitions, with each transition contributing according to a weight given by A^λ. This mixing of independent transitions in the numerator of the dielectric function significantly alters the spectral lineshape.
In this Thesis, the BSE is solved using the YAMBO code. In practice, this involves performing a DFT calculation to obtain Kohn-Sham states and energies, which are then used to construct the static screened interaction W_s within the RPA, as described in Sec. 3.8.1. Using the same set of KS states, the Hermitian excitonic Hamiltonian is constructed according to Eqs. (3.69)-(3.71), with QP energies derived from KS values using Eq. (3.36). Numerically, it is crucial to carefully select both the number of valence and conduction states included in the excitonic Hamiltonian and the

sampling of the BZ, to ensure that the optical spectra are properly converged[26].

3.8.6 Alternative Solutions of the BSE

Computing spectra with Eq. (3.73) requires the full diagonalization of H^{res} (3.72), which is an $(N_v \times N_c \times N_{\mathbf{k}})^2$ square matrix. This procedure can become prohibitively expensive as the size of the e-h space and the number of **k**-points increase. Apart from the aforementioned diagonalization method for solving the BSE, Lanczos-based methods [66] provide a cost-effective alternative for handling sparse matrices [67]. Lanczos approaches avoid the need for inverting the BSE kernel or fully diagonalizing the two-particle Hamiltonian. Instead, these methods express the Hamiltonian as a tridiagonal matrix using recursive relations, leading to an iterative solution that is computationally cheaper than full diagonalization. While the previously described solvers yield the complete set of both excitonic energies and wavefunctions of the system, Lanczos schemes typically offer a partial solution. For instance, Haydock's implementation [68] of the Lanczos method provides matrix elements of the resolvent of the eigenproblem in Eq. (3.72), $\langle S_0|(H^{res} - I\omega)^{-1}|S_0\rangle$, for a given initial (normalized) state $|S_0\rangle$, where I is the identity matrix. Defining $|S_0\rangle$ as $|S_0\rangle = \frac{|P\rangle}{\|P\|}$, with

$$|P\rangle = \lim_{\mathbf{q}\to 0} \frac{1}{|\mathbf{q}|} \sum_{vc\mathbf{k}} \langle v\mathbf{k}|\, e^{i\mathbf{q}\cdot\mathbf{r}}\, |c\mathbf{k}-\mathbf{q}\rangle$$

which allows us to write the macroscopic dielectric function in Eq. (3.73) simply as

$$\varepsilon_{\mathrm{M}}(\omega) = 1 - 4\pi||P^2||\, \langle S_0|\, (H^{res} - I\omega)^{-1}\, |S_0\rangle$$

and use this resolvent. Therefore, Haydock's algorithm can compute the optical spectrum but does not provide the excitonic wavefunctions [68–70]. Haydock's scheme is based on mapping the stationary quantum problem onto a semi-infinite chain model composed of basis states $|V_i\rangle$, referred to as Haydock vectors. The subscript i denotes the iteration and indicates that these states are obtained recursively. In this basis, the Hamiltonian of the problem is represented as a tridiagonal matrix characterized by the coefficients a_i and b_i. Haydock provides a set of recursive relations to compute these coefficients and basis vectors iteratively, starting from $|V_0\rangle$,

$$a_i = \langle V_i|\, H^{res}\, |V_i\rangle$$

$$b_{i+1} = ||(H^{res} - a_i)\, |V_i\rangle - b_i\, |V_{i-1}\rangle\, ||$$

$$|V_{i+1}\rangle = \frac{1}{b_{i+1}}[(H^{res} - a_i)\, |V_i\rangle - b_i\, |V_{i-1}\rangle]$$

[26] In general, to obtain properly converged exciton energies, one needs denser **k**-grids than those used in GW calculations, where QP corrections are computed.

Finally, Haydock's algorithm provides a method for calculating the resolvent matrix element as a continued fraction of the Hamiltonian coefficients a_i and b_i. This continued fraction can then be used to compute the optical spectrum at each iteration i according to:

$$\varepsilon_{\mathrm{M}}^{(i)}(\omega) = 1 - ||P||^2 \frac{1}{(\omega - a_1) - \frac{b_2^2}{(\omega - a_2) - \frac{b_3^2}{\cdots}}} \tag{3.75}$$

The process continues until the difference between the spectra of successive iterations falls below an acceptable threshold. It is important to note that the number of denominators in the continued fraction of Eq. (3.75) depends on the iteration number. For example, the dielectric function at the tenth iteration, $\varepsilon_{\mathrm{M}}^{(10)}$, is calculated using coefficients up to a_{10} and b_{10}.
Despite the numerical advantages offered by Lanczos' solvers, a given system may still be too large for computing optical spectra at the BSE level. Although Lanczos' schemes alleviate the problem of diagonalization, the bottleneck shifts to the earlier step of computing and storing the BSE kernel. This step can become impractical depending on the size of the e-h basis. For instance, a material with 10 bands requiring a 30×30×30 **k**-grid results in a (resonant) BSE kernel matrix with a dimension of 675000, necessitating several terabytes of memory. While some state-of-the-art high-memory nodes might accommodate this, it is near the limits of contemporary supercomputers. Any increase in system size, such as doubling the number of bands to include spin-orbit coupling or using a supercell, could quickly become prohibitive. A possible solution (implemented in the YAMBO code), oftentimes used in this Thesis, is to exploit the subspace iterative algorithm using the SLEPc library [71, 72] (SLEPc solver). This solver outputs the individual exciton energies and composition about an energy value chosen by the user, by diagonalizing only a selected part of the full BSE matrix. It can be applied to medium-large systems but does not provide the overall spectrum. This solver is typically used after obtaining the spectra from the Lanczos-Haydock solver to either analyze a specific peak or getting the energy and composition of a few low-lying excitons. The computational cost grows with the number of excitons one asks to compute.

3.8.7 Including Spin-Orbit in the BSE

The spin-orbit interaction can significantly influence the macroscopic optical properties of materials containing heavy atoms, leading to features such as spin-split peaks and valley-selective optical transitions in their absorption spectra. Additionally, it is responsible for finer details that are crucial for applications in optoelectronic devices. While we do not delve into the detailed derivation here, we follow the work of Marsili et al. [73], which provides a comprehensive derivation of the non-collinear GW-BSE equations. This formulation naturally incorporates SOC at the level of ground-state calculations, making it well-suited for studying the optical properties of many-body quantum systems where spin dependence can be treated as a non-local term in the Hamiltonian.
The starting point is the many-body total Hamiltonian of the system including first order relativistic corrections

$$\hat{H} = \hat{H}^0 + \hat{H}^{(\mathrm{e-e})} + \hat{H}^{(\mathrm{RK})} + \hat{H}^{(\mathrm{SOC})}$$

where $\hat{H}^0$ is the non relativistic one-body Hamiltonian, composed by a kinetic term and the atomic scalar external potential, $H^{(\mathrm{e-e})}$ the electron-electron Coulomb interaction, while $H^{(\mathrm{RK})} + H^{(\mathrm{SOC})}$

are the first order relativistic corrections. $H^{(\mathrm{RK})}$ is the mass-velocity term plus the Darwin term, while $H^{(\mathrm{SOC})}$ is the SOC term. What is relevant here is that $H^{(\mathrm{SOI})}$ can be expressed as a sum of terms which depend on a single spin operator and can thus be conveniently written as a sum of 2×2 matrix in the spin space. Since all other terms are spin-independent, this implies that the whole Hamiltonian can be expressed as a sum of 2×2 matrices. This non-collinear formulation is already incorporated into DFT XC functionals, as discussed in Sec. 2.4.6. When a non-collinear potential is included in the Hamiltonian, the entire formulation of the many-body problem must be rewritten in the spinorial basis. Indeed, in Ref. [73], the authors address this by rewriting the Hedin equations in the spinorial basis. The spinorial BSE can be derived from the general spinorial Hedin equations through specific manipulations. Below, we present the spinorial BSE for a generic transferred momentum $\mathbf{q}$, i.e.

$$\tilde{L}^{\,nn'\mathbf{k}}_{mm'\mathbf{p}}(\mathbf{q},\omega) = L^{0}_{\substack{nn'\mathbf{k}\\ mm'\mathbf{p}}}(\mathbf{q},\omega) + L^{0}_{\substack{nn'\mathbf{k}\\ \bar{n}\bar{n}'\bar{\mathbf{k}}}}(\mathbf{q},\omega) K_{\substack{\bar{n}\,\bar{n}'\bar{\mathbf{k}}\\ \bar{m}\,\bar{m}'\bar{\mathbf{p}}}}(\mathbf{q}) \tilde{L}_{\substack{\bar{m}\,\bar{m}'\bar{\mathbf{p}}\\ mm'\mathbf{p}}}(\mathbf{q},\omega)$$

In the $\mathbf{q} \to 0$ (optical) limit, this equation simplifies to the optical BSE. As in the spin-independent case, the solution of can be recast in an eigenvalue problem with the excitonic Hamiltonian. Starting from the eigenvectors of the excitonic Hamiltonian, we can define the excitonic state wave-function as a linear combination of e-h pairs

$$L^{\,nn'\mathbf{k}}_{mm'\mathbf{p}}(\omega) = \left(\sum_{\lambda} \frac{A^{\lambda,*}_{nn'\mathbf{k}} A^{\lambda}_{mm'\mathbf{p}}}{\omega - E_{\lambda} + i0^{+}} \right)$$

The e-h pairs that contribute to the excitonic wavefunction are vectors in spin space. In the non-collinear case, this means that the exciton is a linear combination of the four possible spin orientations of the electron and hole, effectively forming a tensor.

3.8.8 BSE Calculations in Low-Dimensional Systems

Reduced dimensionality in materials poses significant challenges for *ab initio* calculations of electronic and optical properties. In low-dimensional systems, such as 2D materials, nanowires, and quantum dots (or molecules), electron-electron and e-h interactions are much stronger than in bulk materials due to reduced screening and enhanced Coulomb interactions. These effects lead to pronounced excitonic features, strong quantum confinement, and non-trivial band structures, which require highly accurate and computationally intensive methods to model correctly. Additionally, the reduced dimensionality complicates the convergence of calculations, requiring careful consideration of factors such as BZ sampling, dielectric screening, and boundary conditions. Addressing these challenges is crucial for accurately predicting the electronic and optical properties of low-dimensional materials.

As described in Sec. 3.6.4 for QP calculations, in a PW basis set framework, low-dimensional materials are modeled using a supercell approach. In this method, a Coulomb potential cutoff is required to prevent interactions between periodic images along the non-periodic direction(s). While this technique is essential for accurate calculations of low-dimensional materials, it introduces a significant challenge when calculating optical properties. Specifically, because the system is treated as

isolated within the supercell, the calculated dielectric function essentially represents that of the vacuum, rather than the actual material. To address this issue, a well-defined quantity that is closely related to optical conductivity or absorbance is needed. One such quantity is often the *macroscopic polarizability*. For a 2D system, the macroscopic polarizability $\alpha_{2\mathrm{D}}$ has the dimension of length and is defined as:

$$\alpha_{2\mathrm{D}}(\omega) = -\lim_{\mathbf{q}\to 0} \frac{L}{4\pi q^2}\chi_{00}(\mathbf{q},\omega) \tag{3.76}$$

which is properly renormalized to the non-periodic distance L and is thus vacuum-independent. From $\alpha_{2\mathrm{D}}$, another key quantity can be defined, which will be used throughout this Thesis. This quantity is called *optical absorbance* and it is defined as [74]

$$A(\omega) = \frac{4\pi\omega}{c}\alpha_{2\mathrm{D}}(\omega) \tag{3.77}$$

A similar expression holds also for one-dimensional (1D) and zero-dimensional (0D) systems, given that the polarizability is multiplied by the non-periodic directions L_1 and L_2 and the supercell volume V, respectively. Unless otherwise stated, all optical absorption (3.77) in this Thesis are expressed in atomic units.
For isolated 0D systems, we can also define the *photoabsorption cross-section*

$$\sigma_{xx'}(\omega) = -\frac{4\pi\omega}{c}\mathrm{Im}\sum_s f_x^s\, f_{x'}^s \left(\frac{1}{\omega-\Omega_s+i\eta}+\frac{1}{\omega+\Omega_s+i\eta}\right) \tag{3.78}$$

where Ω_s is the excitonic eigenvalue of the state s, with eigenvector (X^s, Y^s), and f^s are the excitonic oscillator strengths, defined as linear combinations of independent-particle oscillator strengths through the excitonic eigenvectors:

$$f_x^s = \sum_{ia} \langle i|\,\hat{x}\,|a\rangle\ (X_{ia}^s + Y_{ia}^s)$$

The symbol $\hat{x}$ is the position operator along the x direction in space. Unless otherwise stated, all $\sigma_{xx'}$ (3.78) in this Thesis are expressed in atomic units and represent the average value across all directions.
While much of the previous discussion focused on general theoretical aspects that are independent of the system's dimensionality, it is important to note that not all systems can be treated equivalently in practical calculations. For instance, the choice of the basis set used to expand the orbital wavefunctions of the studied system. Using localized Gaussian basis sets instead of PWs for computing the properties of 0D materials offers several advantages. Localized Gaussians are particularly well-suited for capturing the electronic structure of systems with localized states, such as quantum dots or molecules, where the electronic density is confined in space. They can provide a more accurate representation of the electron distribution in these small, finite systems and often require fewer basis functions than plane waves to achieve similar accuracy. Additionally, localized Gaussians typically allow for faster convergence with respect to the number of basis functions and can lead to significant computational savings, especially when dealing with large-scale simulations or complex interactions in 0D materials. While a detailed discussion of computational methods

for clusters and molecules is beyond the scope of this work, it is important to provide a general introduction to the techniques and code employed. A brief overview on this topic is presented in Appendix B.

Chapter 4

Results and Discussions: Two-Dimensional Materials

Over the past 20 years, significant efforts have been dedicated to the search for two-dimensional (2D) materials, which can be derived from van der Waals (vdW) layered solids. Due to their surfaces being naturally terminated by vdW interactions — rather than by dangling bonds — 2D materials tend to be stable under ambient conditions. This stability, combined with their extraordinary mechanical, electrical, and optical properties, makes them highly advantageous. Thanks to quantum confinement effects, 2D materials exhibit properties distinct from their bulk counterparts, drawing significant attention from both academia and industry [75–85].
Due to their atomic-scale thickness, 2D materials are characterized by weak dielectric screening, strong light–matter interaction, and often by the presence of highly bound photo-generated electron-hole pairs, known as excitons, which are central to many of their optoelectronic properties (see Sec. 3.8.3). Moreover, in 2D systems, electrons are directly exposed to the environment because of their reduced thickness, making them highly sensitive to any changes, such as atomic or molecular doping, strain, or external electric and magnetic fields [86–91]. This sensitivity offers exciting potential for applications in electronics, optoelectronics, and energy storage devices, promising increased efficiency, lower costs, and reduced environmental impact [92–94].
To date, a large number of 2D materials have been discovered and fabricated, which can generally be classified into two main categories based on their structures. The first category includes materials such as graphene and hexagonal boron nitride (h-BN) monolayers, which feature a six-membered honeycomb-like structure. The second category consists of triatomic layers, including metal halides (such as PbI_2 and $MgBr_2$), transition metal carbon/nitrogen compounds, transition metal dichalcogenides (MX_2), and elemental 2D materials, other than graphene, known as Xenes. These last two groups, in particular, will be the focus of the following sections.

4.1 Tellurene Polymorphs for Solar Harvesting Applications

4.1.1 Introduction

As mentioned above, the pursuit for 2D materials was motivated by the escalating demand for diverse applications, encouraged by the rapid advancements in the technological industry. Simul-

taneously, solar energy has emerged as a clean and renewable alternative to traditional fossil fuels, addressing the ever-growing global energy needs. However, several challenges, including stability, scalability, large-scale production, and the identification of materials exhibiting power conversion efficiency (PCE) comparable to current silicon-based photovoltaic devices, must be overcome for these next-generation optoelectronic devices to achieve commercial viability. Given the pivotal importance of enhancing optical absorbance while maintaining minimal thickness for the development of new nanoscale devices, the realm of 2D ultra-thin solar cells is currently a focal point of active research [77,95–112]. This area holds the promise of revolutionizing solar energy harvesting, offering potentially higher efficiency, lower cost, and increased flexibility, provided that challenges related to stability, scalability, and material performance are effectively addressed.

Various combinations of nanometer-thick 2D materials, with desirable band alignments and PCE ranging from a few to tenths %, have been either theoretically predicted or synthesized experimentally. However, only a limited number of 2D materials exhibit all the essential properties required for practical solar cells. For instance, graphene is (semi-)metallic and lacks a band gap, MoS_2 has a low carrier mobility [113], and phosphorene, while having an ideal band gap (1.51 eV) and huge carrier mobility [114], readily degrades in ambient conditions [115]. In contrast, 2D tellurium, known as tellurene, emerges as a promising semiconductor of increasing interest [116–119] with a thickness-tunable band gap [120], relatively high carrier mobility (up to 10^3 $cm^2V^{-1}s^{-1}$) [121–123] and it is practically inert when exposed to air, even for a prolonged period of time and without any encapsulation, with stable performances at room temperature [120,121,124]. Furthermore, tellurene shows extraordinary electronic transport properties [125, 126]. Recently, also 2D selenium, a neighbor atomic species of tellurium, has been experimentally proven to be a promising material for high-efficiency solar harvesting applications [127]. These and numerous other attractive features make these materials suitable for both fundamental research and practical applications, including optoelectronics and photovoltaics [128–133].

In this context, employing accurate ground and excited-state first-principles analysis, we demonstrate the remarkable electronic and optical characteristics of tellurene (Te), making it an intriguing contender for highly efficient ultra-thin and flexible solar cell technology. This potential is realized through the strategic use of junctions with other suitable 2D materials, such as transition-metal dichalcogenides (TMDs), and by employing the diverse polymorphs of Te. Indeed, thanks to tellurium's multivalent nature, multiple bonding configurations can occur, resulting in the observation of several allotropic forms. These include the orthorhombic α-phase, which is the most stable in the bulk configuration (known as Te-I), characterized by quasi-1D helical chains, with a two-fold coordination number; the orthorhombic β-phase, featuring a mixture of three-fold and four-fold coordination number and the hexagonal, 1T-MoS_2-like γ-phase, with a six-fold coordination number [134, 135] (Fig. 4.1). Here, unlike in Ref. [134], we adopted the notation from Refs. [136, 137] to distinguish the various allotropic forms. Here, the alphabetical order corresponds to the formation energy of these phases above one layer (1L), listed in ascending order. All three phases have been successfully synthesized experimentally [116, 120, 138, 139]. Scalable and high-quality 2D Te nanoflakes can be efficiently synthesized through various techniques, including physical vapor deposition (PVD), molecular beam epitaxy (MBE), solution synthesis, liquid-phase exfoliation (LPE) methods, and thermal evaporation [121,123,140–143]. These methods hold the potential to produce stable, high-quality, ultra-thin semiconductors with precise control over composition, structure and dimensions.

The α- and β-phases are particularly intriguing due to their pronounced in-plane electronic and optical anisotropy, as shown by various experimental works [121–123], making them very appeal-

ing for applications such as polarization-sensitive photodetectors, linearly polarized pulse generators, high-gain digital inverters and high-performance thermoelectric devices [144–150]. In fact, in-plane anisotropic 2D materials provide not only a rich physics, such as dichroism and birefringence [151, 152], but introduce an additional degree of freedom to regulate the intrinsic optical properties for novel polarization-sensitive applications [153, 154], not achievable with isotropic or out-of-plane optically anisotropic materials.

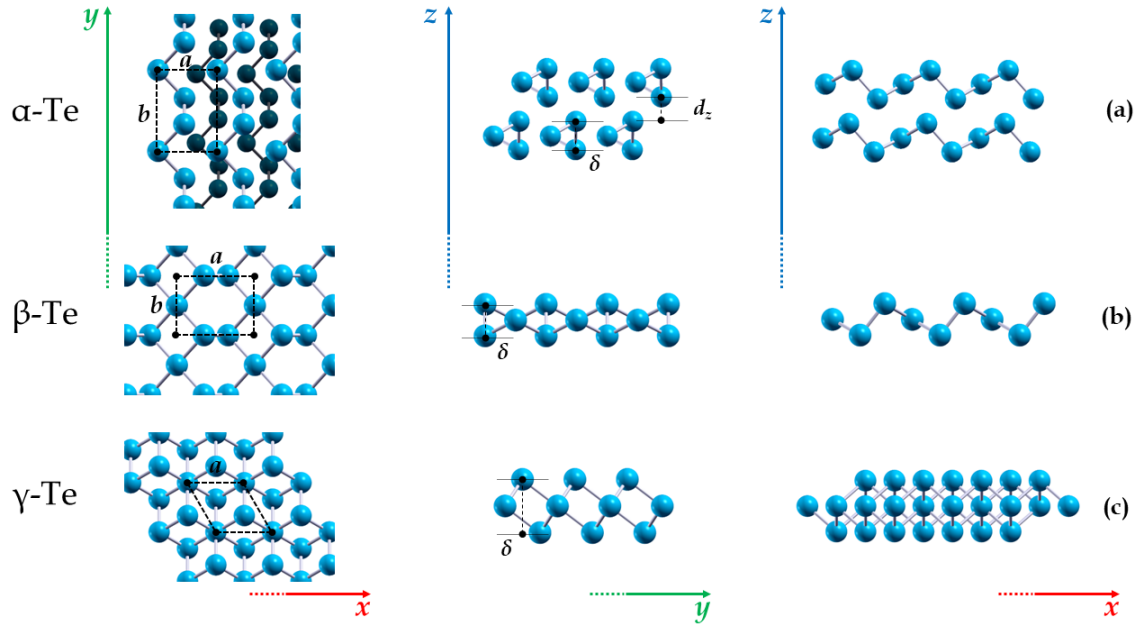

Figure 4.1: *Optimized geometric structures of* (**a**) *2L α-Te,* (**b**) *1L β-Te and* (**c**) *1L γ-Te. The lattice parameters a and b and the layer thickness δ are also displayed. Here we use the notation introduced in Refs. [136, 137] to identify the different allotropic forms, where the alphabetical order follows the formation energy — in ascending order — of these phases, above one layer. Dark and light blue in panel* (**a**) *refers to Te atoms belonging to different layers.*

4.1.2 Methods

DFT and MBPT calculations were performed to investigate the electronic and optical properties of Te, the use of the QE integrated suite [22, 23] and the YAMBO code [48, 49], respectively. GGA Perdew-Burke-Ernzerhof (PBE) functional [155], along with Grimme's DFT-D2 vdW correction [156] were employed to accurately describe electronic and ionic interactions. To account for SOC and to include semi-core electrons of tellurium atoms (specifically those from the fourth shell), a norm-conserving, fully-relativistic pseudopotential from the PseudoDojo repository (v0.4) [157] was used. Convergence of the calculations was achieved with a kinetic energy cutoff of 65 Ry. It was verified that the electronic band structures remained unchanged, except for a rigid shift, with this

Table 4.1: *Optimized lattice parameters* (a, b) *, layer thickness* (δ) *and distance between layers* (d_z) *for 2L* α*-Te. In the case of orthorhombic lattice,* a *and* b *represent the* x *and* y *directions, respectively.*

	a (Å)	b (Å)	δ (Å)	d_z (Å)
2L α-Te	4.230	5.790	2.104	1.820
1L β-Te	5.478	4.175	2.166	-
1L γ-Te	4.150	-	3.677	-

cutoff choice. Uniform Monkhorst-Pack **k**-point meshes with dimensions of $30 \times 28 \times 1$, $24 \times 24 \times 1$, and $36 \times 36 \times 1$ were employed for the α-, β-, and γ-phases, respectively. To prevent interaction between periodic replicas, a minimum vacuum region of 15 Å along the direction perpendicular to the layer planes (z) was introduced. Structural relaxation was considered converged when the maximum component of the residual ionic forces dropped below 10^{-8} Ry/Bohr.
From the obtained DFT eigenvalues and eigenvectors, MBPT calculations were carried out, specifically using the G_0W_0 method for QP corrections and the BSE [158–161] for e-h interaction. These calculations allowed to account for many-body effects and accurately describe the electronic and optical properties of the systems. Energy cutoffs of 60 (6), 70 (6), and 80 (8) Ry were used for the exchange (correlation) part of the self-energy Σ_x (Σ_c), while 306, 478, and 278 empty bands were included in the calculation of Σ_c. A technique, described in Ref. [162], was applied to speed up convergence with respect to empty states, and a cutoff for the Coulomb potential along the non-periodic direction (z) was used, as implemented in the YAMBO code [49]. For the BSE excitonic Hamiltonian, a total of 5 occupied states and 5 unoccupied states (for the α-phase), and 6 occupied states and 6 unoccupied states (for both β- and γ-phases) were employed. This choice facilitated the calculation of the optical response, exciton binding energies, and their spatial localizations. The convergence with respect to the **k**-points for the BSE calculations was carefully checked, and the following **k**-point grids were used: $40 \times 40 \times 1$, $40 \times 40 \times 1$, $42 \times 42 \times 1$ for α-, β-, and γ-phases, respectively. Furthermore, differently from most of the existing literature [163–165], the spinorial nature of the wavefunctions [166] and the full semi-core $n = 4$ tellurium states from DFT were considered up to the many-body analysis.

4.1.3 Structural Properties

The main focus here concerns ultra-thin samples, specifically investigating the 1L configuration for the orthorhombic β- and the hexagonal γ-phase. However, due to instability with just a single atomic layer [135, 167], the orthorhombic chained α-phase is studied in the 2L configuration. For each system, a structural relaxation is performed to obtain optimized lattice parameters and atomic positions (Fig. 4.1). These are reported in Table 4.1. For the 2L α-Te configuration, the system comprises two alternate planes of parallel helical chains, separated by a distance $d_z = 1.820$ Å. It exhibits orthorhombic symmetry ($a = 4.230$ Å, $b = 5.790$ Å), with six atoms per unit cell (Fig. 4.1a). The orthorhombic 1L β-Te is a meta-stable structure, featuring three atoms per unit cell (Fig. 4.1b), with lattice parameters $a = 5.478$ Å and $b = 4.175$ Å. Lastly, the 1L γ-Te adopts a hexagonal sym-

metry lattice ($a = 4.150\,\text{Å}$) with three atoms per unit cell (Fig. 4.1c). This structure exhibits a honeycomb pattern, with an atom in the middle of each hexagon, and a thickness of about $\delta = 3.677\,\text{Å}$. Notably, in free-standing configuration, this allotropic form appears as the most stable in the 1L case. More information about these systems, up to four layers, can be found in our previous work [167].

4.1.4 Electronic Properties

Next, Kohn-Sham eigenvalues and eigenstates are exploited within the many-body approach in order to evaluate the related QP corrections. The DFT and QP-corrected electronic band structures are reported in Fig. 3 of Appendix D. Interestingly, in the case of 2L α-Te (see Figs. 3a and 4.3a), both the indirect and the direct gap are not found along high-symmetry directions. Indeed, in contrast to previous findings [135], and thanks to a very dense sampling of the BZ, we discovered that the indirect gap is located at the **k**-points $\mathbf{q_{VBM}} = \frac{2\pi}{a}(0.2375,\ 0.2283,\ 0)$ and $\mathbf{q_{CBM}} = \frac{2\pi}{a}(0.0125,\ 0.1735,\ 0)$, where a is the lattice parameter. The direct gap is instead located at the **k**-point $\mathbf{q}^* = \frac{2\pi}{a}(0.2125,\ 0.2100,\ 0)$. Both $\mathbf{q}^*$ and $\mathbf{q_{CBM}}$ are found in a direction parallel to $\Gamma \rightarrow S$, which we denote as $\Gamma^* \rightarrow S^*$ (refer to Fig. 4.3a). The minimum indirect and direct band gaps are, respectively, 1.31 and 1.51 eV. To the best of our knowledge, these are the first reported many-body calculations for such a system. Concerning 1L β-Te, our analysis unveils that this phase displays a direct band gap with a QP-corrected value of 1.96 eV at the Γ point (see Fig. 3c). Previously, Min et al. [165] reported a comparable value (1.99 eV) through linear extrapolation. However, it is noteworthy that, by neglecting SOC, they observed an indirect band gap nature. Lastly, the 1L γ-Te is an indirect band gap material with the lowest (indirect) QP gap of 1.02 eV (see Fig. 3e). The CBM is located at the Γ point, while the VBM is situated along the $\Gamma \rightarrow M$ direction. This result is consistent with the findings of Ref. [168]. All the information about electronic band gaps is summarized in Table 4.2.
It is worth highlighting that the majority of previous literature does not consider the inclusion of SOC and the truncation of the Coulomb potential to eliminate spurious interactions between replica [163–165]. In this study, we account for both these factors which are very crucial for reliable predictions of the QP electronic properties.

4.1.5 Optical Properties

In the subsequent discussion, we focus into the optical response of Te polymorphs, examining the important influence of e-h interaction. This exploration is carried out through the resolution of the BSE [41]. Our central focus lies in studying the onset of optical absorption spectra, particularly under the influence of in-plane light polarization. A key aspect of our investigation involves a detailed analysis of the spatial localization of the lowest bright direct excitons, both in real and reciprocal space domains. To provide a comprehensive backdrop, each spectrum is thoughtfully paired with the solar flux within the same energy range. These relationships are visually represented by the filled orange curves of Fig. 4.2. The comparative analysis serves as a valuable tool, offering us insights into the optical features of Te and its potential applications. Moving forward, in the upcoming section, we leverage this wealth of information to present a demonstrative illustration. Specifically, we highlight how the optical absorption spectra of Te polymorphs seamlessly align with the region of maximum solar activity intensity. These findings hold promise for applications and

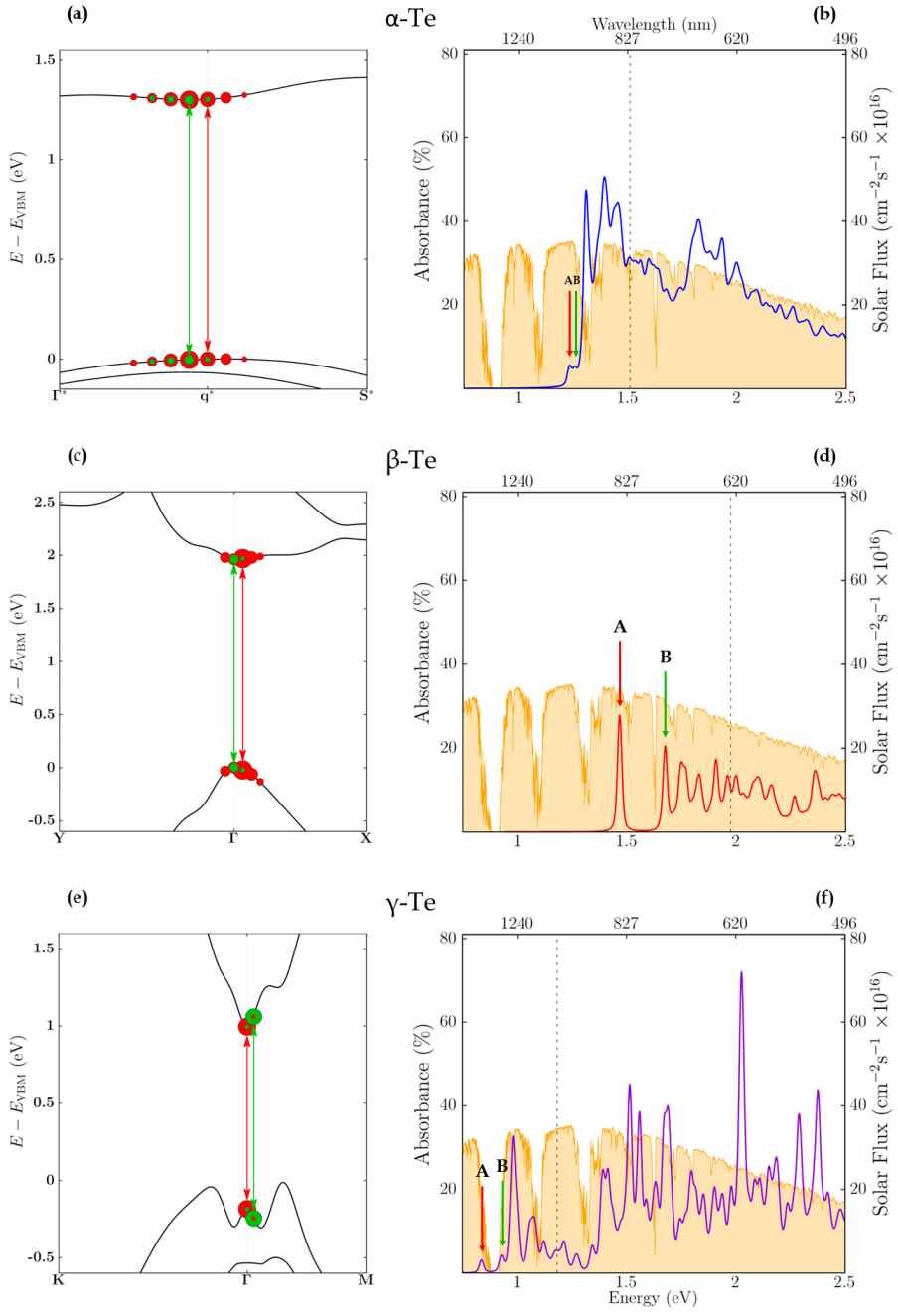

Figure 4.2: [***Left***] *Lowest direct gap region, calculated at the G_0W_0 level, obtained by using a norm-conserving, fully relativistic GGA-PBE pseudopotential, with SOC and semi-core electrons, of 2L α-Te* (**a**)*, 1L β-Te* (**c**) *and 1L γ-Te* (**e**)*, respectively. The dots represent the transitions contributing to the first two bright excitons, indicated with red* (A) *and green* (B) *colours, and their size is proportional to the intensity of the transition. Energy zero is set as the top of the valence bands.* [***Right***] *Optical absorption spectra, expressed in terms of the absorbance $A(\omega)$, calculated at the BSE level, with the inclusion of SOC and semi-core electrons, of 2L α-Te* (**b**, *blue line*)*, 1L β-Te* (**d**, *red line*) *and 1L γ-Te* (**f**, *violet line*)*, respectively. Broadening is set to 0.01 eV. The AM1.5G solar flux $\Phi(\omega)$ [169]* (*orange, right axis*) *is also reported, in terms of both photon energy* (*bottom axis*) *and wavelength* (*top axis*)*.*

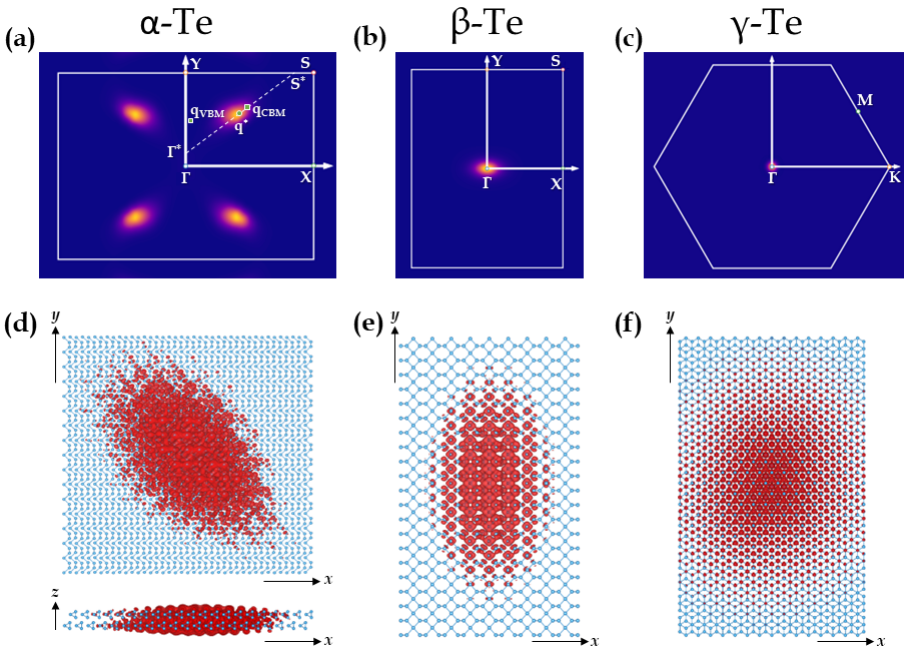

Figure 4.3: [***Top***] *Plot of the weights of the most intense transitions contributing to the first bright exciton, localized in the BZ, of 2L α-Te* (**a**)*, 1L β-Te* (**b**) *and 1L γ-Te* (**c**)*, respectively. In the case of 2L α-Te, the* **k***-points, at which both the indirect and direct band gaps are located, are highlighted. We reference as* Γ^* *and* S^* *the ends of the direction parallel to the high-symmetry* $\Gamma \to S$*.* [***Bottom***] *Excitonic wavefunction plot, in direct space, of 2L α-Te* (**d**)*, 1L β-Te* (**e**) *and 1L γ-Te* (**f**)*, respectively. This is obtained by averaging the position of the hole over the entire unit cell, while increasing the number of cell repetitions in each in-plane direction, until the wavefunction vanishes.*

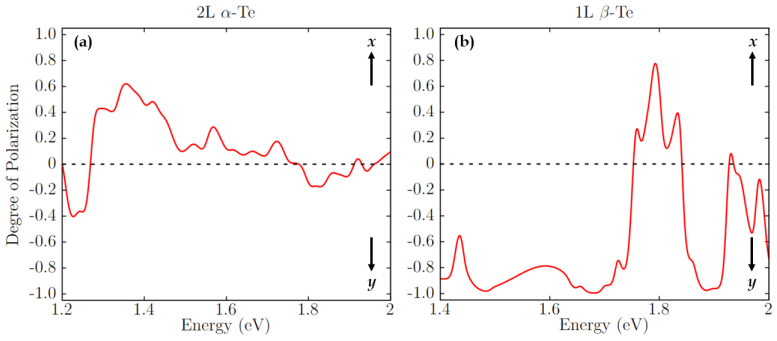

Figure 4.4: *Degree of polarization, defined as the ratio between the difference* $(A_x - A_y)$ *and the sum* $(A_x + A_y)$ *of the absorbance in the two in-plane directions, for 2L α-Te* (**a**) *and 1L β-Te* (**b**)*, respectively. Broadening is set to 0.01 eV.*

Table 4.2: *Calculated lowest direct* (d) *and indirect* (i) *electronic band gaps, with the inclusion of SOC, at the DFT,* G_0W_0 *and BSE level.* E_b^{BSE} *is the excitonic binding energy of the lowest bright exciton, calculated as the difference between the lowest QP direct gap* $E_{g,dir}^{\mathrm{G_0W_0}}$ *and the BSE one* $E_{g,dir}^{\mathrm{BSE}}$. *Between round brackets, the binding energies calculated from the Rytova-Keldysh model [167]. The last two columns show the estimated exciton radiative lifetime of the first bright exciton at 0 K* ($\tau_A(T=0)$) *and the room temperature* ($\mathrm{RT} = 300\,K$) *average radiative lifetime* ($\langle\tau_{\mathrm{eff}}\rangle$).

	$E_{g,i}^{\mathrm{DFT}}$(eV)	$E_{g,d}^{\mathrm{DFT}}$(eV)	$E_{g,i}^{\mathrm{G_0W_0}}$(eV)	$E_{g,d}^{\mathrm{G_0W_0}}$(eV)	$E_{g,d}^{\mathrm{BSE}}$(eV)	E_b^{BSE}(eV)	$\tau_A(0)$ (ps)	$\langle\tau_{\mathrm{eff}}^{\mathrm{RT}}\rangle$ (ns)
2L α-Te	0.67	0.86	1.31	1.51	1.23	0.28 (0.26)	0.7	12
1L β-Te	-	1.02	-	1.96	1.46	0.50 (0.57)	5×10^{-2}	0.9
1L γ-Te	0.42	0.54	1.02	1.18	0.84	0.34 (0.20)	0.2	0.6

advancements in the realms of optical response and solar energy utilization.
The BSE optical spectra are expressed in terms of the optical absorbance, as defined in Eq. 3.77 of Sec. 3.8.8. Upon comparing the spectra obtained at the BSE and the IQP level of approximation (refer to Fig. 3), we observe that a significant energy range of the optical features exhibits an excitonic nature. Specifically, we predict the presence of room temperature-stable excitons with binding energies ranging from 0.28 to 0.50 eV (see Table 4.2). Analyzing the optical absorption of 2L α-Te (Fig. 4.2b), we identify the onset as characterized by two peaks of relatively low intensity, labeled as peak A at 1.23 eV and peak B at 1.26 eV, both four-fold degenerate. Notably, these peaks are situated up to 0.28 eV below the calculated lowest QP direct band gap of 1.51 eV. This difference precisely corresponds to the binding energy E_b^{BSE} of the lowest bright direct exciton (A). The relevant contributions to this excitonic state originate from transitions between valence and conduction bands around the **k**-point $\mathbf{q^*} = \frac{2\pi}{a}(0.2125,\ 0.2100,\ 0)$. This is visually represented in Fig. 4.2a, where the transitions are superimposed on the QP band structure, and in Fig. 4.3a, illustrating the weights of these transitions within the BZ. Exciton B instead arises from similar states but involves the degenerate counterparts of the related bands. This difference may be attributed to a opposite spin orientation of the degenerate bands, as suggested by Wang et al. in Ref. [136].
The distinctive chained structure of the α-phase (Fig. 4.1a) naturally reflects into a strong anisotropy of its optical response. Examining the excitonic wavefunction depicted in Fig. 4.3d, we observe an orientation of approximately 45° with respect to the x, y directions, spanning both intra and inter layer regions. This orientation is attributed to the peculiar band structure around $\mathbf{q}^*$, featuring flat bottom conduction states with anisotropic effective masses. The anisotropy within this material extends beyond the first two excitons, as illustrated in the plot presented in Fig. 4.4a. Here, the degree of polarization (DoP), defined as the ratio between the difference and the sum of the absorbance in the two orthogonal in-plane directions, is reported. The absorbance values in both directions x, y, as well as their difference, are also illustrated in panels a and c of Fig. 4. The

DoP serves as a metric to quantify the predominant portion of light absorbed in each direction at a given photon energy. Notably, the first two excitonic peaks and small energy ranges above 1.8 eV are primarily influenced by absorption along the y direction, i.e. the direction of the chains. In contrast, absorption along the x direction dominates in the remaining spectral regions.
The distinctive optical spectrum of α-Te can be explained by considering the chemical characteristics of the system. In Te-based structures, chemical bonds are predominantly formed by the $5p^4$ electrons [170–172]. In the case of chained structures like that of 2L α-Te, each Tellurium covalently shares two p-electrons with the two adjacent atoms along the chain. Simultaneously, the remaining two p-electrons act as lone pairs situated between the chains. Consequently, the interaction along the chain is strong, whereas the interaction between neighboring chains is weaker (for an extended discussion we refer to our prior publication [167]). The stronger interaction along the chain makes it more energetically favorable to induce excitations in the x direction, contributing to the anisotropic optical response observed in the α-Te spectrum.
Regarding the 1L β-Te allotrope, the optical spectrum at the BSE level is depicted in Fig. 4.2d and compared with the IQP spectrum in Fig. 3d. At the BSE level, the optical onset is marked by a single sharp and highly intense peak at 1.46 eV (labeled A in Fig. 4.2d), corresponding to a doubly degenerate exciton with a binding energy of approximately 0.50 eV. Notably, Pan et al. [164] previously reported a larger binding energy (0.67 eV) due to the absence of SOC. Additionally, a doubly degenerate, optically forbidden dark exciton is identified at a lower energy of around 1.44 eV. Intriguingly, similar to the α-phase, both the VB and the CB are degenerate, and these two excitons share transitions at the same **k**-points but from different bands, causing the latter transition to be dark. The primary contributions to exciton A arise from transitions between the VB and CB near the Γ point, particularly along the armchair k_x direction (i.e., $\Gamma \rightarrow X$). This is illustrated in Fig. 4.2c, as well as in Fig. 4.3b. The second peak (B), which is four-fold degenerate, is situated at 1.67 eV and results from transitions predominantly localized at the Γ point. The plot of the wavefunction of exciton A reveals a significant spatial anisotropy, displaying an elongated shape along the zigzag (y) direction (Fig. 4.3e). This observation is evident from Fig. 4.4b and Fig. 4. Initially, optical transitions are dominant along the zigzag (y) direction, while transitions along the armchair (x) direction are negligile up to energies of approximately 1.7 eV. In order to provide a qualitative explanation for this substantial anisotropy, we briefly analyze some relevant factors. We first extrapolate the electron and hole effective masses along the in-plane armchair (x) and zigzag (y) directions, providing access to the exciton reduced masses μ. Specifically, we obtain $\mu_x = 0.535$ a.u. and $\mu_y = 0.138$ a.u. The significant difference, with the latter being nearly four times smaller than the former, justifies the observed optical anisotropy. Furthermore, we examine the VB and CB wavefunctions at the DFT level. For simplicity, our discussion focuses exclusively on the wavefunctions at the Γ point. While the plot of the conduction band wavefunction (Fig. 5b) does not exhibit an apparent correlation with the optical anisotropy, the VB (Fig. 5a) reveals a distinct p_y-like orbital character. This observation indicates a clear orientation of the electron density, naturally favoring the y direction for the optical response.
As for the 1L γ-Te phase (Fig. 4.2f), our calculations indicate that the first bright exciton (A) appears at approximately 0.84 eV, which is 0.34 eV lower than the IQP onset of 1.18 eV. These findings are in excellent agreement with the work of Villegas et al. [168]. The primary contribution to this excitonic state arises from transitions between the doubly degenerate VB and CB at the Γ point. This is depicted in Fig. 4.2e, as well as in Fig. 4.3c. The second exciton (B), also four-fold degenerate, appears approximately 0.1 eV above the first one, originating from the same transitions as exciton A but with different strengths. The third peak, located at 0.98 eV, is the most intense

excitonic peak and originates from transitions involving **k**-points along the $\Gamma \rightarrow M$ direction, near the VBM of the indirect gap. The localized nature of the first exciton in reciprocal space translates into an highly delocalized excitonic wavefunction in real space, as showcased in Fig. 4.3f, where the wavefunction exhibits marked hexagonal symmetry. In this case, the symmetry of the lattice prevents the emergence of optical anisotropy.
By solving the BSE and examining the excitonic states [79], one can extract information about the radiative lifetimes, which are crucial for understanding the optical properties of materials, especially in the context of radiative processes. A short radiative lifetime, less than a nanosecond (ns), signifies rapid emission or absorption of light in the material. Practically, this indicates that the material can swiftly transition between energy states associated with photon emission or absorption. Table 4.2 shows that the radiative lifetimes of β- and γ-Te are significantly shorter than that of the α-phase, suggesting that these 2D materials are well-suited for high-speed optoelectronic applications where fast response times are crucial, such as in ultrafast lasers, high-speed communication devices, and advanced imaging systems. For solar energy harvesting, longer radiative lifetimes are desirable. This is achieved by considering room temperature and performing a thermal average, which includes dark excitons, resulting in radiative lifetimes of about 1 ns for both β- and γ-Te.
One further remark is worth making. In our previous work [167], we estimated the exciton binding energies of these systems, using a 2D model introduced by Keldysh and Rytova [173, 174]. The model has proven reliable when applied to various types of 2D systems [167, 175–177]. Also in this case, despite the simplicity of the model, the estimates are in fairly good agreement with BSE results. They are reported in Table 4.2, between round brackets.
In conclusion, each Te polimorph exhibits distinct optical fingerprints, enabling the potential differentiation of one phase from another. Collectively, owing to their favorable band gaps, all these materials predominantly absorb light in the near-infrared and visible regions of the solar spectrum, demonstrating remarkable intensity despite their nearly-atomic thickness. This implies the potential use of these materials, in conjunction with other 2D materials, in hetero-structures for innovative light-harvesting devices, as detailed in the subsequent section.

4.1.6 Tellurene for Solar Light Harvesting Applications

Two crucial prerequisites for the development of ultra-thin and efficient solar harvesting devices involve optimizing light absorption across the solar spectrum. This includes tailoring the band gap and absorption coefficients of the constituent layers. Additionally, it is essential to identify the appropriate type II band alignment between two 2D materials to enhance efficient charge transfer across them.
A convenient way for quantifying sunlight absorption is through the maximum short-circuit current density (SCC), denoted as J_{sc}^{max} . Under the assumption that all photo-generated charge carriers are effectively collected, the extracted current from a solar cell can be computed as follows [77, 98]:

$$J_{sc}^{max} = e \int A(\omega)\Phi(\omega)d\omega$$

in units of $\hbar$. Here $\Phi(\omega)$ is the solar photon flux [169], expressed in units of $\mathrm{cm}^{-2}\mathrm{s}^{-1}\mathrm{eV}^{-1}$, $A(\omega)$ is the optical absorbance, as presented in the previous section, and e is the elementary charge. In Fig. 4.2 (right panels) we show the solar photon flux together with the optical absorbance of

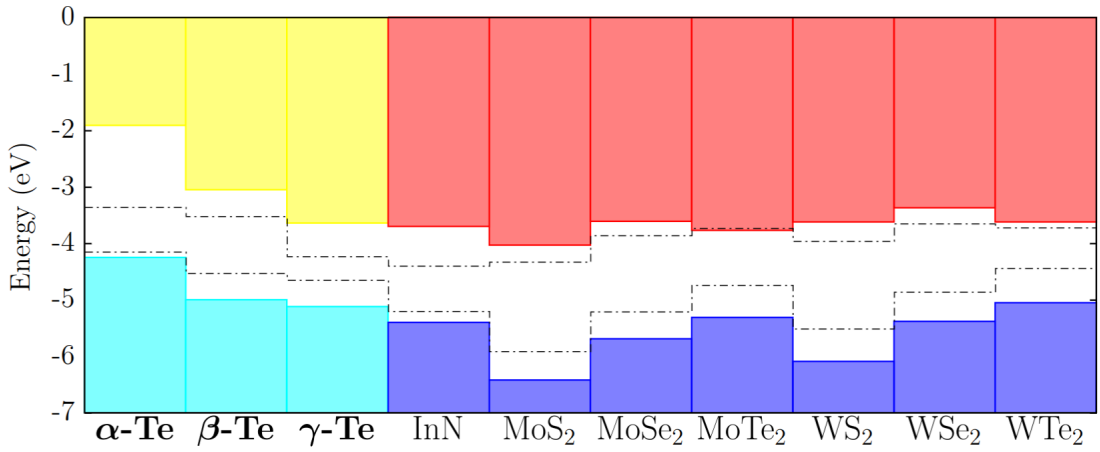

Figure 4.5: *Comparison of the offsets alignment between our calculated 2L α-Te , 1L β-Te, 1L γ-Te and other monolayer systems previously calculated in the literature, namely 2D-InN [178,179] and several TMDs [180]. Yellow (cyan) regions show EA (IE) from our GW calculations, while red (blue) are GW values taken from the literature. Black dashed lines show the relative alignment from DFT calculations. In both cases, the offsets are aligned with respect to the vacuum level, which is set to zero.*

Te allotropes, which display peaks as high as 60 % and a desirable compatibility with the solar activity in its region of maximum intensity. The calculated current densities J_{sc}^{max} are, for the different phases: 8.4 mA/cm^2 (α-Te), 2.2 mA/cm^2 (β-Te), 7.1 mA/cm^2 (γ-Te), the latter in good agreement with the value of 6.7 mA/cm^2 obtained by Villegas et al. [168]. Our predicted current densities are extraordinarily high, given the extremely small thickness of the systems. Indeed, common amorphous (Si-H and GaAs) and organic (PH3T) solar cells show short-circuit current densities lying around 20 to 30 mA/cm^2, for sample thicknesses above 1 μm, dropping much below 1 mA/cm^2 when their thickness is decreased to around 1 nm [181]. Therefore, about tens of nm of these materials are needed to absorb the same fraction of sunlight as Te. Moreover, our results are comparable or higher than those of most of 2D TMDs [77, 98, 182, 183].
Given the very promising estimates of the SCC, it is worth further exploring the capability of Te as an absorber (donor) material, in feasible light harvesting devices. An important quantity in this context is given by the Power Conversion Efficiency (PCE) η. It can be calculated as [95, 184]:

$$\eta = \frac{FF \cdot V_{oc} \cdot \int_{E_d^{opt}}^{\infty} \frac{P(\omega)}{\omega}\, d\omega}{\int_0^{\infty} P(\omega)\, d\omega} \tag{4.1}$$

in units of $\hbar$. Here, FF is the fill factor, an empirical value which we take as 0.65 (a reasonable value in a device with effective carrier transport [77]). $P(\omega)$ is the AM1.5G solar irradiance [169], expressed in terms of W/m^2. V_{oc} is the maximum open circuit voltage, which is usually estimated as $V_{oc} = E_d^{opt} - \Delta E_c - 0.3$. Indeed, $E_d^{opt} - \Delta E_c$ is the effective interface gap, given by the difference

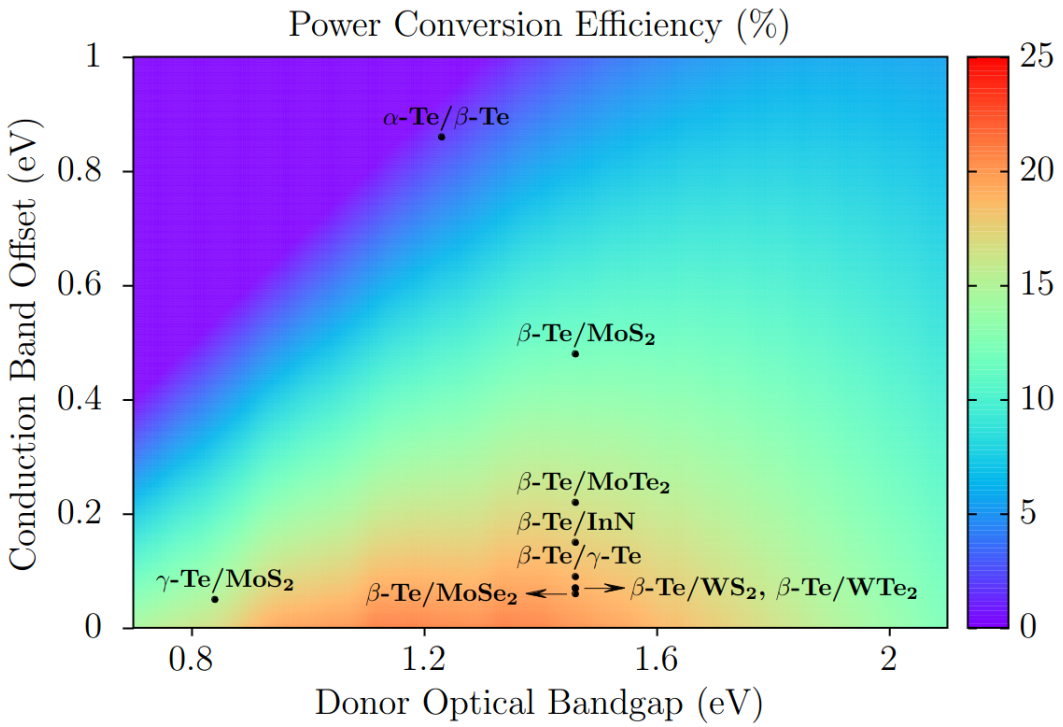

Figure 4.6: *Heatmap of the PCE η plotted as a function of the donor optical gap E_d^{opt} and of the conduction band offsets ΔE_c, obtained by solving Eq. (4.1). The black dots refer to the efficiency of the heterostructures shown in Fig. 4.5 as reported in Table 4.3. A fill factor (FF) of 0.65 was considered.*

between the optical band gap E_d^{opt} of the donor material in the heterostructure (in our case, one of the phases of Te), calculated at the BSE level, and the conduction band offsets difference ΔE_c, calculated between the optical GW+BSE LUMO level of the donor (thus accounting for exciton binding energy) and the GW LUMO level of the acceptor. The term 0.3 eV is empirical and accounts for energy conversion kinetics. This combined scheme, making use of the optical LUMO of the donor and the QP LUMO of the acceptor, takes into account the minimum energy of the exciton formed after photo-absorption that it is assumed to occur mainly in the donor material, as well as the electronic QP level for the transfer of the photo-excited electron to the acceptor. Eq. (4.1) however is valid only if both V_{oc} and ΔE_c are positive definite; that is, we have an actual type II heterostructure. For more details, see [95, 184]. Following Eq. 4.1, we calculate the PCE of several possible hetero-structures of Te polymorphs with other 2D materials, ranging from InN to various TMDs. The alignment and band offsets of the considered 2D materials, shown in Fig. 4.5, were used to estimate ΔE_c. This effective approach, known as the Anderson method [185], has been validated as highly accurate for vdW heterostructures with similar chemistry and/or structure, showing negligible differences compared to actual simulated heterostructures. This has been demonstrated in studies such as Ref. [186] and references therein. The resulting efficiencies

η are reported as a heatmap in Fig. 4.6. In particular, we see that β-Te satisfies the requirements stated above with all the other systems (exception made for WSe_2) and displays very high PCEs, ranging between 11 and 19% (the highest being with $MoSe_2$, WS_2 and WTe_2) [187]. Interestingly, also the β-Te/γ-Te junction, with an estimated efficiency of 19%, is found to be very promising. Overall, our calculations show very competitive PCEs, comparable or even superior to those of other 2D hetero-bilayers previously investigated [77,97,108–112], reported in Table 4.3. It is worth stressing again the outstanding efficiencies of these materials, in relation to their atomic thicknesses, if compared to the current micrometric crystalline silicon devices.

Table 4.3: *Calculated PCE η for Te-based junctions, compared with results taken from the literature. All results have been obtained using FF = 0.65. Also experimental results for silicon, as a reference value, are reported. PCE obtained within the GW-BSE approach is indicated with *.*

System	**Thickness**	**PCE** (%)
Si [188] (Exp.)	$\sim$ 100 μm	18 - 22
α-Te/β-Te*	$\sim$ 1 nm	1.6
β-Te/γ-Te*	$\sim$ 1 nm	19
β-Te/X^{*,1}	$\sim$ 1 nm	11 - 19
γ-Te/MoS_2*	$\sim$ 1 nm	15
2L Phosphorene [97]	$\sim$ 1 μm	16 - 18
Graphene/MoS_2* [77]	$\sim$ 1 nm	1.0
WS_2/MoS_2* [77]	$\sim$ 1 nm	1.5
GeSe/SnSe [108]	$\sim$ 1 nm	21
$PdSe_2$/TMD [110]	$\sim$ 1 nm	6 - 22
InS/GaTe [111]	$\sim$ 1 nm	12
GaSe/GaTe [111]	$\sim$ 1 nm	18
K_2O/Cs_2O [112]	$\sim$ 1 nm	22

[1] *X stands for all the materials shown in Fig. 4.5, apart from WSe_2.*

4.1.7 Conclusions

To summarize, we have presented detailed ab initio calculations of the geometry, electronic, and optical properties of Te in its α-, β-, and γ-phases, incorporating state-of-the-art QP and excitonic effects. Each system exhibits distinct optical characteristics that could facilitate experimental differentiation among the various phases. Despite their nearly-atomic thickness, these materials

demonstrate substantial light absorption, primarily in the near-infrared and visible range. This observation suggests their potential use, in conjunction with other 2D materials, in novel light-harvesting devices. We give support to this hypothesis through an analysis of the PCE of 1 nm-thin Te-based junctions. Our findings indicate an efficiency (η) as high as 19% in heterostructures based on β-Te and TMDs, as well as in the β-Te/γ-Te homojunction. Notably, this efficiency is comparable to that of 100 μm-thick silicon junctions.
In conclusion, our study demonstrates how the exceptional electronic and optical properties of Te position it as a promising candidate for highly efficient solar cell technology. Its versatility is evident not only in junctions with other 2D materials but also in homojunctions, making use of Te polymorphism. These findings lay the groundwork for significant advancements in renewable energy harvesting.
The results of this study are presented in two articles published during my PhD [167, 189].

4.2 Tunable Second-Harmonic Generation in 2D Materials

4.2.1 Introduction

Non-linear optical frequency conversion, where optical fields interact with a non-linear medium to generate new frequencies, is a key phenomenon in modern photonic systems. However, a major challenge with these techniques lies in the difficulty of tuning the non-linear electrical susceptibilities that drive such effects in a given material.
Recently, several experimental groups have shown interest in using external electric fields to induce or modify second-harmonic generation (SHG) in 2D materials[1]. Two distinct strategies have emerged: the first involves applying an electric field in the z-direction to induce an SHG response in materials with inversion symmetry [192–194]; the second focuses on modifying the SHG response in materials that already exhibit it, by inducing doping through an external field and a conductive substrate that supplies electrons or holes [195]. These approaches have also been combined to induce SHG in bilayer materials with inversion symmetry [196]. In this experiment, not only does the external field break the inversion symmetry, but the induced doping charges the two layers oppositely, further amplifying the symmetry breaking. This phenomenon is referred to as charge-induced SHG.
In this work, both mechanisms were investigated: inversion symmetry breaking and induced doping. For these two cases, we focus on systems where experiments have already been conducted — a bilayer of MoS_2 [192, 193] for the symmetry-breaking case and a monolayer of WSe_2 [195] for the induced-doping case. A real-time approach was employed to compute the SHG and its variation in response to external stimuli.
In recent years, the real-time propagation of the Schrödinger equation within the TDDFT framework has become a widely used tool for investigating optical responses in both finite [197, 198] and extended systems [199, 200]. This approach differs slightly from TDDFT, as it is based on the real-time propagation of an effective many-body Hamiltonian derived from Green's function theory [201]. In this method, the coupling with the external field is treated using the length gauge

[1] In SHG, a material is irradiated with a laser at a frequency ω, and it emits light at a frequency 2ω. This phenomenon occurs only in materials lacking inversion symmetry and is highly sensitive to the angle between the laser and the crystal lattice. Due to this sensitivity, SHG has been employed to determine the number of deposited layers [190] and their orientation [191].

and formulated in terms of the dynamical Berry phase [202,203]. This approach has been employed to study various non-linear optical responses, ranging from second- and third-order harmonic generation [201] to two-photon absorption [204]. A detailed discussion of this topic is provided in Appendix C.

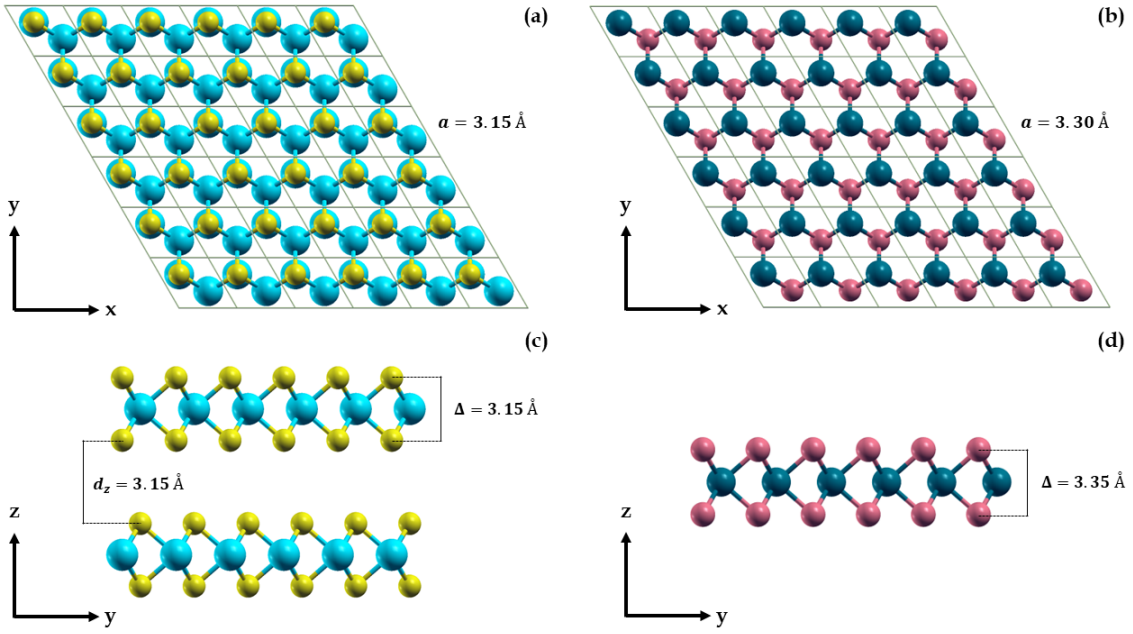

Figure 4.7: *Optimized geometric structures of* $(\mathbf{a},\mathbf{c})$ *2L* MoS_2 *and* $(\mathbf{b},\mathbf{d})$ *1L* WSe_2. *The lattice parameters a, the layer thickness* δ *and the layer distance* d_z *are also displayed.*

4.2.2 Methods

Ground-state properties of both bilayer MoS_2 and monolayer WSe_2 were studied using DFT with the QE code [22,23]. We employed the GGA-PBE functional [155] with scalar-relativistic optimized norm-conserving pseudopotentials from the PseudoDojo repository (v0.4) [157]. Atomic structures were relaxed using a cutoff of 120 eV, a k-point sampling of $32\times32\times1$, and the FIRE minimization algorithm [205], with a force convergence criterion of 10^{-5} atomic units (see Fig. 4.7). An electric field in the z direction, perpendicular to the layers, was applied to the bare ionic potential using a saw-like potential, as implemented in QE. We ensured that the layers were situated in the region where the electric field is constant. SOC was not included since it was not essential to our discussion. Optical susceptibilities were calculated using the YAMBO code [48, 49]. QP corrections to the fundamental band gap were applied as a rigid shift to all bands. Parameters for the linear and non-linear response are detailed in Table 4.4. For WSe_2, to accurately sample the doped configurations, we employed a double-grid approach for the dielectric constant calculation, as described in Ref. [206]. To include excitonic effects, we used the approach described in Sec. 7 of Appendix C, called LSEX

approximation, and employed 1 and 5 G-vectors to model the excitonic response in bilayer MoS_2 and monolayer WSe_2, respectively. This is sufficient to reproduce the lowest excitons in WSe_2 and the C-exciton in the MoS_2 bilayer, which is responsible for the SHG response. We verified that increasing the number of bands in the calculations does not affect the spectra within the energy range considered, as shown in Fig. 8 of Appendix E.

Table 4.4: *Parameters used in the linear and non-linear response calculations for both bilayer MoS_2 and monolayer WSe_2. It includes the* **k***-point sampling, the range of bands considered, and for WSe_2, it also specifies the double-grid approach used for calculating the doped dielectric constants (between brackets). Additionally, the table provides details on the parameters used in constructing $\epsilon^{-1}_{\mathbf{G},\mathbf{G}'}(\omega = 0)$, the scissor operator applied to the Kohn-Sham band structure (ΔE_{GW}), and the effective layer thickness (Δ_{eff}) used in the SHG calculations.*

System	**k**-points	Bands	$\epsilon_{\mathbf{G},\mathbf{G}'}$ size	$\epsilon_{\mathbf{G},\mathbf{G}'}$ bands	ΔE_{GW}	Δ_{eff}
2H-MoS_2	42×42	19 - 34	5 Ha	200	1.058 eV	1.23 nm
WSe_2	21×21	19 - 26	4 Ha	600	0.55 eV	0.648 nm
	(70×70)					

4.2.3 External Electric Field

In this section, we delve into the two mechanisms considered in this manuscript that affect the tunability of the SHG response. First, we examine the impact of an external out-of-plane electric field, followed by the effects of induced doping. We will discuss how each of these factors influences the second-order response functions. Numerical results will be presented in the following section.
We start by discussing the general case of a system subjected to an external field, without any induced doping. As described in Appendix C (Eq. (21)), the polarization can be expanded in a power series of the incident field $\boldsymbol{\mathcal{E}}_j$ as[2]:

$$\begin{aligned}\mathbf{P}_i(\omega) =& \chi^{(1)}_{ij}(\omega)\boldsymbol{\mathcal{E}}_j(\omega) + \\ & \chi^{(2)}_{ijk}(\omega;\omega_1,\omega_2)\boldsymbol{\mathcal{E}}_j(\omega_1)\boldsymbol{\mathcal{E}}_k(\omega_2) + \\ & \chi^{(3)}_{ijkl}(\omega;\omega_1,\omega_2,\omega_3)\boldsymbol{\mathcal{E}}_j(\omega_1)\boldsymbol{\mathcal{E}}_k(\omega_2)\boldsymbol{\mathcal{E}}_l(\omega_3) + \mathcal{O}(\boldsymbol{\mathcal{E}}^4)\end{aligned}$$

where the sum over indexes is understood. The SHG corresponds to the i-th component of the macroscopic second-order polarization

$$\mathbf{P}^{(2)}_i(2\omega) = \sum_{jk} \chi^{(2)}_{ijk}(-2\omega;\omega,\omega)\boldsymbol{\mathcal{E}}_j(\omega)\boldsymbol{\mathcal{E}}_k(\omega) \tag{4.2}$$

[2]Here, we make explicit all the functional dependencies.

where, for two (input) monochromatic fields of equal frequency ω, the (output) polarization frequency is equal to 2ω. For materials with inversion symmetry, such as the bilayer MoS_2 studied here, this term is zero[3].

In our simulations, we apply two external fields: a static one along the z-direction and a time-dependent one in plane. The static one is included directly in the Kohn-Sham Hamiltonian, at the DFT level, while the time-dependent one is introduced to calculate the non-linear response. For the in-plane field, we choose a polarization along the y direction and the polarization is recorded in the same direction, obtaining $\chi^{(2)}_{yyy} = -\chi^{(2)}_{xxy} = -\chi^{(2)}_{yyx} = -\chi^{(2)}_{xyx} = -\chi^{(2)}_{aab}$, that is, the only non-zero component of the second-order susceptibility tensor for the hexagonal D_{3h} crystal class [207], with a and b the in-plane crystal axes. In centrosymmetric systems, $\chi^{(2)}$ is zero if no perpendicular static field is present. For each intensity of the perpendicular static field, we performed a series of real-time simulations at different frequencies ω to extract the $\chi^{(2)}(\omega)$. Finally in order to obtain a SHG signal independent of the dimension of the supercell, we rescaled the calculated $\chi^{(2)}(\omega)$ by an effective thickness of bilayer MoS_2 and monolayer WSe_2 — corresponding to half of c lattice parameter of the bulk structures.

By applying an external static electric field $\Delta\mathbf{E}_l$, an additional term contributes to the response (4.2) at 2ω:

$$P^{(2)}_i(2\omega) = \sum_{jk} \chi^{(2)}_{ijk}(-2\omega;\omega,\omega)\boldsymbol{\mathcal{E}}_j(\omega)\boldsymbol{\mathcal{E}}_k(\omega) + \frac{d\chi^{(2)}_{ijk}(\mathbf{R}(\boldsymbol{\mathcal{E}}),\boldsymbol{\mathcal{E}})}{d\boldsymbol{\mathcal{E}}_l}\Delta\boldsymbol{\mathcal{E}}_l \tag{4.3}$$

The derivative in Eq. (4.3) can be split in two terms, an electronic and a ionic one, respectively:

$$\frac{d\chi^{(2)}_{ijk}(\mathbf{R}(\boldsymbol{\mathcal{E}}),\boldsymbol{\mathcal{E}})}{d\boldsymbol{\mathcal{E}}_l} = \left.\frac{\partial\chi^{(2)}_{ijk}(\mathbf{R_0},\boldsymbol{\mathcal{E}})}{\partial\boldsymbol{\mathcal{E}}_l}\right|_{\boldsymbol{\mathcal{E}}_l=0} + \sum_{n\alpha}\left.\frac{\partial\chi^{(2)}_{ijk}(\mathbf{R},\boldsymbol{\mathcal{E}}=\mathbf{0})}{\partial\tau_{n\alpha}}\right|_{\mathbf{R}=\mathbf{R_0}}\frac{\partial\boldsymbol{\tau}_{n\alpha}}{\partial\boldsymbol{\mathcal{E}}_l} \tag{4.4}$$

where $\boldsymbol{\tau}_{n\alpha} = \mathbf{R}_{n\alpha} - \mathbf{R}_{0,n\alpha}$ represents the displacement of the atom n in the direction α. The first term in Eq. (4.4) is obtained by considering the atoms in their equilibrium positions and accounting only for the electronic contribution to the SHG induced by the external field $\Delta\boldsymbol{\mathcal{E}}_l$. The second term corresponds to the contribution to the SHG arising from the displacement of the atoms in the presence of the external field. The former term is referred to as *electric field-induced second-harmonic generation* (EFISHG) and can be expressed as a third-order polarizability:

$$\left.\frac{\partial\chi^{(2)}_{ijk}(\mathbf{R_0},\boldsymbol{\mathcal{E}})}{\partial\boldsymbol{\mathcal{E}}_l}\right|_{\boldsymbol{\mathcal{E}}_l=0} = \chi^{(3)}_{ijkl}(-2\omega;\omega,\omega,0) \tag{4.5}$$

The two terms in Eq. (4.4) can be calculated directly using the approach described, for example, in Ref. [208]. However, since our goal is to study a system under the influence of a finite field, and given the special configuration of the 2D system that allows us to directly apply a finite electric field in the z-direction, we opted to evaluate the two terms numerically. For the first term, we analyze

[3]The explanation is straightforward: since both $\mathbf{P}$ and $\boldsymbol{\mathcal{E}}$ are vectors, by inverting spatial coordinates ($\mathbf{r} \to -\mathbf{r}$), they must change sign, giving $-\mathbf{P}^{(2)}_i = \chi^{(2)}_{ijk}(-\boldsymbol{\mathcal{E}}_j)(-\boldsymbol{\mathcal{E}}_k) = \chi^{(2)}_{ijk}\boldsymbol{\mathcal{E}}_j\boldsymbol{\mathcal{E}}_k$. If inversion symmetry holds, then the two relations with inverted signs must be equal, meaning $\chi^{(2)}_{ijk} = 0$. Thus, a system with such symmetry (called *centrosymmetric*) does not naturally host SHG.

the electronic response while keeping the ions in their equilibrium positions. For the second term, we relax the atomic structure and then calculate the SHG from the distorted structure without the external field. Finally, we discuss the combined effects of both contributions.
Notably, the applied electric field does not affect the linear response of the system at any level of theory, as demonstrated in Fig. 9 of Appendix E. Although the field modifies the band structure by lifting the degeneracy of the valence and conduction bands, it does not alter the optical onset. Consequently, the intensity of the peaks remains essentially unchanged.

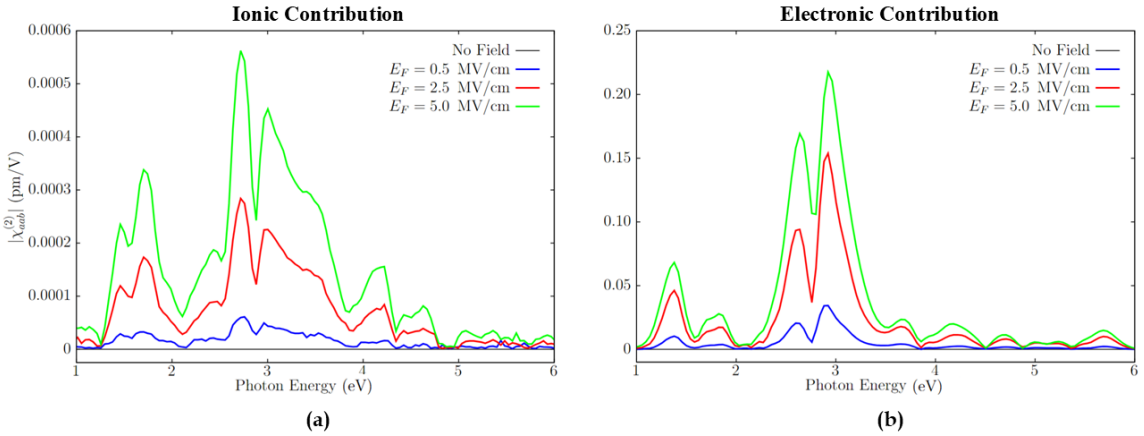

Figure 4.8: *Ionic* (***a***) *and electronic* (***b***) *contributions to the induced SHG* $\chi^{(2)}$ *in bilayer* MoS_2*. In panel* (***a***)*, we show the contribution due to the displacement of the atoms generated by the external field. Note that after atomic relaxation, the external field is turned off to consider only the ionic contribution. In panel* (***b***)*, we present the electronic contribution to the* $\chi^{(2)}$ *induced by the external electric field for frozen ions.*

Bilayer MoS_2

We begin our discussion with the case of bilayer MoS_2. In Fig. 4.8, we present the electronic and ionic contributions to the SHG induced by an external electric field along the z-direction. Panel (a) displays the electronic contribution, corresponding to the first term in Eq. 4.4, obtained without relaxing the atomic structure, while panel (b) shows the ionic contribution, which corresponds to the second term in Eq. 4.4. The results are normalized to an effective thickness, as explained in Sec. 4.2.2.
We find that the ionic contribution is relatively small compared to the electronic counterpart. This small contribution can be rationalized as follows: to induce an atomic displacement, the external electric field must first cause a change in density, which, to linear order, is proportional to $\delta\rho \propto \chi_z \boldsymbol{\mathcal{E}}_z$. However, due to depolarization effects, the response χ_z of a bilayer in the perpendicular direction is quite small, explaining the minor ionic contribution. In contrast, the electronic contribution is much larger because the electric field directly influences the construction of $\chi^{(3)}$, even without considering the induced-density effect. From these results, it is clear that the ionic contribution in this case can be considered negligible. Therefore, in the following analysis, we will use only the equilibrium geometry and exclude the ionic effect on $\chi^{(2)}$. It is important to emphasize that the

induction of SHG via an external electric field is a higher-order effect compared to the intrinsic SHG. This implies that, although the intensity can be increased by raising the amplitude of the applied field, the resultant signal remains significantly weaker. For comparison, the SHG signal in monolayer MoS_2 at the IPA level is shown in Fig. 7 of Appendix E.
In Fig. 4.9, we present the two highest peaks of the induced SHG as a function of the external field. Our observations reveal a linear dependence for small fields and a quadratic dependence at higher fields, consistent with the experimental findings reported in Ref. [192]. We also attempted to incorporate excitonic effects into the SHG response using the parameters listed in Table 4.4. However, due to the very small signal induced by the external field, the results were quite noisy, and we decided not to include them in this manuscript. Nonetheless, even from these noisy results, we are confident that excitonic effects have the potential to more than double the SHG response in these low-dimensional systems. Recently, these effects have been investigated using a simplified model for gated bilayer graphene. Despite its relatively simple excitonic structure, this model captures many of the physical effects we observed in bilayer MoS_2 [209].

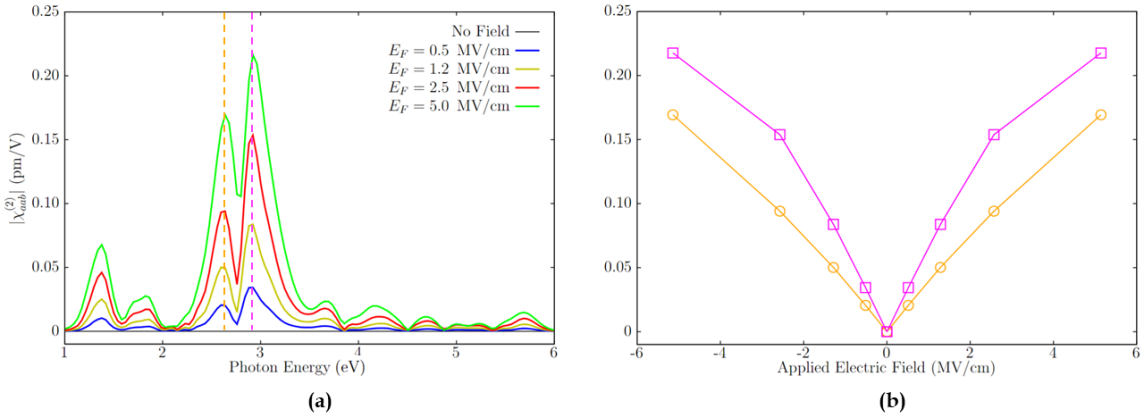

Figure 4.9: *The two highest peaks* (***b***) *of the induced SHG* (***a***) *in bilayer MoS_2 as a function of the external field.*

4.2.4 Induced Doping

Doping a material can significantly alter its optical response in several ways. First, doping affects the electronic structure, such as causing the electronic band gap to narrow. Local or semi-local functionals often do not adequately capture this effect; instead, GW-type corrections are necessary. These corrections directly depend on doping due to changes in the dielectric constant, which influences the definition of W (see Sec. 3.3). Specifically, doping increases screening, which reduces W and causes a reduction of the GW corrections [210]. This electronic gap reduction has been observed in various experiments [211]. Additionally, doping impacts the atomic structure by altering bonding and lattice constants. However, these effects are not considered here because they depend on the substrate, which is not included in the present calculations.
Beyond gap reduction, doping induces other changes in the optical response. The e-h interaction, which depends on $\varepsilon(\omega)$, is reduced, but this effect is offset by the gap shrinking. Consequently,

the exciton peak position remains nearly constant for small doping levels, while its intensity decreases [212]. At higher doping densities, this compensation fails, and the exciton peak position increases linearly with energy. Doping also affects the availability of e-h transition channels due to partial filling (or emptying) of conduction (or valence) bands, leading to the *Pauli blocking effect*, which is significant for the lowest excitons. Furthermore, in doped systems, dynamic effects and the formation of trions can become important. However, our current real-time dynamics approach does not account for these effects; for a discussion, see Refs. [212, 213].
In summary, our real-time approach will only consider doping effects through changes in the dielectric constant, as the dynamical Berry phase approach is not applicable to metal systems, and we have not included diagrams corresponding to trions. Ultimately, we will account for doping effects solely through the change in the dielectric constant that influences the SEX self-energy, which is responsible for exciton formation in our real-time dynamics:

$$\Sigma_{\mathrm{SEX}}[\Delta\gamma](\mathbf{r},\mathbf{r}',t) = W(\mathbf{r},\mathbf{r}')\,\Delta\gamma(\mathbf{r},\mathbf{r}',t) \tag{4.6}$$

$$W(\mathbf{r},\mathbf{r}') = \varepsilon^{-1}(\omega=0)\,v(\mathbf{r}-\mathbf{r}') \tag{4.7}$$

For each doping level, the screened interaction W is recalculated, then the self-energy Σ_{SEX}, and the real-time dynamics, to determine the corresponding SHG response, is performed. Note that the change in W induces a small shift in the exciton position, which in principle should be offset by the shrinking of the gap. However, since we employed a rigid shift approximation, this compensation does not occur. Nonetheless, our primary focus is on studying the changes in the SHG intensity, and this positional shift is generally negligible in the final results. A detailed discussion of this is provided in the next section.

Monolayer WSe_2

The monolayer WSe_2 lacks inversion symmetry and therefore exhibits a SHG signal even in the absence of an external electric field. However, recent studies have explored the possibility of tuning the SHG signal through induced doping. In its optical response, WSe_2 exhibits prominent bright exciton peaks that have been extensively studied both theoretically and experimentally (see Ref. [214] and references therein). The SHG response is maximized at frequencies resonant with the exciton peaks or at half of their energies. The lowest bright exciton peak in the linear response, known as the A-exciton, appears around 1.65 eV and is also observable in SHG at half this energy. Using a field-effect transistor, researchers were able to modify the intensity of the excitonic A-resonance in SHG response, by several orders of magnitude [195].
Indeed, as explained in the previous section, doping introduces two primary effects on the nonlinear response: first, the occupation of certain conduction (or valence) bands by electrons (or holes) makes these levels unavailable for valence-conduction transitions, leading to the so-called Pauli blocking effect [215]; second, doping increases the screening of the electron-electron interaction, which reduces the energy of the excitonic resonances. This latter effect can also be achieved by depositing the material on different substrates—metallic, semiconductor, or insulator—thereby altering the material dielectric screening.
Here we focus solely on the effect of doping on the dielectric constant, as our real-time formulation based on the dynamical Berry phase formalism, does not allow to treat metallic ground states. By

comparing our results with experimental data, we aim to understand the relative importance of this effect compared to others and to estimate how a substrate that modifies the dielectric response might influence the SHG spectrum.

To simulate doping, we introduced additional electron (hole) carriers along with a neutralizing uniform background charge. Specifically, we added a net charge doping of $\approx \pm 0.05e$, corresponding to a charge density of $\pm 5 \times 10^{13}$ e/cm^2, where e is the elementary electric charge. We observed only a minor change at the DFT level, and the dielectric constant is only slightly affected by the doping. However, as we will demonstrate below, these small changes are sufficient to significantly alter the SHG response.

In Fig. 4.10, we present results for three cases: undoped, positively doped with $n = 0.05e$ (holes), and negatively doped with $n = -0.05e$ (electrons). We consider these extreme doping cases that could be realized in a field-effect configuration, with intermediate doping values expected to fall between these extremes. Our findings indicate that doping can enhance the SHG response at the A-resonance in WSe_2 by up to 25% of its intensity. This is significantly less than the order of magnitude reduction observed experimentally [215], suggesting that other effects, such as Pauli blocking, play a crucial role in the observed reduction. This is expected since A excitons are the lowest energy states and are most affected by doping. Additionally, experiments have shown that some of the intensity may be transferred to positively and negatively charged trions, which have not been included in our calculations.

Finally, we note that our calculations show a very tiny shift in the exciton position with doping, which is not observed at experimental level. This discrepancy arises because we used a rigid shift for the QP structure. Ab initio calculations would account for this effect [212], as explained in the previous section.

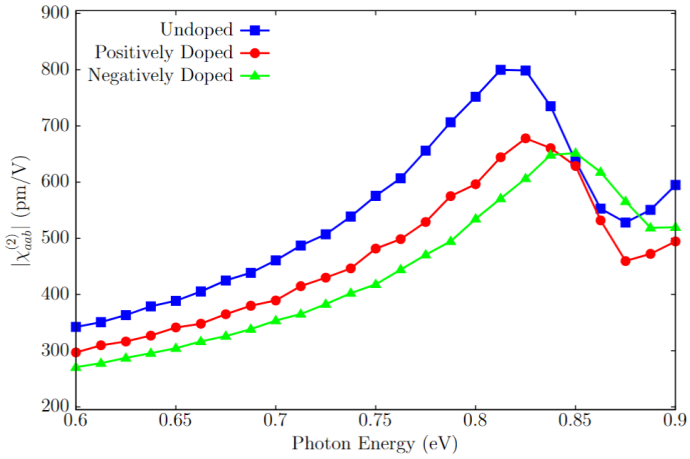

Figure 4.10: *SHG in WSe_2 for the pristine undoped, positively doped with $n = 0.05e$ (holes), and negatively doped with $n = -0.05e$ (electrons) cases. Doping modifies the screened interaction W, Eq. (4.7) that enters in Eq. (30) of Appendix C.*

4.2.5 Conclusions

In conclusion, this work presents an ab initio study of two strategies for tuning the SHG response in 2D systems. In the first case, we investigated a system with no intrinsic SHG due to the presence of inversion symmetry. An external field can induce an SHG response, which remains very weak compared to the intrinsic response of a 2D system. For this case, we found that the ionic contribution is negligible, while excitonic effects have the potential to enhance the SHG response. In the second case, we examined a system with an intrinsic SHG response and explored how doping affects its environment. We demonstrated that changing the dielectric constant can reduce the excitonic peak response up to 20%. This effect could be observed in TMD deposied on metalic substrates or in TMD/graphene heterostructures [216], which also suppresses responses from charged excitons. When we compare our result with the measurements of K. L. Seyler et al. [195], they find a reduction in the SHG response at excitonic resonance of more than 80%. However, for a correct comparison other effects should be taken into account such as Pauli blocking and the transfer of part of the spectral weight to the trions. These effects could be excluded by using heterostructure that generate a remote carrier screening without induce a charge on the material [217]. Overall, our findings illustrate how 2D materials can be employed for nonlinear optical switching. This work demonstrates the feasibility of fully ab initio simulations for predicting nonlinear optical responses in 2D materials.
The results of this study is presented in an article published during my PhD [218].

Chapter 5

Results and Discussions One-Dimensional Materials

The rapid advancements in nanotechnology have sparked increasing interest in one-dimensional (1D) materials due to their unique physical properties and potential for downscaling in next-generation electronic devices. Moreover, 1D systems give rise to fascinating phenomena such as the emergence of charge-density waves [219, 220], Luttinger liquid behavior [221–223], and exciton condensation [224].

Carbon nanotubes (CNTs) have long been emblematic of this pursuit, demonstrating remarkable properties that position them as key building blocks for nanoscale electronics [225–229]. However, managing CNT chirality, and thus their metallic, insulating, or semiconducting properties, presents significant challenges that hinder their seamless integration into scalable applications. Despite these difficulties, 1D materials remain highly compelling as pathways to extremely downscaled electronic components [230, 231], as well as excellent candidates for flexible electronics [232, 233].

In recent years, more complex techniques have enabled the growth of ultrathin nanowires. For instance, multi-walled carbon nanotubes (MWCNTs) have been used to confine the growth of 1D transition metal trichalcogenides (TMTCs), as $HfSe_3$, within their cavities [234, 235]. Single-atom chains have also been realized through encapsulation inside single-walled carbon nanotubes (SWCNTs) [236].

An alternative approach to obtaining freestanding nanowires with diameters of only a few atoms is through directed-agent synthesis [237, 238]. This method has successfully produced Cu-S inorganic core wires with a cross-section of only three atoms, representing the smallest freestanding inorganic nanowires to date [237]. In addition, several techniques for growing 1D nanowires on suitable substrates have emerged [239–245]. The substrate interactions help stabilize the 1D wires, though they may also alter the intrinsic 1D properties of the material [246, 247].

5.1 Exfoliable 1D Semiconducting Materials from High-Throughput Screening

5.1.1 Introduction

Discovering novel 1D systems has proven of great scientific interest over the past few years. A promising new approach for isolating single nanowires involves three-dimensional crystals, where strongly intra-chain bonded inorganic wires are held together by weak vdW interactions [248, 249]. In these materials, individual 1D wires are weakly coupled by interchain forces, forming highly anisotropic 3D systems. The wires can potentially be exfoliated from the bulk using mechanical or chemical exfoliation [230, 231, 250, 251], similar to the exfoliation techniques used for 2D materials, suitable for mass production. Exfoliated atomic wires have great potential for scaled electronics due to their lack of edge scattering [248, 249]. Unlike CNTs, exfoliated 1D wires would have well-defined, reproducible electronic properties. These wires could also prove highly beneficial for photovoltaic applications. Their chain-like structure has no dangling bonds along the orthogonal direction, minimizing recombination losses. This is particularly advantageous in materials like BiSI, BiSeI, Sb_2Se_3, and Bi_2Se_3, which are promising candidates for high-efficiency solar cells [252, 253]. One notable example is the recent exfoliation of $TaSe_3$ into nanowires or bundles as thin as 7 nm in lateral dimension [230, 254, 255]. $TaSe_3$ has undergone chemical and mechanical exfoliation, akin to the techniques used for graphene and MX_2 materials, to reduce the lateral dimensions of the bundles. Other materials, such as $ZrTe_3$, $HfSe_3$, MoI_3 and TiS_3 have also been successfully exfoliated from their vdW crystals using various techniques [231, 251, 256, 257].

High-throughput (HT) materials discovery is an exceptionally powerful tool that allows for the determination of the properties and functionalities of a vast number of materials from first principles, using significantly less time and resources compared to experimental studies. HT studies have already identified a broad range of promising 2D materials suitable for exfoliation into atomically thin layers [258–265], and applying similar approaches to identify new atomic wires is an emerging area of research [266–269]. In recent decades, 1D systems have received significantly less attention compared to their 2D counterparts. The extension of 2D data mining algorithms to identify 1D systems was first conducted in Refs. [261, 264]. In both cases, weakly-bonded subunits of one-, two-, or even mixed-dimensionality were identified, demonstrating the power of high-throughput studies. Currently, these databases contain around 500 exfoliable 1D wires, with the number expected to grow significantly due to element substitution and recent advancements in machine learning methods [269, 270]. The rapid development of HT searches for 1D materials suggests that this is an exciting and emerging field with vast potential.

In this context, Cignarella et al. [271] performed a high-throughput screening of experimentally known compounds, building a database of over 800 1D systems that could be exfoliated from known 3D vdW crystals. The three-dimensional materials used as the starting point for the screening were sourced from three databases: the Crystallographic Open Database (COD) [272], the Inorganic Crystal Structure Database (ICSD) [273–275], and the Pauling File [276], comprising a total of 782,632 compounds. All the structures considered were experimentally reported in their 3D forms. These 815 systems were then optimized in their isolated 1D form using DFT, and their basic properties, such as band structures, were characterized. Finally, the dynamical stability of all structures was assessed by calculating their phonon dispersions.

In the search for building blocks for downscaled electronic devices, we identify, drawing from the above database, novel exfoliable atomic wires that are mechanically stable against common in-

stabilities, offering great promise for future applications. Here, we characterize some of the most promising candidates, investigating their electronic and optical properties at the DFT and MBPT level, with a focus on potential optoelectronic applications.

5.1.2 Methods

In this study, DFT and MBPT calculations were performed to investigate the electronic and optical properties of four different 1D materials (S_3, Te_3 As_2S_3, Bi_2Te_3)[1], selected for their mechanical stability and optimal DFT bandgap. For the DFT part, the QE integrated suite [22, 23] was used. To account for SOC and include semi-core electrons, a norm-conserving, fully-relativistic pseudopotential from the PseudoDojo repository (v0.4) [157] was employed, using GGA-PBE XC functional [155]. Upon convergence, kinetic energy cutoffs of 110 (S_3), 70 (Te_3), 80 (As_2S_3) and 100 (Bi_2Te_3) Ry were chosen. A uniform Monkhorst-Pack **k**-point mesh with dimension of $1 \times 1 \times 12$ was employed. To prevent interaction between periodic replicas, a minimum vacuum region of 16 Å along the non-periodic (xy) directions was introduced. Structural relaxation was considered converged when the maximum component of the residual ionic forces dropped below 10^{-8} Ry/Bohr. From the obtained DFT eigenvalues and eigenvectors, MBPT calculations were carried out, using the YAMBO code [48, 49], specifically using the G_0W_0 and eigenvalue self-consistent GW (evGW) methods for QP corrections and the BSE [158–161] for e-h interaction. These calculations allowed to account for many-body effects and accurately describe the electronic and optical properties of the materials. Energy cutoffs of 47899, 77897, 59075, and 47115 number of G-vectors were used for the exchange part of the self-energy Σ_x, while 12, 12, 20, and 12 Ry were used for the correlation part of the self-energy Σ_c, respectively for S_3, Te_3, As_2S_3 and Bi_2Te_3. Additionally, 1582 (S_3), 1402 (Te_3), 1452 (As_2S_3) and 622 (Bi_2Te_3) empty bands [2] were included in the calculation of the Σ_c. A cylindrical cutoff to the Coulomb potential along the non-periodic directions (xy) was used, as implemented in the YAMBO code [49]. For the BSE Hamiltonian, a total of 12 occupied states and 8 unoccupied states (S_3), 12 and 12 (Te_3), 14 and 12 (As_2S_3), and 8 and 8 (Bi_2Te_3) were employed. The convergence with respect to the **k**-points for the BSE calculations was carefully checked, and the following **k**-point grids were used: $1\times1\times48$ (S_3, Te_3, As_2S_3) and $1\times1\times84$ (Bi_2Te_3).

5.1.3 Structural Properties

The 1D materials presented here (Fig. 5.1) were identified from a HT screening database [271], as described in Sec. 5.1. The screening provided preliminary DFT calculations, including phonon dispersion, relaxation, and band structure. After a first selection, each material underwent an additional full-structure relaxation to obtain optimized lattice parameters and atomic positions using the chosen XC functional. These values are reported in Table 5.1. The structures of S_3 (Fig. 5.1a) and Te_3 (Fig. 5.1b) both consist of a chiral helical chain composed of three atoms, arranged so that the projection of the chain onto a plane forms an equilateral triangle. Such structure is typical of chalcogen elements, even for higher dimensions (see Sec. 4.1). The unit cell of As_2S_3 (Fig. 5.1c) consists of two As atoms and three S atoms, which are alternately bonded to

[1] The nomenclature used corresponds to the number of atoms of each atomic species in the unit cell.

[2] Convergence with respect to empty states has been proven to be a critical factor in 1D systems. For further details, we refer the reader to Appendix F.

form a network of non-planar hexagons. Additionally, there is an extra S atom attached to each hexagon (through an As atom), protruding towards its center. The structure of Bi_2Te_3 (Fig. 5.1d) is specular to that of As_2S_3, Bi and Te replacing As and S, respectively.

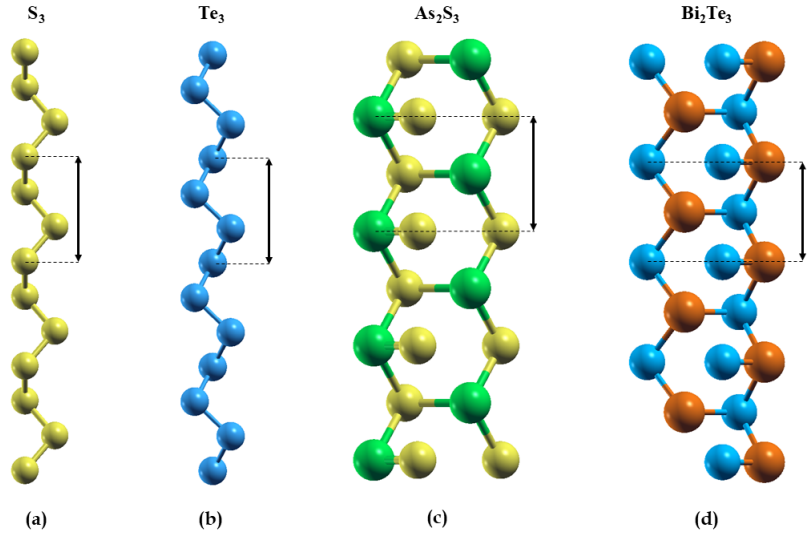

Figure 5.1: *Optimized geometric structures of* (**a**) S_3, (**b**) Te_3, (**c**) As_2S_3 *and* (**d**) Bi_2Te_3. *The optimized lattice parameters are also displayed. Credits to [271] for the structures provided.*

Table 5.1: *Optimized lattice parameter* (a) *of the different systems studied, obtained by full-structure relaxation using a GGA-PBE XC functional.*

	$\mathbf{S_3}$	$\mathbf{Te_3}$	$\mathbf{As_2S_3}$	$\mathbf{Bi_2Te_3}$
a (Å)	4.414	5.697	3.540	4.342

5.1.4 Electronic Properties

In this section, we analyze the band structures of the four different materials under study, first obtained at the DFT level and then refined using *GW* corrections. Given their dimensionality, these materials exhibit exceptionally flat bands, which may harbor a range of exotic properties yet to be investigated, while this also complicates the clear identification of the electronic band gap. The DFT band structures are shown in Fig. 5.2, and the corresponding band gaps are listed in Table 5.2. S_3 is an indirect-gap semiconductor wire with an estimated electronic gap of 2.66 eV (Fig. 5.2a). The CBM is located at the high-symmetry Z point, while the VBM is located between the Γ and Z points of the SOC-split flat valence band. The band structure of Te_3 shows many similarities to that of S_3. It is indeed an indirect-gap semiconductor with an estimated electronic gap of 1.43 eV (Fig. 5.2b). Both the VBM and the CBM are located near the high-symmetry Z

point. The smallest direct electronic gap is only 40 meV greater and it is located close to the Z point. As_2S_3 and Bi_2Te_3 exhibit similar structures and band structures, and both are significantly influenced by SOC. As_2S_3 is an indirect-gap semiconductor with an electronic band gap of 1.16 eV (Fig. 5.2c). In this material, the CBM is located at the Γ point, while the VBM is situated between the Γ and Z points. In contrast, Bi_2Te_3 is a nearly-direct narrow-gap semiconductor with an electronic band gap of 0.419 eV (Fig. 5.2d). Here, the VBM is located at the Γ point, and the CBM is very close to the Γ point. Indeed, the direct band gap at Γ is only 2 meV larger than the indirect band gap.

Starting from the DFT eigenstates and eigenvalues, the QP-corrected bands were calculated. It is important to note that these calculations were significantly affected by the strong dependence of the empty states on the cell vacuum, which hindered the convergence of most key quantities in MBPT. For further details, refer to Appendix F.

The extremely low screening in 1D systems necessitates the use of a methodology similar to that used for isolated systems. To address this, single-shot G_0W_0 calculations were followed by eigenvalue self-consistent calculations on both G and W (referred to as evGW). The details of this approach are discussed in Sec. 3.6.3, and the results are presented in Table 5.2. In S_3, the gap is corrected to 5.46 (G_0W_0) and then to 6.26 eV (evGW). In Te_3, the gap increases from 3.47 (G_0W_0) to 4.27 eV (evGW). In As_2S_3, from 2.28 (G_0W_0) to 3.07 eV (evGW). Finally, in Bi_2Te_3, from 1.42 (G_0W_0) to 1.64 eV (evGW). Remarkably, in this case the electronic band gap undergoes an indirect-to-direct transition, as the QP correction at Γ ends up to be higher than the ones at neighboring **k**-points.

In the next section, we will discuss the absorption spectra of these materials, based on the QP states corrected by the GW approximation, as calculated at the BSE level.

Table 5.2: *Calculated lowest direct* (d) *or indirect* (i) *electronic band gaps* (E_g)*, at the DFT,* G_0W_0 *and* evGW_g *level, together with the BSE optical gaps* (E_o) *and the corresponding binding energies* (E_b) *of the lowest bright exciton. In the case of indirect band gap, the corresponding direct band gap is also reported in square brackets. SOC was included.*

	E_g^{DFT}	$E_g^{G_0W_0}$	$E_o^{G_0W_0+\mathrm{BSE}}$	$E_b^{G_0W_0+\mathrm{BSE}}$	$E_g^{\mathrm{ev}GW}$	$E_o^{\mathrm{ev}GW+\mathrm{BSE}}$	$E_b^{\mathrm{ev}GW+\mathrm{BSE}}$
$\mathbf{S_3}$	2.66 (i) [2.76]	5.46 (i) [5.55]	3.61	1.94	6.26 (i) [6.35]	4.06	2.29
$\mathbf{Te_3}$	1.43 (i) [1.47]	3.47 (i) [3.51]	1.38	2.13	4.27 (i) [4.31]	2.15	2.16
$\mathbf{As_2S_3}$	1.16 (i) [1.26]	2.28 (i) [2.32]	1.43	0.89	3.01 (i) [3.07]	2.62	0.45
$\mathbf{Bi_2Te_3}$	0.419 (i) [0.421]	1.42 (d)	0.66	0.76	1.64 (d)	0.81	0.83

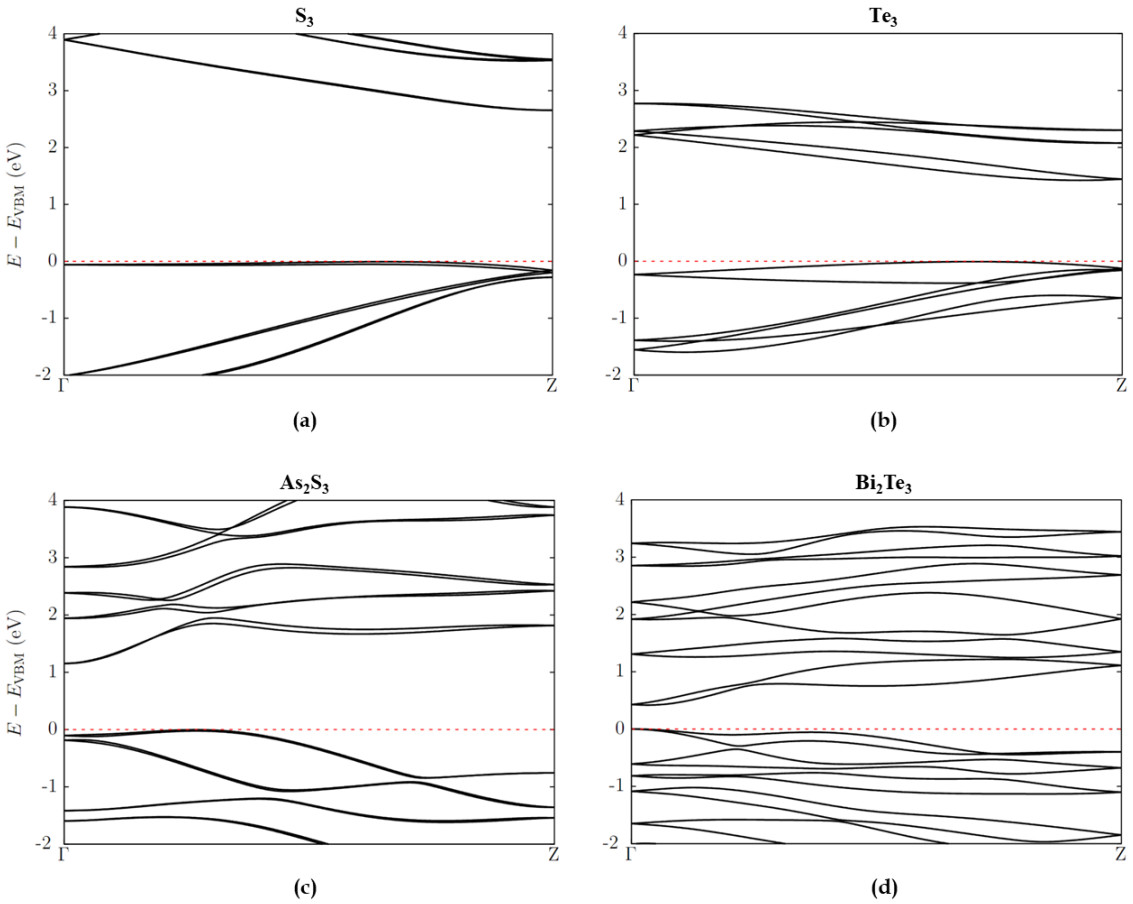

Figure 5.2: *Electronic band structures of* (**a**) S_3, (**b**) Te_3, (**c**) As_2S_3 *and* (**d**) Bi_2Te_3, *calculated at the DFT level, using a GGA-PBE XC functional. SOC was included. The energies were rescaled with respect to the VBM. The zero level is highlighted with a red dotted line.*

5.1.5 Optical Properties

Low screening in low-dimensional systems, and particularly in 1D materials, plays a crucial role in enhancing excitonic effects, which are prominent in the optical absorption spectra of such materials. Due to the reduced dimensionality, electrons and holes experience stronger Coulomb interactions, as screening is less effective in 1D compared to bulk systems. This leads to the formation of tightly bound excitons with large binding energies, significantly influencing the optical properties. The absorption spectra, calculated at the BSE level using evGW-corrected QP states, are presented in Fig. 5.4. For comparison, the spectra derived from G_0W_0-corrected states are shown in Fig. 5.3. Overall, the effect of self-consistency leads to a blueshift in the optical spectra, without altering the underlying transitions. Thus, for the sake of brevity, we focus our discussion on the evGW+BSE spectra. The corresponding optical band gaps are reported in Table 5.2, together with the relative

binding energies of lowest bright excitons.

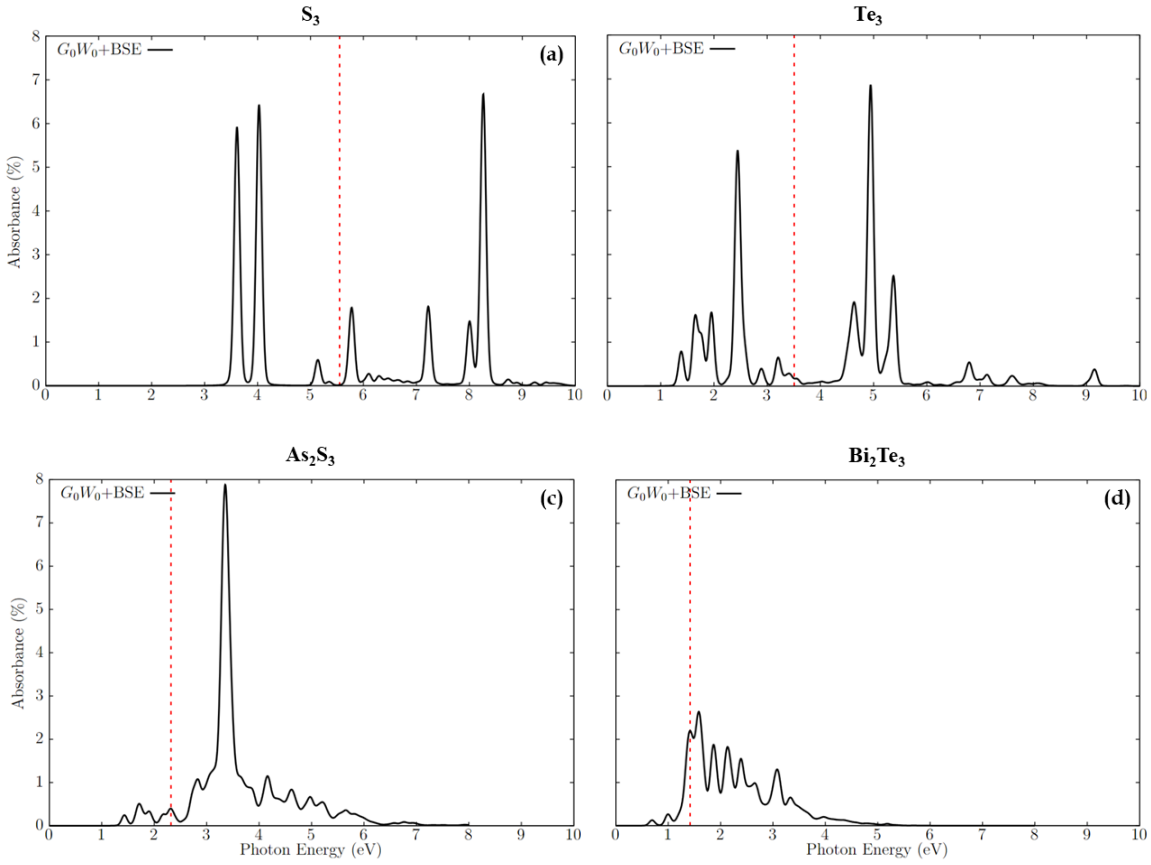

Figure 5.3: *Absorption spectra* (*solid black*) *of* (**a**) S_3, (**b**) Te_3, (**c**) As_2S_3 *and* (**d**) Bi_2Te_3, *expressed in terms of percentage of the optical absorbance* $A(\omega)$, *calculated at the* G_0W_0+*BSE level. SOC was included. The corresponding* G_0W_0*-corrected direct electronic band gaps* (*dashed red*) *are shown as a reference. A broadening of 50 meV was used.*

As shown in Fig. 5.4, for S_3 and Te_3, the spectra consist of a series of transitions that are relatively well-separated in energy, resembling what one might expect from an isolated system. Similar to such systems, the lowest energy excitations, located in the near UV (S_3) and in the visible (Te_3) range, exhibit a significant binding energy (around 2 eV), indicating the highly localized nature of the corresponding excitonic wavefunction. This is confirmed by the plot of the excitonic wavefunctions displayed in Fig. 5.5a and b. In S_3 (Fig. 5.3a), two prominent excitations appear below the direct bandgap (6.35 eV), followed by two smaller peaks. The first excitonic peak occurs at 4.06 eV, with a binding energy of 2.29 eV, and marks the onset of optical absorption. The corresponding excitonic wavefunction is depicted in Fig. 5.3a, exhibiting a localized character. It arises from transitions

involving the first three (degenerate) occupied bands and the (doubly-degenerate) conduction band, at the Γ point. The second peak (4.51 eV) stems from transitions involving the doubly-degenerate valence band and the doubly degenerate second conduction band at the Γ point. The two smaller peaks near the gap (at 5.89 and 6.17 eV) are also localized at the Γ point and primarily involve transitions from lower occupied bands to higher unoccupied bands. In this case, the first dark excitation occurs at 3.05 eV. Regarding Te_3 (Fig. 5.3b), the optical spectrum consists (up to 10 eV) of distinct sharp peaks, with several excitations below the band gap. The first bright exciton appears at 2.15 eV, approximately 2.16 eV below the material's direct electronic band gap (4.31 eV), which corresponds to the lowest (bright) exciton binding energy. The related excitonic wavefunction, illustrated in Fig. 5.5b, extending across five unit cells in the periodic direction. Not surprisingly, this excitonic wavefunction is very similar to that of S_3. The transitions contributing to this peak involve the fourth valence band and the second empty band near the Z point.

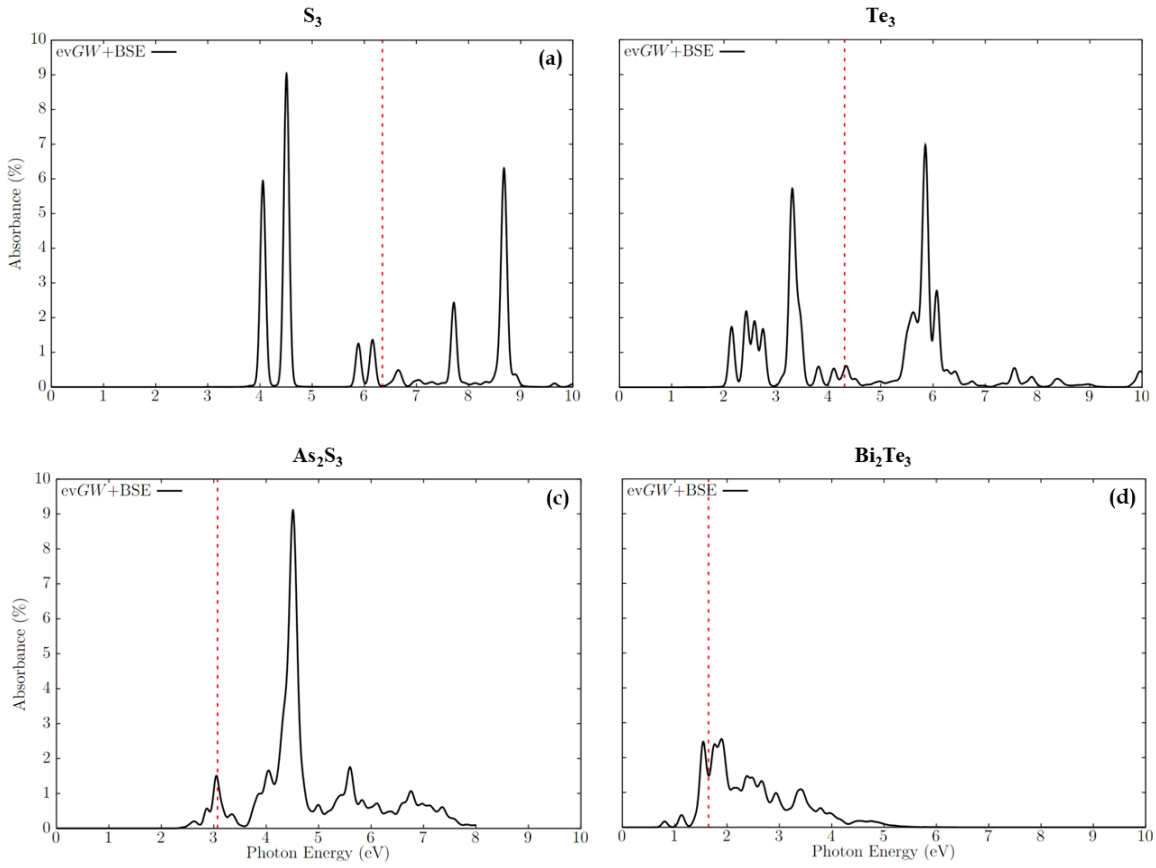

Figure 5.4: *Absorption spectra (solid black) of* (**a**) S_3, (**b**) Te_3, (**c**) As_2S_3 *and* (**d**) Bi_2Te_3, *expressed in terms of percentage of the optical absorbance* $A(\omega)$, *calculated at the* evGW+*BSE level. SOC was included. The corresponding* evGW*-corrected direct electronic band gaps (dashed red) are shown as a reference. A broadening of 50 meV was used.*

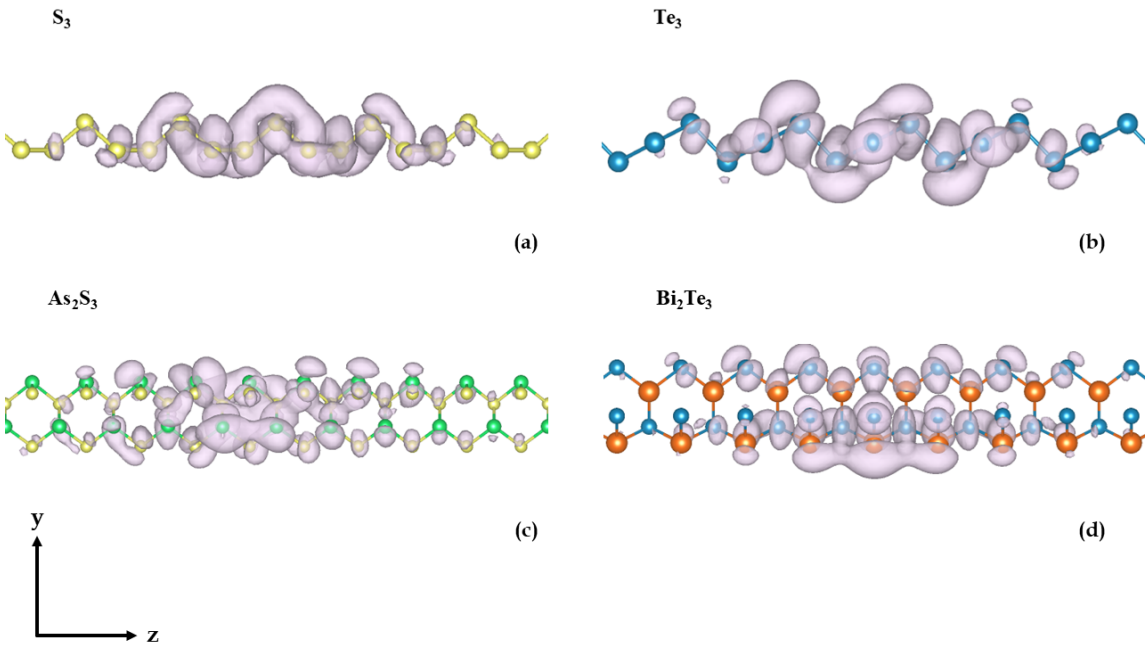

Figure 5.5: *Excitonic wavefunction plots in direct space for*(**a**) S_3, (**b**) Te_3, (**c**) As_2S_3 *and* (**d**) Bi_2Te_3, *calculated using the YAMBO code. The position of the hole was chosen based on the localization of the valence electrons contributing to the exciton. The number of cell repetitions in the periodic direction was increased until the wavefunction decayed to zero.*

Interestingly, the excitations involving transitions between the valence band and the conduction band — starting with the first at 1.83 eV — are mostly dark, meaning no optical absorption occurs around the band gap energy. The only exception is the most intense excitonic peak below the gap, around 3.3 eV, which has minor contributions stemming from these bands.
In contrast to the first two cases, the spectra of As_2S_3 and Bi_2Te_3 resemble a continuum of transitions, similar to those observed in most periodic systems. Also, these materials exhibit low binding energies (< 1 eV), resulting in a more delocalized excitonic wavefunction, as shown in Fig. 5.3c and d. In As_2S_3 (Fig. 5.3c), two excitations appears below the gap (3.07 eV) which represent the optical onset[3]. Occurring at 2.62 and 2.87 eV, these two excitations fall within the blue region of the visible spectrum and exhibit small binding energies of 0.45 and 0.2 eV, respectively. The first one arises from transitions involving the first two doubly degenerate occupied bands, primarily at **k**-points near Γ, and the first two doubly degenerate unoccupied bands. The corresponding excitonic wavefunction (Fig. 5.3c) is highly delocalized, extending over 9 unit cells. Similarly, the second excitation involves transitions between the first two doubly degenerate occupied bands and the first three doubly degenerate unoccupied bands at the Γ point. In this case, the first dark excitation occurs at 1.73 eV. Finally, in Bi_2Te_3 (Fig. 5.3d) the excitations below the gap (1.64 eV) are composed of several transitions, the lowest occurring at 0.81 eV, thus in the near IR region. This

[3]From the diagonalization of the BSE Hamiltonian, we identified three low-lying excitonic states with non-zero (but negligible) oscillator strengths. As a result, we chose not to include these states in the discussion.

gives a binding energy of 0.83 eV, which is again significantly lower than the previous two materials. Indeed, the corresponding excitonic wavefunction (Fig. 5.3d) displays a very delocalized character. This first excitation, as well as the others below the gap, arises from transitions involving the the (doubly-degenerate) valence band and the (doubly-degenerate) conduction band, in an extended with very small dispersion nearby Γ. The first dark excitation occurs at 0.77 eV.

5.1.6 Conclusions

In this study, we present a novel ab initio investigation of real 1D materials, identified through HT screening of a database of potentially exfoliable atomic wires. We explored the electronic and optical properties of four promising 1D materials — S_3, Te_3, As_2S_3, and Bi_2Te_3 — using DFT and MBPT, including *GW* corrections and BSE calculations. These materials exhibit unique band structures with flat bands and substantial band gap separations, indicating potential for exotic electronic phenomena. S_3 and Te_3 show significant exciton binding energies, indicative of highly localized excitonic states, while As_2S_3 and Bi_2Te_3 exhibit a continuum of transitions with smaller binding energies.
Given these properties, S_3 and Te_3 are promising candidates for optoelectronic applications, particularly in UV- and visible-absorption devices due to their strong excitonic effects. The lower exciton binding energies and broader absorption spectra of As_2S_3 and Bi_2Te_3 make them suitable for photovoltaic and infrared applications. These findings suggest that exfoliable 1D wires could be key materials for future nanoscale electronic and optoelectronic technologies.
The results of this study will be the subject of a future publication.

Chapter 6

Results and Discussions Zero-Dimensional Materials

Zero-dimensional (0D) materials, such as quantum dots, nanoclusters, and molecules, have emerged as a significant class of nanomaterials due to their unique electronic and optical properties. In these materials, all three spatial dimensions are confined to the nanoscale, typically less than 10 nm, leading to a discrete energy level structure rather than the continuous band structure seen in periodic materials.
In 0D materials, the quantum confinement effect plays a central role in their electronic and optical properties. When the size of a material — in one or more directions — approaches the order of magnitude of the de Broglie wavelength of the electrons (or holes), their movement becomes restricted, leading to the quantization of energy levels. This effect causes the material's electronic and optical properties to depend strongly on the particle size. For instance:

- The energy gap increases as the size of the 0D material decreases, resulting in tunable electrical characteristics.
- The absorption and emission spectra are size-dependent. Smaller particles exhibit blue-shifted optical spectra, while larger particles exhibit red-shifts.

The electronic properties of 0D materials are largely governed by their confined geometry. As mentioned, the quantum confinement leads to a discrete set of energy levels, which mimics the behavior of atoms. Electrons can only occupy specific energy states, making these materials highly tunable for electronic applications. These discrete energy levels result in sharp absorption and emission peaks, unlike the broader spectra observed in bulk materials. This property is useful for applications in light-emitting diodes (LEDs) and lasers. The interaction between electrons and holes, forming excitons, plays a key role in determining the optical response. In 0D materials, the exciton binding energy increases significantly due to spatial confinement, leading to enhanced excitonic effects that are observable even at room temperature.
The unique combination of electronic and optical properties of 0D materials makes them highly versatile in a range of advanced technological applications, from optoelectronic devices to quantum information technologies [277–280]. The continued exploration of the behavior of 0D materials promises to drive advances in nanotechnology, providing new insights into fundamental physics as

well as practical innovations in industry and medicine.

6.1 Tunable Electric-Field-Driven Terahertz Splitting in Polyyne C_{18} Carbon Ring

6.1.1 Introduction

The terahertz (THz) range, often referred to as the "terahertz gap", bridges the gap between microwave and infrared frequencies in the electromagnetic spectrum, boasting a wealth of portable, affordable, coherent sources and detectors that can operate at room temperature [281, 282]. Operating in the frequency range of approximately 0.1 to 10 THz, this technology is known for its unique capabilities, including high-resolution imaging and spectroscopy. THz radiation, with wavelengths ranging from millimeters to sub-millimeters, can penetrate a variety of materials, providing valuable insights in fields such as security screening, material science, and medical diagnostics.
One approach to addressing this THz gap is through low-dimensional carbon structures [283]. Carbon, one of the most abundant elements in nature, is renowned for its ability to form a wide variety of allotropes. Carbon atoms can form multiple covalent bonds with other elements, leading to a diverse range of structures and compounds. This versatility results in a broad spectrum of properties and applications. In recent decades, new carbon allotropes have been discovered, sparking new fields of basic research and practical applications. Notable examples include fullerenes [284], carbon nanotubes [225], and graphene [285]. Another interesting form of carbon allotropy is the long linear carbon chains [286]. These chains are categorized as *cumulene* when composed of a sequence of double bonds of equal length, or as *polyyne* when they feature alternating short (triple) and long (single) bonds [287]. When carbon atoms form a closed cyclic chain, it is referred to as *cyclo*[*n*]*carbon* (CC), which can also adopt either a polyyne or cumulene form [288–291]. Unlike conjugated π-bond systems like fullerenes, nanotubes, or graphene, which have a coordination number of three, CC allotrope has a coordination number of two.
In recent years many experimental studies were conducted to observe carbon rings. Despite their apparent simplicity, these systems present significant challenges from both synthetic and theoretical perspectives. One of the most significant recent achievements is the successful synthesis and characterization of the closed-circle polyyne containing 18 sp-hybridized carbon atoms, known as cyclo[18]carbon (C_{18}). Kaiser et al. [292, 293] characterized C_{18} using high-resolution AFM. Their AFM study, corroborated by computational simulations, confirmed the polyynic (D_{9h}) structure of C_{18} adsorbed on a bilayer NaCl on a Cu(111) surface at 5 K [294]. The synthesis of C_{18} has opened new avenues for research, and understanding the electronic structure of this material is crucial for elucidating its properties and interactions [295, 296].
Prior to this experiment, there was significant theoretical debate regarding the most stable structure of C_{18}[1]. Numerous electronic structure calculations of C_{18} have been conducted at various levels of theory. These include HF [301–303], Self-Consistent Field (SCF) [288, 304, 305], Multi-configurational SCF (MCSCF) [290], Møller-Plesset Perturbation Theory (MP2) [304, 305], DFT [287, 289, 291, 303, 304, 306–313], Coupled Cluster with Single and Double excitations (CCSD) [288, 291], and Quantum Monte Carlo (QMC) [290]. However, only HF, QMC, and CCSD meth-

[1] Calculations have predicted the ground-state structure of C_6 [297–299] and C_{10} [299, 300]. However, for higher members of the C_{4n+2} series, theoretical results remain contradictory.

ods are able to successfully predict the polyyne structure as the ground state. Indeed, even most common DFT hybrid functionals (such as B3LYP, BLYP, and PBE0) predict the non-bond-length alternating cumulene structure as ground state geometry for C_{18}. Many studies [290, 294, 311–313] attribute the failure of DFT to its overestimation of electronic correlation effects at the expense of exchange energy, demonstrating that increasing the HF exchange component in an XC functional tends to stabilize the polyyne structure over the cumulenic one[2], leading to the experimentally observed structure of C_{18}.
Since the first synthesis in 1989 [301], CCs have drawn particular attention due to the competing many-body effects of Hückel aromaticity[3], the second-order Jahn-Teller effect (SOJTE), and Peierls instability at larger sizes. These effects lead to possible ground-state structures with aromatic, bond-angle, or bond-length alternated geometries. Notably, odd- and even-dimer rings have been shown to alternate in their relative stability [306, 314–316]. For instance, in C_{4n+2} rings, the SOJTE causes the single-triple bond alternation typical of the polyyne structure [317]. In these rings, the SOJTE can lead to spontaneous symmetry breaking, removing degeneracy and creating an intrinsic gap between previously degenerate levels.
THz radiation generation can occur by lifting energy level degeneracy in semiconducting quantum rings via magnetic and in-plane electric fields [318–320]. In a recent work, by exploiting a tight-binding model, Ng et al. [321] demonstrated that the absence of inversion symmetry results in a striking contrast between odd- (C_{4n+2}) and even-dimer (C_{4n}) polyynic rings. Indeed, in C_{4n+2} rings the degeneracy splitting is linear with respect to the applied electric field, while C_{4n} rings preserve inversion symmetry, preventing linear splitting. By tuning an external electric field, the THz range can be reached, making CCs a potential candidate for THz applications.
Inspired by this work, by means of DFT and MBPT calculations, we explore the potential of C_{18} rings under experimentally achievable in-plane electric fields for THz generation.

6.1.2 Methods

In this work, two different approaches have been employed to investigate the electronic and optical properties of the C_{18} ring, providing a comprehensive understanding of how these properties are modified under the influence of an electric field.
The first approach utilizes a PW-based method within the framework of DFT, as implemented in the QE package [22, 23]. A norm-conserving, scalar relativistic pseudopotential from the PseudoDojo repository (v0.4) [157], with a kinetic energy cutoff of 90 Ry, was used. The optimal polyyne geometry was obtained through atomic relaxation, using the range-separated hybrid functional HSE [21] based on the GGA-PBE XC functional. A high fraction of HF exchange, $a = 0.8$ (see Sec. 2.3.7),

[2] As a general rule, choosing the correct functional method is essential for predicting the accurate geometry of these highly delocalized structures. To date, only functionals with a high proportion of exact-like exchange (not lower than 40%) or those incorporating exchange range-separation have been successful in correctly predicting the polyyne structure as the most stable, contrary to conventional semi-local or standard hybrid functionals, which favor the cumulene form. It is important to note that the degree of density localization in both polyyne and cumulene forms differs, and density functionals are known to suffer from delocalization error, which significantly impacts result accuracy. This error tends to increase with system size, making it challenging to draw solid conclusions without a systematic investigation.

[3] Notably, CCs exhibit "double" aromaticity due to the delocalization of two sets of π-electrons: one set lies in the plane of the ring and the other is perpendicular to it. This concept of double aromaticity was first introduced by Diederich et al. [301] and further developed by Fowler et al. [303]. Moreover, in C_{4n+2} carbon rings, Hückel's rule for aromaticity adds stability to the rings.

was employed, as suggested by previous studies [292,313]. After convergence, a vacuum distance of ≈ 13 Å along the in-plane (xy) directions and ≈ 20 Å in the out-of-plane (z) direction were used to prevent spurious interactions with periodic replicas. To avoid overestimating the HOMO-LUMO gap, subsequent calculations were performed using a standard GGA-PBE functional. The inclusion of SOC lifts the spin degeneracy (≈ 1 meV) but does not change the value of the degeneracy splitting due to the electric field, so it was not considered in the following investigations.
Based on the DFT results, the electronic structure calculations were further refined using MBPT via the YAMBO code [48,49], to study the excited-state properties. Single-shot G_0W_0 calculations were followed by eigenvalues self-consistent calculations on both G and W (see Sec. 3.6.3), which is essential for isolated systems such as CCs, where the gap is typically underestimated. This procedure also eliminates dependence on the initial DFT results. Finally, optical absorption spectra were computed at the BSE level on top of the QP-corrected eigenvalues, accurately accounting for excitonic transitions. Further details about the parameters used in the calculations are reported in Sec. 6.1.5.
In the second approach, a Gaussian-type orbitals (GTOs) basis set method was employed, using the MOLGW code [322] (see Appendix B). This method is well-suited for finite systems and enables accurate treatment of localized orbitals and electronic excitations. This allows for a detailed analysis of electronic and optical properties, offering a robust comparison with PW-based results. Starting from the relaxed polyyne structure, both DFT — using a GGA-PBE XC functional — and MBPT calculations were performed. The aug-cc-pV5Z basis and the aug-cc-pV5Z-RI auxiliary basis — which represent the most refined GTOs of their kind — were used, after careful convergence tests. Core states were neglected. Also in this case, eigenvalues self-consistent GW calculations were performed, up to convergence. BSE calculations were performed on top of the QP-corrected eigenvalues.
In both cases, an in-plane static electric field was applied to the system, and the results were compared with those obtained in the unperturbed state. The details of these calculations are discussed in Sec. 6.1.4.

6.1.3 Structural Properties

The final stable polyyne structure of C_{18}, shown in Fig. 6.1, exhibits short bonds (l_1) measuring 1.204 Å and long bonds (l_2) measuring 1.359 Å, consistent with previous studies [292,301,313]. This structure was obtained by carefully adjusting the HF exchange fraction in the selected XC hybrid functional. As shown in Table 6.1, starting from the default value of $a = 0.2$, a transition from a cumulene to a polyyne structure occurs at values greater than 0.4, resulting in larger differences in bond lengths. We confirmed that there were no significant differences between various types of hybrid functionals, including PBE0, B3LYP, and HSE. However, the range-separated hybrid functional HSE was selected because standard hybrid functionals tend to overestimate the band gap for the same exchange fraction.
It is important to note that the structural change between the cumulene and polyyne forms is minimal. The difference in bond lengths — from equal bonds in the cumulene to alternating short and long bonds in the polyyne form — is less than 0.16 Å. This indicates that the transition path from the cumulene structure to the polyyne structure is small and is accompanied by only slight changes in bond angles. These changes are relatively insignificant when compared to the overall radius of C_{18}, which is approximately 3.7 Å. Moreover, tests conducted on even-dimer CCs (C_{4n}),

specifically C_{16} and C_{20}, demonstrated that no such transition occurs in these systems, even for exchange fractions as high as 0.8. This finding is crucial for understanding the behavior of CCs under an applied electric field, as will be discussed in the following sections.

Figure 6.1: *Optimized polyyne (D_{9h}) structure of C_{18} ring, relaxed using the range-separated hybrid functional HSE [21] based on the GGA-PBE XC functional. A high fraction of HF exchange of $a = 0.8$ was employed, as suggested by previous studies [292, 313].*

A detailed analysis of the frontier orbitals of C_{18} reveals distortions in some orbitals, leading the molecule to adopt a less symmetric structure than expected for a CC. These distortions, not detected in C_{4n} rings, are explained by the interaction between the excited-state and ground-state eigenfunctions of the unstable cumulene structure. We refer the reader to Ref. [313] for further details.

Table 6.1: *Evolution of the bond length (l_1 and l_2) and relative structure type of the C_{18} ring as a function of the HF exchange fraction used in the HSE hybrid functional.*

HF Exchange Fraction	l_1 (Å)	l_2 (Å)	Structure Type
0.2	1.278	-	cumulene (D_{18h})
0.4	1.234	1.325	polyyne (D_{9h})
0.6	1.215	1.347	polyyne (D_{9h})
0.8	1.205	1.359	polyyne (D_{9h})

6.1.4 Electronic Properties: Field-Induced Degeneracy Splitting

At this stage, the electronic properties were investigated using the QE DFT package, which employs a PW basis set.

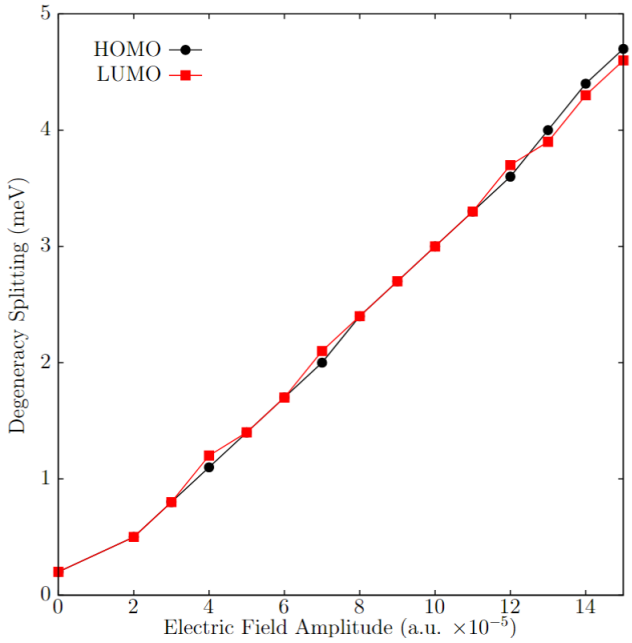

Figure 6.2: *Tuning of the HOMO (black) and LUMO (red) degeneracy splitting, as a function of the applied electric field amplitude, in the C_{18} ring. A 4 meV (i.e. 1 THz) degeneracy splitting is achieved with an electric field intensity of $\simeq 13 \times 10^{-5}$ a.u. $\simeq 6.7 \times 10^{7}$ V·m^{-1}. This value is of the same order of magnitude as predicted by Ng et al. [321], who also foresaw a linear dependence of the splitting with respect to the intensity of the applied field. Calculations were performed using the QE DFT package, employing standard GGA-PBE XC functional.*

Starting from the optimized polyyne geometry, as described in the previous section, calculations were performed using the standard GGA-PBE functional to avoid overestimating the HOMO-LUMO gap. First, we explored the possibility of tuning the degeneracy splitting of the HOMO and LUMO levels. To achieve this, an in-plane (static) electric field of increasing amplitude was applied, using a saw-like potential. As shown in Fig. 6.2, the splitting of these levels follows a nearly perfect linear trend as a function of the field amplitude. Our results indicate that an electric field intensity on the order of 10^{-5} a.u., equivalent to 10^{7} V·m^{-1}, is required to achieve a degeneracy splitting of the HOMO and LUMO levels in the THz range, corresponding to few meV energy differences. For example, an amplitude of approximately 13×10^{-5} a.u. ($\simeq 6.7 \times 10^{7}$ V·m^{-1}) induces a splitting of exactly 1 THz, i.e., 4 meV. This result aligns very well with the predictions of Ng et al. [321], who estimated a value of 1.8×10^{7} V·m^{-1} to achieve a 1 THz splitting, using tight-binding calculations. In the same study, Ng et al. also predicted a linear dependence of the splitting on the applied field

intensity. Notably, they found this behavior to occur only for odd-dimer rings, specifically C_{4n+2} rings. In contrast, for even-dimer rings (C_{4n}), the electric-field-driven splitting of the HOMO and LUMO levels is proportional to the product of the square of the electric field amplitude and the ring radius R. Given the small size of R, which ranges from 3.3 to 4.2 Å as one moves from a C_{16} to a C_{20} ring, the splitting becomes unobservable at reasonable field amplitudes[4].

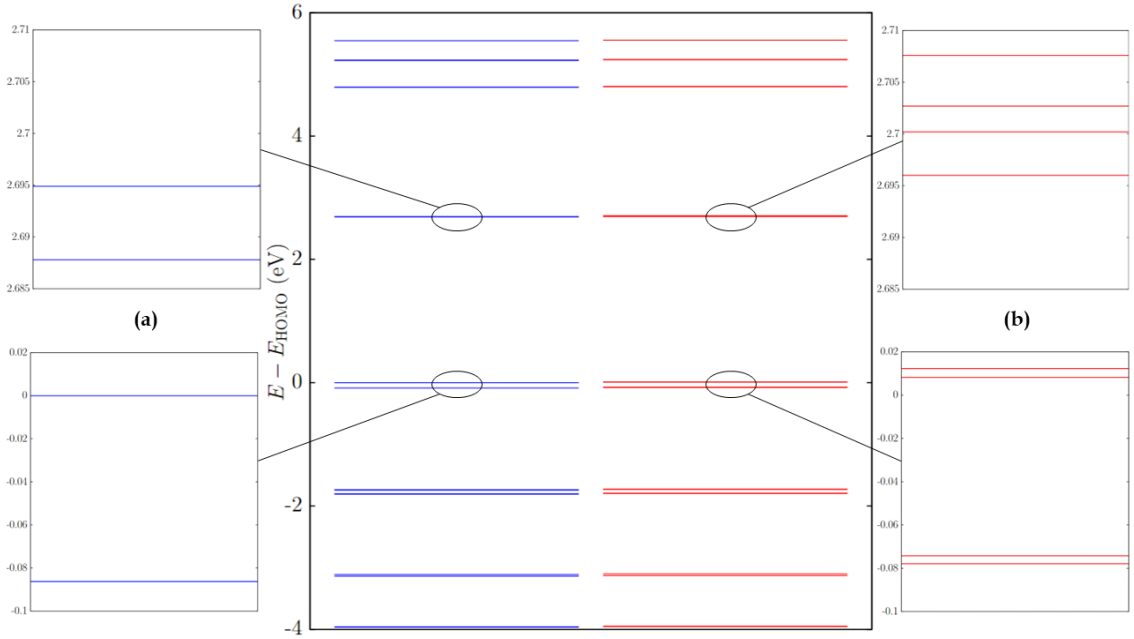

Figure 6.3: *Energy levels of the C_{18} ring without (blue, left) and with (red, right) applied electric field ($E_F \simeq 13 \times 10^{-5}$ a.u. $\simeq 6.7 \times 10^{7}$ V·m^{-1}), as calculated with the QE DFT package, employing standard GGA-PBE XC functional. Energies where rescaled with respect to the pristine HOMO level. The DFT HOMO-LUMO gap was estimated to be 2.69 eV (without) and 2.68 eV (with), respectively.* (**a**) *Focus of the frontier states in the absence of electric field, showing no relevant degeneracy splitting.* (**b**) *Focus of the frontier states with applied electric field, showing a degeneracy splitting of $\simeq 4$ meV, i.e. 1 THz.*

As discussed in Sec. 6.1, in C_{4n+2} rings, the SOJTE can induce spontaneous symmetry breaking, lifting the degeneracy and creating an intrinsic gap between previously degenerate levels. This is evident in Fig. 6.2, where even in the absence of a field, an initial splitting of approximately 0.2 meV is observed. In contrast, this splitting does not occur in C_{4n} rings. Notably, such splitting, which is essential for further tunability via an electric field, can only be detected in even-dimer rings through ab initio calculations.
Fig. 6.3 presents the calculated energy levels around the HOMO-LUMO gap of the C_{18} ring, both

[4]Indeed, by repeating the simulations for C_{16} and C_{20} rings, we were able to demonstrate ab initio that this is the case, even for fields as high as 10^{11} V·m^{-1}.

without (blue, left) and with (red, right) an applied electric field of $\simeq 13 \times 10^{-5}$ a.u. $\simeq 6.7 \times 10^{7}$ V·m^{-1}. The DFT GGA-PBE HOMO-LUMO gap was estimated to be 2.69 eV (without) and 2.68 eV (with), respectively. In the absence of an electric field, the frontier states do not exhibit significant degeneracy splitting, as shown in the left panel of Fig. 6.3. However, when the electric field is applied, a splitting of exactly 4 meV is observed, corresponding to a frequency of 1 THz.

6.1.5 Electronic Properties: Many-Body Approach

The underestimation of the gap is a well-known issue in DFT (see Sec. 2.3.3) and it is generally more pronounced in 0D systems for several reasons, especially due to the local or semi-local nature of the XC functionals used in DFT. This problem can sometimes be addressed using hybrid functionals, particularly range-separated functionals like HSE, which is employed in this Thesis. However, even with these advanced functionals, systems such as CCs still face a significant underestimation of the exact exchange. As a result, the HF exchange fraction must be substantially increased to achieve accurate results. While this approach is effective for obtaining the correct polyyne geometry in C_{4n+2} rings (as discussed in Sec. 6.1.3), it may negatively affect the accuracy of the HOMO-LUMO gap. Therefore, we opted to use a standard GGA-PBE functional as a starting point to include QP corrections using the *GW* approach.
In this study, both a PW- and a GTO-based approach were employed to calculate the many-body corrections to the electronic levels, respectively using the YAMBO code [48, 49] and the MOLGW code [322]. In both cases, single-shot G_0W_0 calculations were followed by eigenvalues self-consistent calculations on both G and W (evGW). To the best of our knowledge, these are the first reported MBPT calculations involving C_{18} rings.
We start the discussion with the former approach. The DFT KS states were initially calculated using the GGA-PBE XC functional, both without and with an applied electric field, employing the QE package, as discussed in the previous section. We chose a field amplitude of $\simeq 13 \times 10^{-5}$ a.u. $\simeq 6.7 \times 10^{7}$ V·m^{-1} to obtain an initial splitting of exactly 1 THz. In the following MBPT calculations, an energy cutoff of 60 (6) Ry was used for the exchange (correlation) part of the self-energy Σ_x (Σ_c), while 64 empty bands (72 in the electric field case) were included in the calculation of Σ_c. A spherical cutoff to the Coulomb potential was used, as implemented in YAMBO [49]. In the absence of an electric field, the starting HOMO-LUMO gap was 2.69 eV. Single-shot G_0W_0 calculations corrected this gap to 5.66 eV, while the evGW approach yielded a gap of 6.28 eV, converging in three steps within a threshold of less than 0.02 eV. With the applied electric field, the DFT-calculated HOMO-LUMO gap of 2.68 eV was corrected to 5.50 eV using G_0W_0, and further refined to 6.07 eV after self-consistency. These values are reported in Table 6.2. Notably, the effect of the electric field on the DFT wavefunctions and levels results in a moderate reduction of the HOMO-LUMO gap at the *GW* level.
The GTO-based approach was also used to calculate the QP-corrected states both without and with an applied electric field. All values are reported in Table 6.2. The same XC functional was used in the DFT calculations, yielding a HOMO-LUMO gap of 2.68 eV, both without and with electric field. The G_0W_0 corrections returned a gap of 5.93 (without) and 5.81 (with) eV, while the self-consistency yielded a final value of 6.75 eV, both without and with electric field, converging in five steps within a threshold of less than 1 meV[5]. This value is ≈ 0.5 eV higher than the corresponding

[5]The fact that we obtained the same evGW band gap is not surprising, given the negligible difference between the starting DFT eigenvalues.

PW one[6].
At this stage of the study, it is unclear whether the discrepancy should be solely attributed to the different approaches used in the calculations. For example, in YAMBO, the 0th step of the self-consistency in *GW* corresponds to a single-shot *GW* calculation. However, this is not the case in MOLGW, which employs a different strategy[7]. Another important difference between the two approaches is that YAMBO employs the PPA (see Sec. 3.6.1) to calculate the QP corrections. This method may introduce error propagation through the self-consistency steps in the ev*GW* calculation. Finally, the starting DFT electronic wavefunctions are constructed using different basis sets: GTOs, which are naturally localized, and plane waves PWs, which are highly delocalized.

Table 6.2: *HOMO-LUMO gaps at the DFT* (E_g^{DFT})*, single-shot* ($E_g^{G_0W_0}$) *and eigenvalue self-consistent* ($E_g^{\mathrm{ev}GW}$) *GW level, calculated using both a PW-based and a GTO-based approach — without and with an applied electric field* (*EF*) *of* $\simeq 13\times10^{-5}$ *a.u.* $\simeq 6.7\times10^{7}$ $V{\cdot}m^{-1}$*. Optical gaps were calculated, at the BSE level, upon* G_0W_0*-* ($E_g^{G_0W_0+\mathrm{BSE}}$) *and* ev*GW -corrected* ($E_g^{\mathrm{ev}GW+\mathrm{BSE}}$) *electronic states. The corresponding lowest excitonic binding energies* (E_b) *are reported. All energies are express in eV.*

Approach	E_g^{DFT}	$E_g^{G_0W_0}$	$E_g^{G_0W_0+\mathrm{BSE}}$	$E_b^{G_0W_0+\mathrm{BSE}}$	$E_g^{\mathrm{ev}GW}$	$E_g^{\mathrm{ev}GW+\mathrm{BSE}}$	$E_b^{\mathrm{ev}GW+\mathrm{BSE}}$
PW	2.69	5.66	2.96	2.70	6.28	3.62	2.66
PW (EF)	2.68	5.50	2.90	2.60	6.07	3.52	2.55
GTO	2.68	5.93	3.88	2.05	6.75	5.17	1.58
GTO (EF)	2.68	5.81	3.94	1.87	6.75	5.17	1.58

6.1.6 Optical Properties

In this section, we focus on the optical properties of the C_{18} ring, specifically its absorption spectra, both without and with an applied electric field, using the approaches discussed in the previous sections at different levels of theory.
We begin our analysis by examining the results obtained by the PWs approach, specifically the spectra obtained using the QE package at DFT IPA level (see Sec. 3.8.1). Since the differences between the spectra with and without the applied electric field are negligible, we limit our discussion to the former case[8], as shown in Fig. 6.4. Following a similar approach to Sec. 4.1, we express the optical spectra in terms of the optical absorbance, as described in Sec. 3.8.8. This definition ensures that the results are independent of the choice of simulation cell. The onset of the optical transitions, corresponding to the DFT optical gap, coincides with the HOMO-LUMO gap ($\simeq$ 2.69 eV). The transitions contributing to the first peak in the spectrum originate from the occupied HOMO and HOMO-1 states (which correspond to the split pristine HOMO level, see lower panel *b* in Fig. 6.3)

[6]In comparison, calculations using hybrid functionals (with HF exchange fraction of 0.8) yielded HOMO-LUMO gaps of 7.73 eV (PBE0) and 5.32 eV (HSE), at the DFT level.
[7]In the single-shot *GW*, MOLGW solves the QP equation using a graphical solution.
[8]The amplitude of the applied field is the same as describe in the previous sections. This means that the degeneracy splitting of the HOMO and LUMO levels is equal to 4 meV, i.e. 1 THz.

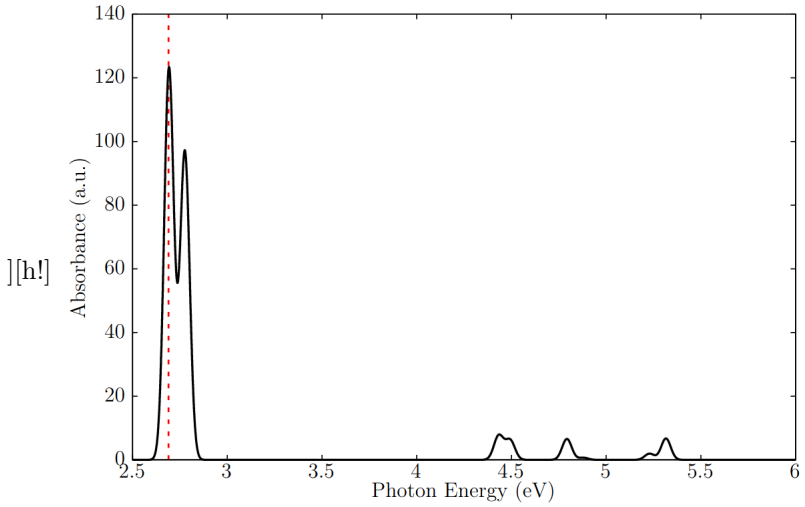

]][h!]

Figure 6.4: *Absorption spectrum (solid black), calculated at the DFT IPA level, with an applied electric field of* $\simeq 13 \times 10^{-5}$ *a.u.* $\simeq 6.7 \times 10^{7}$ $V{\cdot}m^{-1}$*, using the QE package. The spectrum is expressed in terms of the optical absorbance. The underlying energy levels are those shown in Fig. 6.3 (in red). The DFT HOMO-LUMO gap of* 2.69 *eV (dashed red) is also reported. A broadening of* 25 *meV was used.*

and the unoccupied LUMO, LUMO+1, LUMO+2, and LUMO+3 states (corresponding to the pristine LUMO and LUMO+1 levels, see upper panel *b* in Fig. 6.3).
In contrast, the second peak arises from transitions involving the occupied HOMO-2 and HOMO-3 states (corresponding to the split pristine HOMO-1 level, see lower panel *b* in Fig. 6.3) and the same unoccupied LUMO, LUMO+1, LUMO+2, and LUMO+3 states. This important result suggests that, at the DFT level, a C_{18} ring subjected to a constant electric field is optically active primarily in the visible range (blue-violet). In principle, an electron could be excited from an occupied frontier state to, for instance, the LUMO+1 level. This electron would eventually de-excite back to a lower energy state, either below or above the gap. In the latter case, a transition from the LUMO+1 to the LUMO could occur, potentially leading to the emission of a photon in the THz regime. As we will see, this description is incomplete and lacks important levels of theory necessary for an accurate portrayal of the physics of the system.
To achieve a more precise understanding, we must rely on more advanced and refined methods of investigation. Following the same PW approach, we now discuss our results pertaining to state-of-the-art BSE calculations. As detailed in the previous section, first the KS states obtained within DFT were corrected using MBPT with the YAMBO code. Then the BSE spectra were calculated, based on both the QP-corrected G_0W_0 and evGW states. For constructing the BSE Hamiltonian, we used a total of 8 occupied and 8 unoccupied states without an applied electric field, and 6 occupied and 6 unoccupied states when an electric field was applied. The results are presented in Fig. 6.5 and calculated optical gaps are reported in Table 6.2. A key observation from these findings is that the optical transition corresponding to the QP-corrected HOMO-LUMO gap is quenched in all the cases under examination.

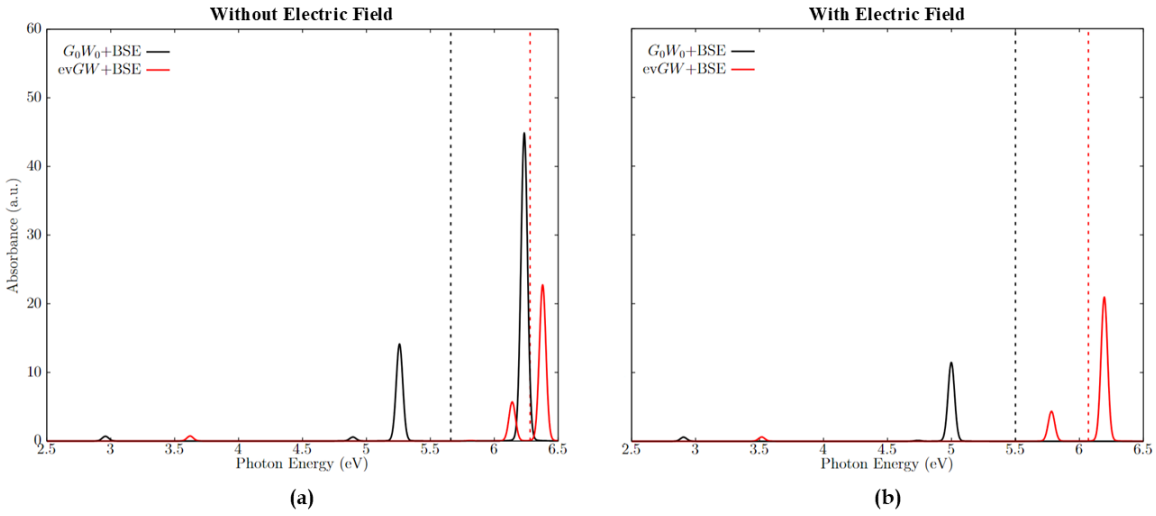

Figure 6.5: *G_0W_0+BSE (solid black) and* evGW*+BSE (solid red) spectra, without* (**a**) *and with* (**b**) *an applied electric field, of the C_{18} ring, calculated with the YAMBO code. The estimated G_0W_0* $(5.66\,(\mathbf{a}), 5.50\,(\mathbf{b})$ *eV) and* evGW $(6.28\,(\mathbf{a}), 6.07\,(\mathbf{b})$ *eV) HOMO-LUMO gaps are denoted by black and red dashed lines, respectively. A broadening of* 25 *meV was used.*

We found that this effect is entirely due to the BSE calculations, as the IQP spectra exhibit only a rigid shift of the IP spectra. We now focus our analysis on the excitonic transitions, beginning with the spectra obtained without an applied electric field (see Fig. 6.5a). In the G_0W_0+BSE spectrum, the first weak excitation, corresponding to the optical onset, occurs at 2.96 eV, with an estimated binding energy of 2.70 eV. This excitation arises from transitions involving the occupied states HOMO, HOMO-1, HOMO-2, HOMO-3 and the unoccupied states LUMO, LUMO+1, LUMO+2, LUMO+3. Interestingly, these transitions are alternately coupled, with HOMO and HOMO-1 coupled to LUMO+2 and LUMO+3, and HOMO-2 and HOMO-3 coupled to LUMO and LUMO+1. This alternating coupling holds for all other transitions, which also involve higher and lower energy states. In contrast, the first dark excitation, located at 2.64 eV, arises primarily from a HOMO-LUMO transition. The self-consistency increases the QP HOMO-LUMO gap from 5.66 to 6.28 eV, causing all excitations to blueshift, the first peak now occuring at 3.62 eV, with a binding energy of about 2.66 eV. The overall nature of the transitions remains unchanged, although the intensity of the higher-energy peaks increases. Similarly, the first dark excitation is blueshifted to 3.31 eV. When a static electric field is applied, the entire spectrum undergoes a redshift, and the intensity of the excitation peaks slightly decreases (see Fig. 6.5b). Notably, the most intense peak present in the absence of the field is now entirely quenched. However, the nature of the excitations remains unchanged, as analyzed in the previous case. The G_0W_0+BSE (evGW+BSE) optical onset is now located at 2.90 (3.52) eV, thus giving a binding energy of about 2.60 (2.55) eV, as reported in Table 6.2. Overall, the effect of the electric field does not significantly alter the optical absorption of the ring, with the energies being redshifted by a maximum of only 0.2 eV.

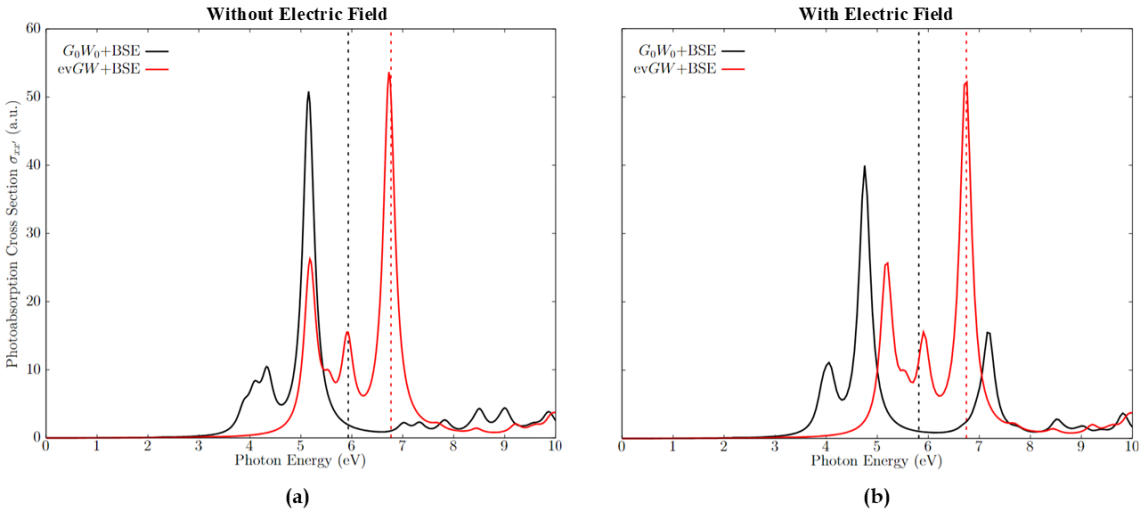

Figure 6.6: *G_0W_0+BSE (solid black) and* ev*GW+BSE (solid red) spectra, without* (**a**) *and with* (**b**) *an applied electric field, of the C_{18} ring, calculated with the MOLGW code. The estimated G_0W_0* (5.93 (**a**), 5.81 (**b**) *eV*) *and* ev*GW* (6.75 *eV*) *HOMO-LUMO gaps are denoted by black and red dashed lines, respectively. A broadening of* 25 *meV was used.*

We continue our discussion by analyzing the results obtained by the GTOs approach, with the optical absorption investigated at the BSE level using the MOLGW code, both without and with applied electric field. The GTO-based approach is undoubtedly more suitable for handling finite systems, and these results are expected to be more reliable than those obtained using the PW approach. The resulted spectra are shown in Fig. 6.6. The BSE calculations on G_0W_0-corrected energy levels (Fig. 6.6) returned an optical gap of 3.88 (without, Fig. 6.6a, solid black) and 3.94 (with, Fig. 6.6b, solid black) eV. This gives an estimated binding energy of the lowest bright exciton of 2.05 (without) and 1.87 (with) eV, about 0.7 eV lower than the corresponding PW calculations. The lowest dark excitations are instead located at 2.06 (without) and 1.98 (with) eV. Also in this case, all HOMO-LUMO transitions are dark or sensibly quenched. The self-consistency increases the QP HOMO-LUMO gaps, with the resulting spectra being blueshifted. The first optically active excitations are now located at 5.17 eV (both with and without electric field, Fig. 6.6a-b, solid red), with a binding energy of 1.58 eV, about 1 eV lower than the corresponding PW calculation. In this case, the lowest dark excitation is instead located at 2.89 eV, with all other HOMO-LUMO transitions dark or sensibly quenched. Overall, the electric field only slightly modifies the optical response at the G_0W_0+BSE level. While the field induces a splitting in the degeneracy of the HOMO and LUMO levels, its strength is insufficient to significantly alter the system's optical properties.

6.1.7 Towards THz Applications: Size vs Electric Field

To conclude this investigation, we will briefly discuss the relevance of these results in the context of potential optoelectronic applications for THz technologies. Although ab initio calculations confirm

the possibility of tuning the HOMO and LUMO level splitting in the THz regime, by applying a reasonably intense in-plane static electric field, the magnitude of the estimated optical gaps (which are located in the UV range), along with the optical inactivity of the HOMO(-1)-LUMO(+1) transitions, somehow limits the potential use of C_{18} rings in practical optoelectronic devices.

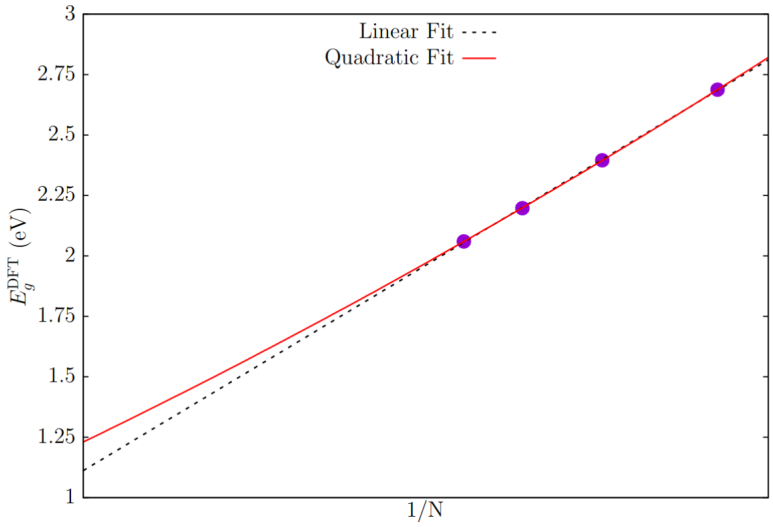

Figure 6.7: *Linear* ($R^2 = 0.999789$) *and quadratic* ($R^2 = 0.999986$) *best-fit of the HOMO-LUMO GGA-PBE gap of* C_{4n+2} *polyyne rings for increasing number of carbon atoms* $N = 4n + 2$ (*with* $N = 18, 22, 26, 30$)*, as a function of* $1/N$*. Extrapolated values* ($N \to \infty$) *of the gap: 1.11 eV for the linear and 1.23 eV for the quadratic fit.*

To this end, Encouraged by the recent synthesis of C_{18} [292, 293], we explored the possibility of reducing the energy gap by increasing the size of the ring. Odd-dimer CCs exhibit similar physical properties, allowing for the tuning of energy levels in the THz regime. In Fig. 6.7, the HOMO-LUMO GGA-PBE gap of C_{4n+2} polyyne rings, with an increasing number of carbon atoms $N = 4n + 2$ ($N = 18, 22, 26, 30$), is plotted as a function of $1/N$. By fitting the calculated gaps linearly and quadratically, we extrapolated gap values of 1.11 eV and 1.23 eV, respectively, as $N \to \infty$. For instance, a C_{36} ring, double the size of C_{18}, would have a DFT gap of approximately 1.90 eV. Using the results obtained for C_{18} as a reference, the evGW-corrected gap would increase to about 5.50 eV in the PW approach and around 6.00 eV in the GTO approach. This implies that the binding energy for the lowest optically active excitation would lead to an optical gap of approximately 2.8 eV and 4.39 eV, respectively. Finally, applying an electric field could further reduce these gaps by 0.1 to 0.2 eV. While these are rough estimates, these findings suggest that with continued research and refinement, polyyne rings may offer viable pathways for THz optoelectronic applications.
A more conservative approach involves increasing the amplitude of the applied field. Our calculations indicate that even when the field amplitude is increased by up to two orders of magnitude, the linear splitting trend remains intact. For instance, a field amplitude of 13×10^{-4} a.u. (approximately 6.7×10^{8} V·m^{-1}) results in a degeneracy splitting of about 40 meV. When the amplitude is increased to 13×10^{-3} a.u. (approximately 6.7×10^{9} V·m^{-1}), the degeneracy splitting rises up

to around 400 meV.

Table 6.3: *HOMO-LUMO gaps at the DFT* (E_g^{DFT})*, single-shot* ($E_g^{G_0W_0}$) *and eigenvalue self-consistent* ($E_g^{\mathrm{ev}GW}$) *GW level, calculated using a GTO-based approach, with an applied electric field of* $\simeq 13 \times 10^{-5}$ *a.u.* $\simeq 6.7 \times 10^{7}$ $V{\cdot}m^{-1}$ (*denoted as low field, LF*) *and* $\simeq 13 \times 10^{-3}$ *a.u.* $\simeq 6.7 \times 10^{9}$ $V{\cdot}m^{-1}$ (*denoted as high field, HF*)*. Optical gaps were calculated, at the BSE level, upon* G_0W_0- ($E_g^{G_0W_0+\mathrm{BSE}}$) *and* ev$GW$*-corrected* ($E_g^{\mathrm{ev}GW+\mathrm{BSE}}$) *electronic states. The corresponding lowest excitonic binding energies* (E_b) *are reported. All energies are express in eV.*

Approach	E_g^{DFT}	$E_g^{G_0W_0}$	$E_g^{G_0W_0+\mathrm{BSE}}$	$E_b^{G_0W_0+\mathrm{BSE}}$	$E_g^{\mathrm{ev}GW}$	$E_g^{\mathrm{ev}GW+\mathrm{BSE}}$	$E_b^{\mathrm{ev}GW+\mathrm{BSE}}$
GTO (LF)	2.68	5.81	3.94	1.87	6.75	5.17	1.58
GTO (HF)	2.20	5.00	2.07	2.93	6.00	3.12	2.88

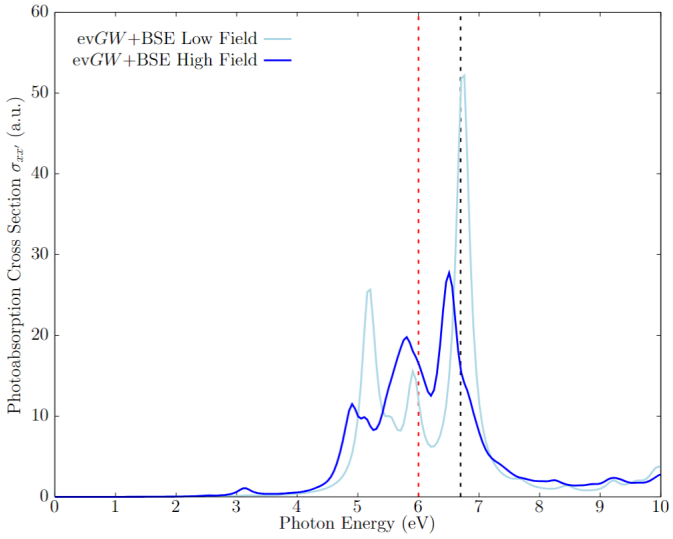

Figure 6.8: evGW*+BSE spectra of the* C_{18} *ring, with an applied electric field amplitude of* $\simeq 13 \times 10^{-5}$ *a.u.* $\simeq 6.7 \times 10^{7}$ $V{\cdot}m^{-1}$ (*solid light blue, denoted as low field, LF*) *and of* $\simeq 13 \times 10^{-3}$ *a.u.* $\simeq 6.7 \times 10^{9}$ $V{\cdot}m^{-1}$ (*solid blue, denoted as high field, HF*)*, calculated with the MOLGW code. The estimated* evGW (6.75 *and* 6.00 *eV*) *HOMO-LUMO gaps are denoted by black and red dashed lines, respectively. A broadening of* 25 *meV was used.*

It is thus intriguing to examine how the electronic and optical properties evolve as the field strength increases. To this end, we compare two cases: a field amplitude of 13×10^{-5} a.u. (approximately 6.7×10^{7} V·m^{-1}), referred to as the low field (LF) case — discussed in previous sections — and a field amplitude of 13×10^{-3} a.u. (approximately 6.7×10^{9} V·m^{-1}), referred to as the high field (HF) case. The calculated electronic and optical gaps are presented in Table 6.3. We observe that, as the field amplitude increases, the DFT electronic gap decreases from 2.68 eV to 2.20 eV, leading

to significantly lower QP-corrected gaps in both the single-shot (5.00 eV) and self-consistent (6.00 eV) *GW* calculations. On top of QP-corrected levels, the absorption spectra, at the BSE level, were also computed. For simplicity, we focus our discussion on the evGW+BSE results. The corresponding spectra are displayed in Fig. 6.8. Notably, we observe the emergence of an excitonic peak significantly lower in energy than those detected at lower field intensities. It stems from transitions involving the occupied levels from HOMO-3 to HOMO and the unoccupied levels from LUMO to LUMO+3, thereby including the THz-split frontier states. This peak shifts the optical gap from 5.17 (LF) to 3.12 (HF) eV, placing it within the range between visible light and near UV. This paramount result opens up new possibilities for efficient light absorption and emission in THz technology. Moreover, the presence of THz-split frontier states indicates that the material can support strong excitonic interactions, which are vital for the realization of novel photonic devices. These interactions may enhance the efficiency of THz generation and detection processes. The ability to manipulate the optical gap through external fields could lead to the development of tunable THz sources and detectors.
Further experimental validation and detailed theoretical studies will be crucial for advancing the potential use of these systems in next-generation THz technologies.

6.1.8 Conclusions

In conclusion, this study provides a comprehensive exploration of the electronic and optical properties of the C_{18} ring, employing both PW and GTO approaches to reveal the intricate effects of an applied electric field. To the best of our knowledge, this work provides the first reported results on the topic.
Through detailed calculations using DFT and MBPT, we demonstrated that an electric field can effectively tune the degeneracy splitting of the HOMO and LUMO levels, achieving a noteworthy splitting in the THz range. The observed behavior aligns with prior theoretical predictions, highlighting the unique properties of odd-dimer carbon rings, such as C_{4n+2}, which exhibit spontaneous symmetry breaking and an intrinsic gap even in the absence of an electric field.
Additionally, the analysis of the optical absorption spectra revealed that the C_{18} ring remains predominantly optically active in the UV range, with excitonic transitions primarily involving the frontier states. While the application of an electric field induces slight modifications to the optical response, including redshifts in energy levels, the fundamental nature of the excitations remains largely intact. However, further investigations suggests that increasing the amplitude of the field could sensibly reduce the optical gap, with the emergence of excitonic peaks in the visible range, opening new possibilities for efficient light absorption and emission in THz technology.
These findings underscore the potential of C_{18} rings for applications in THz technologies and optoelectronic devices, paving the way for further investigations into the tunability of their electronic and optical properties through external perturbations.
The results of this study will be the subject of a future publication.

Chapter 7

Conclusions

This Thesis has presented an in-depth ab initio investigation into the electronic and optical properties of low-dimensional materials, including 2D, 1D, and 0D systems. By employing advanced computational techniques such as DFT and MBPT, we have gained significant insights into the unique properties and potential applications of these materials in optoelectronic technologies.

In the study of 2D materials, we discovered substantial light absorption in the near-infrared and visible ranges of tellurene polymorphs. These properties make tellurene an excellent candidate for novel light-harvesting devices. The predicted PCEs of tellurene-based heterostructures were found to be competitive, even surpassing some previously investigated 2D hetero-bilayers, with efficiencies reaching up to 19%. Furthermore, we explored how SHG in MoS_2 and WSe_2 can be induced and modulated by the application of an electric field or by charge doping. This tunability in SHG response suggests potential applications in frequency doubling, all-optical signal processing, and the development of novel optoelectronic devices that exploit non-linear optical phenomena.

Our investigation into 1D atomic wires — including S_3, Te_3, As_2S_3, and Bi_2Te_3 — revealed unique band structures and significant exciton binding energies. S_3 and Te_3 demonstrated strong excitonic effects, suggesting their suitability for UV- and visible-range absorption applications. In contrast, As_2S_3 and Bi_2Te_3 exhibited broader absorption spectra with lower exciton binding energies, indicating their potential for photovoltaic and infrared applications. These findings highlight the promise of exfoliable 1D wires as novel key materials for future nanoscale electronic and optoelectronic technologies.

The research on 0D materials focused on the potential of C_{4n+2} polyyne rings for THz applications. with a focus on the C_{18} ring . By examining the electronic and optical properties under an applied electric field, we identified a linear relationship between the electric field and the degeneracy splitting of the HOMO-LUMO levels. Although the optical gaps of C18 rings are located in the UV range, which limits their immediate application in THz technologies, we showed that increasing the amplitude of the applied field sensibly reduces the optical gap, with the emergence of excitonic peaks in the visible range, opening new possibilities for efficient light absorption and emission in THz technology.

Overall, this work demonstrates the rich potential of low-dimensional materials, particularly in advancing optoelectronic technologies. The findings lay the groundwork for future experimental validation and the exploration of these materials in practical applications, including light-harvesting devices, non-linar optics, UV-absorption technologies, and potentially THz optoelectronics. Fur-

ther research in this direction will continue to uncover the diverse and innovative applications that low-dimensional materials can offer.

Publications

Related to this Thesis:
- **Grillo, S.**, Pulci, O., and Marri, I. "Evolution of the Electronic and Optical Properties of Meta-Stable Allotropic Forms of 2D Tellurium for Increasing Number of Layers". *Nanomaterials*, 12(14), 2503.
- **Grillo, S.**, Postorino, P., Palummo, M., and Pulci, O. "Tellurene Polymorphs: A New Frontier for Solar Harvesting with Strong Exciton Anisotropy and High Optical Absorbance". *Advanced Energy Materials*, 2400674.
- **Grillo, S.**, Cannuccia, E., Palummo, M., Pulci, O., and Attaccalite, C. "Tunable Second-Harmonic Generation in 2D Materials". *SciPost Phys. Core 7, 081.*
- **Grillo, S.**, Hartmann, R. R., Brozzesi, S., Pulci, O., and Portnoi, M. E. "Tunable Electric-Field-Driven Terahertz Splitting in Polyyne C_{18} Carbon Ring". *In Preparation*
- **Grillo, S.**, Cignarella, C., Campi, D., Palummo, M., Pulci, O., and Marzari, N. "Excitonic Effects in Exfoliable 1D Semiconducting Materials from High-Throughput Screening". *In Preparation*

Others:
- Bechstedt, F., **Grillo, S.**, Pulci, O., and Gori, P. "Thermal properties of Dirac fermions in Xenes: Model studies". *Physical Review B*, 104(16), 165420.
- Marri, I., **Grillo, S.**, Amato, M., Ossicini, S., and Pulci, O. "Interplay of Quantum Confinement and Strain Effects in Type I to Type II Transition in GeSi Core–Shell Nanocrystals". *The Journal of Physical Chemistry C*, 127(2), 1209-1219.
- Mendoza, B. S., **Grillo, S.**, Juárez-Reyes, L., and Fregoso, B. M. "Pure spin current injection of single-layer monochalcogenides". *Materials Research Express*, 10(3), 035003.

Research Projects

Erasmus+ Programme's Visiting PhD Student at Aix-Marseille University
9 January - 9 March 2024
Collaboration with Dr. E. Cannuccia and Dr. C. Attaccalite within the Erasmus+ Programme at the Aix-Marseille Université and CNRS (France).
Related publication: **Grillo, S.**, Cannuccia, E., Palummo, M., Pulci, O., and Attaccalite, C. "Tunable Second-Harmonic Generation in 2D Materials". *SciPost Phys. Core 7, 081.*

NCCR MARVEL's Visiting PhD Student at EPFL
11 September - 20 December 2023
Collaboration with Prof. N. Marzari within the NCCR MARVEL at the EPFL (Switzerland).
Related publication: **Grillo, S.**, Cignarella, C., Campi, D., Palummo, M., Pulci, O., and Marzari, N. "Excitonic Effects in Exfoliable 1D Semiconducting Materials from High-Throughput Screening". *In Preparation*

MSCA-RISE DiSeTCom (G.A. ID: 823728) Project's Visiting PhD Student at Exeter University
6 March - 18 March 2022 & 21 November - 8 December 2022
Collaboration with Prof. M. Portnoi and Prof. F. Ogrin at the University of Exeter and MaxLLG Ltd. (UK).
Related publication: **Grillo, S.**, Hartmann, R. R., Brozzesi, S., Pulci, O., and Portnoi, M. E. "Tunable Electric-Field-Driven Terahertz Splitting in Polyyne C_{18} Carbon Ring". *In Preparation*

Scientific Projects

- MSCA-RISE "DiSeTCom" (G.A ID: 823728)
- INFN Time2Quest
- 2020 PRIN "PHOTO" (Prot. 2020RPEPNH)
- 2022 PRIN "IRIDE" (Prot. 2022T2ZJZF)

HPC Projects

- [**PI**] CINECA class C ISCRA project "SAGACE" (50.000 sh) on the MARCONI cluster, 2018
- CINECA class B ISCRA project "NaLiBat" (750.000 sh) on the MARCONI100 cluster, 2021
- [**PI**] CINECA class C ISCRA project "SWYFT" (32.000 sh) on the MARCONI100 cluster, 2021
- [**PI**] CINECA class C ISCRA project "MT-SENS" (22.400 sh) on the MARCONI100 cluster, 2021
- CINECA class B ISCRA project "TUTTO" (790.000 sh) on the MARCONI100 cluster, 2021
- CINECA class B ISCRA project "STRANO" (750.640 sh) on the MARCONI100 cluster, 2022
- [**PI**] CINECA class C ISCRA project "TeB2LowD" (24.000 sh) on the MARCONI100 cluster, 2022
- CINECA class C ISCRA project "CBNtwist" (32.000 sh) on the MARCONI100 cluster, 2022
- CINECA class C ISCRA project "AlNWS2" (22.400 sh) on the MARCONI100 cluster, 2023
- CINECA class B ISCRA project "ANODE" (800.000 sh) on the MARCONI100 cluster, 2023
- CINECA class B ISCRA project "NHCOSURF" (520.000 sh) on the GALILEO100 cluster, 2023
- CINECA class C ISCRA project "BN4MIB" (16.667 sh) on the GALILEO100 cluster, 2023
- CINECA class C ISCRA project "2DSe" (25.000 sh) on the GALILEO100 cluster, 2023
- [**PI**] CINECA class B ISCRA project "WeDiTe" (1.560.000 sh) on the LEONARDO cluster, 2024

Talks & Posters

International School of Solid State Physics (EPIOPTICS-17 & XENES-5)
6 July - 12 July 2024
Contributed talk: "Tunable Second Harmonic Generation in 2D Materials from First-Principles". Best student award winner. Erice, Italy.

27th ETSF Workshop on Electronic Excitations
3 June - 7 June 2024
Contributed talk: "Tunable Second Harmonic Generation in 2D Materials from First-Principles". Marseille, France.

CMD30 FisMat 2023
4 September - 8 September 2023
Contributed talk: "Non-Trivial Excitonic Fingerprints and Optical Anisotropy of 2D Tellurium". Milan, Italy.

19th ETSF Young Researchers' Meeting 2023
11 June - 16 June 2023
Contributed talk: "Non-Trivial Excitonic Fingerprints and Optical Anisotropy of 2D Tellurium". Zaragoza, Spain.

EMRS Spring Meeting 2023
29 May - 2 June 2023
Contributed talk: "Ground and Excited State Properties of Meta-Stable Allotropic Forms of 2D Tellurium from First Principles Approaches". Strasbourg, France.

GDR HOWDI Annual Meeting 2023
8 May - 12 May 2023
Contributed talk: "Non-Trivial Excitonic Fingerprints and Optical Anisotropy of 2D Tellurium". Porquerolles Island, France.

Nanoscience & Nanotechnology Conference 2022
13 December - 14 December 2022
Contributed talk: "Evolution of the Electronic and Optical Properties of Meta-Stable Allotropic Forms of 2D Tellurium for Increasing Number of Layers". LNF, Frascati, Italy.

International School of Solid State Physics (EPIOPTICS-16 & XENES-4)
3 July - 9 July 2022
Poster presentation. Best student award winner. Erice, Italy.

25th ETSF Workshop on Electronic Excitations
13 June - 17 June 2022
Poster presentation. Leuven, Belgium.

GDR HOWDI Annual Meeting 2022
9 May - 13 May 2022
Poster presentation. Dourdan, France.

Appendix A

Response Functions

The aim of MBPT is to study how a system behaves under the action of an external perturbation, which is generally weak. This perturbation can induce finite polarization due to charge redistribution, charge/spin density waves, or plasmonic excitations. The quantity that describes this response of the system is called the response function.
Consider a generic Hamiltonian $\hat{H} = \hat{H}_0 + \hat{H}_1(t)$, where $\hat{H}_1(t) = \theta(t)\hat{U}_1(t)$ is the perturbed, time- (and generally space-) dependent part of the Hamiltonian. The response functions describe the change in the expectation value of an operator $\hat{O}(t)$[1]. If we limit ourselves to linear response theory[2], considering only the first-order response function, we obtain the *Kubo formula* [32, 33]:

$$\delta \langle N| \hat{O}(t) |N\rangle = \int_0^t dt' \langle N| [\hat{H}_1(t), \hat{O}(t)] |N\rangle \tag{1}$$

which describes the variation of the observable, represented by the operator $\hat{O}(t)$, at time t due to a perturbation switched on at $t = 0$. We can express a general form of the interacting part of the Hamiltonian as $\hat{H}_1(t) = \int d\mathbf{r}\, \phi(\mathbf{r}, t)\hat{B}(\mathbf{r})$, where $\phi(\mathbf{r}, t)$ is the external perturbation and $\hat{B}(\mathbf{r})$ is an operator acting on the system. In this way, we can rewrite Eq. (1) as

$$\delta \langle N| \hat{O}(t) |N\rangle = \int dt' \int d\mathbf{r}\, \chi(\mathbf{r}, \mathbf{r}', t - t')\phi(\mathbf{r}', t')$$

where we have defined a (retarded) correlation function $\chi(\mathbf{r}, \mathbf{r}', t - t')$, the so-called *linear response function*:

$$\chi(\mathbf{r}, \mathbf{r}', t - t') = -i\theta(t - t') \langle N| [\hat{O}(\mathbf{r}, t), B(\mathbf{r}', t')] |N\rangle \tag{2}$$

Now, we should consider what happens when our electronic system, where the electrostatic interaction is described via the instantaneous Coulomb potential $v(|r - r'|) = \frac{4\pi}{|r-r'|}$ is perturbed by a longitudinal external potential $\phi(\mathbf{r}, t) = V_{\text{ext}}(\mathbf{r}, t)$. This is physically interpreted as the injection of an external charge into the system. Under the action of this field, the system may react by reorganizing its charge density $\rho(\mathbf{r}, t)$ in an attempt to create an opposing polarization field. This

[1] We consider the operator in the Heisenberg representation.
[2] Indeed, this is the regime where most of the spectroscopic measurements are performed.

results in a variation $\delta\rho(\mathbf{r},t)$, called the induced charge density, which generates a modification of the total potential: $V_{\rm tot} = V_{\rm ext} + V_{\rm ind}$, where $V_{\rm ind}$ is the new induced potential, described classically as

$$V_{\rm ind}(\mathbf{r},t) = \int d\mathbf{r}'\, v(|r-r'|)\delta\rho(\mathbf{r}',t) \tag{3}$$

In this case, the interacting term of the Hamiltonian is

$$\hat{H}_1(t) = \int d\mathbf{r}\, \rho(\mathbf{r},t) V_{\rm ext}(\mathbf{r},t)$$

Using Eq. (1), we obtain the induced charge density as:

$$\delta\rho(\mathbf{r},t) = \int d\mathbf{r}' \int dt'\, \chi(\mathbf{r},\mathbf{r}',t-t') V_{\rm ext}(\mathbf{r}',t') \tag{4}$$

where we have defined the reducible polarizabilty

$$\begin{aligned}\chi(\mathbf{r},\mathbf{r}',t-t') &= -i\theta(t-t')\left\langle N\right|\left[\rho(\mathbf{r},t),\rho(\mathbf{r}',t')\right]\left|N\right\rangle \\ &= \frac{\delta\rho(\mathbf{r},t)}{\delta V_{\rm ext}(\mathbf{r}',t')}\end{aligned} \tag{5}$$

A complete and exhaustive mathematical treatment of this topic is beyond the scope of this Thesis. For more detailed information, we refer the reader to specific references [32, 33]. Here we just show that the polarizability χ can be rewrite in the Fourier space to show its explicit analytic structure

$$\chi(\mathbf{r},\mathbf{r}',\omega) = \sum_i \left[\frac{f_i(\mathbf{r}) f_i^*(\mathbf{r}')}{\omega - \Omega_i + i\eta} + \frac{f_i(\mathbf{r}') f_i^*(\mathbf{r})}{\omega + \Omega_i + i\eta}\right] \tag{6}$$

The quantities $f_i(\mathbf{r})$ are defined as the oscillator strengths of the i-th transition contributing to the excited state of the system. The poles $\Omega_i = E_0^N - E_i^N$ are the exact excitation energies of the interacting N-particle system. The first (second) term of Eq. (6) is defined as the resonant (antiresonant) part of the polarizability χ.
If we now consider a a non-interacting system, and its corresponding ground state, by using Eq. (6) we can define the independent-particle polarizability as:

$$\chi_0(\mathbf{r},\mathbf{r}',\omega) = \sum_{i,i'} \frac{(f_i - f_{i'})\phi_{i'}(\mathbf{r})\phi_i^*(\mathbf{r})\phi_{i'}^*(\mathbf{r}')\phi_i(\mathbf{r}')}{\omega - \omega_{i,i'} + i\eta} + \text{antiresonant} \tag{7}$$

Now the quantities f_i and $\omega_{i,i'} = \epsilon_i - \epsilon_{i'}$ represent the occupation number and the excitation energies in the independent-particle case. For periodic systems, described in a PW basis, Eq. (7) assumes a tensorial form in the reciprocal space:

$$\chi^0_{\mathbf{G}\mathbf{G}'}(\mathbf{q},\omega) = 2\sum_{nm}\int_{BZ}\frac{d\mathbf{k}}{(2\pi)^3}\rho_{nm}(\mathbf{k},\mathbf{q},\mathbf{G})\rho^*_{nm}(\mathbf{k},\mathbf{q},\mathbf{G}')f_{n,\mathbf{k}-\mathbf{q}}(1-f_{m\mathbf{k}}) \times\left[\frac{1}{\omega+\epsilon_{n,\mathbf{k}-\mathbf{q}}-\epsilon_{m\mathbf{k}}+i0^+}-\frac{1}{\omega-\epsilon_{n,\mathbf{k}-\mathbf{q}}+\epsilon_{m\mathbf{k}}-i0^+}\right] \tag{8}$$

where the $\rho_{nm}(\mathbf{k},\mathbf{q},\mathbf{G}) = \langle n\mathbf{k}|\, e^{i(\mathbf{q}+\mathbf{G})\cdot\mathbf{r}}\,|m\mathbf{k}-\mathbf{q}\rangle$ are the dipole matrix elements of orbital pairs, also known as screening matrix elements. The matrix elements ρ_{nm} implicitly contain a delta function of $\mathbf{q}$ and $\mathbf{G}$. The wavevector $\mathbf{q}$ of the absorbed photon is in most cases very small compared to any reciprocal lattice vector $\mathbf{G}\neq 0$. Thus, for optical transitions, the only non-vanishing terms in Eq (8) are those with $\mathbf{G}=\mathbf{G}'=0$.
As already shown throughout this Thesis, to practically compute Eq. (8), the integral over the BZ is transformed into a discrete sum:

$$\int_{BZ}\frac{d\mathbf{k}}{(2\pi)^3}\rightarrow\frac{1}{N_{\mathbf{k}}\Omega}\sum_{\mathbf{k}}$$

Microscopic Dielectric Function

Using Eq. (3) and (4), the total potential V_{tot} can be expressed as a response to the external potential as

$$\begin{aligned}V_{\text{tot}}(\mathbf{r},t) &= V_{\text{ext}}(\mathbf{r},t)+V_{\text{ind}}(\mathbf{r},t)\\ &= V_{\text{ext}}(\mathbf{r},t)+\int dt''\int d\mathbf{r}''\int d\mathbf{r}' v(|\mathbf{r}-\mathbf{r}''|)\chi(\mathbf{r}'',\mathbf{r}',t-t')V_{\text{ext}}(\mathbf{r}',t')\\ &= \int dt'\int d\mathbf{r}'\varepsilon^{-1}(\mathbf{r},\mathbf{r}',t-t')V_{\text{ext}}(\mathbf{r}',t')\end{aligned}$$

where we have defined the inverse microscopic dielectric function

$$\varepsilon^{-1}(\mathbf{r},\mathbf{r}',t-t') = \delta(\mathbf{r}-\mathbf{r}')\delta(t-t')+\int d\mathbf{r}'' v(|\mathbf{r}-\mathbf{r}''|)\chi(\mathbf{r}'',\mathbf{r}',t-t') \tag{9}$$

For periodic systems, using a PW basis and Fourier-transforming in space and time, Eq. (9) reads:

$$\varepsilon^{-1}(\mathbf{q},\omega) = \delta_{\mathbf{G}\mathbf{G}'}+v(\mathbf{q}+\mathbf{G})\chi_{\mathbf{G}\mathbf{G}'}(\mathbf{q},\omega) \tag{10}$$

where the $\mathbf{G}$ are reciprocal lattice vectors, $\mathbf{q}$ is a vector in the first BZ, and the $v(\mathbf{q}+\mathbf{G}) = \frac{4\pi}{|\mathbf{q}+\mathbf{G}|^2}$ is the Fourier transform of the Coulomb interaction. The physical meaning of the total field V_{tot} is now clear: it represents the screened interaction that the electrons (or, more generally, the particles in the system) experience. This interaction is generated partly by the external field and partly by the response of all the charges to it. We can then define the *screened Coulomb interaction* W as:

$$
\begin{aligned}
W_{\mathbf{GG'}}(\mathbf{q},\omega) &= \varepsilon^{-1}_{\mathbf{GG'}}(\mathbf{q},\omega) v(\mathbf{q}+\mathbf{G'}) \\
&= v(\mathbf{q}+\mathbf{G}) + v(\mathbf{q}+\mathbf{G})\chi_{\mathbf{GG'}}(\mathbf{q},\omega)v(\mathbf{q}+\mathbf{G'}) \\
&= v(\mathbf{q}+\mathbf{G}) + W^{p}_{\mathbf{GG'}}(\mathbf{q},\omega)
\end{aligned}
\tag{11}
$$

where, following the notation of Ref. [33], we defined $W^{p}_{\mathbf{GG'}}(\mathbf{q},\omega)$ as the polarization contribution to the screened interaction. It is important to note that this contribution is dynamic, as indicated by its frequency dependence. This represents the momentum-energy (or space-time) response of the system to the external perturbation. It is convenient to our scope to define the irreducible polarizability $\tilde{\chi}$, starting from Eq. (5), as[3]:

$$
\tilde{\chi}(\mathbf{r},\mathbf{r'},t-t') = \frac{\delta\rho(\mathbf{r},t)}{\delta V_{\mathrm{tot}}(\mathbf{r'},t')} \tag{12}
$$

If we expand the functional derivative of Eq. (5) in terms of V_{tot} and use Eq. (12), we obtain the Dyson equation for the reducible polarizability:

$$
\chi = \tilde{\chi} + \tilde{\chi} v \chi
$$

which gives us the solution, written in PW basis:

$$
\chi_{\mathbf{GG'}}(\mathbf{q},\omega) = [\delta_{\mathbf{GG'}} - v(\mathbf{q}+\mathbf{G''})\tilde{\chi}_{\mathbf{GG''}}(\mathbf{q},\omega)]^{-1}\tilde{\chi}_{\mathbf{G''G}}(\mathbf{q},\omega) \tag{13}
$$

which is the fundamental result of this section. Starting from Eq. (13), it is common to set $\tilde{\chi}$ equal to the independent-particle polarizability χ_0 (8), obtaining:

$$
\chi_{\mathbf{GG'}}(\mathbf{q},\omega) = \chi^{0}_{\mathbf{GG'}}(\mathbf{q},\omega) + \sum_{\mathbf{G''}} \chi^{0}_{\mathbf{GG''}}(\mathbf{q},\omega) v(\mathbf{q}+\mathbf{G''})\chi_{\mathbf{G''G'}}(\mathbf{q},\omega) \tag{14}
$$

This allows to partially solve the many-body problem of charged excitations.
Within the time-dependent DFT (TDDFT) formalism, Eq. (14) is often rewritten as:

$$
\chi_{\mathbf{GG'}}(\mathbf{q},\omega) = \chi^{0}_{\mathbf{GG'}}(\mathbf{q},\omega) + \sum_{\mathbf{G_2},\mathbf{G''}} \chi^{0}_{\mathbf{GG_2}}(\mathbf{q},\omega)[v(\mathbf{q}+\mathbf{G_2})\delta_{\mathbf{G_2},\mathbf{G''}} + f^{\mathrm{xc}}_{\mathbf{G_2},\mathbf{G''}}]\chi_{\mathbf{G''G'}}(\mathbf{q},\omega) \tag{15}
$$

where f^{xc} is the XC kernel, defined as the functional derivative of the XC potential V_{xc} with respect to the density. Naturally, this kernel is not known exactly and must be approximated, similar to how V_{xc} is treated in standard DFT.

[3] This is often denoted as P, see Sec. 3.5

Macroscopic Dielectric Function and Local-Field Effects

Microscopic quantities are generally local both in space and time, such as $\varepsilon^{-1}(\mathbf{r}, \mathbf{r}', t-t')$. However, their macroscopic counterparts must be represented by averaging the microscopic quantities. This averaging allows us to transition from microscopic to macroscopic quantities, such as absorption or energy loss spectra. According to Eq. (10), the dielectric function can be obtained from the reducible polarizability as

$$\varepsilon^{-1}(\mathbf{q}, \omega) = \delta_{\mathbf{G}\mathbf{G}'} + v(\mathbf{q}+\mathbf{G})\chi_{\mathbf{G}\mathbf{G}'}(\mathbf{q}, \omega) \tag{16}$$

The average procedure connecting the microscopic properties to the macroscopic quantities can be performed in two ways. In Chapter IV, for Eq. (3.46) it was assumed that, for optical transitions, $\mathbf{G} = \mathbf{G}' = 0$ and $\mathbf{q} \to 0$, and the average was taken directly in ε by setting $\mathbf{G} = \mathbf{G}' = 0$, i.e.,

$$\varepsilon_{\mathrm{M}}(\omega) = \lim_{\mathbf{q}\to 0} \varepsilon_{\mathbf{G}=\mathbf{G}'=0(\mathbf{q},\omega)} \tag{17}$$

However, from Eq. (3.41) we see that the total electric field $\mathbf{E}$ is related to the applied field $\mathbf{D}$ as $\mathbf{E} = \varepsilon^{-1}\mathbf{D}$. Therefore, it is more correct to take the average on ε^{-1} [33, 41] as

$$\epsilon_{\mathrm{M}}(\omega) = \lim_{\mathbf{q}\to 0} \frac{1}{[\epsilon^{-1}(\mathbf{q}, \omega)]_{\mathbf{G}=\mathbf{G}'=0}} \tag{18}$$

Eq. (17) and (18) are equal only if the dielectric matrix is diagonal in $\mathbf{G}$, $\mathbf{G}'$, which is not the case in realistic solids[4]. In real materials, the inhomogeneity of the density distribution leads to internal electric fields, known as *local fields*, which vary over distances comparable to the lattice constant. These *local-field effects* (LFE) can be significant in spectroscopies because they account for the fact that all elements in the dielectric matrix contribute to a single element of the inverse matrix. The macroscopic dielectric function without local-field effects, given in Eq. (17), is an approximation which is usually valid for delocalized states for which the electronic density is more homogeneous. However, for transitions involving localized states (like d states), the local fields are more important and one should use Eq. (18).
In the long-wavelength limit (i.e. vertical transitions), this allows us to compute the photoabsorption spectrum[5] as

$$\mathrm{Abs}\,(\omega) = \mathrm{Im}\,\varepsilon_{\mathrm{M}}(\omega)$$

The macroscopic dielectric function is not simply the reciprocal of the head of the matrix $\varepsilon(\mathbf{q}, \omega)$, but rather the reciprocal of the first element of its inverse. This definition effectively mixes all the $\mathbf{G}, \mathbf{G}'$ components when performing the inversion. The physical reason for this method is that an external perturbation induces charge fluctuations and potentials at both macroscopic (described by the long-range part $\mathbf{G} = 0$) and microscopic (short-range, $\mathbf{G} \neq 0$) levels. By including these short-range effects (the LFE), we account for the inhomogeneity of the system and accurately describe experiments that probe shorter distances with increasing momentum transfer.

[4] It holds only for the homogeneous electron gas.

[5] More precisely, the absorption signal is defined by the absorption coefficient $\alpha(\omega) \propto \omega \frac{\mathrm{Im}\,[\varepsilon_{\mathrm{M}}(\omega)]}{\mathrm{Re}\,[n(\omega)]}$, $n(\omega)$ being the refractive index. Anyhow, in general, its frequency dependence is generally well captured by the sole $\mathrm{Im}\,\varepsilon_{\mathrm{M}}(\omega)$.

Appendix B

Excited-State Calculations of Isolated Systems

The application of excited-state calculations to finite systems dates back to the origins of these methods [323]. Over the following decades, there has been increasing interest in studying the excited states of atoms, molecules, and clusters [324–329]. This interest has been partly driven by the need to develop efficient techniques to address mixed systems, such as molecular junctions, and to characterize nanostructured architectures. Historically, MBPT-derived methods have been implemented in PW basis set algorithms, which posed practical challenges, particularly in terms of convergence, when calculating isolated or finite systems compared to extended periodic systems.
In this context, it is advantageous to use a code that combines the accuracy of GW-BSE calculations with the precision of localized basis sets, which are better suited to describing spatially finite systems. The MOLGW code [322], selected for the calculations of isolated systems (see Sec. 6.1) performed in this Thesis, implements both DFT and MBPT within a Gaussian basis set framework. The code includes the implementation of the GW approximation (Sec. 3.5.1) and the solution of the BSE (Sec. 3.8.4) for evaluating electronic levels and optical spectra, respectively. In MOLGW, the process begins with the calculation of the ground-state properties of the system within DFT. Various XC functionals are implemented, including standard LDA, GGA (Sec. 2.3.4), and hybrid functionals, such as B3LYP and HSE06 (Sec. 2.3.7). There is also the option to perform a preliminary HF calculation, which can be used as a starting point for the self-consistent ground-state calculations. The resulting output provides single-particle eigenvalues and eigenfunctions, which are then used to construct the screening matrix and the QP Green's function for the subsequent steps. QP calculations can be performed at different levels of approximation, specifically, one-shot (G_0W_0) or eigenvalue self-consistent GW (evGW), as discussed in Sec. 3.6.3. Finally, after computing the screening and obtaining the eigenvalues from the GW calculation and the KS (or HF) eigenfunctions, the BSE is solved to obtain the photoabsorption spectra.

Basis Sets

In the condensed matter physics community, most DFT and MBPT codes are based on periodic boundary conditions, with Bloch wavefunctions expanded over a PW basis sets. In contrast, within the quantum chemistry community, the standard approach is to expand molecular orbitals (MOs), $\phi_i(r)$, using localized basis sets such as Slater-type, Gaussian-type, or numerical atomic orbitals [330]:

$$\phi_i(r) = \sum_{\alpha=1}^{N} C_{\alpha,i} G_\alpha(r) \tag{19}$$

where $G_\alpha(\mathbf{r})$ are the fixed basis functions and $C_{\alpha i}$ are the coefficients determined by solving the self-consistent calculations. In this Thesis, both the self-consistent Kohn-Sham equations of DFT (or HF) and the MBPT equations are solved using the MOLGW code. In MOLGW, a Gaussian-type orbital (GTO) basis is preferred over the more formally accurate Slater-type orbitals (STOs) due to the more efficient computation of single-particle and two-particle molecular integrals. Fig. 1 illustrates the difference between a Slater orbital and a single Gaussian orbital.
A single (primitive) Gaussian function can be expressed in "pure" spherical form as (see Fig. 2 for s, p, and d orbitals):

$$g_v(r) = Y_{lm}(\theta, \varphi)\, r^l e^{-z_v(x^2+y^2+z^2)}$$

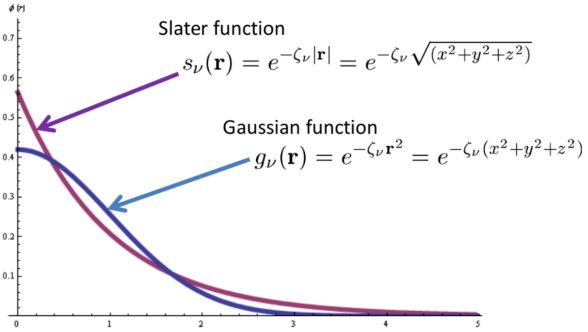

Figure 1: *Comparison between Slater and Gaussian functions. The Slater function has a cusp at the origin and a slower decay than the Gaussian function.*

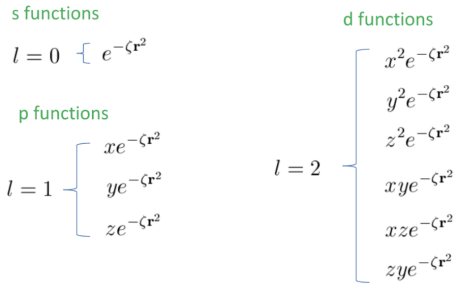

Figure 2: *Cartesian Gaussian functions for describing orbitals with $l = 0, 1, 2$.*

Since a single Gaussian cannot accurately describe a STO, it is common practice to use a linear combination of primitive Gaussian functions to better approximate a Slater function. This combination, known as a "Contracted Gaussian" (CG), is written as:

$$G_\alpha(r) = \sum_{v=1}^{N_\alpha} = c_v g_v(r)$$

The expansion coefficients c_v are fixed in the contracted Gaussians, which serve as the basis functions introduced in Eq. (19). The simplest type of Gaussian basis sets are the minimal basis STO-nG type. These basis sets attempt to approximate each STO by a single contracted Gaussian composed of n primitive Gaussians. It is evident that, as the number of Gaussians increases, the approximation of the Slater function improves. The flexibility of a basis set can be enhanced by including one CG for each inner shell orbital and more than one CG for each valence shell orbital.

This approach, described by Pople [331], leads to the nomenclature x-yzG, where x indicates the number of primitive Gaussians used for each core orbital. The valence orbitals are represented by two CGs, each consisting of a linear combination of y and z primitive Gaussians, respectively. Valence orbitals are generally described using two, three, four, or five CGs, and are commonly referred to as Double, Triple, Quadruple, or Quintuple Zeta. These basis sets are known as "split valence" or "double zeta" (DZ) sets.
Further improvements to describe MOs are obtained by adding other types of CGs in the expansion such as *polarization* and *diffuse functions*:

- "Polarization functions" offer higher basis set flexibility by helping to describe the formation of chemical bonds in any direction within molecules.
- "Diffuse functions" having a low exponent improve the predicted properties of species with extended electronic densities such as anions or molecules forming hydrogen bonds.

Both polarization and diffuse functions and another improvements are included in basis sets developed by Dunning [332] and which are one of the most widely used basis sets in post-HF and post-DFT calculations. For this set the typical nomenclature is (aug)-cc-pVαZ, where:

- "cc" stands for correlation-consistent: these sets have been developed using post-HF methods to better describe e-e repulsion beyond the average coulomb Hartree and exchange terms.
- "p" indicates the presence of successively larger shells of polarization (correlating) functions (d, f, g, etc.).
- "V" indicates they are valence-only basis sets.
- The presence of "aug" means that the sets are augmented with further diffuse functions in order to describe extended electronic densities.
- The αZ indicates the size (zeta) of the basis (number of CGs for each atomic orbital).

Auxiliary Basis Sets

While standard atomic orbital basis sets are used to expand one-electron functions, such as molecular orbitals, auxiliary basis sets are often employed in quantum chemistry codes to efficiently approximate products of one-electron functions, which arise in the evaluation of four-center integrals. For a molecule of fixed size, increasing the number of basis functions per atom, n, leads to an $O(n^4)$ growth in the number of significant four-center (two-electron) integrals. Consequently, using large (high-quality) basis expansions becomes computationally expensive. The most practical solution to this "basis set quality" bottleneck is the use of auxiliary basis expansions. The auxiliary basis $\{|K\rangle\}$ is used to approximate products of Gaussian basis functions:

$$|\mu\nu\rangle \approx |\bar{\mu\nu}\rangle = \sum_K |K\rangle\, C^K_{\mu\nu}$$

The use of auxiliary basis expansions is also known as resolution of the identity (RI) or density fitting (DF). When employing auxiliary basis expansions, the rate of growth in computational cost for large-scale electronic structure calculations with increasing n is reduced to approximately $O(n^3)$.

Appendix C

Non-Linear Optics

The effects of an electric field $\mathcal{E}$ on a material can be understood in terms of the polarization P it induces. Polarization represents the dipole moment per unit volume resulting from the charge displacements caused by the electric field. These effects are mathematically described by a response function or susceptibility, $\chi(\mathcal{E})$, which quantifies the relationship between the electric field $\mathcal{E}$ and the polarization P. Although this response function generally depends on the intensity of the electric field, it is often a good approximation to neglect this dependency,

$$P = \chi(\mathcal{E})\mathcal{E} \quad \rightarrow \quad P = \chi\,\mathcal{E} \tag{20}$$

where the tensorial nature of these variables is ignored for simplicity, as well as their time and space dependencies. Eq. (20) embodies the physics of the linear regime, which captures the predominant effects of optical excitations and successfully describes a wide variety of optical phenomena, e.g., absorption.
The linearity proposed in Eq. (20) can be seen as the leading term of an expansion in powers of the electric field,

$$P = \chi^{(1)}\mathcal{E} + \chi^{(2)}\mathcal{E}^2 + \chi^{(3)}\mathcal{E}^3 + \mathcal{O}(\mathcal{E}^4) \tag{21}$$

where $\chi^{(n)}$ is the n-th order susceptibility [333] and is, in general, a tensor. The fact that higher-order response functions are several orders of magnitude smaller than $\chi^{(1)}$ explains why non-linear effects only become significant at high-intensity electric fields. Such high-intensity fields became available only after the invention of the laser in 1960, which provided a highly coherent, high-intensity monochromatic light beam. This advancement enabled the observation of second optical harmonics in crystalline quartz [334], marking the first non-linear optics experiment of the laser era. This milestone ushered in a new chapter in the field of non-linear optics, which has since continued to thrive and evolve.
Advancements in this field have led to several applications, notably non-linear optical spectroscopies, which have become invaluable tools for investigating material properties. This is primarily due to second harmonic generation (SHG) and its dependence on symmetry: SHG is forbidden in systems with inversion symmetry. Consequently, SHG has traditionally been employed to study surfaces and interfaces [335–337], and more recently, to characterize and image two-dimensional materials [338–341]. Additionally, SHG serves as a highly sensitive probe for magnetic ordering in atomically thin materials [342–344] and multiferroics [345, 346]. In particular, SHG is a valuable

tool for investigating two-dimensional antiferromagnets, especially when a phase transition breaks inversion symmetry. This capability bridges a gap between traditional magnetometric techniques, which require large sample volumes, and magneto-optical Kerr effect microscopies, which detect two-dimensional magnetism only if the net magnetization is non-zero, typically applicable to ferromagnets [347]. Furthermore, due to its sensitivity to changes in electric polarization, SHG can also probe the dynamics of excited systems, such as tracking exciton formation, exciton-phonon coupling, and the demagnetization of antiferromagnets [348, 349].
The non-linear optical regime is typically addressed with non-perturbative methods based on explicit time propagation, which makes them computationally costly. We tackle this issue by proposing a reformulation of the so-called *real-time approach* [201] based on Floquet theory, which leads to a self-consistent time-independent eigenvalue problem.

Real-Time Approach

We consider the Hamiltonian of a crystalline solid coupled to a time-dependent electric field, namely

$$\hat{H} = \hat{H}_0 + \hat{H}_{\mathcal{E}}$$

where $\hat{H}_0$ is the unperturbed Hamiltonian in the absence of an external field, and $\hat{H}_{\mathcal{E}}$ represents the perturbation due to the electric field. The Bloch eigenstates of the cell-periodic part of the unperturbed Hamiltonian, $e^{-i\mathbf{k}\cdot\mathbf{r}}\hat{H}_0 e^{i\mathbf{k}\cdot\mathbf{r}}$, are denoted as $\mu_{n\mathbf{k}}(\mathbf{r})$. The wavefunctions $\psi_{n\mathbf{k}}(\mathbf{r}) = e^{i\mathbf{k}\cdot\mathbf{r}}\mu_{n\mathbf{k}}(\mathbf{r})$ are the eigenstates of the unperturbed Hamiltonian $\hat{H}_0$. In this context, the periodic part of these functions is referred to as the zero-field time-zero states, $|\mu_{n\mathbf{k}}\rangle$, which will be used as the starting point for time integration or as a basis. In practice, these time-zero states are defined at the DFT level, i.e., $\psi_{n\mathbf{k}}(\mathbf{r}) \equiv \phi^{\mathrm{KS}}_{n\mathbf{k}}(\mathbf{r})$.

Equation of Motion

The real-time approach to non-linear optics discussed in this Thesis follows the methodology established by Refs. [201, 350, 351], and is based on the scheme introduced by Souza et al. [202] for dynamical Berry-phase polarization. In this formalism, the central elements are the time-dependent Bloch states, $|v_{n\mathbf{k}}\rangle$, which represent the periodic part of the states. These are expressed as $\psi_{n\mathbf{k}}(\mathbf{r}, t) = e^{i\mathbf{k}\cdot\mathbf{r}} v_{n\mathbf{k}}(\mathbf{r}, t)$. The states $|v_{n\mathbf{k}}\rangle$ are obtained by time-evolving the time-zero states $|\mu_{n\mathbf{k}}\rangle$ according to the equation of motion (EOM),

$$\left(\hat{H}^{\mathrm{eff}}_{\mathbf{k}} - i\partial_t\right)|v_{n\mathbf{k}}\rangle = 0 \tag{22}$$

coupled with the boundary condition

$$|v_{n\mathbf{k}}\rangle\,(t=0) = |\mu_{n\mathbf{k}}\rangle$$

and the effective Hamiltonian

$$\hat{H}^{\mathrm{eff}} = \hat{H}_0 + \hat{W}(\mathcal{E}) \tag{23}$$

The unperturbed Hamiltonian $\hat{H}_0$ in Eq. (23) is a single-particle operator that varies depending on the level of theory employed [350–352]. The perturbation, $\hat{W}(\mathcal{E})$, represents the interaction with the external field $\mathcal{E}$.
The real-time approach is then based on integrating the EOM (22) numerically, using a suitable integration method. This process is carried out in Kohn-Sham space, resulting in several EOMs for the projections $\langle \mu_{i\mathbf{k}} | v_{n\mathbf{k}} \rangle(t)$. The accuracy and stability of this numerical integration depend on using a short time step, typically in the range of 1-10 attoseconds. This time step is material-dependent and reflects the rate at which the dynamics of a given system evolve. Ultimately, having access to the time-dependent Bloch states $|v_{n\mathbf{k}}\rangle$ allows us to compute dynamical properties, such as polarization as a function of time. From this, susceptibilities of any order with respect to the electric field can be extracted.

Levels of Theory

In the real-time approach, three main levels of theory are considered for electron-electron correlation, each manifesting in the expressions for the effective Hamiltonian in Eq. (23). We start with the IPA level [201, 350, 351], i.e.

$$\hat{H}^{\mathrm{IPA}} = \hat{H}_0^{\mathrm{IPA}} + \hat{W}(\mathcal{E}) = \hat{H}^{\mathrm{KS}}[\rho_0] + \hat{\Delta}_{\mathrm{QP}}[\rho_0] + \hat{W}(\mathcal{E}) \tag{24}$$

Here, $\hat{H}_0^{\mathrm{IPA}}$ represents the corresponding unperturbed Hamiltonian. This includes the KS Hamiltonian, $\hat{H}^{\mathrm{KS}}[\rho_0]$, which is a functional of the ground-state density ρ_0, as well as the QP corrections, $\hat{\Delta}_{\mathrm{QP}}[\rho_0]$. These QP corrections could be as simple as a rigid shift (scissor operator) or more complex, involving corrections obtained from a G_0W_0 scheme, which formally depend on the ground-state density matrix. In any case, $\hat{H}_0^{\mathrm{IPA}}$ is a functional of only ground-state quantities and is therefore time-independent. The time dependence of the effective Hamiltonian at the IPA level is thus confined to the electron-field coupling operator, $\hat{W}(\mathcal{E})$.
The first step beyond the IPA level is to include the Hartree potential, $V_{\mathrm{H}}[\rho]$, in the effective Hamiltonian [201, 350, 351],

$$\hat{H}^{\mathrm{TDH}} = \hat{H}^{\mathrm{KS}}[\rho_0] + \hat{\Delta}_{\mathrm{QP}}[\rho_0] + V_{\mathrm{H}}[\rho] + \hat{W}(\mathcal{E}) \tag{25}$$

which represents the so-called time-dependent Hartree (TDH) level. The Hartree term is simply the classical Coulomb potential originating from the time-dependent electron density. The ground-state Hartree potential is already taken into account at the DFT level (see Sec. 2.3) and, therefore, included in $\hat{H}_0^{\mathrm{IPA}}$. As a result, the Hartree potential added at the TDH level should represent the difference respect to the ground-state contribution. This is achieved by subtracting the ground state density, i.e. $\hat{V}_{\mathrm{H}}[\rho - \rho_0]$.
Finally, we address the inclusion of correlation effects in the real-time approach. In principle, this could be achieved by adding a time-dependent exchange-correlation functional to Eq. (25), thus reaching the TDDFT level. However, the currently available approximations to this functional face limitations when attempting to describe excitons in extended systems [61], as previously discussed. Therefore, we opt to incorporate correlation effects by adding the screened-exchange self-energy, $\hat{\Sigma}^{\mathrm{SEX}}[\rho]$, into the effective Hamiltonian [201, 350, 351], obtaining

$$\hat{H}^{\mathrm{H+SEX}} = \hat{H}^{\mathrm{KS}}[\rho_0] + \hat{\Delta}_{\mathrm{QP}}[\rho_0] + V_{\mathrm{H}}[\rho] + \hat{\Sigma}^{\mathrm{SEX}}[\rho] + \hat{W}(\mathcal{E}) \tag{26}$$

as a functional of the density matrix. This approximation is sometimes called TD-BSE. We will refer to this as the Hartree plus screened exchange (H+SEX) level of theory[6]. However, H-SEX can sometimes be computationally demanding. In such cases, additional approximations are necessary. This will be discussed further in the next section.
The real-time approach incorporates electron-electron correlation within a non-perturbative framework, enabling the description of excitonic effects in non-linear optical phenomena [201, 351]. A key advantage of this approach is evident in Eqs. (24)-(26): the inclusion of many-body effects is as straightforward as adding terms to the effective Hamiltonian in Eq. (22) [351]. This flexibility stands in stark contrast to perturbative methods, where the complexity of the formulations increases significantly as correlation effects are incorporated into the formalism (e.g., [353]).

Long-Range Screened Exchange (LSEX) Approximation

In real-time simulations, time-dependent electric fields are essential for computing the time evolution of the polarization response. However, introducing a time-dependent electric field breaks time-reversal symmetry. This presents a significant challenge, particularly for systems with a large number of electrons, such as when SOC is included, and when dense **k**-grids are used. Most computational codes for simulating periodic systems rely on symmetries to reduce computational costs and enhance performance, making the inclusion of time-dependent fields computationally demanding. Additionally, as discussed in Sec. 4.2 for bilayer MoS_2, a static electric field can induce a non-linear response, further breaking additional symmetries. This adds to the complexity of simulating such systems.
To incorporate excitonic effects into real-time dynamics, we derive a simplified screened exchange term, which we defined as long-range screened exchange (LSEX). As a starting point, we refer to the Appendix of Ref. [350]. The Kadanoff-Baym equation includes the matrix elements $\langle m, \mathbf{k}| \hat{\Sigma}^{\mathrm{SEX}} |m', \mathbf{k}\rangle$:

$$\Sigma^{\mathrm{SEX}}_{mm',\mathbf{k}}(t) = i \sum_{n,n'} \sum_{\mathbf{G},\mathbf{G}',\mathbf{q}} \rho_{mn}(\mathbf{k},\mathbf{q},\mathbf{G}')\rho^*_{m'n'}(\mathbf{k},\mathbf{q},\mathbf{G})\, W_{\mathbf{G},\mathbf{G}'}(\mathbf{q})\, \Delta\gamma_{\substack{nn' \\ \mathbf{k}-\mathbf{q}}}(t) \tag{27}$$

where $\Delta\gamma$ is the variation of the density matrix, and:

$$\rho_{mn}(\mathbf{k},\mathbf{q},\mathbf{G}) = \int \varphi^*_{m,\mathbf{k}}(\mathbf{r})\varphi_{n,\mathbf{k}-\mathbf{q}}(\mathbf{r})e^{i(\mathbf{G}+\mathbf{q})\cdot\mathbf{r}}$$

The LSEX approximation involves retaining only the long-range component of the screened interaction, i.e., $W(\mathbf{q}) = W_{\mathbf{G}=0,\mathbf{G}'=0}(\mathbf{q})$. Therefore, Eq. (27) simplifies to:

$$\Sigma^{\mathrm{LSEX}}_{mm',\mathbf{k}}(t) = i \sum_{n,n'} \sum_{\mathbf{q}} \rho_{mn}(\mathbf{k},\mathbf{q})\rho^*_{m'n'}(\mathbf{k},\mathbf{q})\, W(\mathbf{q})\, \Delta\gamma_{\substack{nn' \\ \mathbf{k}-\mathbf{q}}}(t) \tag{28}$$

[6]Notably, the TDH and H+SEX levels of theory reduce to the RPA and the BSE, respectively, in the linear response limit [350]

By noting that the density matrix can be expanded as:

$$\Delta\gamma_{nm,\mathbf{k}}(t) = \sum_{l=1}^{N_v} \langle u_m|v_{l\mathbf{k}}\rangle\langle v_{l\mathbf{k}}|u_n\rangle - \delta_{nm} f(\epsilon_{n\mathbf{k}})$$

where l is an index running over valence bands, n, n', m, m' are indeces over all bands, and $f(\epsilon_{n\mathbf{k}})$ are the occupation functions, we can rewrite Eq (28) as:

$$\Sigma^{\mathrm{LSEX}}_{mm',\mathbf{k}} = i \sum_{l,n,n'} \sum_{\mathbf{q}} \rho_{mn}(\mathbf{k},\mathbf{q})\rho^*_{m'n'}(\mathbf{k},\mathbf{q})\, W(\mathbf{q})\, \langle u_{n'}|v_{l\mathbf{k-q}}\rangle\langle v_{l\mathbf{k-q}}|u_n\rangle - \Sigma^{\mathrm{eq}}_{mm',\mathbf{k}} \tag{29}$$

where Σ^{eq} is the self-energy at equilibrium, defined as:

$$\Sigma^{\mathrm{eq}}_{mm',\mathrm{eq}} = i \sum_{n} \sum_{\mathbf{q}} \rho_{mn}(\mathbf{k},\mathbf{q})\rho^*_{m'n'}(\mathbf{k},\mathbf{q})\, W(\mathbf{q})\, f(\epsilon_{n\mathbf{k-q}})$$

We then define the oscillators ρ between time-dependent valence bands and Kohn-Sham states as:

$$\tilde{\rho}_{ml}(\mathbf{k},\mathbf{q}) = \sum_{n} \rho_{mn}(\mathbf{k},\mathbf{q})\langle v_{l\mathbf{k-q}}|u_n\rangle$$

and Eq. (29) reduces to:

$$\Sigma^{\mathrm{LSEX}}_{mm',\mathbf{k}} = i \sum_{l}^{N_v} \sum_{\mathbf{q}} \tilde{\rho}_{ml}(\mathbf{k},\mathbf{q})\, W(\mathbf{q})\, \tilde{\rho}_{m'l}(\mathbf{k},\mathbf{q}) - \Sigma^{\mathrm{eq}}_{mm',\mathbf{k}} \tag{30}$$

To be consistent with this approximation, we excluded the LFE in the dynamics. This approach is similar to that used in simple models, with the key difference that we explicitly calculate the matrix elements of the Coulomb interaction between different bands at finite $\mathbf{q}$.
We tested this approximation on monolayer WSe_2 and bilayer MoS_2, comparing the results with available experimental measurements (see Fig. 10 of Appendix E). We found that only a few $\mathbf{G}$-vectors (see Eq. (27)) are required to reproduce the first excitons, while peaks at higher energies demand a larger number of $\mathbf{G}$-vectors. This makes the approach less appropriate, if compared to the one in Ref. [350], for the description of the full spectrum, but very advantageous if one is interested only in the lowest excitonic peaks.

The Berry-Phase Formulation

In extended systems, direct coupling to the electric field in the length gauge, $-e\mathbf{rE}$, should be avoided because the position operator is ill-defined under periodic boundary conditions [354–356]. In the linear regime, this issue is typically circumvented using the commutation relation $[\hat{H}, \hat{r}] = \hat{p} + [\hat{V}_{\mathrm{NL}}, \hat{r}]$, where $\hat{V}_{\mathrm{NL}}$ is the non-local part of the Hamiltonian. However, since the real-time approach aims to describe non-linear optical processes, an electron-field coupling operator that remains valid beyond the linear regime is required. This challenge is addressed through a Berry-phase formulation

of the dynamical polarization, leading to a dipole operator expressed as a covariant k-derivative. This formulation is incorporated into the electron-field coupling operator [202],

$$\hat{W}_{\mathbf{k}}(\mathcal{E}) = \hat{w}_{\mathbf{k}}(\mathcal{E}) + \hat{w}^{\dagger}_{\mathbf{k}}(\mathcal{E}) \tag{31}$$

In Eq. (31), $\hat{w}_{\mathbf{k}}(E)$ is the electron-field coupling operator in its Berry-phase formulation, as outlined in Refs. [201] and [202].
Within this Berry-phase framework [202], the Lagrangian of the system gives rise to the EOMs for the time-dependent Bloch states, which are central to the real-time approach described in Eq. (22) [201, 351]. As discussed earlier, by numerically integrating Eq. (22), we can obtain the time-dependent states $|v_{n\mathbf{k}}\rangle$ at each time step t_i. These states allow us to update the overlaps $[S_{\mathbf{k}\mathbf{k}^{\sigma}_{\alpha}}]_{nm} = \langle v_{n\mathbf{k}} | v_{m\mathbf{k}^{\sigma}_{\alpha}} \rangle$, defined as

$$[S_{\mathbf{k}\mathbf{k}^{\sigma}_{\alpha}}]_{nm} = \langle v_{n\mathbf{k}} | v_{m\mathbf{k}^{\sigma}_{\alpha}} \rangle \tag{32}$$

where the state $\left|v_{m\mathbf{k}^{\sigma}_{\alpha}}\right\rangle$ is the so-called dual of the state $|v_{n\mathbf{k}}\rangle$. Ultimately, the overlaps in Eq. (32) can be used to compute the polarization using the Berry-phase formulation:

$$\mathbf{P}_{\alpha} = -\frac{ef}{2\pi v}\frac{\mathbf{a}_{\alpha}}{N^{\perp}_{\alpha}}\sum_{\mathbf{k}^{\perp}_{\alpha}} \mathrm{Im}\left[\ln\left(\prod_{i=1}^{N^{\parallel}_{\alpha}-1}(S_{\mathbf{k}_i\mathbf{k}^{\sigma}_{\alpha}})\right)\right] \tag{33}$$

with the electron charge e, occupation factor f, unit cell volume v. Eq. (33) provides the dynamical polarization in the direction α of the lattice vector $\mathbf{a}_{\alpha}$. The corresponding reciprocal lattice vector $\mathbf{b}_{\alpha}$ is used to determine the number of $\mathbf{k}$-points in a string along its direction, $N^{\parallel}_{\alpha}$, as well as the number of $\mathbf{k}$-points in a plane perpendicular to $\mathbf{b}_{\alpha}$, namely $N^{\perp}_{\alpha}$.

Response Functions

In the regime where the dynamical polarization is time-periodic, with the same periodicity as the perturbation, ω_0, it can be expressed as a Fourier series:

$$P(t) = \sum_{n} p^{(n)} e^{in\omega_0 t} \tag{34}$$

where scalar magnitudes are used for simplicity. In addition, one can consider its expansion in orders of the electric field E (21),

$$P(t) = \chi^{(1)}\mathcal{E}(t) + \chi^{(2)}\mathcal{E}^2(t) + \chi^{(3)}\mathcal{E}^3(t) + \mathcal{O}(\mathcal{E}^4(t)) \tag{35}$$

The tensor nature and time dependence of the susceptibilities $\chi^{(n)}$ are omitted for brevity. By comparing Eqs. (34) and (35), we can extract susceptibilities of any order. The relationship between the Fourier coefficients $p^{(n)}$ and the corresponding susceptibilities depends on both the order n and the form of the electric field, which is typically chosen to be a sine function, $(e^{i\omega_0 t} - e^{-i\omega_0 t})/2i$.

This procedure highlights another significant advantage of the real-time approach. As a non-perturbative method, it enables the simultaneous determination of susceptibilities at various orders in the electric field. This is made possible by the use of a Berry-phase-derived electron-field coupling operator, which remains valid at all orders of the electric field. In contrast, perturbative approaches require distinct formulations for each order of susceptibility they aim to calculate.

Dephasing

The electronic systems examined in this Thesis are considered perfectly isolated due to the approximations employed, such as the Born-Oppenheimer approximation and fixed nuclei. This means that important dissipative effects, such as inelastic electron scattering or interactions with other degrees of freedom like phonons or defects, are neglected. These dissipative processes represent the interaction of electrons with their environment and contribute to the decay of excited electronic populations, thus providing a finite lifetime for excitations. Omitting these effects results in an incomplete representation of the dynamics of open systems.
To address this limitation, dissipative effects are included phenomenologically in the real-time approach through a dephasing term. This involves incorporating, to the EOM for $|v_{n\mathbf{k}}\rangle$ (22), a dephasing operator,

$$\mathbf{\Gamma}_{ph} = -i\nu \left(|v_{n\mathbf{k}}\rangle \langle v_{n\mathbf{k}}| - |\mu_{n\mathbf{k}}\rangle \langle \mu_{n\mathbf{k}}| \right) \tag{36}$$

In Eq. (36), ν is a positive number, with the dimension of an energy, chosen to provide a desired broadening to the spectra. In the EOMs, this operator acts as a restoring force proportional to the departure of the state $|v_{n\mathbf{k}}\rangle$ from equilibrium, $|\mu_{n\mathbf{k}}\rangle$, thus limiting the population of empty states upon excitation.
Another role of the dephasing term is to address the requirement that, to extract non-linear response functions at frequency ω_0, the system must be driven by a monochromatic perturbation of the same frequency. This ensures that the resulting dynamical polarization is time-periodic with the same period, which is essential for expanding it as a Fourier series (see Eq. (34) and extracting the non-linear susceptibilities as described above. Only under these conditions can one ensure that, for instance, $p^{(2)}$ from Eq. (34) accurately reflects $\chi^{(2)}$ from Eq. (35). In a real-time calculation, the system is initially perturbed by an electric field at t_0, which is typically non-periodic. This initial perturbation introduces transient excitations across all electronic transitions in the material. To address this, the dephasing term is used to suppress these unwanted excitations, allowing the system to settle into a regime where it is primarily driven by a monochromatic electric field with frequency ω_0 for $t \gg t_0$. Once this periodic state is achieved, the dynamical polarization becomes time-periodic with the same frequency as the perturbation, and non-linear susceptibilities can be accurately extracted. The duration of simulated time required to reach this stable periodic regime, and thus to properly dephase the response, is a critical convergence parameter for the real-time approach.

Appendix D

Supplementary Material of "Tellurene Polymorph for Solar Harvesting Applications"

Electronic Structure

The DFT band structures are shown in Fig. 3 (dashed red lines) and the information about the band gaps are summed up in Table II. 2L α-Te is a semiconductor with an indirect gap of 0.67 eV (Fig. 3a), while the minimum direct gap is of about 0.86 eV. 1L β-Te is a direct gap semiconductor, with an electronic gap (located at Γ) of 1.02 eV (Fig. 3c). Similarly to 2L α-Te, 1L γ-Te is a semiconductor with an indirect gap of 0.42 eV, whereas the lowest direct gap (at Γ) is 0.54 eV (Fig. 3e). For a detailed discussion of the DFT results, we refer the reader to our previous work [167].
Overall, the DFT bands dispersions are only slightly modified by the many-body e-e interaction, and an almost rigid shift appears. The calculated QP band gaps are about 1 eV larger than the DFT ones (see Table 4.2). In the case of the 2L α-Te allotrope, we observe a significant change in its indirect gap, from 0.67 to 1.31 eV, when incorporating many-body effects. Additionally, the direct gap is found to be about 1.51 eV (Fig. 3a). To the best of our knowledge, these are the first reported many-body calculations for such a system. Regarding 1L β-Te, we find that this phase exhibits a QP-corrected direct gap of 1.96 eV at the Γ point (Fig. 3c), which is in excellent agreement with a previous study that also includes SOC [164]. Min et al. [165] found, through linear extrapolation, a similar value (1.99 eV), but obtained instead an indirect gap because they neglect SOC. Finally, 1L γ-Te indirect band gap passes from 0.42 to 1.02 eV, while its lowest direct gap is of about 1.18 eV (Fig. 3e), in excellent agreement with the work of Villegas et al. [168], which also includes SOC and Coulomb truncation. All this highlights and confirms the importance of including SOC and the Coulomb cutoff in accurately predicting the electronic (and optical) properties of these systems. Finally, we would like to point out that since the QP corrections change only slightly (or not at all) the band dispersion around the VBM and the CBM, valuable information like the effective masses values can be extracted already from the DFT band structures. This finding is particularly useful for the subsequent discussion and analysis of the excitonic states.

Exciton Radiative Lifetime

Starting from the radiative decay rate γ_S of an exciton in a state S and taking into account the in-plane anisotropy, we have estimated the exciton radiative lifetime at $T = 0$ K using [79, 357]:

$$\gamma_S(0) = \tau_S^{-1}(0) = \frac{8\pi e^2 E_S}{A_{uc}\hbar^2 c} \frac{d_{S,x}^2 + d_{S,y}^2}{2} \tag{37}$$

Here, E_S is the energy of the exciton in state S, $d_{S,i}^2$ is the square modulus of the BSE exciton transition dipole in the direction $i = x, y$, divided by the number of unit cells in the 2D system (i.e., the number of 2D **k**-points employed in the calculations), A_{uc} is the area of the unit cell and c the speed of light. By following Ref. [357], we have then calculated the average radiative lifetime $\langle \tau_S \rangle$ at temperature T as:

$$\langle \tau_S \rangle = \tau_S(0) \frac{3}{4} \left(\frac{2\sqrt{\mu_x \mu_y} c^2}{E_S^2} \right) k_B T \tag{38}$$

where μ_x and μ_y are the exciton reduced masses in the two in-plane directions. For isotropic 2D materials (such as γ-Te), we have that $d_{S,x}^2 = d_{S,y}^2 = d_S^2$ and $\sqrt{\mu_x \mu_y} = \mu$ and we reduce to the same case as Ref. [79]. At room temperature, we define an effective radiative lifetime $\langle \tau_{eff}^{RT} \rangle$ obtained by further averaging the rates in Eq. 38 over the lowest-energy bright and dark excitons within $k_B T$ from the optical onset, obtaining [79]:

$$\langle \tau_{eff} \rangle^{-1} = \frac{\sum_S \langle \tau_S \rangle^{-1} e^{-E_S/k_B T}}{\sum_S e^{-E_S/k_B T}} \tag{39}$$

The calculated radiative lifetimes are reported in Table 4.2.

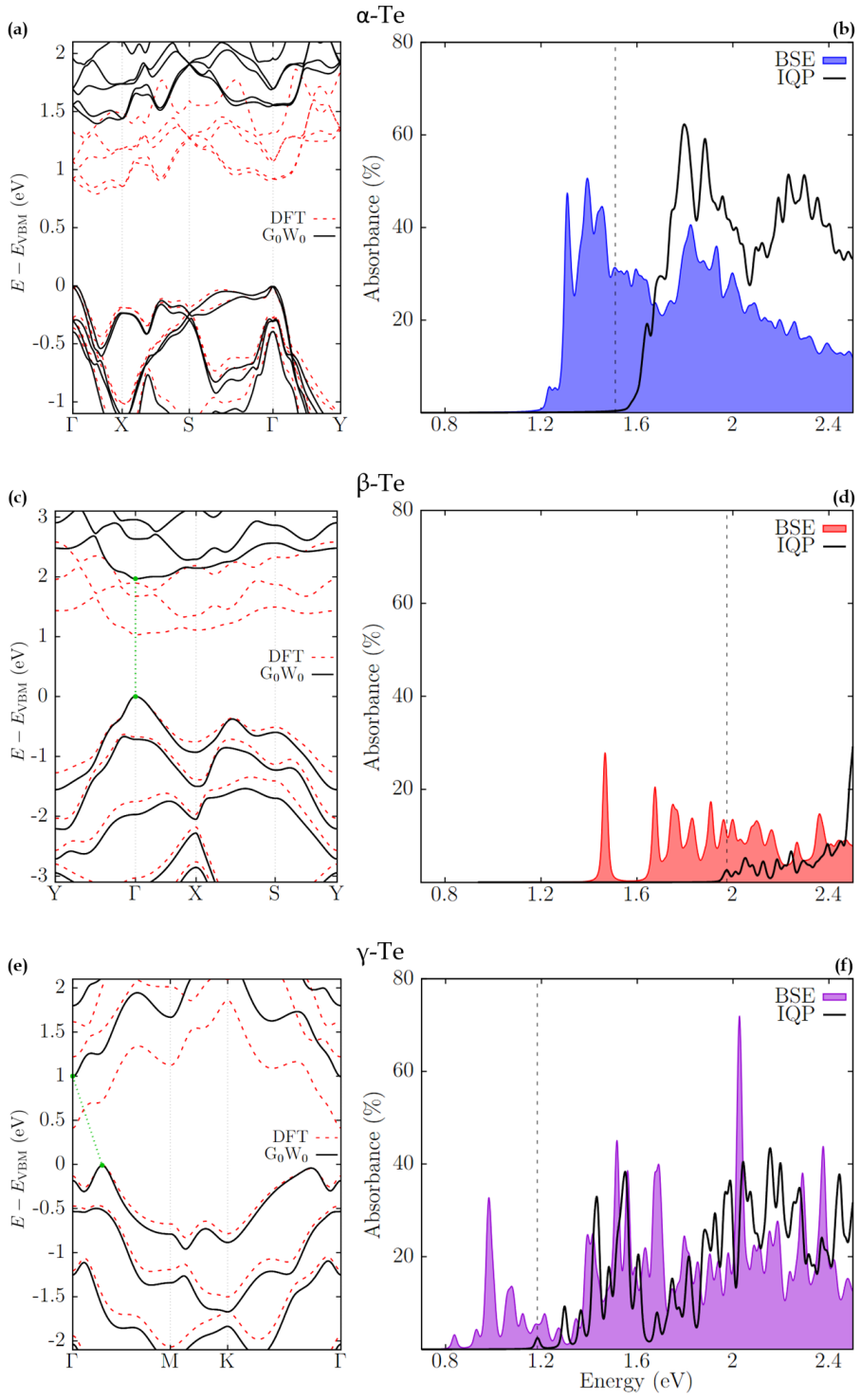

Figure 3: [***Left***] *G_0W_0 (solid black lines) and DFT (dashed red lines) band structures, obtained by using a norm-conserving, fully relativistic GGA-PBE pseudopotential, with SOC and semi-core electrons, of 2L α-Te* (**a**)*, 1L β-Te* (**c**) *and 1L γ-Te* (**e**)*, respectively. Energy zero is set as the top of the valence bands.* [***Left***] *Optical absorption spectra, expressed in terms of the absorbance $A(\omega)$, calculated at the G_0W_0-IQP (black lines) and BSE level (color), with the inclusion of SOC and semi-core electrons, of 2L α-Te* (**b**)*, 1L β-Te* (**d**) *and 1L γ-Te* (**f**)*, respectively. Broadening is set to 0.01 eV.*

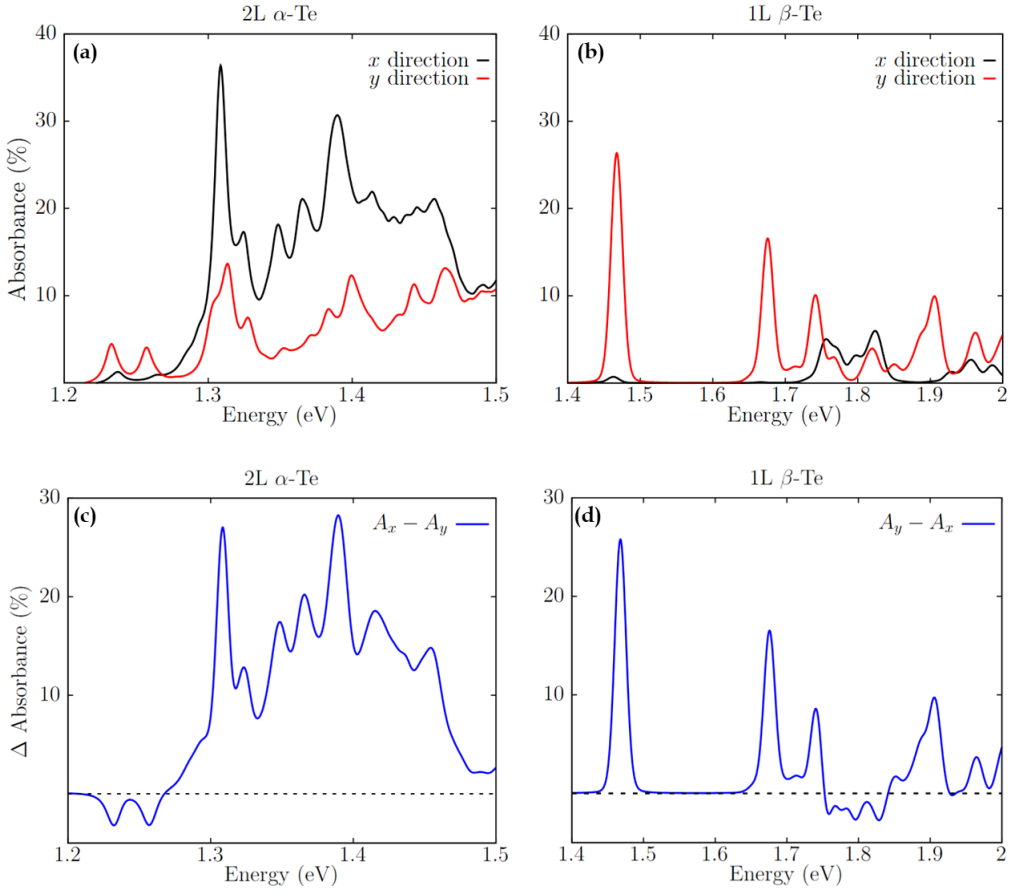

Figure 4: [***Top***] *Comparison of the optical absorption spectra, calculated at the BSE level and expressed in terms of the absorbance $A(\omega)$, along the two in-plane directions x and y, of respectively 2L α-Te* (**a**) *and 1L β-Te* (**b**). [***Bottom***] *Difference of the optical absorption spectra, calculated at the BSE level and expressed in terms of $A(\omega)$, between the two in-plane directions, of respectively 2L α-Te* (**c**) *and 1L β-Te* (**d**). *Broadening is set to 0.01 eV.*

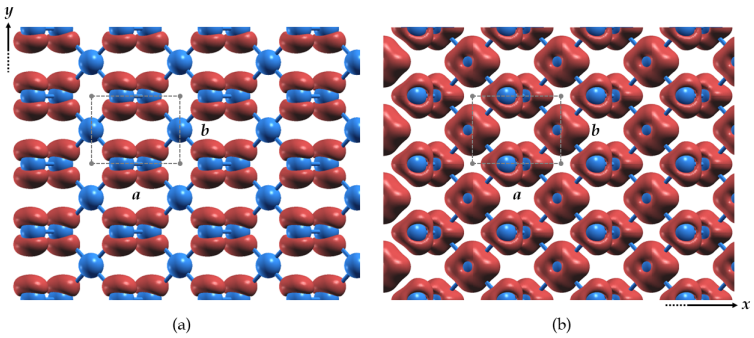

Figure 5: *Valence* (**a**) *and conduction* (**b**) *band wavefunctions of 1L β-Te at* Γ. *The* p_y*-like character of the valence band wavefunction appears manifest.*

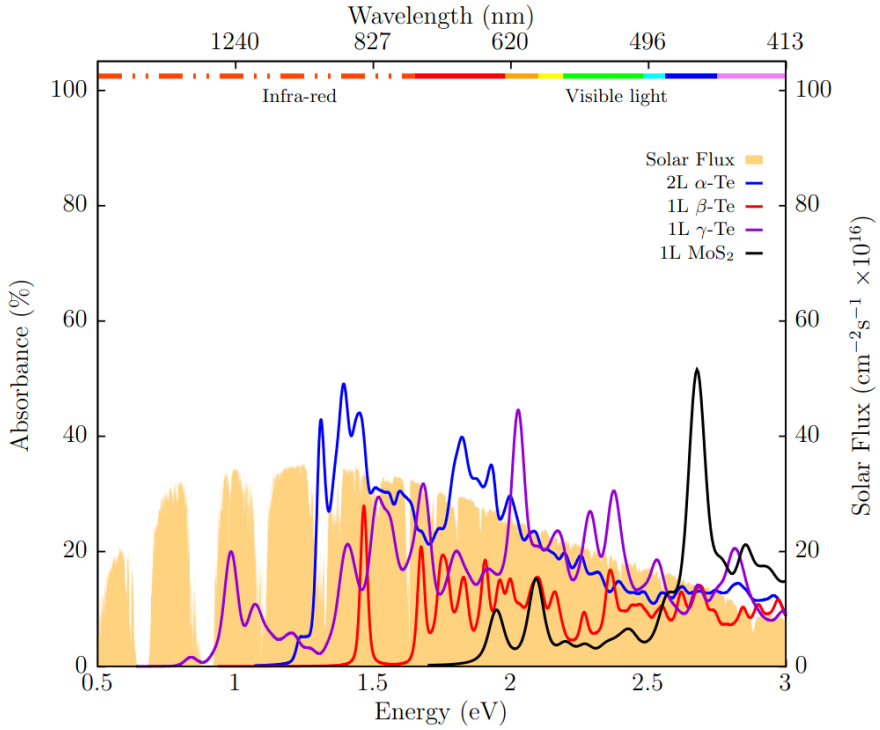

Figure 6: *Optical absorption spectra comparison with* MoS_2 (*black*), *expressed in terms of the absorbance* $A(\omega)$ (*left axis*), *calculated at the BSE level, with the inclusion of SOC, of 2L α-Te* (*blue*), *1L β-Te* (*red*) *and 1L γ-Te* (*violet*), *respectively. Broadening is set to 0.02 eV. The AM1.5G solar flux* $\Phi(\omega)$ *[169]* (*orange, right axis*) *and the relative color spectrum* (*IR in dashed light red*) *are also reported, in terms of both photon energy* (*bottom axis*) *and wavelength* (*top axis*). *Be aware that the optical spectra colors are arbitrary and are not related to the light spectrum ones.*

Appendix E

Supplementary Material of "Tunable Second-Harmonic Generation in 2D Materials"

Here we report computational results not included in the main discussion in Sec. 4.2.

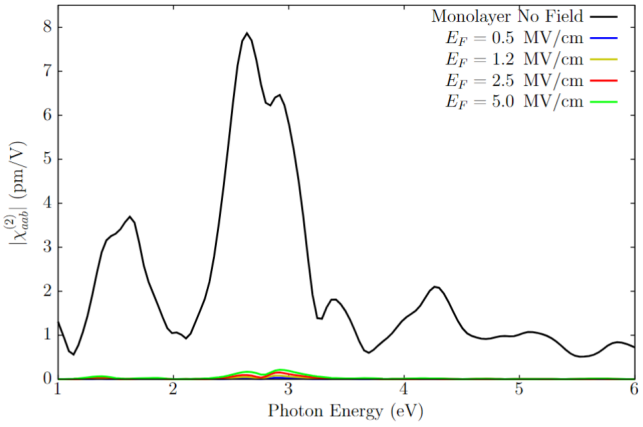

Figure 7: *Intrinsic SHG (i.e. without applied electric field) in monolayer MoS_2 at the IPA level, compared to the induced SHG in bilayer MoS_2.*

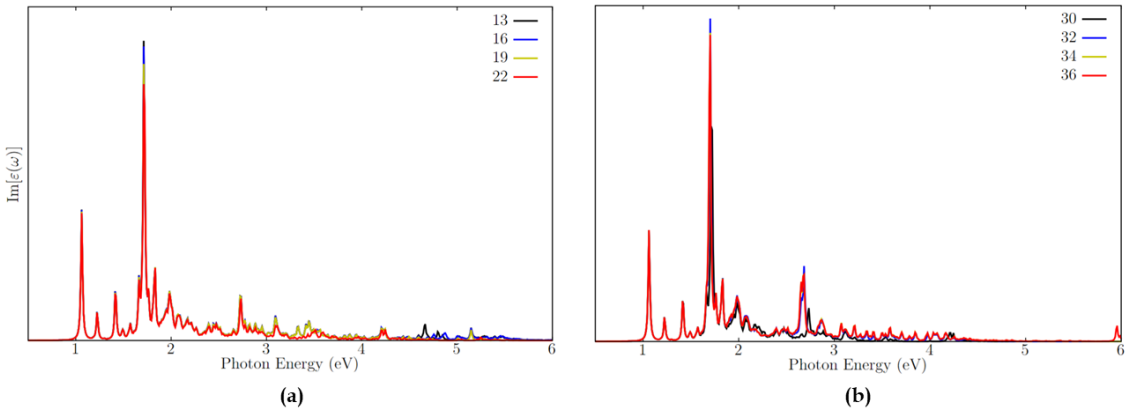

Figure 8: *Convergence of imaginary part of the dielectric function of bilayer MoS_2, at the BSE level, with respect to the number of occupied* (***a***) *and unoccupied* (***b***) *bands.*

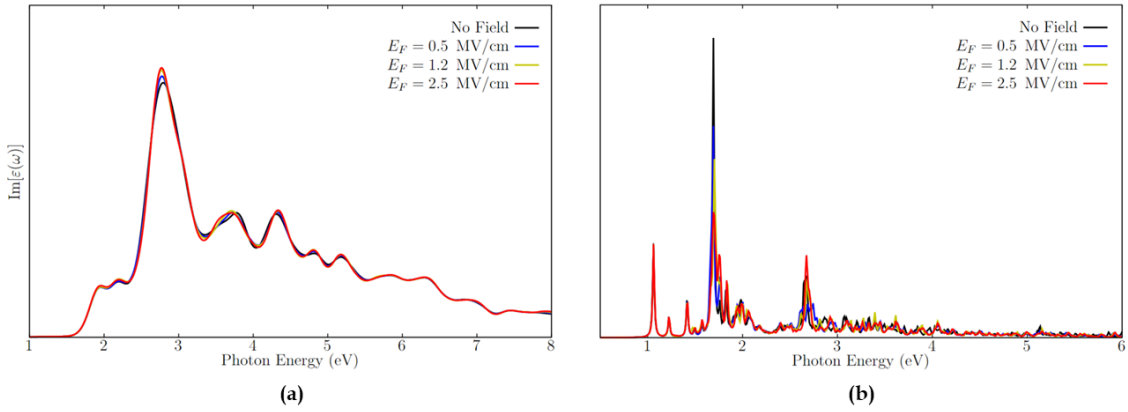

Figure 9: *Imaginary part of the dielectric function of bilayer MoS_2 at the IPA* (***a***) *and BSE* (***a***) *level as a function of the external field.*

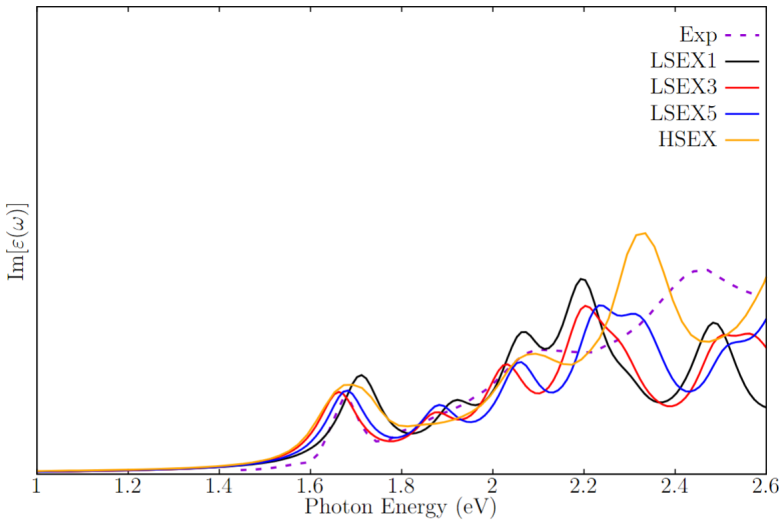

Figure 10: *Imaginary part of the dielectric function of monolayer WSe_2, calculated at the BSE level both using HSEX and LSEX approximations (with different numbers of* **G***-vectors). Our results are compared with the experimental measurements of Ref. [358] (dotted curve).*

Appendix F

Supplementary Material of "Exfoliable 1D Semiconducting Materials from High-Throughput Screening"

Dependence of the Empty States on the Cell Vacuum: the Prototypical Case of MgN_2

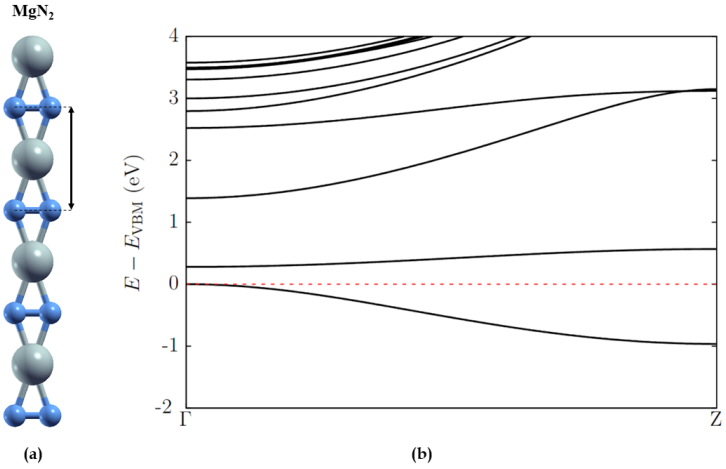

Figure 11: *Optimized geometric structures* (**a**) *and electronic band structures* (**b**) *of* MgN_2. *Credits to [271] for the structures provided. The energies were rescaled with respect to the VBM. The zero level is highlighted with a red dotted line.*

In DFT calculations for periodic low-dimensional materials such as nanowires, 2D materials, and thin films, the inclusion of a vacuum region is essential for achieving accurate results. These materials are often simulated using periodic boundary conditions, which replicate the unit cell throughout space. For low-dimensional systems, this periodic replicas can cause unintended interactions between the material and its periodic images in the non-periodic directions. By including a sufficiently large vacuum region around the material, typically in the range of $15 - 20$ Å, one tries to minimize these spurious interactions, particularly vdW forces and electrostatic interactions. The inclusion of

vacuum is therefore a fundamental step in DFT simulations of low-dimensional materials to ensure the physical relevance and reliability of the calculated properties.
In recent years, researchers have been developing advanced techniques within DFT to address the limitations of the traditional approach of including large vacuum regions around low-dimensional materials. While adding vacuum is effective in reducing interactions between periodic images, it significantly increases the computational cost, especially for large supercells. To make these calculations more efficient, efforts have been directed toward implementing Coulomb cutoff methods. Coulomb cutoffs are designed to selectively limit the range of the Coulomb interaction in certain directions, effectively reducing the artificial electrostatic interactions between periodic images without the need for extensive vacuum regions. By truncating the Coulomb potential, these methods ensure that the interaction decays rapidly beyond a certain distance, which allows for the use of smaller unit cells and less vacuum. This reduction not only decreases computational resources but also improves the accuracy of simulations by focusing on the intrinsic properties of the material itself rather than the vacuum-induced artifacts.
In particular, in the QE community, two Coulomb cutoff techniques were implemented for both 1D [359] and 2D [360] systems. These methods have proven to be highly effective in accelerating the convergence of ground-state properties — such as the total energy, the Fermi level, and the phonon dispersion — without the need for excessively large vacuum regions. However they are less effective in the calculation of the energy dispersion, particularly for empty states. This limitation is especially pronounced in 1D systems, where achieving convergence of the band structure with respect to the vacuum region is virtually impossible.
Here, we present the prototypical study of MgN_2, which represents a particularly pathological case. The relaxed structure and the converged DFT electronic band structure are displayed in Fig. 11. For the DFT part, the QE integrated suite [22, 23] was used. A norm-conserving, scalar-relativistic pseudopotential from the PseudoDojo repository (v0.4) [157] was employed, using GGA-PBE XC functional [155]. Upon convergence, kinetic energy cutoffs of 80 was chosen. A uniform Monkhorst-Pack **k**-point mesh with dimension of $1 \times 1 \times 24$ was employed. To prevent interaction between periodic replicas, a minimum vacuum region of 16 Å along the non-periodic (xy) directions was introduced. Structural relaxation was considered converged when the maximum component of the residual ionic forces dropped below 10^{-8} Ry/Bohr. MgN_2 unit cell (Fig. 11a), with a lattice parameter of 3.823 Å, is composed of a single Mg atom bonded with two N atoms with an angle of about 38°, forming a triangle in the bonding plane. MgN_2 is direct-gap semiconductor wire, with a calculated narrow-gap of 0.26 eV at the Γ point (Fig. 5.2a). Interestingly, the extremely flat conduction band is separated from the next empty band by an energy gap (≈ 1.2 eV at the Γ point) that is larger than the electronic gap itself. This gap is even greater for the valence band relative to the closest occupied band, measuring approximately 5 eV at the Z point. These substantial energy separations suggest that interactions or mixing between these bands are minimal and that they could be associated with different atomic orbitals or electronic configurations that are well separated in energy. In Fig. 12 we present the band structure of MgN_2, calculated with two different vacuum regions: 16 Å (cyan) and 18 Å (blue). Even with a small increase of just 2 Å, the electronic bands are well converged only up to few eV above the Fermi level (red dashed line). This difficulty can be attributed to the reduced dimensionality of 1D systems. In these systems, electronic screening is significantly less effective compared to 2D or bulk materials, leading to stronger Coulomb interactions. As a result, the electron wavefunctions become highly delocalized into the vacuum region, making it challenging to isolate the system's intrinsic properties. This issue significantly hinders the calculation of excited-state properties in 1D systems. Indeed, most computational codes

available for simulating such properties in periodic materials rely on summations over empty states to compute key quantities like the correlation self-energy Σ_c. Therefore, the inability to properly converge the band structure of 1D materials due to insufficient vacuum can lead to inaccuracies in predicting excited-state phenomena. To bypass the issue, we employed the following strategy:

- The QP corrections to the band gap were calculated simultaneously for varying amounts of vacuum.
- For each vacuum level, the summations over empty states were truncated at an increasing energy threshold.

The reference for the zero energy should be chosen accordingly, preferably starting from the Fermi level. An example of this procedure is shown in Fig. 13 for MgN_2. As the vacuum increases, the number of empty states within each energy threshold also increases, leading to a significantly higher computational cost at each step. Our calculations indicate that a vacuum of 15–16 Å and an energy threshold of 20 eV (from the Fermi level) are generally sufficient to converge the correction to the band gap, resulting in a discrepancy of less than 1% compared to a vacuum of up to 30 Å. This "recipe" allows for simultaneous control of the convergence with respect to both vacuum and empty states in MBPT calculations, with the QP correction to the band gap serving as the convergence parameter, bypassing the direct dependence of the results on these quantities while reducing the computational cost.

Table 1: *Parameters used in the GW and BSE calculations for* MgN_2.

Σ_x	Σ_c	Empty bands	BSE **k**-points mesh	BSE valence bands	BSE conduction bands
212878 G-vecs	20 Ry	1990	$1 \times 1 \times 48$	4	10

Hereafter, we discuss the results of the many-body calculations carried on for MgN_2 following the procedure described. MBPT calculations were carried out, using the YAMBO code [48, 49], specifically using the G_0W_0 and eigenvalue self-consistent GW (evGW) methods for QP corrections and the BSE [158–161] for e-h interaction. The converged parameters used are reported in Table 1. Our findings show that in MgN_2, the gap increases from 4.76 (G_0W_0) to 5.59 eV (evGW), thus with a final correction of nearly 5.2 eV. Interestingly, the energy gap separating the conduction band from the higher empty states in DFT is now completely closed, leading to a swap between the first and second empty bands. The absorption spectrum, calculated at the BSE level using evGW-corrected QP states, is presented in Fig. 14b. For comparison, the spectrum derived from G_0W_0-corrected states is shown in Fig. 14a. Overall, the effect of self-consistency leads to a blueshift, without altering the underlying transitions. Thus, for the sake of brevity, we focus our discussion on the evGW+BSE spectrum. This consists of a series of transitions that are relatively well-separated in energy, very close to what one might expect from an isolated system. Similar to such systems, the lowest energy excitation, located in the near UV range, exhibits a significant binding energy (around 2 eV), indicating the highly localized nature of the corresponding excitonic wavefunction. This is confirmed by the plot of the excitonic wavefunction displayed in Fig. 15, which represents the first bright exciton.

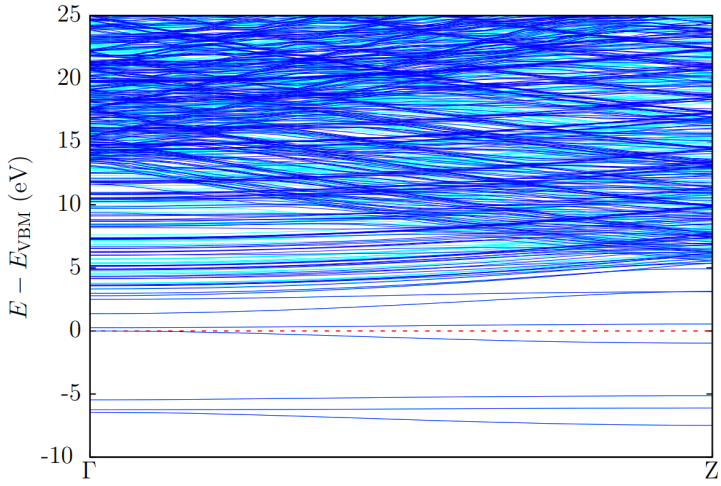

Figure 12: *Calculated band structure, at the DFT level, of the MgN_2 wire using a vacuum of* 16 Å (*cyan*) *and* 18 Å (*blue*) *in the non-periodic directions. The electronic bands are well converged only up to few eV above the Fermi level (red dashed line). Energies are rescaled with respect to the VBM.*

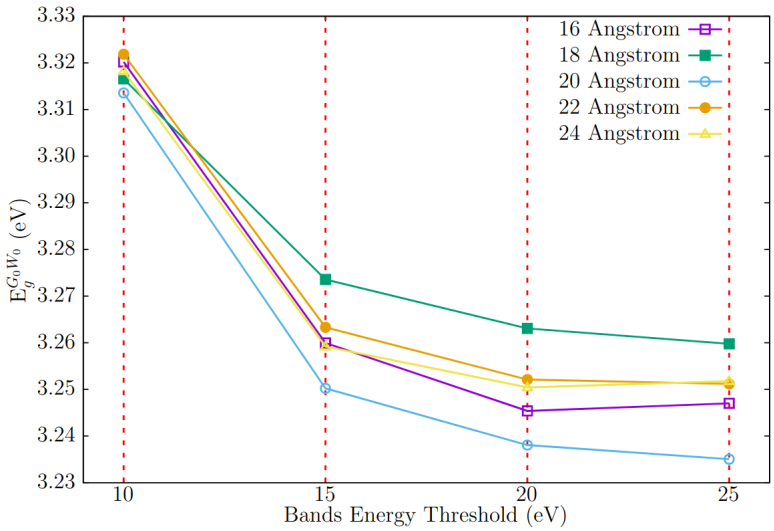

Figure 13: *Convergence of the G_0W_0-correct band gap of MgN_2 with respect to the energy threshold for empty bands included the summations. The different curves represent the different vacuum used in the calculations. A vacuum of* 15–16 Å *and an energy threshold of* 20 *eV (from the Fermi level) are generally sufficient to converge the correction to the band gap, resulting in a discrepancy of less than* 1% *compared to a vacuum of up to* 30 Å.

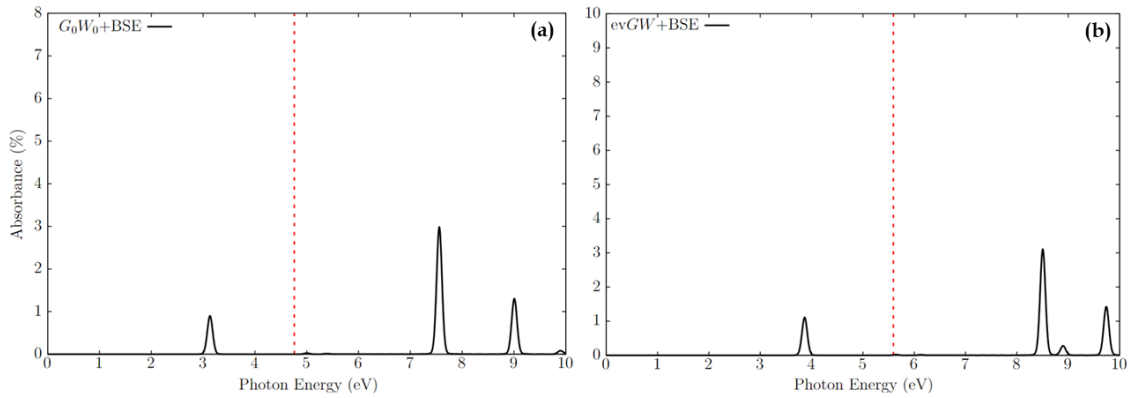

Figure 14: *Absorption spectra (solid black) of* MgN_2*, calculated at the* G_0W_0*+BSE* (**a**) *and the* eV*GW+BSE level* (**b**)*, expressed in terms of percentage of the optical absorbance* $A(\omega)$*. The corresponding QP-corrected direct electronic band gaps (dashed red) are shown as a reference. A binding energy of 1.63 and 1.89 eV were found in the* G_0W_0*+BSE and* eV*GW+BSE, respectively. A broadening of 50 meV was used.*

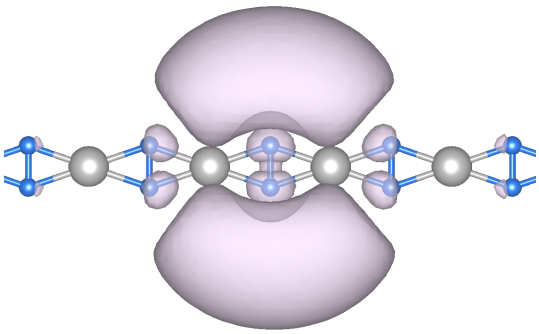

Figure 15: *Excitonic wavefunction plots in direct space for* MgN_2*, calculated using the YAMBO code. The position of the hole was chosen based on the localization of the valence electrons contributing to the exciton. The number of cell repetitions in the periodic direction was increased until the wavefunction decayed to zero.*

This is localized on the N atoms and extends across four unit cells in the periodic direction, as well as in the non-periodic y direction. This exciton appears at 3.70 eV, approximately 1.89 eV below the material's direct electronic band gap (5.59 eV), which corresponds to its binding energy. The transitions contributing to this peak involve the valence band and the fourth conduction band near the Γ point. Interestingly, all excitations involving transitions between the valence band and the conduction band — starting with the first at 0.78 eV — are dark, meaning no optical absorption occurs around the band gap energy.

Bibliography

[1] Max Born. Born-oppenheimer approximation. Ann. Phys, 84:457–484, 1927.

[2] Llewellyn H Thomas. The calculation of atomic fields. In Mathematical proceedings of the Cambridge philosophical society, volume 23, pages 542–548. Cambridge University Press, 1927.

[3] Enrico Fermi. Statistical method to determine some properties of atoms. Rend. Accad. Naz. Lincei, 6(602-607):5, 1927.

[4] JC Slater and HM Krutter. The thomas-fermi method for metals. Physical Review, 47(7):559, 1935.

[5] Pierre Hohenberg and Walter Kohn. Inhomogeneous electron gas. Physical review, 136(3B):B864, 1964.

[6] Walter Kohn and Lu Jeu Sham. Self-consistent equations including exchange and correlation effects. Physical review, 140(4A):A1133, 1965.

[7] Richard M Martin. Electronic structure: basic theory and practical methods. Cambridge university press, 2020.

[8] Tjalling Koopmans. Über die zuordnung von wellenfunktionen und eigenwerten zu den einzelnen elektronen eines atoms. physica, 1(1-6):104–113, 1934.

[9] John P Perdew and Mel Levy. Physical content of the exact kohn-sham orbital energies: band gaps and derivative discontinuities. Physical Review Letters, 51(20):1884, 1983.

[10] Reiner M Dreizler and Eberhard KU Gross. Density functional theory: an approach to the quantum many-body problem. Springer Science & Business Media, 2012.

[11] John P Perdew, Robert G Parr, Mel Levy, and Jose L Balduz Jr. Density-functional theory for fractional particle number: derivative discontinuities of the energy. Physical Review Letters, 49(23):1691, 1982.

[12] Eugene Wigner. On the interaction of electrons in metals. Physical Review, 46(11):1002, 1934.

[13] David M Ceperley and Berni J Alder. Ground state of the electron gas by a stochastic method. Physical review letters, 45(7):566, 1980.

[14] John P Perdew and Alex Zunger. Self-interaction correction to density-functional approximations for many-electron systems. Physical review B, 23(10):5048, 1981.

[15] Axel D Becke. Density-functional exchange-energy approximation with correct asymptotic behavior. Physical review A, 38(6):3098, 1988.

[16] John P Perdew, Matthias Ernzerhof, and Kieron Burke. Rationale for mixing exact exchange with density functional approximations. The Journal of chemical physics, 105(22):9982–9985, 1996.

[17] Ks Kim and KD Jordan. Comparison of density functional and mp2 calculations on the water monomer and dimer. The Journal of Physical Chemistry, 98(40):10089–10094, 1994.

[18] Philip J Stephens, Frank J Devlin, Cary F Chabalowski, and Michael J Frisch. Ab initio calculation of vibrational absorption and circular dichroism spectra using density functional force fields. The Journal of physical chemistry, 98(45):11623–11627, 1994.

[19] Christopher J Cramer. Computational chemistry: Theories and models, 2004.

[20] Seymour H Vosko, Leslie Wilk, and Marwan Nusair. Accurate spin-dependent electron liquid correlation energies for local spin density calculations: a critical analysis. Canadian Journal of physics, 58(8):1200–1211, 1980.

[21] Jochen Heyd, Gustavo E Scuseria, and Matthias Ernzerhof. Hybrid functionals based on a screened coulomb potential. The Journal of chemical physics, 118(18):8207–8215, 2003.

[22] Paolo Giannozzi, Stefano Baroni, Nicola Bonini, Matteo Calandra, Roberto Car, Carlo Cavazzoni, Davide Ceresoli, Guido L Chiarotti, Matteo Cococcioni, Ismaila Dabo, et al. Quantum espresso: a modular and open-source software project for quantum simulations of materials. Journal of physics: Condensed matter, 21(39):395502, 2009.

[23] Paolo Giannozzi, Oliviero Andreussi, Thomas Brumme, Oana Bunau, M Buongiorno Nardelli, Matteo Calandra, Roberto Car, Carlo Cavazzoni, Davide Ceresoli, Matteo Cococcioni, et al. Advanced capabilities for materials modelling with quantum espresso. Journal of physics: Condensed matter, 29(46):465901, 2017.

[24] Neil W Ashcroft. N. david mermin solid state physics, 1976.

[25] Conyers Herring. A new method for calculating wave functions in crystals. Physical Review, 57(12):1169, 1940.

[26] Cédric Robert, Raphaël Picard, David Lagarde, Gang Wang, JP Echeverry, Fabian Cadiz, Pierre Renucci, Alexander Högele, Thierry Amand, Xavier Marie, et al. Excitonic properties of semiconducting monolayer and bilayer mot e 2. Physical Review B, 94(15):155425, 2016.

[27] Hendrik J Monkhorst and James D Pack. Special points for brillouin-zone integrations. Physical review B, 13(12):5188, 1976.

[28] Ferdi Aryasetiawan and Silke Biermann. Generalized hedin's equations for quantum many-body systems¡? format?¿ with spin-dependent interactions. Physical review letters, 100(11):116402, 2008.

[29] Gerhard Theurich and Nicola A Hill. Self-consistent treatment of spin-orbit coupling in solids using relativistic fully separable ab initio pseudopotentials. Physical Review B, 64(7):073106, 2001.

[30] Andrea Dal Corso and Adriano Mosca Conte. Spin-orbit coupling with ultrasoft pseudopotentials: Application to au and pt. Physical Review B—Condensed Matter and Materials Physics, 71(11):115106, 2005.

[31] Leonard Kleinman. Relativistic norm-conserving pseudopotential. Physical Review B, 21(6):2630, 1980.

[32] Alexander L Fetter and John Dirk Walecka. Quantum theory of many-particle systems. Courier Corporation, 2012.

[33] Richard M Martin, Lucia Reining, and David M Ceperley. Interacting electrons. Cambridge University Press, 2016.

[34] Stefan Hüfner. Photoemission of Valence Electrons from Metallic Solids in the One-Electron Approximation. Springer Berlin Heidelberg, Berlin, Heidelberg, 2003.

[35] Ke Wang, Ben Ecker, and Yongli Gao. Angle-resolved photoemission study on the band structure of organic single crystals. Crystals, 10(9), 2020.

[36] Gianluca Stefanucci and Robert Van Leeuwen. Nonequilibrium many-body theory of quantum systems: a modern introduction. Cambridge University Press, 2013.

[37] Eberhard KU Gross and Erich Runge. Many-particle theory, 1986.

[38] Gian-Carlo Wick. The evaluation of the collision matrix. Physical review, 80(2):268, 1950.

[39] Richard D Mattuck. A guide to Feynman diagrams in the many-body problem. Courier Corporation, 1992.

[40] Freeman J Dyson. The s matrix in quantum electrodynamics. Physical Review, 75(11):1736, 1949.

[41] Friedhelm Bechstedt. Many-body approach to electronic excitations. Springer, 2016.

[42] Lars Hedin. New method for calculating the one-particle green's function with application to the electron-gas problem. Physical Review, 139(3A):A796, 1965.

[43] Eric L Shirley. Self-consistent gw and higher-order calculations of electron states in metals. Physical Review B, 54(11):7758, 1996.

[44] Mark van Schilfgaarde, Takao Kotani, and Sergey Faleev. Quasiparticle self-consistent gw theory. Physical review letters, 96(22):226402, 2006.

[45] Ferdi Aryasetiawan and Olle Gunnarsson. The gw method. Reports on progress in Physics, 61(3):237, 1998.

[46] Rex W Godby and RJ Needs. Metal-insulator transition in kohn-sham theory and quasiparticle theory. Physical review letters, 62(10):1169, 1989.

[47] Martin Stankovski, G Antonius, David Waroquiers, Anna Miglio, H Dixit, Kiroubanand Sankaran, Matteo Giantomassi, Xavier Gonze, M Côté, and G-M Rignanese. G 0 w 0 band gap of zno: Effects of plasmon-pole models. Physical Review B—Condensed Matter and Materials Physics, 84(24):241201, 2011.

[48] Andrea Marini, Conor Hogan, Myrta Grüning, and Daniele Varsano. Yambo: an ab initio tool for excited state calculations. Computer Physics Communications, 180(8):1392–1403, 2009.

[49] Davide Sangalli, Andrea Ferretti, Henrique Miranda, Claudio Attaccalite, Ivan Marri, Elena Cannuccia, Pedro Melo, Margherita Marsili, Fulvio Paleari, Antimo Marrazzo, et al. Many-body perturbation theory calculations using the yambo code. Journal of Physics: Condensed Matter, 31(32):325902, 2019.

[50] Mark S Hybertsen and Steven G Louie. Electron correlation in semiconductors and insulators: Band gaps and quasiparticle energies. Physical Review B, 34(8):5390, 1986.

[51] Sergey V Faleev, Mark Van Schilfgaarde, and Takao Kotani. All-electron self-consistent gw approximation: Application to si, mno, and nio. Physical review letters, 93(12):126406, 2004.

[52] Lucia Reining. The gw approximation: content, successes and limitations. Wiley Interdisciplinary Reviews: Computational Molecular Science, 8(3):e1344, 2018.

[53] Carina Faber, Paul Boulanger, Ivan Duchemin, Claudio Attaccalite, and Xavier Blase. Many-body green's function gw and bethe-salpeter study of the optical excitations in a paradigmatic model dipeptide. The Journal of chemical physics, 139(19), 2013.

[54] Carlo A Rozzi, Daniele Varsano, Andrea Marini, Eberhard KU Gross, and Angel Rubio. Exact coulomb cutoff technique for supercell calculations. Physical Review B—Condensed Matter and Materials Physics, 73(20):205119, 2006.

[55] Sohrab Ismail-Beigi. Truncation of periodic image interactions for confined systems. Physical Review B—Condensed Matter and Materials Physics, 73(23):233103, 2006.

[56] Thomas Wolfram and Sinasi Ellialtioglu. Electronic and optical properties of d-band perovskites. Cambridge University Press, 2006.

[57] Martin Dressel and George Grüner. Electrodynamics of solids: optical properties of electrons in matter, 2002.

[58] Jacov Frenkel. On the transformation of light into heat in solids. i. Physical Review, 37(1):17, 1931.

[59] Gregory H. Wannier. The structure of electronic excitation levels in insulating crystals. Phys. Rev., 52:191–197, Aug 1937.

[60] Giancarlo Strinati. Application of the green's functions method to the study of the optical properties of semiconductors. La Rivista del Nuovo Cimento (1978-1999), 11(12):1–86, 1988.

[61] Giovanni Onida, Lucia Reining, and Angel Rubio. Electronic excitations: density-functional versus many-body green's-function approaches. Reviews of modern physics, 74(2):601, 2002.

[62] Ig. Tamm. Relativistic Interaction of Elementary Particles. Springer Berlin Heidelberg, Berlin, Heidelberg, 1991.

[63] SM Dancoff. Non-adiabatic meson theory of nuclear forces. Physical Review, 78(4):382, 1950.

[64] Michael Rohlfing and Steven G. Louie. Electron-hole excitations and optical spectra from first principles. Phys. Rev. B, 62:4927–4944, Aug 2000.

[65] R. Del Sole and Raffaello Girlanda. Optical properties of semiconductors within the independent-quasiparticle approximation. Phys. Rev. B, 48:11789–11795, Oct 1993.

[66] Cornelius Lanczos. An iteration method for the solution of the eigenvalue problem of linear differential and integral operators, 1950.

[67] Michele Cini. Topics and methods in condensed matter theory, volume 1. Springer, 2007.

[68] Roger Haydock. The recursive solution of the schrödinger equation. Computer Physics Communications, 20(1):11–16, 1980.

[69] Lorin X Benedict, Eric L Shirley, and Robert B Bohn. Optical absorption of insulators and the electron-hole interaction: An ab initio calculation. Physical review letters, 80(20):4514, 1998.

[70] Lorin X Benedict and Eric L Shirley. Ab initio calculation of ε 2 (ω) including the electron-hole interaction: Application to gan and caf 2. Physical Review B, 59(8):5441, 1999.

[71] V. Hernandez, J. E. Roman, and V. Vidal. SLEPc: Scalable Library for Eigenvalue Problem Computations. Lect. Notes Comput. Sci., 2565:377–391, 2003.

[72] Vicente Hernandez, Jose E. Roman, and Vicente Vidal. SLEPc: A scalable and flexible toolkit for the solution of eigenvalue problems. ACM Trans. Math. Software, 31(3):351–362, 2005.

[73] Margherita Marsili, Alejandro Molina-Sánchez, Maurizia Palummo, Davide Sangalli, and Andrea Marini. Spinorial formulation of the g w-bse equations and spin properties of excitons in two-dimensional transition metal dichalcogenides. Physical Review B, 103(15):155152, 2021.

[74] Li Yang, Jack Deslippe, Cheol-Hwan Park, Marvin L Cohen, and Steven G Louie. Excitonic effects on the optical response of graphene and bilayer graphene. Physical review letters, 103(18):186802, 2009.

[75] Andrea Splendiani, Liang Sun, Yuanbo Zhang, Tianshu Li, Jonghwan Kim, Chi-Yung Chim, Giulia Galli, and Feng Wang. Emerging photoluminescence in monolayer mos2. Nano letters, 10(4):1271–1275, 2010.

[76] Di Xiao, Gui-Bin Liu, Wanxiang Feng, Xiaodong Xu, and Wang Yao. Coupled spin and valley physics in monolayers of mos 2 and other group-vi dichalcogenides. Physical review letters, 108(19):196802, 2012.

[77] Marco Bernardi, Maurizia Palummo, and Jeffrey C. Grossman. Extraordinary sunlight absorption and one nanometer thick photovoltaics using two-dimensional monolayer materials. Nano Letters, 13(8):3664–3670, 2013.

[78] Ganesh R Bhimanapati, Zhong Lin, Vincent Meunier, Yeonwoong Jung, Judy Cha, Saptarshi Das, Di Xiao, Youngwoo Son, Michael S Strano, Valentino R Cooper, et al. Recent advances in two-dimensional materials beyond graphene. ACS nano, 9(12):11509–11539, 2015.

[79] Maurizia Palummo, Marco Bernardi, and Jeffrey C Grossman. Exciton radiative lifetimes in two-dimensional transition metal dichalcogenides. Nano letters, 15(5):2794–2800, 2015.

[80] Letizia Chiodo. Two-dimensional innovative materials for photovoltaics. Current Opinion in Green and Sustainable Chemistry, 17:49–56, 2019.

[81] Massimiliano Bartolomei, Estela Carmona-Novillo, Marta I Hernández, José Campos-Martínez, Fernando Pirani, and Giacomo Giorgi. Graphdiyne pores:"ad hoc" openings for helium separation applications. The Journal of Physical Chemistry C, 118(51):29966–29972, 2014.

[82] Massimiliano Bartolomei, Estela Carmona-Novillo, Marta I Hernández, José Campos-Martínez, Fernando Pirani, Giacomo Giorgi, and Koichi Yamashita. Penetration barrier of water through graphynes' pores: first-principles predictions and force field optimization. The Journal of Physical Chemistry Letters, 5(4):751–755, 2014.

[83] Massimiliano Bartolomei, Estela Carmona-Novillo, and Giacomo Giorgi. First principles investigation of hydrogen physical adsorption on graphynes' layers. Carbon, 95:1076–1081, 2015.

[84] Massimiliano Bartolomei and Giacomo Giorgi. A novel nanoporous graphite based on graphynes: first-principles structure and carbon dioxide preferential physisorption. ACS Applied Materials & Interfaces, 8(41):27996–28003, 2016.

[85] Maurizia Palummo, Koichi Yamashita, and Giacomo Giorgi. Advances in two-dimensional green materials for organic electronics applications. In Sustainable Strategies in Organic Electronics, pages 391–422. Elsevier, 2022.

[86] Peng Luo, Fuwei Zhuge, Qingfu Zhang, Yuqian Chen, Liang Lv, Yu Huang, Huiqiao Li, and Tianyou Zhai. Doping engineering and functionalization of two-dimensional metal chalcogenides. Nanoscale Horizons, 4(1):26–51, 2019.

[87] M Palummo, AN D'Auria, JC Grossman, and G Cicero. Tailoring the optical properties of mos2 and ws2 single layers via organic functionalization. Journal of Physics: Condensed Matter, 31(23):235701, 2019.

[88] Zhaohe Dai, Luqi Liu, and Zhong Zhang. Strain engineering of 2d materials: issues and opportunities at the interface. Advanced Materials, 31(45):1805417, 2019.

[89] Geun Ho Ahn, Matin Amani, Haider Rasool, Der-Hsien Lien, James P Mastandrea, Joel W Ager Iii, Madan Dubey, Daryl C Chrzan, Andrew M Minor, and Ali Javey. Strain-engineered growth of two-dimensional materials. Nature communications, 8(1):1–8, 2017.

[90] Shikai Deng, Anirudha V Sumant, and Vikas Berry. Strain engineering in two-dimensional nanomaterials beyond graphene. Nano Today, 22:14–35, 2018.

[91] Sara Postorino, Davide Grassano, Marco D'Alessandro, Andrea Pianetti, Olivia Pulci, and Maurizia Palummo. Strain-induced effects on the electronic properties of 2d materials. Nanomaterials and Nanotechnology, 10:1847980420902569, 2020.

[92] Zhao Cheng, Rui Cao, Kangkang Wei, Yuhan Yao, Xinyu Liu, Jianlong Kang, Jianji Dong, Zhe Shi, Han Zhang, and Xinliang Zhang. 2d materials enabled next-generation integrated optoelectronics: from fabrication to applications. Advanced Science, 8(11):2003834, 2021.

[93] Chunsen Liu, Huawei Chen, Shuiyuan Wang, Qi Liu, Yu-Gang Jiang, David Wei Zhang, Ming Liu, and Peng Zhou. Two-dimensional materials for next-generation computing technologies. Nature Nanotechnology, 15(7):545–557, 2020.

[94] S Marconi, MA Giambra, A Montanaro, V Mišeikis, S Soresi, S Tirelli, P Galli, F Buchali, W Templ, C Coletti, et al. Photo thermal effect graphene detector featuring 105 gbit s- 1 nrz and 120 gbit s- 1 pam4 direct detection. Nature communications, 12(1):1–10, 2021.

[95] Marco Bernardi, Maurizia Palummo, and Jeffrey C Grossman. Semiconducting monolayer materials as a tunable platform for excitonic solar cells. ACS nano, 6(11):10082–10089, 2012.

[96] Frank Ceballos, Matthew Z Bellus, Hsin-Ying Chiu, and Hui Zhao. Ultrafast charge separation and indirect exciton formation in a mos2–mose2 van der waals heterostructure. ACS nano, 8(12):12717–12724, 2014.

[97] Jun Dai and Xiao Cheng Zeng. Bilayer phosphorene: effect of stacking order on bandgap and its potential applications in thin-film solar cells. The journal of physical chemistry letters, 5(7):1289–1293, 2014.

[98] Lorenzo Bastonero, Giancarlo Cicero, Maurizia Palummo, and Michele Re Fiorentin. Boosted solar light absorbance in pds2/pts2 vertical heterostructures for ultrathin photovoltaic devices. ACS Applied Materials & Interfaces, 13(36):43615–43621, 2021.

[99] Yaroslav E Romanyuk, Harald Hagendorfer, Patrick Stücheli, Peter Fuchs, Alexander R Uhl, Carolin M Sutter-Fella, Melanie Werner, Stefan Haass, Josua Stückelberger, Cédric Broussillou, et al. All solution-processed chalcogenide solar cells–from single functional layers towards a 13.8% efficient cigs device. Advanced Functional Materials, 25(1):12–27, 2015.

[100] Bat-El Cohen, Małgorzata Wierzbowska, and Lioz Etgar. High efficiency and high open circuit voltage in quasi 2d perovskite based solar cells. Advanced Functional Materials, 27(5):1604733, 2017.

[101] Koosha Nassiri Nazif, Alwin Daus, Jiho Hong, Nayeun Lee, Sam Vaziri, Aravindh Kumar, Frederick Nitta, Michelle E Chen, Siavash Kananian, Raisul Islam, et al. High-specific-power flexible transition metal dichalcogenide solar cells. nature Communications, 12(1):7034, 2021.

[102] Sachin A Pawar, Donghwan Kim, Ansoon Kim, Joo Hyung Park, Jae Cheol Shin, TaeWan Kim, and Hyo Jin Kim. Heterojunction solar cell based on n-mos2/p-inp. Optical Materials, 86:576–581, 2018.

[103] Liyong Niu, Kan Li, Hongyu Zhen, Ying-San Chui, Wenjun Zhang, Feng Yan, and Zijian Zheng. Salt-assisted high-throughput synthesis of single-and few-layer transition metal dichalcogenides and their application in organic solar cells. Small, 10(22):4651–4657, 2014.

[104] Elaine McVay, Ahmad Zubair, Yuxuan Lin, Amirhasan Nourbakhsh, and Tomás Palacios. Impact of al2o3 passivation on the photovoltaic performance of vertical wse2 schottky junction solar cells. ACS Applied Materials & Interfaces, 12(52):57987–57995, 2020.

[105] Bora Kim, Moonhoe Kim, Hyojung Kim, Sohee Jeong, JungYup Yang, and Mun Seok Jeong. Improved stability of mapbi3 perovskite solar cells using two-dimensional transition-metal dichalcogenide interlayers. ACS Applied Materials & Interfaces, 14(31):35726–35733, 2022.

[106] Meng-Lin Tsai, Sheng-Han Su, Jan-Kai Chang, Dung-Sheng Tsai, Chang-Hsiao Chen, Chih-I Wu, Lain-Jong Li, Lih-Juann Chen, and Jr-Hau He. Monolayer mos2 heterojunction solar cells. ACS nano, 8(8):8317–8322, 2014.

[107] Xing He, Yuta Iwamoto, Toshiro Kaneko, and Toshiaki Kato. Fabrication of near-invisible solar cell with monolayer ws2. Scientific reports, 12(1):11315, 2022.

[108] Yuliang Mao, Congsheng Xu, Jianmei Yuan, and Hongquan Zhao. A two-dimensional gese/snse heterostructure for high performance thin-film solar cells. Journal of Materials Chemistry A, 7(18):11265–11271, 2019.

[109] Xinyi Zheng, Yadong Wei, Kaijuan Pang, Ngeywo Kaner Tolbert, Dalin Kong, Xiaodong Xu, Jianqun Yang, Xingji Li, and Weiqi Li. Pn/pas-wse2 van der waals heterostructures for solar cell and photodetector. Scientific Reports, 10(1):17213, 2020.

[110] Mukesh Jakhar, Jaspreet Singh, Ashok Kumar, and Ravindra Pandey. First-principles study of the hexagonal t-phase pdse2 monolayer and its application in solar cells. The Journal of Physical Chemistry C, 124(49):26565–26571, 2020.

[111] Jianhui Chen, Xiaojun He, Baisheng Sa, Jian Zhou, Chao Xu, Cuilian Wen, and Zhimei Sun. Iii–vi van der waals heterostructures for sustainable energy related applications. Nanoscale, 11(13):6431–6444, 2019.

[112] Ashima Rawat, Anu Arora, and Abir De Sarkar. Interfacing 2d m2x (m= na, k, cs; x= o, s, se, te) monolayers for 2d excitonic and tandem solar cells. Applied Surface Science, 563:150304, 2021.

[113] W Zhang, Z Huang, W Zhang, and Y Li. Two-dimensional semiconductors with possible high room temperature mobility. nano res 7: 1731–1737, 2014.

[114] Ruixiang Fei and Li Yang. Strain-engineering the anisotropic electrical conductance of few-layer black phosphorus. Nano letters, 14(5):2884–2889, 2014.

[115] Andres Castellanos-Gomez, Leonardo Vicarelli, Elsa Prada, Joshua O Island, KL Narasimha-Acharya, Sofya I Blanter, Dirk J Groenendijk, Michele Buscema, Gary A Steele, JV Alvarez, et al. Isolation and characterization of few-layer black phosphorus. 2D Materials, 1(2):025001, 2014.

[116] Xiaochun Huang, Rui Xiong, Chunxue Hao, Wenbin Li, Baisheng Sa, Jens Wiebe, and Roland Wiesendanger. Experimental realization of monolayer α-tellurene. Advanced Materials, 36(6):2309023, 2024.

[117] Zhenyu Pan, Xinbo Zhang, Isabella DiSturco, Yuanbing Mao, Xian Zhang, and Heng Wang. The potential of tellurene-like nanosheets as a solution-processed room-temperature thermoelectric material. Small Science, page 2300272, 2024.

[118] Gen Li, Hairui Bao, Yange Peng, Xi Fu, Wenhu Liao, and Changqing Xiang. Strain controllable band alignment, interfacial and optical properties in tellurene/gaas van der waals heterostructures. Physical Chemistry Chemical Physics, 2024.

[119] Bolim You, Jeechan Yoon, Yuna Kim, Mino Yang, Jina Bak, Jihyang Park, Un Jeong Kim, Myung Gwan Hahm, and Moonsang Lee. An extremely low-power-consumption reconfigurable two-dimensional tellurene artificial synapse for bio-inspired wearable edge computing. Journal of Materials Chemistry C, 12(18):6596–6605, 2024.

[120] Xiaochun Huang, Jiaqi Guan, Zijian Lin, Bing Liu, Shuya Xing, Weihua Wang, and Jiandong Guo. Epitaxial growth and band structure of te film on graphene. Nano letters, 17(8):4619–4623, 2017.

[121] Yixiu Wang, Gang Qiu, Ruoxing Wang, Shouyuan Huang, Qingxiao Wang, Yuanyue Liu, Yuchen Du, William A Goddard III, Moon J Kim, Xianfan Xu, et al. Field-effect transistors made from solution-grown two-dimensional tellurene. Nature Electronics, 1(4):228–236, 2018.

[122] Lei Tong, Xinyu Huang, Peng Wang, Lei Ye, Meng Peng, Licong An, Qiaodong Sun, Yong Zhang, Guoming Yang, Zheng Li, et al. Stable mid-infrared polarization imaging based on quasi-2d tellurium at room temperature. Nature Communications, 11(1):2308, 2020.

[123] Matin Amani, Chaoliang Tan, George Zhang, Chunsong Zhao, James Bullock, Xiaohui Song, Hyungjin Kim, Vivek Raj Shrestha, Yang Gao, Kenneth B Crozier, et al. Solution-synthesized high-mobility tellurium nanoflakes for short-wave infrared photodetectors. ACS nano, 12(7):7253–7263, 2018.

[124] Xiao Hua Wang, Ai Jun Yang, Nikhil Koratkar, Ji Feng Chu, Pin Lei Lv, Ming Zhe Rong, et al. Effects of adatom and gas molecule adsorption on the physical properties of tellurene: a first principles investigation. Physical Chemistry Chemical Physics, 20(6):4058–4066, 2018.

[125] Yuanyue Liu, Wenzhuo Wu, and William A Goddard III. Tellurium: fast electrical and atomic transport along the weak interaction direction. Journal of the American Chemical Society, 140(2):550–553, 2018.

[126] Cong Wang, Xieyu Zhou, Jingsi Qiao, Linwei Zhou, Xianghua Kong, Yuhao Pan, Zhihai Cheng, Yang Chai, and Wei Ji. Charge-governed phase manipulation of few-layer tellurium. Nanoscale, 10(47):22263–22269, 2018.

[127] Rasmus Nielsen, Andrea Crovetto, Alireza Assar, Ole Hansen, Ib Chorkendorff, and Peter CK Vesborg. Monolithic selenium/silicon tandem solar cells. PRX Energy, 3(1):013013, 2024.

[128] Wenzhuo Wu, Gang Qiu, Yixiu Wang, Ruoxing Wang, and Peide Ye. Tellurene: its physical properties, scalable nanomanufacturing, and device applications. Chemical Society Reviews, 47(19):7203–7212, 2018.

[129] Kai Wu, Huanhuan Ma, Yunzhi Gao, Wei Hu, and Jinlong Yang. Highly-efficient heterojunction solar cells based on two-dimensional tellurene and transition metal dichalcogenides. Journal of Materials Chemistry A, 7(13):7430–7436, 2019.

[130] Xiaolin Cai, Xiaoyu Han, Chunxiang Zhao, Chunyao Niu, and Yu Jia. Tellurene: An elemental 2d monolayer material beyond its bulk phases without van der waals layered structures. Journal of Semiconductors, 41(8):081002, 2020.

[131] Xiaolin Cai, Weiguang Chen, Xingtao Jia, Liwei Zhang, Qin Wang, Baoji Wang, Xuefeng Yang, Yujin Liu, and Yu Jia. Transition from an indirect type-i to a direct type-ii bandgap in α-tellurene/ca (oh) 2 heterostructures with excellent optical properties. Journal of Materials Chemistry C, 8(35):12291–12301, 2020.

[132] Zhe Shi, Rui Cao, Karim Khan, Ayesha Khan Tareen, Xiaosong Liu, Weiyuan Liang, Ye Zhang, Chunyang Ma, Zhinan Guo, Xiaoling Luo, et al. Two-dimensional tellurium: Progress, challenges, and prospects. Nano-Micro Letters, 12:1–34, 2020.

[133] Ayesha Khan Tareen, Karim Khan, Muhammad Aslam, Han Zhang, and Xinke Liu. Recent progress, challenges, and prospects in emerging group-via xenes: Synthesis, properties and novel applications. Nanoscale, 13(2):510–552, 2021.

[134] Zhili Zhu, Xiaolin Cai, Seho Yi, Jinglei Chen, Yawei Dai, Chunyao Niu, Zhengxiao Guo, Maohai Xie, Feng Liu, Jun-Hyung Cho, et al. Multivalency-driven formation of te-based monolayer materials: a combined first-principles and experimental study. Physical review letters, 119(10):106101, 2017.

[135] Jingsi Qiao, Yuhao Pan, Feng Yang, Cong Wang, Yang Chai, and Wei Ji. Few-layer tellurium: one-dimensional-like layered elementary semiconductor with striking physical properties. Science bulletin, 63(3):159–168, 2018.

[136] Yao Wang, Chengcheng Xiao, Miaogen Chen, Chenqiang Hua, Junding Zou, Chen Wu, Jianzhong Jiang, Shengyuan A Yang, Yunhao Lu, and Wei Ji. Two-dimensional ferroelectricity and switchable spin-textures in ultra-thin elemental te multilayers. Materials Horizons, 5(3):521–528, 2018.

[137] Yuan Xiang, Shengjie Gao, Rong-Guang Xu, Wenzhuo Wu, and Yongsheng Leng. Phase transition in two-dimensional tellurene under mechanical strain modulation. Nano Energy, 58:202–210, 2019.

[138] Jinglei Chen, Yawei Dai, Yaqiang Ma, Xianqi Dai, Wingkin Ho, and Maohai Xie. Ultrathin β-tellurium layers grown on highly oriented pyrolytic graphite by molecular-beam epitaxy. Nanoscale, 9(41):15945–15948, 2017.

[139] Salma Khatun, Arnab Banerjee, and Amlan J Pal. Nonlayered tellurene as an elemental 2d topological insulator: Experimental evidence from scanning tunneling spectroscopy. Nanoscale, 11(8):3591–3598, 2019.

[140] Amey Apte, Elisabeth Bianco, Aravind Krishnamoorthy, Sadegh Yazdi, Rahul Rao, Nicholas Glavin, Hiroyuki Kumazoe, Vikas Varshney, Ajit Roy, Fuyuki Shimojo, et al. Polytypism in ultrathin tellurium. 2D Materials, 6(1):015013, 2018.

[141] Qisheng Wang, Muhammad Safdar, Kai Xu, Misbah Mirza, Zhenxing Wang, and Jun He. Van der waals epitaxy and photoresponse of hexagonal tellurium nanoplates on flexible mica sheets. ACS nano, 8(7):7497–7505, 2014.

[142] Zhongjian Xie, Chenyang Xing, Weichun Huang, Taojian Fan, Zhongjun Li, Jinlai Zhao, Yuanjiang Xiang, Zhinan Guo, Jianqing Li, Zhigang Yang, et al. Ultrathin 2d nonlayered tellurium nanosheets: facile liquid-phase exfoliation, characterization, and photoresponse with high performance and enhanced stability. Advanced Functional Materials, 28(16):1705833, 2018.

[143] Qiyuan He, Yuan Liu, Chaoliang Tan, Wei Zhai, Gwang-hyeon Nam, and Hua Zhang. Quest for p-type two-dimensional semiconductors. Acs Nano, 13(11):12294–12300, 2019.

[144] Hongtao Yuan, Xiaoge Liu, Farzaneh Afshinmanesh, Wei Li, Gang Xu, Jie Sun, Biao Lian, Alberto G Curto, Guojun Ye, Yasuyuki Hikita, et al. Polarization-sensitive broadband photodetector using a black phosphorus vertical p–n junction. Nature nanotechnology, 10(8):707–713, 2015.

[145] Fucai Liu, Shoujun Zheng, Xuexia He, Apoorva Chaturvedi, Junfeng He, Wai Leong Chow, Thomas R Mion, Xingli Wang, Jiadong Zhou, Qundong Fu, et al. Highly sensitive detection of polarized light using anisotropic 2d res2. Advanced Functional Materials, 26(8):1169–1177, 2016.

[146] Enze Zhang, Peng Wang, Zhe Li, Haifeng Wang, Chaoyu Song, Ce Huang, Zhi-Gang Chen, Lei Yang, Kaitai Zhang, Shiheng Lu, et al. Tunable ambipolar polarization-sensitive photodetectors based on high-anisotropy rese2 nanosheets. ACS nano, 10(8):8067–8077, 2016.

[147] Qiushi Guo, Andreas Pospischil, Maruf Bhuiyan, Hao Jiang, He Tian, Damon Farmer, Bingchen Deng, Cheng Li, Shu-Jen Han, Han Wang, et al. Black phosphorus mid-infrared photodetectors with high gain. Nano letters, 16(7):4648–4655, 2016.

[148] Diao Li, Henri Jussila, Lasse Karvonen, Guojun Ye, Harri Lipsanen, Xianhui Chen, and Zhipei Sun. Polarization and thickness dependent absorption properties of black phosphorus: new saturable absorber for ultrafast pulse generation. Scientific reports, 5(1):15899, 2015.

[149] Erfu Liu, Yajun Fu, Yaojia Wang, Yanqing Feng, Huimei Liu, Xiangang Wan, Wei Zhou, Baigeng Wang, Lubin Shao, Ching-Hwa Ho, et al. Integrated digital inverters based on two-dimensional anisotropic res2 field-effect transistors. Nature communications, 6(1):6991, 2015.

[150] Li-Dong Zhao, Shih-Han Lo, Yongsheng Zhang, Hui Sun, Gangjian Tan, Ctirad Uher, Christopher Wolverton, Vinayak P Dravid, and Mercouri G Kanatzidis. Ultralow thermal conductivity and high thermoelectric figure of merit in snse crystals. nature, 508(7496):373–377, 2014.

[151] Jingsi Qiao, Xianghua Kong, Zhi-Xin Hu, Feng Yang, and Wei Ji. High-mobility transport anisotropy and linear dichroism in few-layer black phosphorus. Nature communications, 5(1):4475, 2014.

[152] Yijun Liu, Minghui Wu, Zhaoyang Sun, Shengxue Yang, Chunguang Hu, Li Huang, Wanfu Shen, Bin Wei, Zhongchang Wang, Shiqi Yang, et al. Synthesis of low-symmetry 2d ge (1-

x) sn x se 2 alloy flakes with anisotropic optical response and birefringence. Nanoscale, 11(48):23116–23125, 2019.

[153] Wanfu Shen, Chunguang Hu, Jin Tao, Jun Liu, Shuangqing Fan, Yaxu Wei, Chunhua An, Jiancui Chen, Sen Wu, Yanning Li, et al. Resolving the optical anisotropy of low-symmetry 2d materials. Nanoscale, 10(17):8329–8337, 2018.

[154] Xu Li, Haiyang Liu, Congming Ke, Weiqing Tang, Mengyu Liu, Feihong Huang, Yaping Wu, Zhiming Wu, and Junyong Kang. Review of anisotropic 2d materials: Controlled growth, optical anisotropy modulation, and photonic applications. Laser & Photonics Reviews, 15(12):2100322, 2021.

[155] John P. Perdew, Kieron Burke, and Matthias Ernzerhof. Generalized gradient approximation made simple. Phys. Rev. Lett., 77:3865–3868, Oct 1996.

[156] Stefan Grimme. Semiempirical gga-type density functional constructed with a long-range dispersion correction. Journal of Computational Chemistry, 27(15):1787–1799, 2006.

[157] M.J. van Setten, M. Giantomassi, E. Bousquet, M.J. Verstraete, D.R. Hamann, X. Gonze, and G.-M. Rignanese. The pseudodojo: Training and grading a 85 element optimized norm-conserving pseudopotential table. Computer Physics Communications, 226:39 – 54, 2018. `http://www.pseudo-dojo.org/`.

[158] Giovanni Onida, Lucia Reining, and Angel Rubio. Electronic excitations: density-functional versus many-body green's-function approaches. Rev. Mod. Phys., 74:601–659, Jun 2002.

[159] G. Strinati, H. J. Mattausch, and W. Hanke. Dynamical aspects of correlation corrections in a covalent crystal. Phys. Rev. B, 25:2867–2888, Feb 1982.

[160] W. Hanke and L. J. Sham. Many-particle effects in the optical spectrum of a semiconductor. Phys. Rev. B, 21:4656–4673, May 1980.

[161] W. Hanke and L. J. Sham. Dielectric response in the wannier representation: Application to the optical spectrum of diamond. Phys. Rev. Lett., 33:582–585, Sep 1974.

[162] Fabien Bruneval and Xavier Gonze. Accurate *gw* self-energies in a plane-wave basis using only a few empty states: Towards large systems. Phys. Rev. B, 78:085125, Aug 2008.

[163] Qiang Gao, Xueping Li, Lizhen Fang, Tianxing Wang, Shuyi Wei, Congxin Xia, and Yu Jia. Exciton states and oscillator strength in few-layer α-tellurene. Applied Physics Letters, 114(9):092101, 2019.

[164] Yuanyuan Pan, Shiyuan Gao, Li Yang, and Jing Lu. Dependence of excited-state properties of tellurium on dimensionality: From bulk to two dimensions to one dimensions. Phys. Rev. B, 98:085135, Aug 2018.

[165] Jingjing Min, Chunxiang Zhao, Zaiping Zeng, Yu Jia, and Zuliang Du. Tunable visible-light excitonic absorption and high photoconversion efficiency in two-dimensional group-vi monolayer materials. Phys. Rev. B, 100:085402, Aug 2019.

[166] Margherita Marsili, Alejandro Molina-Sánchez, Maurizia Palummo, Davide Sangalli, and Andrea Marini. Spinorial formulation of the g w-bse equations and spin properties of excitons in two-dimensional transition metal dichalcogenides. Physical Review B, 103(15):155152, 2021.

[167] Simone Grillo, Olivia Pulci, and Ivan Marri. Evolution of the electronic and optical properties of meta-stable allotropic forms of 2d tellurium for increasing number of layers. Nanomaterials, 12(14):2503, 2022.

[168] Cesar EP Villegas and Alexandre R Rocha. Near-infrared optical response and carrier dynamics for high photoconversion in tellurene. The Journal of Physical Chemistry C, 126(14):6129–6134, 2022.

[169] National Renewable Energy Laboratory (accessed July 2023). http://rredc.nrel.gov/solar/spectra/am1.5/.

[170] Huanhuan Ma, Wei Hu, and Jinlong Yang. Control of highly anisotropic electrical conductance of tellurene by strain-engineering. Nanoscale, 11(45):21775–21781, 2019.

[171] David K Sang, Bo Wen, Shan Gao, Yonghong Zeng, Fanxu Meng, Zhinan Guo, and Han Zhang. Electronic and optical properties of two-dimensional tellurene: from first-principles calculations. Nanomaterials, 9(8):1075, 2019.

[172] David Kipkemoi Sang, Teng Ding, Meng Nan Wu, Yu Li, Junqin Li, Fusheng Liu, Zhinan Guo, Han Zhang, and Heping Xie. Monolayer β-tellurene: a promising p-type thermoelectric material via first-principles calculations. Nanoscale, 11(39):18116–18123, 2019.

[173] LV Keldysh. Coulomb interaction in thin semiconductor and semimetal films. Soviet Journal of Experimental and Theoretical Physics Letters, 29:658, 1979.

[174] Natalia S Rytova. Screened potential of a point charge in a thin film. arXiv preprint arXiv:1806.00976, 2018.

[175] O Pulci, P Gori, M Marsili, V Garbuio, R Del Sole, and F Bechstedt. Strong excitons in novel two-dimensional crystals: Silicane and germanane. Europhysics Letters, 98(3):37004, 2012.

[176] O Pulci, Margherita Marsili, V Garbuio, P Gori, I Kupchak, and F Bechstedt. Excitons in two-dimensional sheets with honeycomb symmetry. physica status solidi (b), 252(1):72–77, 2015.

[177] Maria Stella Prete, Davide Grassano, Olivia Pulci, Ihor Kupchak, Valerio Olevano, and Friedhelm Bechstedt. Giant excitonic absorption and emission in two-dimensional group-iii nitrides. Scientific reports, 10(1):10719, 2020.

[178] Maria Stella Prete, Adriano Mosca Conte, Paola Gori, Friedhelm Bechstedt, and Olivia Pulci. Tunable electronic properties of two-dimensional nitrides for light harvesting heterostructures. Applied Physics Letters, 110(1):012103, 2017.

[179] Maria Stella Prete, Olivia Pulci, and Friedhelm Bechstedt. Strong in- and out-of-plane excitons in two-dimensional inn nanosheets. Phys. Rev. B, 98:235431, Dec 2018.

[180] Han-gyu Kim and Hyoung Joon Choi. Thickness dependence of work function, ionization energy, and electron affinity of mo and w dichalcogenides from dft and gw calculations. Physical Review B, 103(8):085404, 2021.

[181] Lucio Claudio Andreani, Angelo Bozzola, Piotr Kowalczewski, Marco Liscidini, and Lisa Redorici. Silicon solar cells: toward the efficiency limits. Advances in Physics: X, 4(1):1548305, 2019.

[182] Marco Bernardi, Derek Vigil-Fowler, Johannes Lischner, Jeffrey B Neaton, and Steven G Louie. Ab initio study of hot carriers in the first picosecond after sunlight absorption in silicon. Physical review letters, 112(25):257402, 2014.

[183] Cesar EP Villegas and AR Rocha. Elucidating the optical properties of novel heterolayered materials based on mote2–inn for photovoltaic applications. The Journal of Physical Chemistry C, 119(21):11886–11895, 2015.

[184] Markus C Scharber, David Mühlbacher, Markus Koppe, Patrick Denk, Christoph Waldauf, Alan J Heeger, and Christoph J Brabec. Design rules for donors in bulk-heterojunction solar cells—towards 10% energy-conversion efficiency. Advanced materials, 18(6):789–794, 2006.

[185] Richard L Anderson. Experiments on ge-gaas heterojunctions. Solid-State Electronics, 5(5):341–351, 1962.

[186] Daniel S Koda, Friedhelm Bechstedt, Marcelo Marques, and Lara K Teles. Tuning electronic properties and band alignments of phosphorene combined with mose2 and wse2. The Journal of Physical Chemistry C, 121(7):3862–3869, 2017.

[187] The 2L α-Te/1L β-Te junction turns out to be unstable and relaxes in a simple 3L α-Te, at least for small, commensurate unit cells and free-standing calculations. However, by playing with charge doping, twist angles or strain [137], metastable structures with reduced quasi-covalent interactions within the interface could result, preventing the monolayer phase transition from beta to alpha in the heterostructure.

[188] Crystalline Silicon Photovoltaics Research. https://www.energy.gov/eere/solar/crystalline-silicon-photovoltaics-research.

[189] Simone Grillo, Sara Postorino, Maurizia Palummo, and Olivia Pulci. Tellurene polymorphs: A new frontier for solar harvesting with strong exciton anisotropy and high optical absorbance. Advanced Energy Materials, page 2400674, 2024.

[190] Yilei Li, Yi Rao, Kin Fai Mak, Yumeng You, Shuyuan Wang, Cory R. Dean, and Tony F. Heinz. Probing symmetry properties of few-layer mos2 and h-bn by optical second-harmonic generation. Nano Letters, 13(7):3329–3333, 2013.

[191] Xiaobo Yin, Ziliang Ye, Daniel A. Chenet, Yu Ye, Kevin O'Brien, James C. Hone, and Xiang Zhang. Edge nonlinear optics on a mos¡sub¿2¡/sub¿ atomic monolayer. Science, 344(6183):488–490, 2014.

[192] Julian Klein, Jakob Wierzbowski, Alexander Steinhoff, Matthias Florian, M Rosner, Florian Heimbach, K Muller, Frank Jahnke, Tim O Wehling, Jonathan J Finley, et al. Electric-field switchable second-harmonic generation in bilayer mos2 by inversion symmetry breaking. Nano letters, 17(1):392–398, 2017.

[193] Shivangi Shree, Delphine Lagarde, Laurent Lombez, Cedric Robert, Andrea Balocchi, Kenji Watanabe, Takashi Taniguchi, Xavier Marie, Iann C Gerber, Mikhail M Glazov, et al. Interlayer exciton mediated second harmonic generation in bilayer mos2. Nature Communications, 12(1):6894, 2021.

[194] Jing Wang, Nannan Han, Zheng-Dong Luo, Mingwen Zhang, Xiaoqing Chen, Yan Liu, Yue Hao, Jianlin Zhao, and Xuetao Gan. Electrically tunable second harmonic generation in atomically thin res2. ACS nano, 16(4):6404–6413, 2022.

[195] Kyle L Seyler, John R Schaibley, Pu Gong, Pasqual Rivera, Aaron M Jones, Sanfeng Wu, Jiaqiang Yan, David G Mandrus, Wang Yao, and Xiaodong Xu. Electrical control of second-harmonic generation in a wse2 monolayer transistor. Nature nanotechnology, 10(5):407–411, 2015.

[196] Huakang Yu, Deep Talukdar, Weigao Xu, Jacob B. Khurgin, and Qihua Xiong. Charge-induced second-harmonic generation in bilayer wse_2. Nano Letters, 15(8):5653–5657, 2015. PMID: 26203670.

[197] K. Yabana and G. F. Bertsch. Time-dependent local-density approximation in real time. Phys. Rev. B, 54:4484–4487, Aug 1996.

[198] F Calvayrac, PG Reinhard, and E Suraud. Nonlinear plasmon response in highly excited metallic clusters. Physical Review B, 52(24):R17056, 1995.

[199] George F Bertsch, J-I Iwata, Angel Rubio, and Kazuhiro Yabana. Real-space, real-time method for the dielectric function. Physical Review B, 62(12):7998, 2000.

[200] Nicolas Tancogne-Dejean, Oliver D Mücke, Franz X Kärtner, and Angel Rubio. Impact of the electronic band structure in high-harmonic generation spectra of solids. Physical review letters, 118(8):087403, 2017.

[201] Claudio Attaccalite and M Grüning. Nonlinear optics from an ab initio approach by means of the dynamical berry phase: Application to second-and third-harmonic generation in semiconductors. Physical Review B—Condensed Matter and Materials Physics, 88(23):235113, 2013.

[202] Ivo Souza, Jorge Íniguez, and David Vanderbilt. Dynamics of berry-phase polarization in time-dependent electric fields. Physical Review B, 69(8):085106, 2004.

[203] Giovanni Cistaro, Mikhail Malakhov, Juan José Esteve-Paredes, Alejandro José Uría-Álvarez, Rui EF Silva, Fernando Martin, Juan José Palacios, and Antonio Picon. Theoretical approach for electron dynamics and ultrafast spectroscopy (edus). Journal of Chemical Theory and Computation, 19(1):333–348, 2022.

[204] Claudio Attaccalite, Myrta Grüning, Hakim Amara, Sylvain Latil, and François Ducastelle. Two-photon absorption in two-dimensional materials: The case of hexagonal boron nitride. Physical Review B, 98(16):165126, 2018.

[205] Julien Guénolé, Wolfram G Nöhring, Aviral Vaid, Frédéric Houllé, Zhuocheng Xie, Aruna Prakash, and Erik Bitzek. Assessment and optimization of the fast inertial relaxation engine (fire) for energy minimization in atomistic simulations and its implementation in lammps. Computational Materials Science, 175:109584, 2020.

[206] David Kammerlander, Silvana Botti, Miguel A L Marques, Andrea Marini, and Claudio Attaccalite. Speeding up the solution of the bethe-salpeter equation by a double-grid method and wannier interpolation. Physical Review B—Condensed Matter and Materials Physics, 86(12):125203, 2012.

[207] R. W. Boyd. Nonlinear Optics. Academic Press, 3rd edition, 2008.

[208] Lucie Prussel, Rita Maji, Elena Degoli, Eleonora Luppi, and Valérie Véniard. Ab initio nonlinear optics in solids: linear electro-optic effect and electric-field induced second-harmonic generation. The European Physical Journal Special Topics, 232(13):2231–2240, 2023.

[209] M. F. C. Martins Quintela, N. M. R. Peres, and T. Garm Pedersen. Tunable nonlinear excitonic optical response in biased bilayer graphene. Phys. Rev. B, 110:085433, Aug 2024.

[210] A Oschlies, RW Godby, and RJ Needs. Gw self-energy calculations of carrier-induced band-gap narrowing in n-type silicon. Physical Review B, 51(3):1527, 1995.

[211] Shyam Bharadwaj, SM Islam, Kazuki Nomoto, Vladimir Protasenko, Alexander Chaney, Huili Grace Xing, and Debdeep Jena. Bandgap narrowing and mott transition in si-doped al0. 7ga0. 3n. Applied Physics Letters, 114(11), 2019.

[212] Shiyuan Gao, Yufeng Liang, Catalin D Spataru, and Li Yang. Dynamical excitonic effects in doped two-dimensional semiconductors. Nano letters, 16(9):5568–5573, 2016.

[213] Mikhail Vasilievich Durnev and Mikhail Mikhailovich Glazov. Excitons and trions in two-dimensional semiconductors based on transition metal dichalcogenides. Physics-Uspekhi, 61(9):825, 2018.

[214] Yun-Chen Shih, Fredrik Andreas Nilsson, and Guang-Yu Guo. Electron energy-loss spectrum and exciton band structure of wse_2 monolayer studied by ab initio bethe-salpeter equation calculations. `https://arxiv.org/abs/2407.15039`, 2024.

[215] Wilfried Schäfer and Martin Wegener. Semiconductor optics and transport phenomena. Springer Science & Business Media, 2013.

[216] Etienne Lorchat, Luis E Parra López, Cédric Robert, Delphine Lagarde, Guillaume Froehlicher, Takashi Taniguchi, Kenji Watanabe, Xavier Marie, and Stéphane Berciaud. Filtering the photoluminescence spectra of atomically thin semiconductors with graphene. Nature nanotechnology, 15(4):283–288, 2020.

[217] Thibault Sohier, Marco Gibertini, and Matthieu J Verstraete. Remote free-carrier screening to boost the mobility of fröhlich-limited two-dimensional semiconductors. Physical Review Materials, 5(2):024004, 2021.

[218] Simone Grillo, Elena Cannuccia, Maurizia Palummo, Olivia Pulci, and Claudio Attaccalite. Tunable second harmonic generation in 2D materials: Comparison of different strategies. SciPost Phys. Core, 7:081, 2024.

[219] George Gruner. Density waves in solids. CRC press, 2018.

[220] Rudolf Ernst Peierls. Quantum theory of solids, volume 9. Clarendon Press, 1964.

[221] JM Luttinger. An exactly soluble model of a many-fermion system. Journal of mathematical physics, 4(9):1154–1162, 1963.

[222] F Duncan M Haldane. 'luttinger liquid theory'of one-dimensional quantum fluids. i. properties of the luttinger model and their extension to the general 1d interacting spinless fermi gas. Journal of Physics C: Solid State Physics, 14(19):2585, 1981.

[223] Johannes Voit. One-dimensional fermi liquids. Reports on Progress in Physics, 58(9):977, 1995.

[224] Daniele Varsano, Sandro Sorella, Davide Sangalli, Matteo Barborini, Stefano Corni, Elisa Molinari, and Massimo Rontani. Carbon nanotubes as excitonic insulators. Nature communications, 8(1):1461, 2017.

[225] Sumio Iijima. Helical microtubules of graphitic carbon. nature, 354(6348):56–58, 1991.

[226] Sumio Iijima and Toshinari Ichihashi. Single-shell carbon nanotubes of 1-nm diameter. nature, 363(6430):603–605, 1993.

[227] PM Ajayan and TW Ebbesen. Nanometre-size tubes of carbon. Reports on Progress in Physics, 60(10):1025, 1997.

[228] Sander J Tans, Michel H Devoret, Hongjie Dai, Andreas Thess, Richard E Smalley, LJ Geerligs, and Cees Dekker. Individual single-wall carbon nanotubes as quantum wires. Nature, 386(6624):474–477, 1997.

[229] Philip Kim, Li Shi, Arun Majumdar, and Paul L McEuen. Thermal transport measurements of individual multiwalled nanotubes. Physical review letters, 87(21):215502, 2001.

[230] Maxim A Stolyarov, Guanxiong Liu, Matthew A Bloodgood, Ece Aytan, Chenglong Jiang, Rameez Samnakay, Tina T Salguero, Denis L Nika, Sergey L Rumyantsev, Michael S Shur, et al. Breakdown current density in h-bn-capped quasi-1d tase 3 metallic nanowires: prospects of interconnect applications. Nanoscale, 8(34):15774–15782, 2016.

[231] A Geremew, MA Bloodgood, E Aytan, BWK Woo, SR Corber, G Liu, K Bozhilov, TT Salguero, S Rumyantsev, MP Rao, et al. Current carrying capacity of quasi-1d zrte 3 van der waals nanoribbons. IEEE Electron Device Letters, 39(5):735–738, 2018.

[232] Shu Gong and Wenlong Cheng. One-dimensional nanomaterials for soft electronics. Advanced Electronic Materials, 3(3):1600314, 2017.

[233] Zhe Liu, Jing Xu, Di Chen, and Guozhen Shen. Flexible electronics based on inorganic nanowires. Chemical Society Reviews, 44(1):161–192, 2015.

[234] Scott Meyer, Thang Pham, Sehoon Oh, Peter Ercius, Christian Kisielowski, Marvin L Cohen, and Alex Zettl. Metal-insulator transition in quasi-one-dimensional hfte 3 in the few-chain limit. Physical Review B, 100(4):041403, 2019.

[235] Scott Stonemeyer, Jeffrey D Cain, Sehoon Oh, Amin Azizi, Malik Elasha, Markus Thiel, Chengyu Song, Peter Ercius, Marvin L Cohen, and Alex Zettl. Stabilization of nbte3, vte3, and tite3 via nanotube encapsulation. Journal of the American Chemical Society, 143(12):4563–4568, 2020.

[236] Reza J Kashtiban, Maria G Burdanova, Andrij Vasylenko, Jamie Wynn, Paulo VC Medeiros, Quentin Ramasse, Andrew J Morris, David Quigley, James Lloyd-Hughes, and Jeremy Sloan. Linear and helical cesium iodide atomic chains in ultranarrow single-walled carbon nanotubes: Impact on optical properties. ACS nano, 15(8):13389–13398, 2021.

[237] Hao Yan, J Nathan Hohman, Fei Hua Li, Chunjing Jia, Diego Solis-Ibarra, Bin Wu, Jeremy EP Dahl, Robert MK Carlson, Boryslav A Tkachenko, Andrey A Fokin, et al. Hybrid metal–organic chalcogenide nanowires with electrically conductive inorganic core through diamondoid-directed assembly. Nature materials, 16(3):349–355, 2017.

[238] Qiran Xiao, Joseph A Burg, Yao Zhou, Hao Yan, Can Wang, Yichuan Ding, Evan Reed, Robert D Miller, and Reinhold H Dauskardt. Electrically conductive copper core–shell nanowires through benzenethiol-directed assembly. Nano Letters, 18(8):4900–4907, 2018.

[239] Changgan Zeng, PRC Kent, Tae-Hwan Kim, An-Ping Li, and Hanno H Weitering. Charge-order fluctuations in one-dimensional silicides. Nature materials, 7(7):539–542, 2008.

[240] Paul C Snijders and Hanno H Weitering. Colloquium: Electronic instabilities in self-assembled atom wires. Reviews of Modern Physics, 82(1):307–329, 2010.

[241] JN Crain, JL McChesney, Fan Zheng, MC Gallagher, PC Snijders, M Bissen, C Gundelach, Steven C Erwin, and FJ Himpsel. Chains of gold atoms with tailored electronic states. Physical Review B, 69(12):125401, 2004.

[242] Pietro Gambardella, A Dallmeyer, K Maiti, MC Malagoli, W Eberhardt, K Kern, and C Carbone. Ferromagnetism in one-dimensional monatomic metal chains. Nature, 416(6878):301–304, 2002.

[243] Shasha Guo, Jiecai Fu, Peikun Zhang, Chao Zhu, Heming Yao, Manzhang Xu, Boxing An, Xingli Wang, Bijun Tang, Ya Deng, et al. Direct growth of single-metal-atom chains. Nature Synthesis, 1(3):245–253, 2022.

[244] Pascal Ferstl, Lutz Hammer, Christopher Sobel, Matthias Gubo, Klaus Heinz, M Alexander Schneider, Florian Mittendorfer, and Josef Redinger. Self-organized growth, structure, and magnetism of monatomic transition-metal oxide chains. Physical Review Letters, 117(4):046101, 2016.

[245] Jing-Kai Qin, Gang Qiu, Wen He, Jie Jian, Meng-Wei Si, Yu-Qin Duan, Adam Charnas, Dmitry Y Zemlyanov, Hai-Yan Wang, Wen-Zhu Shao, et al. Epitaxial growth of 1d atomic chain based se nanoplates on monolayer res2 for high-performance photodetectors. Advanced Functional Materials, 28(48):1806254, 2018.

[246] Priyanka Yogi, Julian Koch, Simone Sanna, and Herbert Pfnür. Electronic phase transitions in quasi-one-dimensional atomic chains: Au wires on si (553). Physical Review B, 105(23):235407, 2022.

[247] S Sanna, T Lichtenstein, Z Mamiyev, C Tegenkamp, and H Pfnür. How one-dimensional are atomic gold chains on a substrate? The Journal of Physical Chemistry C, 122(44):25580–25588, 2018.

[248] Alexander A Balandin, Fariborz Kargar, Tina T Salguero, and Roger K Lake. One-dimensional van der waals quantum materials. Materials Today, 55:74–91, 2022.

[249] You Meng, Wei Wang, and Johnny C Ho. One-dimensional atomic chains for ultimate-scaled electronics. ACS nano, 16(9):13314–13322, 2022.

[250] Joshua O Island, Aday J Molina-Mendoza, Mariam Barawi, Robert Biele, Eduardo Flores, José M Clamagirand, José R Ares, Carlos Sánchez, Herre SJ Van Der Zant, Roberto D'Agosta, et al. Electronics and optoelectronics of quasi-1d layered transition metal trichalcogenides. 2D Materials, 4(2):022003, 2017.

[251] Alexey Lipatov, Michael J Loes, Haidong Lu, Jun Dai, Piotr Patoka, Nataliia S Vorobeva, Dmitry S Muratov, Georg Ulrich, Bernd Kästner, Arne Hoehl, et al. Quasi-1d tis3 nanoribbons: mechanical exfoliation and thickness-dependent raman spectroscopy. ACS nano, 12(12):12713–12720, 2018.

[252] Ying Zhou, Liang Wang, Shiyou Chen, Sikai Qin, Xinsheng Liu, Jie Chen, Ding-Jiang Xue, Miao Luo, Yuanzhi Cao, Yibing Cheng, et al. Thin-film sb2se3 photovoltaics with oriented one-dimensional ribbons and benign grain boundaries. Nature Photonics, 9(6):409–415, 2015.

[253] Alex M Ganose, Keith T Butler, Aron Walsh, and David O Scanlon. Relativistic electronic structure and band alignment of bisi and bisei: candidate photovoltaic materials. Journal of Materials Chemistry A, 4(6):2060–2068, 2016.

[254] Guanxiong Liu, Sergey Rumyantsev, Matthew A Bloodgood, Tina T Salguero, Michael Shur, and Alexander A Balandin. Low-frequency electronic noise in quasi-1d tase3 van der waals nanowires. Nano letters, 17(1):377–383, 2017.

[255] Thomas A Empante, Aimee Martinez, Michelle Wurch, Yanbing Zhu, Adane K Geremew, Koichi Yamaguchi, Miguel Isarraraz, Sergey Rumyantsev, Evan J Reed, Alexander A Balandin, et al. Low resistivity and high breakdown current density of 10 nm diameter van der waals tase3 nanowires by chemical vapor deposition. Nano letters, 19(7):4355–4361, 2019.

[256] Fariborz Kargar, Zahra Barani, Nicholas R Sesing, Thuc T Mai, Topojit Debnath, Huairuo Zhang, Yuhang Liu, Yanbing Zhu, Subhajit Ghosh, Adam J Biacchi, et al. Elemental excitations in moi3 one-dimensional van der waals nanowires. Applied Physics Letters, 121(22), 2022.

[257] Alexey Lipatov, Jehad Abourahma, Gauthami Viswan, Khimananda Acharya, Tula R Paudel, Michael J Loes, Saman Bagheri, Esha Mishra, Thilini Kumari Ekanayaka, Mohammad Zaz, et al. Electronic transport and polarization-dependent photoresponse in few-layered hafnium trisulfide (hfs 3) nanoribbons. Journal of Materials Chemistry C, 11(28):9425–9437, 2023.

[258] Sébastien Lebègue, T Björkman, Mattias Klintenberg, Risto M Nieminen, and Olle Eriksson. Two-dimensional materials from data filtering and ab initio calculations. Physical Review X, 3(3):031002, 2013.

[259] Michael Ashton, Joshua Paul, Susan B Sinnott, and Richard G Hennig. Topology-scaling identification of layered solids and stable exfoliated 2d materials. Physical review letters, 118(10):106101, 2017.

[260] Kamal Choudhary, Irina Kalish, Ryan Beams, and Francesca Tavazza. High-throughput identification and characterization of two-dimensional materials using density functional theory. Scientific reports, 7(1):5179, 2017.

[261] Gowoon Cheon, Karel-Alexander N Duerloo, Austin D Sendek, Chase Porter, Yuan Chen, and Evan J Reed. Data mining for new two-and one-dimensional weakly bonded solids and lattice-commensurate heterostructures. Nano letters, 17(3):1915–1923, 2017.

[262] Nicolas Mounet, Marco Gibertini, Philippe Schwaller, Davide Campi, Andrius Merkys, Antimo Marrazzo, Thibault Sohier, Ivano Eligio Castelli, Andrea Cepellotti, Giovanni Pizzi, et al. Two-dimensional materials from high-throughput computational exfoliation of experimentally known compounds. Nature nanotechnology, 13(3):246–252, 2018.

[263] Sten Haastrup, Mikkel Strange, Mohnish Pandey, Thorsten Deilmann, Per S Schmidt, Nicki F Hinsche, Morten N Gjerding, Daniele Torelli, Peter M Larsen, Anders C Riis-Jensen, et al. The computational 2d materials database: high-throughput modeling and discovery of atomically thin crystals. 2D Materials, 5(4):042002, 2018.

[264] Peter Mahler Larsen, Mohnish Pandey, Mikkel Strange, and Karsten Wedel Jacobsen. Definition of a scoring parameter to identify low-dimensional materials components. Physical Review Materials, 3(3):034003, 2019.

[265] Davide Campi, Nicolas Mounet, Marco Gibertini, Giovanni Pizzi, and Nicola Marzari. Expansion of the materials cloud 2d database. ACS nano, 17(12):11268–11278, 2023.

[266] Chanjuan Shang, Li Fu, Si Zhou, and Jijun Zhao. Atomic wires of transition metal chalcogenides: A family of 1d materials for flexible electronics and spintronics. JACS Au, 1(2):147–155, 2020.

[267] Yanbing Zhu, Daniel A Rehn, Evan R Antoniuk, Gowoon Cheon, Rodrigo Freitas, Aditi Krishnapriyan, and Evan J Reed. Spectrum of exfoliable 1d van der waals molecular wires and their electronic properties. ACS nano, 15(6):9851–9859, 2021.

[268] Hadeel Moustafa, Peter Mahler Larsen, Morten N Gjerding, Jens Jørgen Mortensen, Kristian S Thygesen, and Karsten W Jacobsen. Computational exfoliation of atomically thin one-dimensional materials with application to majorana bound states. Physical Review Materials, 6(6):064202, 2022.

[269] Hadeel Moustafa, Peder Meisner Lyngby, Jens Jørgen Mortensen, Kristian S Thygesen, and Karsten W Jacobsen. Hundreds of new, stable, one-dimensional materials from a generative machine learning model. Physical Review Materials, 7(1):014007, 2023.

[270] Yanbing Zhu, Evan R Antoniuk, Dylan Wright, Fariborz Kargar, Nicholas Sesing, Austin D Sendek, Tina T Salguero, Ludwig Bartels, Alexander A Balandin, Evan J Reed, et al. Machine-learning-driven expansion of the 1d van der waals materials space. The Journal of Physical Chemistry C, 127(44):21675–21683, 2023.

[271] Chiara Cignarella, Davide Campi, and Nicola Marzari. Searching for the thinnest metallic wire. ACS nano, 2024.

[272] Saulius Gražulis, Adriana Daškevič, Andrius Merkys, Daniel Chateigner, Luca Lutterotti, Miguel Quiros, Nadezhda R Serebryanaya, Peter Moeck, Robert T Downs, and Armel Le Bail. Crystallography open database (cod): an open-access collection of crystal structures and platform for world-wide collaboration. Nucleic acids research, 40(D1):D420–D427, 2012.

[273] FIZ Karlsruhe. Inorganic crystal structure database (icsd). FIZ Karlsruhe: Karlsruhe, Germany, 2019.

[274] Guenter Bergerhoff, R Hundt, R Sievers, and ID Brown. The inorganic crystal structure data base. Journal of chemical information and computer sciences, 23(2):66–69, 1983.

[275] P Villars, N Onodera, and S Iwata. The linus pauling file (lpf) and its application to materials design. Journal of Alloys and Compounds, 279(1):1–7, 1998.

[276] The pauling file exposed through the materials platform for data science. https://mpds.io/. Database version: 1.0.0, access date: 02-01-2019.

[277] Debasis Bera, Lei Qian, Teng-Kuan Tseng, and Paul H. Holloway. Quantum dots and their multimodal applications: A review. Materials, 3(4):2260–2345, 2010.

[278] Günter Schmid, Monika Bäumle, Marcus Geerkens, Ingo Heim, Christoph Osemann, and Thomas Sawitowski. Current and future applications of nanoclusters. Chem. Soc. Rev., 28:179–185, 1999.

[279] Peihui Li, Li Zhou, Cong Zhao, Hongyu Ju, Qinghua Gao, Wei Si, Li Cheng, Jie Hao, Mengmeng Li, Yijian Chen, et al. Single-molecule nano-optoelectronics: insights from physics. Reports on Progress in Physics, 85(8):086401, 2022.

[280] Oksana Ostroverkhova. Organic optoelectronic materials: mechanisms and applications. Chemical reviews, 116(22):13279–13412, 2016.

[281] Daniela Dragoman and Mircea Dragoman. Terahertz fields and applications. Progress in quantum electronics, 28(1):1–66, 2004.

[282] Mark Lee and Michael C Wanke. Searching for a solid-state terahertz technology. Science, 316(5821):64–65, 2007.

[283] Richard R Hartmann, Junichiro Kono, and Mikhail E Portnoi. Terahertz science and technology of carbon nanomaterials. Nanotechnology, 25(32):322001, 2014.

[284] Gert Von Helden, Nigel G Gotts, and Michael T Bowers. Experimental evidence for the formation of fullerenes by collisional heating of carbon rings in the gas phase. Nature, 363(6424):60–63, 1993.

[285] K. S. Novoselov, A. K. Geim, S. V. Morozov, D. Jiang, Y. Zhang, S. V. Dubonos, I. V. Grigorieva, and A. A. Firsov. Electric field effect in atomically thin carbon films. Science, 306(5696):666–669, 2004.

[286] Alan Van Orden and Richard J Saykally. Small carbon clusters: spectroscopy, structure, and energetics. Chemical reviews, 98:2313–2358, 1998.

[287] Christian Neiss, Egor Trushin, and Andreas Görling. The nature of one-dimensional carbon: Polyynic versus cumulenic. ChemPhysChem, 15(12):2497–2502, 2014.

[288] Jan ML Martin, Jamal El-Yazal, and Jean-Pierre François. Structure and vibrational spectra of carbon clusters cn (n= 2–10, 12, 14, 16, 18) using density functional theory including exact exchange contributions. Chemical physics letters, 242(6):570–579, 1995.

[289] Mineo Saito and Yasuharu Okamoto. Second-order jahn-teller effect on carbon 4 n+ 2 member ring clusters. Physical Review B, 60(12):8939, 1999.

[290] Tommaso Torelli and Lubos Mitas. Electron correlation in c 4 n+ 2 carbon rings: aromatic versus dimerized structures. Physical review letters, 85(8):1702, 2000.

[291] Sundaram Arulmozhiraja and Takahisa Ohno. Ccsd calculations on c14, c18, and c22 carbon clusters. The Journal of chemical physics, 128(11), 2008.

[292] Katharina Kaiser, Lorel M Scriven, Fabian Schulz, Przemyslaw Gawel, Leo Gross, and Harry L Anderson. An sp-hybridized molecular carbon allotrope, cyclo [18] carbon. Science, 365(6459):1299–1301, 2019.

[293] Lorel M Scriven, Katharina Kaiser, Fabian Schulz, Alistair J Sterling, Steffen L Woltering, Przemyslaw Gawel, Kirsten E Christensen, Harry L Anderson, and Leo Gross. Synthesis of cyclo [18] carbon via debromination of c18br6. Journal of the American Chemical Society, 142(30):12921–12924, 2020.

[294] Glib V Baryshnikov, Rashid R Valiev, Artem V Kuklin, Dage Sundholm, and Hans Ågren. Cyclo [18] carbon: Insight into electronic structure, aromaticity, and surface coupling. The journal of physical chemistry letters, 10(21):6701–6705, 2019.

[295] Yueze Gao, Florian Albrecht, Igor Rončević, Isaac Ettedgui, Paramveer Kumar, Lorel M Scriven, Kirsten E Christensen, Shantanu Mishra, Luca Righetti, Max Rossmannek, et al. On-surface synthesis of a doubly anti-aromatic carbon allotrope. Nature, 623(7989):977–981, 2023.

[296] Pooja, Sarita Yadav, and Ravinder Pawar. Chemistry of cyclo [18] carbon (c18): A review. The Chemical Record, page e202400055, 2024.

[297] Jürg Hutter and Hans Peter Lüthi. The molecular structure of c6: a theoretical investigation. The Journal of chemical physics, 101(3):2213–2216, 1994.

[298] V Pless, HU Suter, and B Engels. Ab initio study of the energy difference between the cyclic and linear forms of the c6 molecule. The Journal of chemical physics, 101(5):4042–4048, 1994.

[299] Jan ML Martin and Peter R Taylor. Structure and vibrations of small carbon clusters from coupled-cluster calculations. The Journal of Physical Chemistry, 100(15):6047–6056, 1996.

[300] John D Watts and Rodney J Bartlett. The nature of monocyclic c10. a theoretical investigation using coupled-cluster methods. Chemical physics letters, 190(1-2):19–24, 1992.

[301] François Diederich, Yves Rubin, Carolyn B Knobler, Robert L Whetten, Kenneth E Schriver, Kendall N Houk, and YI Li. All-carbon molecules: evidence for the generation of cyclo [18] carbon from a stable organic precursor. Science, 245(4922):1088–1090, 1989.

[302] Dietmar A Plattner and KN Houk. C18 is a polyyne. Journal of the American Chemical Society, 117(15):4405–4406, 1995.

[303] Patrick W Fowler, Noriyuki Mizoguchi, David E Bean, and Remco WA Havenith. Double aromaticity and ring currents in all-carbon rings. Chemistry–A European Journal, 15(28):6964–6972, 2009.

[304] Vudhichai Parasuk, Jan Almlof, and Martin W Feyereisen. The [18] all-carbon molecule: cumulene or polyacetylene? Journal of the American Chemical Society, 113(3):1049–1050, 1991.

[305] Martin Feyereisen, Maciej Gutowski, Jack Simons, and Jan Almlöf. Relative stabilities of fullerene, cumulene, and polyacetylene structures for cn: n= 18–60. The Journal of chemical physics, 96(4):2926–2932, 1992.

[306] Juerg Hutter, Hans Peter Luethi, and Francois Diederich. Structures and vibrational frequencies of the carbon molecules c2-c18 calculated by density functional theory. Journal of the American Chemical Society, 116(2):750–756, 1994.

[307] Adina K Ott, Gregory A Rechtsteiner, Christian Felix, Oliver Hampe, Martin F Jarrold, Richard P Van Duyne, and Krishnan Raghavachari. Raman spectra and calculated vibrational frequencies of size-selected c 16, c 18, and c 20 clusters. The Journal of chemical physics, 109(22):9652–9655, 1998.

[308] AE Boguslavskiy, H Ding, and JP Maier. Gas-phase electronic spectra of c18 and c22 rings. The Journal of chemical physics, 123(3), 2005.

[309] Karunakaran Remya and Cherumuttathu H Suresh. Carbon rings: a dft study on geometry, aromaticity, intermolecular carbon–carbon interactions and stability. RSC advances, 6(50):44261–44271, 2016.

[310] Veronica L Murphy, Camille Farfan, and Bart Kahr. Chiroptical structure-property relations in cyclo [18] carbon and its in silico hydrogenation products. Chirality, 30(4):325–331, 2018.

[311] Sheik Haseena, K Rudharachari Maiyelvaganan, Muthuramalingam Prakash, and Mahesh Kumar Ravva. Cyclo [18] carbon-a new class of electron acceptor for organic solar cells applications. Journal of Molecular Structure, 1271:134025, 2023.

[312] E Brémond, AJ Pérez-Jiménez, Carlo Adamo, and Juan-Carlos Sancho-Garcia. Stability of the polyynic form of c 18, c 22, c 26, and c 30 nanorings: a challenge tackled by range-separated double-hybrid density functionals. Physical Chemistry Chemical Physics, 24(7):4515–4525, 2022.

[313] Zenner S Pereira and Edison Z da Silva. Spontaneous symmetry breaking in cyclo [18] carbon. The Journal of Physical Chemistry A, 124(6):1152–1157, 2020.

[314] TW Yen and SK Lai. Use of density functional theory method to calculate structures of neutral carbon clusters cn ($3 \leq n \leq 24$) and study their variability of structural forms. The Journal of chemical physics, 142(8), 2015.

[315] Eric J Bylaska, John H Weare, and Ryoichi Kawai. Development of bond-length alternation in very large carbon rings: Lda pseudopotential results. Physical Review B, 58(12):R7488, 1998.

[316] Eric J Bylaska, Ryoichi Kawai, and John H Weare. From small to large behavior: The transition from the aromatic to the peierls regime in carbon rings. The Journal of Chemical Physics, 113(15):6096–6106, 2000.

[317] Iuegyun Hong, Jeonghwan Ahn, Hyeondeok Shin, Hyeonhu Bae, Hoonkyung Lee, Anouar Benali, and Yongkyung Kwon. Competition between hückel's rule and jahn-teller distortion in small carbon rings: A quantum monte carlo study. The Journal of Physical Chemistry A, 124(18):3636–3640, 2020.

[318] AM Alexeev and ME Portnoi. Electric dipole moment oscillations in aharonov-bohm quantum rings. Physical Review B—Condensed Matter and Materials Physics, 85(24):245419, 2012.

[319] AM Alexeev and ME Portnoi. Terahertz transitions in aharonov-bohm quantum rings in an external electric field. physica status solidi c, 9(5):1309–1314, 2012.

[320] AM Alexeev, IA Shelykh, and ME Portnoi. Aharonov-bohm quantum rings in high-q microcavities. Physical Review B—Condensed Matter and Materials Physics, 88(8):085429, 2013.

[321] RA Ng, ME Portnoi, and RR Hartmann. Tuning terahertz transitions in cyclo [n] carbon rings. Physical Review B, 106(4):L041403, 2022.

[322] Fabien Bruneval, Tonatiuh Rangel, Samia M. Hamed, Meiyue Shao, Chao Yang, and Jeffrey B. Neaton. molgw 1: Many-body perturbation theory software for atoms, molecules, and clusters. Computer Physics Communications, 208:149–161, 2016.

[323] Giovanni Onida, Lucia Reining, RW Godby, R Del Sole, and Wanda Andreoni. Ab initio calculations of the quasiparticle and absorption spectra of clusters: the sodium tetramer. Physical review letters, 75(5):818, 1995.

[324] Eric L Shirley and Richard M Martin. Gw quasiparticle calculations in atoms. Physical Review B, 47(23):15404, 1993.

[325] Jeffrey C Grossman, Michael Rohlfing, Lubos Mitas, Steven G Louie, and Marvin L Cohen. High accuracy many-body calculational approaches for excitations in molecules. Physical Review Letters, 86(3):472, 2001.

[326] Thomas Körzdörfer and Noa Marom. Strategy for finding a reliable starting point for g 0 w 0 demonstrated for molecules. Physical Review B—Condensed Matter and Materials Physics, 86(4):041110, 2012.

[327] Maurizia Palummo, Conor Hogan, Francesco Sottile, Paolo Bagalá, and Angel Rubio. Ab initio electronic and optical spectra of free-base porphyrins: The role of electronic correlation. The Journal of chemical physics, 131(8), 2009.

[328] Carsten Rostgaard, Karsten Wedel Jacobsen, and Kristian Sommer Thygesen. Fully self-consistent gw calculations for molecules. Physical Review B—Condensed Matter and Materials Physics, 81(8):085103, 2010.

[329] Letizia Chiodo, Martin Salazar, Aldo H Romero, Savio Laricchia, Fabio Della Sala, and Angel Rubio. Structure, electronic, and optical properties of tio2 atomic clusters: An ab initio study. The Journal of chemical physics, 135(24), 2011.

[330] Susi Lehtola. A review on non-relativistic, fully numerical electronic structure calculations on atoms and diatomic molecules. International Journal of Quantum Chemistry, 119(19):e25968, 2019.

[331] RHWJ Ditchfield, Warren J Hehre, and John A Pople. Self-consistent molecular-orbital methods. ix. an extended gaussian-type basis for molecular-orbital studies of organic molecules. The Journal of Chemical Physics, 54(2):724–728, 1971.

[332] Thom H Dunning Jr. Gaussian basis sets for use in correlated molecular calculations. i. the atoms boron through neon and hydrogen. The Journal of chemical physics, 90(2):1007–1023, 1989.

[333] Robert W Boyd, Alexander L Gaeta, and Enno Giese. Nonlinear optics. In Springer Handbook of Atomic, Molecular, and Optical Physics, pages 1097–1110. Springer, 2008.

[334] PA Franken, Alan E Hill, CW el Peters, and Gabriel Weinreich. Generation of optical harmonics. Physical review letters, 7(4):118, 1961.

[335] Nicolaas Bloembergen, Richard K Chang, SS Jha, and CH Lee. Optical second-harmonic generation in reflection from media with inversion symmetry. Physical Review, 174(3):813, 1968.

[336] YR Shen. Surface second harmonic generation: a new technique for surface studies. Annual Review of Materials Science, 16(1):69–86, 1986.

[337] Yuen-Ron Shen. Optical second harmonic generation at interfaces. Annual Review of Physical Chemistry, 40(1):327–350, 1989.

[338] Yilei Li, Yi Rao, Kin Fai Mak, Yumeng You, Shuyuan Wang, Cory R Dean, and Tony F Heinz. Probing symmetry properties of few-layer mos2 and h-bn by optical second-harmonic generation. Nano letters, 13(7):3329–3333, 2013.

[339] Xiaobo Yin, Ziliang Ye, Daniel A Chenet, Yu Ye, Kevin O'Brien, James C Hone, and Xiang Zhang. Edge nonlinear optics on a mos2 atomic monolayer. Science, 344(6183):488–490, 2014.

[340] Wei-Ting Hsu, Zi-Ang Zhao, Lain-Jong Li, Chang-Hsiao Chen, Ming-Hui Chiu, Pi-Shan Chang, Yi-Chia Chou, and Wen-Hao Chang. Second harmonic generation from artificially stacked transition metal dichalcogenide twisted bilayers. ACS nano, 8(3):2951–2958, 2014.

[341] RI Woodward, RT Murray, CF Phelan, REP De Oliveira, TH Runcorn, EJR Kelleher, S Li, EC De Oliveira, GJM Fechine, GJDM Eda, et al. Characterization of the second-and third-order nonlinear optical susceptibilities of monolayer mos2 using multiphoton microscopy. 2D Materials, 4(1):011006, 2016.

[342] Zeyuan Sun, Yangfan Yi, Tiancheng Song, Genevieve Clark, Bevin Huang, Yuwei Shan, Shuang Wu, Di Huang, Chunlei Gao, Zhanghai Chen, et al. Giant nonreciprocal second-harmonic generation from antiferromagnetic bilayer cri3. Nature, 572(7770):497–501, 2019.

[343] Zhuoliang Ni, Nan Huang, Amanda V Haglund, David G Mandrus, and Liang Wu. Observation of giant surface second-harmonic generation coupled to nematic orders in the van der waals antiferromagnet feps3. Nano Letters, 22(8):3283–3288, 2022.

[344] Hao Chu, Chang Jae Roh, Joshua O Island, Chen Li, Sungmin Lee, Jingjing Chen, Je-Geun Park, Andrea F Young, Jong Seok Lee, and David Hsieh. Linear magnetoelectric phase in ultrathin mnps 3 probed by optical second harmonic generation. Physical review letters, 124(2):027601, 2020.

[345] J-Y Chauleau, Eloi Haltz, C Carrétéro, S Fusil, and Michel Viret. Multi-stimuli manipulation of antiferromagnetic domains assessed by second-harmonic imaging. Nature materials, 16(8):803–807, 2017.

[346] Shuai Xu, Jiesu Wang, Pan Chen, Kuijuan Jin, Cheng Ma, Shiyao Wu, Erjia Guo, Chen Ge, Can Wang, Xiulai Xu, et al. Magnetoelectric coupling in multiferroics probed by optical second harmonic generation. Nature communications, 14(1):2274, 2023.

[347] Bevin Huang, Genevieve Clark, Efrén Navarro-Moratalla, Dahlia R Klein, Ran Cheng, Kyle L Seyler, Ding Zhong, Emma Schmidgall, Michael A McGuire, David H Cobden, et al. Layer-dependent ferromagnetism in a van der waals crystal down to the monolayer limit. Nature, 546(7657):270–273, 2017.

[348] H Regensburger, R Vollmer, and J Kirschner. Time-resolved magnetization-induced second-harmonic generation from the ni (110) surface. Physical Review B, 61(21):14716, 2000.

[349] Houk Jang, Krishna P Dhakal, Kyung-Il Joo, Won Seok Yun, Sachin M Shinde, Xiang Chen, Soon Moon Jeong, Suk Woo Lee, Zonghoon Lee, JaeDong Lee, et al. Transient shg imaging on ultrafast carrier dynamics of mos2 nanosheets. Advanced Materials, 30(14):1705190, 2018.

[350] Claudio Attaccalite, M Grüning, and A Marini. Real-time approach to the optical properties of solids and nanostructures: Time-dependent bethe-salpeter equation. Physical Review B—Condensed Matter and Materials Physics, 84(24):245110, 2011.

[351] Myrta Grüning and Claudio Attaccalite. Second harmonic generation in h-bn and mos 2 monolayers: Role of electron-hole interaction. Physical Review B, 89(8):081102, 2014.

[352] Myrta Grüning, D Sangalli, and Claudio Attaccalite. Dielectrics in a time-dependent electric field: A real-time approach based on density-polarization functional theory. Physical Review B, 94(3):035149, 2016.

[353] JE Sipe and Ed Ghahramani. Nonlinear optical response of semiconductors in the independent-particle approximation. Physical Review B, 48(16):11705, 1993.

[354] RD King-Smith and David Vanderbilt. Theory of polarization of crystalline solids. Physical Review B, 47(3):1651, 1993.

[355] David Vanderbilt and RD King-Smith. Electric polarization as a bulk quantity and its relation to surface charge. Physical Review B, 48(7):4442, 1993.

[356] Raffaele Resta. Macroscopic electric polarization as a geometric quantum phase. Europhysics Letters, 22(2):133, 1993.

[357] R. Bogad, "Radiative lifetimes of anisotropic 2D excitons", Master Thesis, Universitaet Wien. https://utheses.univie.ac.at/detail/47496.

[358] Daichi Kozawa, Rajeev Kumar, Alexandra Carvalho, Kiran Kumar Amara, Weijie Zhao, Shunfeng Wang, Minglin Toh, Ricardo M Ribeiro, Antonio H Castro Neto, Kazunari Matsuda, et al. Photocarrier relaxation pathway in two-dimensional semiconducting transition metal dichalcogenides. Nature communications, 5(1):4543, 2014.

[359] Norma Rivano, Nicola Marzari, and Thibault Sohier. Density functional perturbation theory for one-dimensional systems: Implementation and relevance for phonons and electron-phonon interactions. Physical Review B, 109(24):245426, 2024.

[360] Thibault Sohier, Matteo Calandra, and Francesco Mauri. Density functional perturbation theory for gated two-dimensional heterostructures: Theoretical developments and application to flexural phonons in graphene. Physical Review B, 96(7):075448, 2017.